Bauhaus Summer School

023

"Model Validation and Simulation"
Graduate Courses for Structural Engineering Applications

Schriftenreihe des Instituts
für Konstruktiven Ingenieurbau
Bauhaus-Universität Weimar

INSTITUT FÜR KONSTRUKTIVEN INGENIEURBAU

Bauhaus Summer School

"Model Validation and Simulation"

Graduate Courses for Structural Engineering Applications

6th – 17th August 2012

Content

Foreword

The past decade has seen a rapid development of numerical methods and sophisticated modelling in different areas of civil engineering, especially in constructions for a sustainable environment. Both scientific approaches and practical solutions using recent developments of data acquisition and data management related to structural engineering and earth sciences are of major interest. Advanced education has to consider that most of the challenging future constructions will require further theoretical and practical developments in a close collaboration of engineering practice and research. The Bauhaus Summer School series provides an international forum for such an exchange of methods and skills related to the interaction between different disciplines of modern engineering science.

The 2012 civil engineering course was held in August over two weeks at Bauhaus-Universität Weimar. The overall aim was the exchange of research and modern scientific approaches in the field of model validation and simulation between well-known experts acting as lecturers and active students. Besides these educational intentions the social and cultural component of the meeting has been in the focus. 48 graduate and doctoral students from 20 different countries and 22 lecturers from 12 countries attended this summer school. Among other aspects, this activity can be considered successful as it raised the sensitivity towards both the significance of research in civil engineering and the role of intercultural exchange.

This volume summarizes and publishes some of the results: abstracts of key note papers presented by the experts and selected student research works. The overview reflects the quality of this summer school. Furthermore the individual contributions confirm that for active students this event has been a research forum and a special opportunity to learn from the experiences of the researchers in terms of methodology and strategies for research implementation in their current work.
On behalf of the Faculty of Civil Engineering, Bauhaus-Universität

Weimar, I would like to thank everyone for their contribution to the scientific content, the social events, the organization and the realization of the Bauhaus Summer School 2012. Particular thanks to all the lecturers who spent part of their annual leave to come to Weimar, to Frank Werner and Jochen Schwarz as the initiators, to Lars Abrahamczyk and Daniela Raddi for the excellent organization. In addition, the Faculty of Civil Engineering is extremely grateful for the sponsorship from German Academic Exchange Service (DAAD). The successful Bauhaus Summer School 2012 and this book would not have been possible without this generous financial support.

Weimar, April 2013
Karl J. Witt, Dean of the Faculty

Course Description

WERNER, Frank and
SCHWARZ, Jochen
Bauhaus-Universität Weimar

Introduction

Bauhaus Summer School has a long tradition that goes back to a series of Summer Academies, "Advanced Studies — Structural Engineering and CAE", offered by the Faculty of Civil Engineering. From the early beginning of these courses, it was agreed among the contributing departments, lecturers and supervisors that on the basis of demanding engineering projects an advanced level of qualification should be ensured. The experiences from previous summer schools at the Bauhaus-Universität Weimar, conducted in the years from 1998 until 2008, show that there is an increasing demand in training fields between studies and business requirements.

In 1998, twenty students participated in the first summer school. In 2008, 122 international students applied for the participation in the summer school. In 2012, 48 students from 20 different countries could be admitted (Figure 1). Since 2011, the Summer School has been supported by the Lifelong Learning Programme. Its innovative character results from the ambitious engineering tasks derived from current research topics by the participating institutions, the intensive assistance, and the project related training of simulation and modeling techniques introduced by key lectures in civil engineering.

The acquired knowledge is applied to scientific and practically relevant projects within a compact course. Such a "hands-on approach" is commonly not included in regular teaching programmes. Several targets harmonically overlap. The students will be trained in the use of modern software tools, design concepts and their practical applications. The course targets postgraduate students (i.e. second cycle (M.Sc.) and third cycle (PhD)) from different institutions and countries to enable knowledge transfer between the participants. The interdisciplinary teamwork in the projects combined with an intensive assistance by the academic staff shall enable the students to prepare and present a final presentation of the project results.

Targets and Objectives

Different language skills of the participants pose high demands on the management abilities and will train the ability to work in a team. The current state-of-the-art in the above mentioned fields will be presented to the participants during the lectures. Recent developments in Model Validation and Simulation will be added by additional presentations of the partner institutions or other invited experts. Special topics from the mentioned fields will be dealt with during the project work in small groups.

The young scientists will be offered the possibility to exchange modern scientific knowledge in a realistic training setting. Towards the end of the course, students are requested to present and discuss their own work in front of a broad scientific audience. The results from several national and international projects of the Center for Structural Dynamics and Earthquake Engineering of the Bauhaus-Universität Weimar are included in the programme.

The management and presentation skills of the participants will be improved and a training opportunity will be provided to share the work and experience in a team. The participants are invited to find the value of new partnerships and creative networking by the participating institutions (Fig. 2).

Figure 1 — Home countries of the Participants of summer course

Figure 2 — European Project Partners

Current Course Topics

At the national level, no similar workshop to the International Summer Academy "Model Validation and Simulation" is known. The relevance of the course topics themselves is undisputable; model validation and simulation play a central role in the work of civil and structural engineers. In practice day-by-day, engineers deal with models supporting the solution specific design problems. Because of the increasing demand of sophistication, more and more structures are designed by groups of engineers from different countries.Different substructures or materials with different properties are often combined or interacting (e.g. soil and structure, structures and components). Due to this, models have to be validated by measurements, experimental testing and simulations. Therefore, the course topics include hybrid methods of model calibration using instrumental testing methods.

Experimental facilities are used or being implemented for providing the database for the numerical reinterpretation. Excursion to building sites and leading companies illustrate the practical link between advanced modeling and simulation techniques and qualified structural solutions. The transfer of real existing building data into different basic structural models and the comparison of their robustness with respect to increasing abstractness and reduced dimensionality are major points of discussion. The effect of model assumptions will be studied on the basis of different software tools, including considerations of the uncertainty and the scatter of building response quantities.

Referring to recent code developments, participants are requested to present national design practice and experience from applications, focusing on the efforts that contribute to new concepts, evaluation strategies and the quality assurance of structural models. In general, the Summer School combines theoretical and practical tasks. The participants are invited to use modern analyses methods in the field of structural engineering and dynamics.

By providing students with advanced, scientifically-based interdisciplinary knowledge, skills and methods, they are trained to react to demanding engineering tasks in the areas of planning, construction and realization of structures under specific impact and action conditions. They are also able to carry out site- or structure-specific risk analyses using modern tools for gauging the threat of extreme loadings. In order to structure and reflect the complexity of the chain of reactions inherent to the impact side, various disciplines and engineering-related areas of the natural sciences are explored.

The Bauhaus Summer School examines the central role that civil engineering plays in lessening the impact of extreme loadings e.g. natural disasters and focuses on the engineering methods that can be used to assess and reduce the vulnerability of buildings and their structural systems.

The need of hazard and impact–resistant structural systems requires specific and innovative solutions in cases where extreme loads from different hazard types have to be sustained, including concepts to combine conventional engineered systems (R.C., steel) with locally available materials and construction types. By offering international projects the programme provides insight to the challenges from a global perspective.

The modular structure of the programme allows the participants to address current and trendsetting problems and research topics. Key aspects of the Summer School are linked to the Research Training Group 1462 ("Model Validation in Structural Engineering"), which is involved with the project "Calibration of Numerical Models in Civil Engineering Applications".

The topics of the 2012 course highlight the broad spectrum of engineering tasks in the following fields of modeling and simulation:

- Structural Engineering (incl. requirements on structural models, model verification, validation and updating);
- Geodynamics (incl. fundamentals in soil dynamics, analytical and numerical strategies, concepts of soil-structure interaction, dynamic laboratory and field testing);
- Earthquake Hazard and Risk engineering (incl. Description of seismic action, engineering approaches of seismic hazard assessment, Interpretation of earthquake damage cases, Recent projects and risk studies);
- Simulation and Testing of Steel and Glass Structures (incl. Computational models for linear and nonlinear analysis, Practical demonstration and simulation, Finite element modeling and analysis of stresses);
- Calibration of Numerical Models in Civil Engineering Applications (incl. Calibration of models as optimization, parameter identification of a dynamically driven bar and calibration of a multifield model of a gravity dam);
- Long-Span Bridge Aeroelasticity (incl. Dynamic analysis of long-span cable-supported bridges, realistic simulation of the structural behaviour and Models for Predicting Wind-induced Vibrations of Long-span Bridges);

The Summer School is divided into two parts. The first part concentrates on the theoretical fundamentals and the current state of research related to projects and special lectures from members of partner institutions. An introduction to specific research themes of all partners will be offered through special lectures.

The second part focuses on interdisciplinary team work within the project groups under intensive supervision. Following a pre-selection and review of the submitted papers, participants are invited to present the advanced state of their research in Special Theme Sessions. The outcome — presented by the herein compiled reports — reaches an impressive level of results and graphical elaboration.

Guest Lecturer

Numerical modelling of non linear constitutive laws

BOSO, Daniela
University of Padova

Abstract

In the past, linear constitutive laws were mostly considered for the modelling of material behaviours. However, during last decades there has been a definite trend toward a better understanding and consequently to an enhanced exploit of material performances. Non-linear constitutive laws are very common, one can immediately think of yielded steel or reinforced concrete. Furthermore, the modern technology gives the opportunity to develop advanced, knowledge-based materials, to use features and qualities of the individual components for an optimal performance.

Composite materials are more and more applied in engineering practice. They allow to take advantage of the different properties of the initial materials, of the geometric structure and of the interaction between the constituents to obtain a tailored behaviour as a final result.

Therefore, it seems clear that modern engineers will have to deal with the modeling and verification of nonlinear materials and structures. In these cases, the constitutive law in closed form is not always obtainable. When this is not possible, numerical methods and computational approaches allow likewise for a detailed description of the non linear behaviour. In this lecture some of the approaches used for computational modeling will be presented, such as virtual testing, and asymptotic homogenization. In addition, some soft computing techniques, based on artificial neural networks, will be illustrated as they are a powerful and promising tool both for modeling of composite materials and improvement of computational efficiency.

Modeling of composite steel — concrete bridges

VAYAS, Ioannis
National Technical University of Athens

Abstract

The lecture presents in eight sections modeling alternatives for composite bridges. Section 1 shows the current types of composite bridges that include plate girders, box girders, trusses, arches and cable-stayed bridges. Section 2 shows models for global analysis appropriate for the determination of internal forces and moments, deformations and vibrations. It includes the presentation of beam models, grillage models and 3-D models with the relevant field of application, their benefits, drawbacks and limits. Section 3 introduces cracking of concrete slab, the extent of cracked regions and how they are modeled. Section 4 deals with the effective width in wide flanges due to shear lag and shows methods for its determination in concrete and steel flanges. Section 5 deals with lateral stability of girders that is of importance specifically during construction stages. Section 6 indicates the effects of bracings both in transverse direction and in plan, with examples in curved bridges and at the service stage. Section 7 introduces the effects of the rheological behavior of concrete. It shows the determination of creep shrinkage and their introduction in analysis and design. Finally section 8 show Finite Element models that are appropriate for local analyses and for validation of simpler models.

Evaluation Methods for Prediction Quality of Coupled Partial Models

KEITEL, Holger

Abstract

The process of analysis and design in structural engineering requires the consideration of different partial models of loading, structural material, structural elements and analysis type, among others. The various partial models are combined by coupling of their several components. Due to a large number of available partial models describing similar phenomena many different model combinations are possible to simulate the same quantities of a structure. The challenging task of an engineer is to select a model combination that ensures a sufficient reliable prognosis. In order to achieve this reliable prognosis of the overall structural behavior, on the one hand a high individual quality of the partial models and on the other hand an adequate coupling of the partial models is needed.

Therefore, this lecture gives an introduction into the field of model quality evaluation. First, the basics of partial models and their coupling are given and the major modeling techniques — inverse modeling, stochastic modeling, adaptive modeling, and multiscale modeling — are presented. Further, several model properties are explained that allow for a quantitative model comparison. In order to give an example of model quality evaluation the field of stochastic modeling is shown more detailed and this technique is applied for the evaluation of concrete creep models. The benefits of choosing the most appropriate creep model are demonstrated. Finally, the prediction quality of several coupled partial models is exploited by means of sensitivity analysis and graph theory using an example of a bridge structure.

Unsaturated soils — Fundamentals and Overview of Applications

TRIPATHY, Snehasis
School of Engineering, Cardiff University, UK

Abstract

The main focus of the lecture will be to create an awareness concerning the role of negative pore-water pressure (suction) on the engineering behaviour of soils. The presentation will cover an introduction to saturated and unsaturated soil mechanics, examples of classical Geotechnical and Geoenvironmental engineering problems, roles of pore-water on the engineering behaviour of soils with aids of video demonstration of simple laboratory-scale experiments, definitions of suction, need for a saturated/unsaturated mechanics of soils, how to measure and induce suction in soils via video demonstration of some laboratory tests. The presentation will close by emphasizing the applications of suction on engineering behaviour of unsaturated soils.

Advanced transmitting boundary conditions for large-scale SSI problems and applications on parallel computing platforms

GENES, M. Cemal
Mustafa Kemal University,
Civil Engineering Department,
31200 Iskenderun/Hatay,
Turkey

Abstract

The dynamic response of massive, stiff, and embedded structures in relatively soft soil conditions such as nuclear reactors, tunnels, liquid-storage tanks, gravity dams, and high-rise buildings are affected by soil-structure interactions (SSI) as well as the dynamic characteristics of the exciting loads (i.e. earthquake, wind, explosion, machinery vibrations) and the structures. The effect of the SSI may alter the dynamic characteristics of the stiff, rigid and massive structures resting on or embedded in relatively soft and/or layered media significantly.

Soil region, which in many cases presents a complex and non-linear behaviour, can be discretized using the Finite Element Method (FEM), the Boundary Element Method (BEM) or hybrid models (Figure 1). All of these have advantages and disadvantages depending on the applied problem.

In this course, two finite element and boundary element based SSI models will be presented.

The first model: A finite element (FE) based SSI model and its parallelized algorithm for applications on distributed systems will be presented. The SSI model is established by combining two methods: the Consistent Infinitesimal FE Cell Method (also referred to as 'the scaled boundary-finite element method') proposed by Wolf and Song (Finite-element modelling of unbounded media, Wiley, England, 1996) for modelling the soil region extending to infinity (far-field), and the standard FE for the finite region (near-field) and the structure. By using this combined model, a computer program for harmonic and transient analyses of soil-structure systems is coded. In order to decrease the computation time and achieve the solution of large-scale problems, the model is parallelized. As a result of this parallel solution, significant time is saved for large-scale problems.

The second model: a coupled model based on finite element method (FEM), boundary element method (BEM) and scaled boundary FEM (SBFEM) for dynamic response of 2D structures resting on layered soil media will be presented. The SBFEM and BEM are used for modelling the dynamic response of the unbounded media (far-field). The standard FEM is used for modelling the finite region (near-field) and the structure. The objective of the development of this coupled model is to combine advantages of above-mentioned three numerical models to solve various SSI problems efficiently and effectively. These three methods are coupled (FE–BE–SBFEM) via substructuring method, and a computer programme is developed for the harmonic analyses of SSI systems. The results of the proposed model agree with the results presented in the literature for the chosen problems. The advantages of the model are demonstrated through these comparisons.

For this model also, an algorithm for a parallelized FE–BE–SBFEM for harmonic and transient dynamic response of large-scale 2D structures embedded in or on layered soil media will be presented. The objective of the development of this parallelized coupled model is to use the power of high performance computing, and to take into account the advantages and evade the disadvantages of the above mentioned numerical methods for modelling of the unbounded media in SSI systems. The development of the parallel algorithm for this model is essential for solving arbitrarily shaped large-scale SSI problems, which cannot be solved within reasonable elapsed times by a serial algorithm. The efficiency of the proposed parallel algorithm and the validity of the coupled model are shown by means of several numerical examples, indicating the excellent accuracy and applicability of the parallel algorithm with considerable time-savings in large-scale problems.

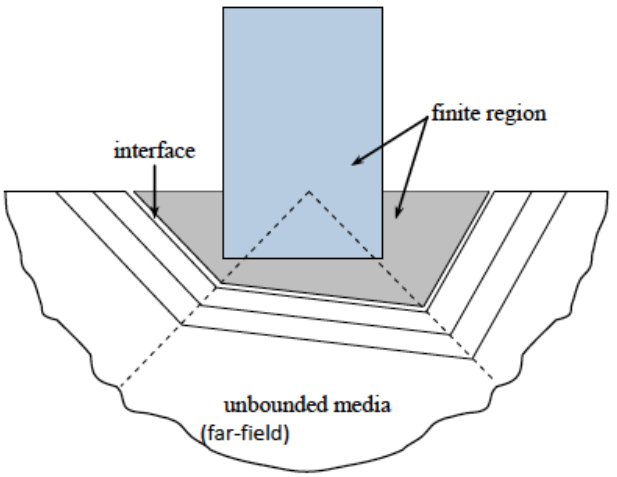

Figure 1 – Concept of the SSI Problem

Seismic design of tall and slender structures including rotational components of the ground motion: EN 1998-6 approach

VASILEV, G.
University of Architecture, Civil Engineering & Geodesy, Faculty of Civil Engineering, Bulgaria

BONEV, Zdravko
University of Architecture, Civil Engineering & Geodesy, Faculty of Civil Engineering, Bulgaria

Abstract

First part of the study deals with implementation of an advanced model of seismic action — ground accelerations, which allow for taking into account the spatial variability of seismic action. According to this approach for certain types of structures (tall and slender structures, long in plan and irregular structures) inclusion of translational acceleration components only into the analysis is not sufficient to reach safe design solution. For this kind of structures the use of advanced modeling of seismic action requires inclusion of rotational components of the ground motion (rotational accelerations). The well known model of seismic action containing three translational acceleration components, now should be upgraded by adding three rotational components of accelerations. All ground acceleration components are represented by their response spectra. Looking then to response spectrum method and linear analysis, it should be generalized and extended to be capable of evaluating the mixed spectral response derived as a result of translational/rotational components.

As a result of the analysis it is proven, that the action effects generated by mixed translation — rotational seismic input are greater than the corresponding action effects resulting from translational seismic input only. The general idea is that the missing of rotational components contribution leads to unfavorable type of loading and unsafe design solutions.

The general purpose of the second part of the study is the evaluation of seismic soil-foundation-structure interaction effects on overall seismic behavior. Seismic input is assumed to be free field motion of the site, being represented by ground accelerations in Fourier power series format. The analysis is carried out in time domain, assuming linear behavior of the structure and soil. Upper structure, on one hand, and

foundation-soil system on the other hand, are considered separately by means of substructure approach assuming steady-state response under sine signal with specific external frequency.

Steady state response of the foundation-soil system is represented through foundation impedances. They are input frequency dependent. Foundation impedances are implemented as a system of spring and dashpot elements (Kelvin–Vogt model). Impedances are used to connect the structure with the foundation, forming the flexible base boundary conditions. Impedance functions for rigid foundations and elastic homogeneous half space are available from the literature as typically classic case. For specific soil conditions such as layered or discontinuous media impedances should be found in advance using boundary element method as more general and numerically efficient computational technology.

As a result of the research a general algorithm for approximate evaluation of soil-foundation-structure interaction effects is provided. Dynamic amplification factor and amplitude magnification are studied as being dependent on input frequency. A comparative analysis with fixed-base supporting conditions is carried out. Numerical results concerning separate steps of the computational process are graphically illustrated and discussed.

Vibration serviceability of footbridges

VAN DEN BROECK, Peter
KU Leuven, Belgium

VAN NIMMEN, Katrien
KU Leuven, Belgium

Abstract

Predicting the dynamic performance of civil engineering structures due to crowd induced loading is an increasingly critical aspect of the vibration serviceability design process. Due to the increasing strength of materials and the trend towards greater slenderness, modern pedestrian bridges are very often lively structures prone to human induced vibrations. This presentation will discuss the current codes of practice (the European guideline HiVoSS [1–2] and the French guideline Setra [3]) that provide a methodology to assess the dynamic behaviour at design stage.

A slender steel footbridge (Eeklo, Belgium) is applied as case study. The operational modal analysis is performed to obtain the operational modal characteristics of the footbridge. These results are applied for the updating procedure of the numerical model (FE model) of the footbridge, improving the accuracy of the numerical predictions of the dynamic response of the bridge to pedestrian loading. The vibration serviceability check according to the current codes of practice is performed for both the initial versus the updated model of the footbridge. In some cases this results into a different evaluation, indicating the difficulty of making a reliable assessment of the dynamic performance of a the footbridge in the design phase.

[1] *HiVoSS, R. f. (2008). Design of footbridges.*

[2] *Butz, e. a. (2007). Advanced load models for synchronous pedestrian excitation and optimised design guidelines for steel footbridges (SYNPEX). Research Fund for Coal and Steel.*

[3] *Charles, P., & Hoorpah, W. (2006). Évaluation du comportement vibratoire des passerelles piétonnes sous l'action des piétons. France: Association Française de Génie Civil, Sétra/AFGC.*

Analysis and design of non-conventional cold-formed steel structures

DUNAI, László
Budapest University of Technology and Economics, Hungary

Abstract

Due to the development in galvanized high strength sheet production and cold-rolling technology the geometrical shape and size of cold-formed profiles significantly extended in the last two decades. The qualitative and quantitative changes of the profiles provide with the opportunity to use them in new functions, applying non-conventional structural solutions. The new arrangements, however, result in complex structural behavior which is not covered by standardized application rules.

Major fundamental and applied research activities have been completed on non-conventional cold-formed steel and composite structures at the Department of Structural Engineering of the Budapest University of Technology and Economics under the supervision of the author. The developed and investigated structures are as follows:

Cold-formed frames for smaller industrial buildings and for residential houses; the structural elements are single and double — hollow-type — cold-formed C-profiles, laterally not, or partially supported; the structural joints are self-drilling screwed or bolted connections of beams and columns in web-to-web arrangement.

Composite floor beams with cold-formed C-profiles, trapezoidal sheeting and partially drilled self-drilling screw shear connectors. Cold-formed roof trusses; the structural elements are single and double — hollow- and I-type — cold-formed C-profiles; the structural joints are bolted web, flange or web/flange connections.

The above arrangements of the cold-formed structural elements and the interaction with the eccentrically connected joints resulted in complex stability behavior with interacting local plate buckling, distortional buckling and global flexural/flexural-torsional and/or lateral torsional buckling, under compression and biaxial bending.

In the presentation the stability phenomena are discussed on the basis of interacting experimental and numerical research. In the first phase of the research fundamental experiments are completed on separated structural elements and joints. The stability behaviour modes are observed and numerical and design models are developed and verified. These results provided with a background for the design of complex structures.

In the next phase of the research the global and interacting stability phenomena are investigated on full-scale specimens of cold-formed frames, composite beams and trusses. By extending the tests using nonlinear finite element analysis the complicated behavior modes are characterized and applicable design methods are developed.

Acknowledgement: the research work is conducted under the financial support of the Hungarian OTKA T035147 and T049305 projects and the Lindab Ltd.

Asynchronous ground excitation and soil-structure interaction in the design of long bridges

SEXTOS, Anastasios G.
Aristotle University of Thessaloniki, Department of Civil Engineering

Abstract

Although bridge structures might seem at a first sight as rather linear and simple structural systems, their actual performance under earthquake loading is more complicated than that of ordinary buildings, because bridges have typically an order of magnitude larger overall and cross-sectional dimensions, different energy absorption mechanisms, more significant contribution of higher modes, while they are most commonly crossing non-uniform soil profiles.

Notwithstanding the significant research progress made to date which has already shed some light on many bridge engineering problems, the development of a "realistic" earthquake motion scenario is still associated with the highest relative uncertainty compared to maybe all other design and construction aspects. This is even more pronounced in the case of long bridges, where the variation of ground motion among its supports in terms of arrival time, frequency content and amplitude, can strongly affect both the pseudo-static and the dynamic components of the system. The objective of the presentation is to discuss the recent findings on the impact of asynchronous (i.e.- spatially variable) seismic excitation on the response of long bridges. The study focuses on the recently constructed 780 km Egnatia highway in northern Greece, and the 400 m cable-stayed Evripos bridge that connects the Evia island to the Greek mainland.

Despite the long distance from the earthquake source, the simultaneous free-field and on-structure recordings reveal interesting patterns of higher mode excitation and subsequent dynamic behavior. Based on the above comparative studies, an effort is made to focus on the dynamic response of the entire, interacting soil-structure system under asynchronous excitation and to propose means for assessing in advance the degree of its potential detrimental influence.

An analytical perspective for performance limits for structural walls

GÜLKAN, Polat
Çankaya University, Civil Eng. Department, 06810, Ankara, Turkey

Abstract

Proposed changes to modeling and acceptance criteria in seismic regulations for both flexure and shear dominated reinforced concrete structural walls suggest that a comprehensive examination is required for improved limit state definitions. This study uses a computational tool to investigate the deformation measures defined in terms of plastic rotations and local concrete and steel strains at the extreme fiber of rectangular structural walls. I compare requirements in ASCE/SEI 41, Eurocode 8 and the Turkish Seismic Code. This way, a critical evaluation is possible for the requirements embedded in these documents. I conclude that the performance limits must be refined by introducing additional parameters. Recommendations are provided for Eurocode 8 and the Turkish Seismic Code.

Earthquakes in developed mountainous regions

Jan Laue,
Institute for Geotechnical Engineering, ETH Zurich

Abstract

In geotechnical earthquake engineering, a subdivision is made into primary and secondary effects. Primary effects cover the behaviour of the soil under cyclic loadings leading to an amplification of the incoming waves. The term secondary effects umbrellas the effects of an earthquake to the surface like e.g. liquefaction, slope failures or rockfalls.

This contribution deals with the primary and secondary effects covered by geotechnical earthquake engineering. Focus is given to moderate events, which even though of magnitudes till 6 or 6.5 can have significant effects in mountainous regions. Valleys consisting of deep soft deposits and topographic effect can lead to high amplification of the event and lengthen the earthquake in time. Soft deposits are prone to liquefaction and slopes have in a static case already factors or safety of around one. In addition to the physical description of these risks for infrastructure and inhabitants, political issues like microzonation and their effects are discussed.

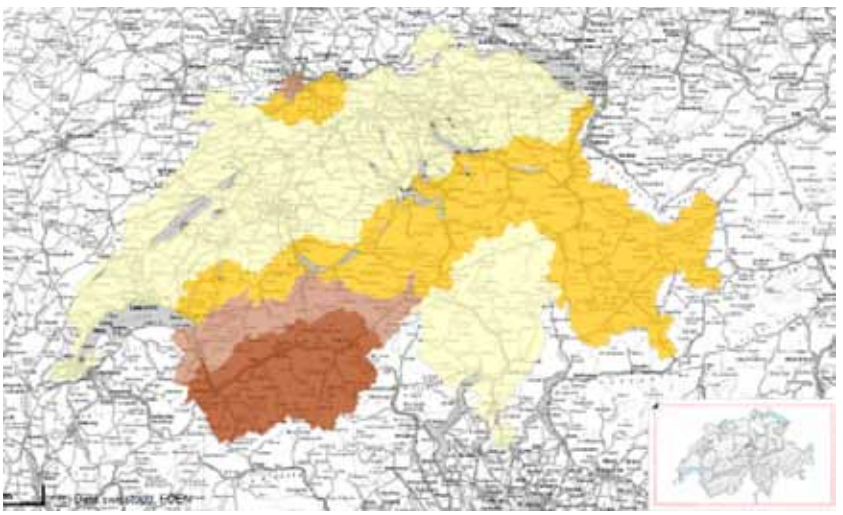

Participants

Vibration Based Post-Earthquake Damage Assessment of Structures

ANDIC, Halil Ibrahim
Middle East Technical University, Turkey

GUNES, Burcu
Atılım University, Turkey

GUNES, Oguz
Çankaya University, Turkey

Abstract

A large portion of Turkey's geography and population is prone to earthquake induced hazards and it is a priority need to take measures towards mitigating such hazards. In this manner, rapid damage assessment of structures after earthquakes has a vital importance for initiating effective emergency response. However, post-earthquake damage assessments of structures are required a detailed investigation that should be made by a professional engineer. These kinds of evaluations take very long time after especially severe earthquakes, and while this evaluation process delays, economic and social losses arising from earthquake increase. Therefore, safe and rapid post-earthquake damage assessment of structures is required. In parallel with this purpose, as a non-destructive in-situ alternative technology, vibration based assessment method provides an opportunity of condition assessment in a manner of structural integrity with the help of dynamic response which is recorded from structure. Especially, as it is possible to get environmental vibration data from structure easily before and after earthquake, researches on damage assessment methods which use these data is getting more popular. In this study, methods that are used to determine the structural damage assessment with using environmental vibration data which is belong to before and after earthquake will be summarized, and the developing method for RC frame structure will be introduced. An experimental study will be prepared in order to load RC frame gradually up to its ultimate load bearing capacity and simulate various damage levels. At each damage level, damage condition will be determined with the help of acceleration data which is obtained by both environmental vibration and impact testing. As a pre-stage of the study, vibration properties of RC frame for before and after damage scenario is determined with a comparative numerical study, and damage is tried to determine by using Damage Locating Vector (DLV) method.

Introduction

Structural health monitoring (SHM) is the process of implementing a damage identification strategy for civil infrastructures. Damage identification problem involves detection, localization and assessment of the extent of damage in a structure so that its remaining life can be predicted and possibly extended. SHM encompasses both local and global methods of damage identification. The local methods include visual inspections and non-destructive evaluation tools such as acoustic emission, ultrasonic, magnetic particle inspection, radiography and eddy current. All these techniques, however, require apriori localization of the damaged zone and easy access to the portion of the structure under inspection. As an alternative that overcomes these limitations, global vibration based methods have been widely developed over the years ([1], [2], [3], [4], [5], [6]).

SHM based on vibration measurements involves temporal observation of a structure using periodically sampled vibration measurements, extraction of damage sensitive features from these measurements and assessment of the current health state/integrity of the system. The basic premise of the vibration-based techniques is that the vibration characteristics or the so-called modal parameters (frequencies, mode shapes and modal damping) are functions of the physical properties of the structure (mass, energy dissipation mechanisms and stiffness) and changes in these physical properties cause changes in the modal properties. This postulation, however, is compromised by the fact that temperature changes, moisture and other environmental factors also produce changes in dynamic characteristics. If the causes of changes in dynamic characteristics other than damage are considered to be noise in the measurement, then the changes due to damage must be significantly larger than the noise in order for the techniques to work. Usually four different levels of damage identification are studied [7]: damage detection (Level 1), damage localization (Level 2), damage quantification (Level 3), and prediction of the remaining service life of the damaged structure, or the acceptable load level to reach the intended service life (Level 4).

Damage Detection Methods

Most of the existing damage identification methods can be classified into two groups: model-based and non-model or feature-based methods. The model-based methods are essentially model updating procedures in which the mathematical model or the physical parameters of a structure is calibrated or updated using vibration measurements from the physical structure ([8], [9]). Analytical sensitivities of response parameters to changes in physical properties are used to update modeling assumptions, physical sizing, elastic moduli, etc. The

feature-based approaches detect structural changes by detecting damage features in the measured data without the need for an analytical model of the structure. The main task here is the extraction of damage features sensitive to structural changes so that damage can be identified from the measured vibration response of civil engineering structures. The following methods were proposed in the literature for feature-based damage detection in civil engineering structures ([10], [4], [11], [12]):

- Natural frequency based metrics
- Mode shape based metrics
- Structural damping based metrics
- Modal strain energy based metrics
- Flexibility based methods and other matrix perturbation approaches
- Pattern Recognition, neural networks and other statistical approaches
- Non-linear methods based on advanced time-variant transforms
- Other methods

The civil engineering community has been studying the vibration-based damage assessment of bridge and building structures since the early 1980s. Both model-based and non-model based approaches utilizing the measured data in time-domain, frequency domain or modal domain were investigated. While measurements were always performed in the time domain, data could be analyzed in any of the three domains. Although conversion between domains involves some data compression, Friswell and Penny [13] argued that loss of information during conversion was minimal for linear systems and that the frequency domain may be more advantageous in reducing the effects of random noise. Modal domain introduces further reduction of the measured data since only the modes within a frequency band are considered. Friswell and Penny find this acceptable unless the out of band modes are very close, i.e. the response is dominated by the in-band modes. Lee and Shin [14] disagree with this argument pointing out the fact that the modal data can be contaminated by modal extraction error which the frequency response function data does not possess.

Vibration Based Modal Parameter Determination

Eigensystem Realization Algorithm with Observer Kalman Filter, ERA-OKID, [15] which is used for defining the vibration based linear system in the time-space is the most commonly used methods in the literature. With this algorithm system is carried out and vibration inputs (u) system outputs (y) are correlated with system matrices (A, B, C, D) as seen in equation 1.

(1) $$\dot{x} = Ax + Bu$$
$$y = Cx + Du$$

The state matrix [A] obtained in discrete time is first transformed into continuous time and then eigenvalues (Λ) and eigenvectors (Ψ) of this matrix in continuous time are calculated to obtain system's natural vibration frequencies (f^{ID}), energy dissipation ratios (ξ^{ID}) and randomly scaled mode shapes (φ).

(2) $$\Lambda_i = \alpha_i \pm \beta_i$$

(3) $$f_i^{ID} = \frac{\sqrt{\alpha_i^2 + \beta_i^2}}{2\pi}$$

(4) $$\zeta_i = \frac{-\alpha_i}{\sqrt{\alpha_i^2 + \beta_i^2}}$$

(5) $$\varphi = C\ \Phi\ \Lambda^{-p}$$

Variable "p" in the equation 5 must be taken as 0,1 or 2 depends on whether output data (sensor measurements) are velocity or acceleration respectively. For the later evaluation steps, mass normalized mode shapes of equation (5) may be required. It is possible to reach this type of mass normalized mode shapes with using B which is obtained during system realization [16].

Altuzay Algorithm [17] can be used in a condition of vibration inputs are not known but system is accepted as stochastic. In this case, system is represented with these equations.

(6) $$\dot{x} = Ax + w$$
$$y = Cx + v$$

In here, w and v are noise vectors, A and C are obtained system matrices. System's natural vibration frequencies, energy dissipation ratios and randomly scaled mode shapes can be calculated by using equations (2–6). The point is, for a stochastic system that vibration inputs are not known and matrix B has not been generated, a different method is required to make the calculated mode shapes mass normalized [18].

Damage Localization

After the detection of damage in the structure, Damage Locating Vector — DLV method which is based on the flexibility difference due to damage is used for damage localization. This method (see reference [19] and [20] for further information) can be summarized like this:

Flexibility matrix can be calculated in the sensor locations with the help of dynamic response data that obtained from the structure:

$$F = \Phi_n \, \Omega^{-1} \Phi_n \qquad (7)$$

In the formulation, Φ_n is the matrix of mass normalized mode shapes and Ω is the diagonal matrix that includes the square of corresponded natural vibration frequencies. F_U and F_D matrices can be obtained when the before and after damage data are used with equation (7) respectively. Load distributions that create the exact deformations for non-damaged and damaged systems create L matrix. Then, this equation can be written:

$$(F_D - F_U)\, L = DF \cdot L = 0 \qquad (8)$$

The only condition that equation (8) is valid, except the condition of there is no damage in the system which means flexibility matrix difference is zero (DF = 0), occurs when DF which is obtained from the L matrix's flexibility matrices difference includes all vectors of the null-space. If "Singular Value Decomposition (SVD)" is applied to the flexibility matrix difference (DF), load distribution which is called as DLV can be obtained. When each DLV is applied to the non-damaged system's analytical model as a load distribution, deformations and stresses corresponded to this statical loading are calculated. Theoretically, stress on a damaged member must be zero [19]. In practical, due to both the noise during evaluation and model assumptions, this stress is not zero and it comprises smaller values than the stated limit [20].

A Case Study: One-Story One-Bay Reinforced Concrete Frame

Reinforced concrete frame type structures take an important place in Turkey's structural inventory. However, it is too hard to find a research about this type of structure in the literature. Therefore, one-story one-bay reinforced concrete frame (Figure 1) is selected to apply vibration tests. Accelerometers on beams and columns are indicated as B and C respectively. Before the experimental study, in order to understand the behavior, the frame is modeled in 3-D with MARC/Mentat which is finite element software like in Figure 2a. In Figure 2b, damaged area is indicated with dark color and thereby reducing the elasticity modulus of this region with 25% and 50%, two different damage scenarios are simulated to represent the post-earthquake situation.

Frame model is distributed with vibration input (u) as indicated in Figure 2 for pre-damage and two different post-damage scenarios. Acceleration responses are gathered from sensors locations on the frame. Structure's modal properties are determined thereby processing these inputs with ERA-OKID algorithm. Natural vibration frequencies from algorithm (f^{id}) and model (f^{model}) are presented in Table 1 with comparison. First five modes are clearly determined, the frequency

difference between the analytical calculated and the obtained from vibration input is limited in 1%, for further modes the difference reaches at most 7%. As the contribution of these modes to the response is minimal, increasement in the observed error level is an expected result.

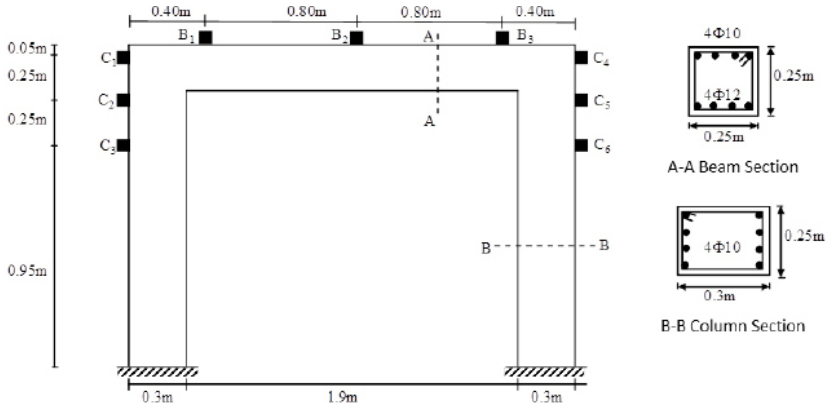

Figure 1 — RC frame test mechanism: Geometry and accelerometer locations

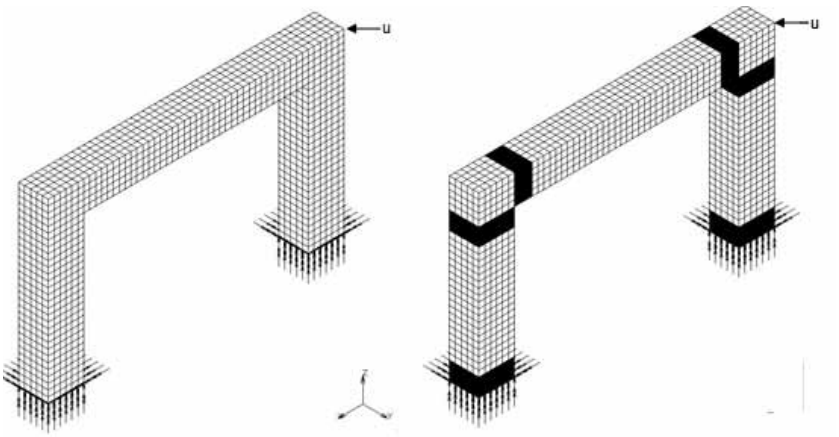

(a) (b)

Figure 2 — 3-D MARC/Mentat model of the frame:
(a) Pre-damage
(b) Post- damage

Mode	No Damage			25 % Damage			50 % Damage		
	f^{model} (Hz)	f^{id} (Hz)	Diff. %	f^{model} (Hz)	f^{id} (Hz)	Diff. %	f^{model} (Hz)	f^{id} (Hz)	Diff. %
1	34.9	34.9	0.0	33.4	33.3	0.1	30.9	30.9	0.1
2	62.8	62.6	0.4	59.3	59.1	0.3	54.2	54.1	0.2
3	64.4	64.3	0.1	61.3	61.2	0.2	56.5	56.4	0.1
4	138.6	136.8	1.3	133.7	132.1	1.2	127.0	125.6	1.1
5	142.9	141.0	1.4	140.0	138.2	1.3	135.4	133.7	1.3
6	292.4	281.4	3.8	280.0	273.0	2.5	262.0	260.0	0.8
7	297.5	298.3	0.3	287.8	290.7	1.0	272.9	278.9	2.2
8	316.6	338.0	6.7	307.6	324.1	5.4	293.6	303.6	3.4
9	364.5	354.2	2.8	347.8	346.0	0.5	323.7	333.0	2.9
10	380.2	410.1	7.9	370.4	395.7	6.8	354.9	377.2	6.3

Table 1 — Comparison of frequencies obtained from finite element model and vibration input

After detection of damage by use of frequency differences, next step would be damage localization with the help of DLV method. At the accelerometer locations, system's pre-damage (F_U) and post-damage (F_D) flexibility matrices are determined by using vibration inputs that are obtained from the structure (Figure 3a). Singular Value Decomposition (SVD) is applied to the difference matrix (DF) and Damage Locating Vector (DLV) is determined. This vector (Figure 3b) is applied on structural modal as statical load and stresses on the structure are calculated, thereby normalizing these stresses, an index that is defined as nsi is formed. In this project, as mentioned structure is a moment resisting frame, bending stresses are used and for 50% damage scenario, *nsi* values are obtained as shown in Figure 4 throughout beams and columns. Regions that are under the limit which is pointed by *nsi* may be potentially damaged and for these regions, more detailed investigations should be accomplished. Therefore, if *nsi* < 0,2 condition is chosen as the damage localization limit, it is possible to say true damaged regions on both columns and beams are under this limit and potentially problem regions that are pointed by DLV method includes the damaged regions.

Conclusion

Development of rapid and safe post-earthquake damage evaluation methods has a vital importance in earthquake-prone countries like Turkey where structural inventory is consisted of mostly reinforced concrete buildings. In this manner, vibration based evaluation methods are

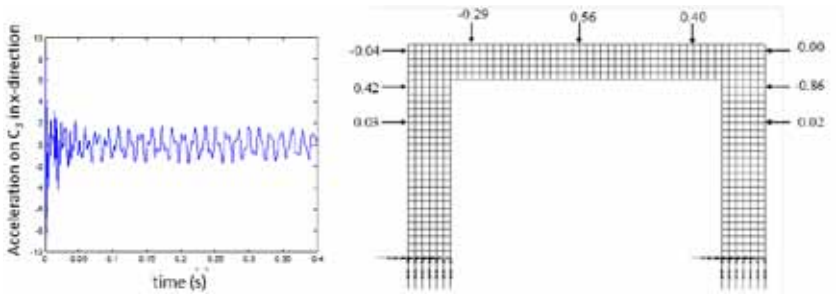

(a) (b)

Figure 3 — (a) Sample acceleration output at location C_3 on column (b) DLV applying statical load to sensor locations on modal

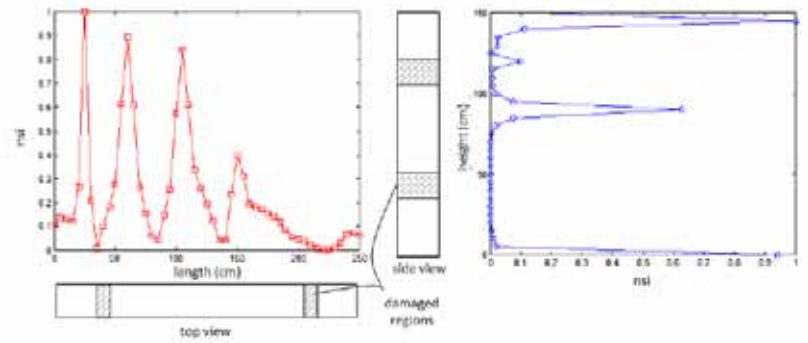

(a) (b)

Figure 4 — Damage detection on frame with DLV method: nsi values (a) along beam (b) along column

presented. They provide an opportunity of in-place non-destructive damage detection by using dynamic response data obtained from the structure. If the algorithms which enable the usage of these methods into civil engineering structures work, both normally functional usage and rapid, safe and inexpensive post-earthquake evaluation of primarily strategical structures would have been provided. Besides, contribution of this method to evaluation and strengthening of priceless historical buildings cannot be ignored. Simulation based damage detection studies presented in this article show that success rate of pre and post-dam age dynamical properties determination for frame that would be evaluated with experiments is high. However, it may have difficulties about damage localization and magnitude estimation. Additional simulation studies and experiments will be held in order to obtain more accurate damage localization and magnitude estimation with optimum measurement parameters and damage detection methods.

References

[1] *Farrar, C.R., Baker, W.E., Bell, T.M., Cone, K.M.,Darling, T.W., Duffey, T.A., Eklund, A. ve Miglori, A. (1994). Dynamic characterization and damage detection in the I-40 bridge over the Rio Grande. Los Alamos National Laboratory Report LA-12767-MS, Los Alamos National Laboratory, P.O. Box 1193, Los Alamos, NM, 87544, USA.*

[2] *Salawu, O.S. (1997). Detection of structural damage through changes in frequency: a review. Engineering Structures, 19(9), 718–723.*

[3] *Doebling SW, Farrar CR, Prime MB (1998). A summary review of vibration-based damage identification methods. Shock and Vibration Digest; 30, 91–105.*

[4] *Sohn H, Farrar CR, Hemez FM, Shunk DD, Stinemates DW, ve Nadler BR (2003). A review of structural health monitoring literature: 1996–2001, Los Alamos National Laboratory, USA.*

[5] *Chang, P. C., Flatau, A. ve Liu, S. C. (2003). Review Paper: Health Monitoring of Civil Infrastructure. Structural Health Monitoring 2003; 2(3); 257–267.*

[6] *Farrar, C. R. ve Worden, K. (2007). An Introduction to Structural Health Monitoring. Philosophical Transactions of the Royal Society A: Mathematical, Physical and Engineering Sciences, 365, pp. 303–315.*

[7] *Rytter, A. (1993). Vibration based inspection of civil engineering structures. Ph.D. Dissertation, Department of Building Technology and Structural Engineering, Aalborg University, Denmark*

[8] *Zimmerman DC, Kaouk M. (1992). Eigenstructure assignment approach for structural damage detection. AIAA Journal, 30(12):1848–55.*

[9] *Fritzen CP, Jennewein D, Kiefer T. (1998). Damage detection based on model updating methods. Mech Syst Signal Process ;12(1), 163–86.*

[10] *Doebling, S.W., Farrar, C.R., Prime, M.B. ve Shevitz, D.W. (1996). Damage identification and health monitoring of structural and mechanical systems from changes in their vibration characteristics: a literature review. Technical Report LA-13070-MS, Los Alamos National Laboratory, Los Alamos, NM*

[11] *Randall, B. R. 2004a State of the art in monitoring rotating machinery — part 1. Journal of Sound and Vibration, 38, pp. 14–21.*

[12] *Randall, B. R. 2004b State of the art in monitoring rotating machinery — part 2. Journal of Sound and Vibration, 38, pp. 10–17.*

[13] *Friswell, M.I. and Penny, J.E.T. (1997). Is damage location using vibration measurements practical, euromech 365 international workshop: damas 97, Structural Damage Assessment using Advanced Signal Processing Procedures, Sheffield, UK, June/July.*

[14] *Lee, U. and Shin, J. (2002). A frequency response function-based structural damage identification method. Computers and Structures, 80, 117–132.*

[15] *Juang, J. (1994). Applied System Identification, Prentice-Hall, Englewood Cliffs, N.J.*

[16] *Gunes, B (2002). Identification and localization of damage , PhD Thesis, Northeastern University., Boston, MA.*

[17] *Vanoverschee, P. ve Moor, B. L. R. (1996). Subspace Identification for Linear Systems, Kluwer Academic Publishers, Boston.*

[18] *Bernal, D. (2006). Flexibility-based damage localization from stochastic realization results, Journal of Engineering Mechanics, 132(6), 651–658.*

[19] *Bernal, D. (2002). Load vectors for damage localization. Journal of Engineering Mechanics, 128(1), 7–14.*

[20] *Bernal, D. ve Gunes, B (2004). A flexibility based approach for the localization and quantification of damage: A benchmark application. Journal of Engineering Mechanics, 130, 61–70.*

Fragility of Shear Wall Buildings with Torsional Irregularity

AKANSEL,Vesile Hatun
Middle East Technical University, Civil Engineering Department, Turkey

GÜLKAN, Polat
Çankaya University, Civil Engineering Department, Turkey

YAKUT, Ahmet
Middle East Technical University, Civil Engineering Department, Turkey

Abstract

Buildings with torsional irregularity represent the main focus of many current investigations. However, despite this volume of research, there is no established framework that describes adequately the seismic vulnerability of reinforced concrete shear wall systems. In this study, the three dimensional behavior of a ¼ scaled 3 story shear wall structure which is a part of a nuclear plant was taken into account under different seismic excitations. This structure was subjected to AZALEE shaking table tests in Saclay, France under the project of "SMART 2008" which was led by CEA (Atomic Energy Agency).

The main purpose of this study is that to capture the experimental results with the numerical model and to calculate the fragility curves of the structure. In experimental phase, three real and ten synthetic accelerograms was used for shaking table tests. For the calculation of the fragility curves, maximum inter-story drift values have been used as the damage indicator to obtain the fragility curves and different seismic intensity measures have been used. Thirty bi-directional syntetic horizontal ground motions in the ranges of 0.1 g and 1.0 g, have been applied for the time history analyses. Fragility curves of shear wall building have been calculated according to pre-established damage indicators.

Introduction

Calculation of three dimensional seismic effects on buildings involving torsion is a challenge for structural engineering, especially for non–linear behavior under earthquake effects. Modeling these types of buildings

needs much more care to generate acceptable results. In spite of the developing computer technology and existence of many numerical models, there are still deficiencies in modeling because of the assumptions made in the numerical models for material and seismic excitation estimation. One way to test the versatility of a model is to do parametric studies which may be helpful for identifying the importance of the variables in the models.

The other crucial concept is the fragility curves for different structural categories. These statistically-evaluated or empirically-derived curves provide a basis for the assessment of the performance of buildings under different ground motion intensities so that loss estimates can be made.

Literature Survey

For walls two main modeling approaches are used as macro and micro modeling depending on the chosen finite element technology. Micro modeling is a continuum mechanics based approach and uses two or three dimensional solid or shell finite elements. Non–linear behavior of concrete and steel can be applied in the model on the basis of material constitutive relationships from experimental results ([5], [6], [10], [7] and [4]). Micro modeling is suitable for representing the local behavior in the structure. ANSYS, ABAQUS, ADINA and DIANA are sample software packages that include a variety of element and material models in their libraries for micro modeling. Many researchers have used micro modeling approach to simulate the experimental measurements ([11], [14]).

In performing a seismic risk analysis of a structural system, the vulnerability information in the form of fragility curves is a widely practiced approach. Performance–based design is a powerful tool for the assessment of buildings under earthquake effects. In recent decades, the probabilistic approaches have become popular than deterministic approaches for the determination of fragility curves of structures. Shinozuka et al. [17], developed fragility curves associated with different states of damage of bridges from observations following the 1995 Kobe earthquake event. They introduced the uncertainty and statistical interpretation of randomness through the notation of combined and composite fragility curves.

Shear wall building behavior under earthquake effects and its performance are observed from past earthquakes and experimental results. It has been noted that for shear wall buildings there is no collapse under earthquake effects. The inadequate number of research on the performance limits of shear wall buildings indicates conflicting results ([12], [18]).

Jeong and Elnashai ([8], [9]) proposed a new three dimensional damage index which takes into account the bidirectional and torsional response effects. The main purpose in their study is to estimate three dimensional damage capacity indexes, namely the global response of the structure under earthquake effects by way of simple frame systems. Aziminejad and Moghadam [3], investigate the different configurations of centers of stiffness and strength to generate the fragility curves. In this study, only the results of the non linear time history analysis and damage states specified "by SMART 2008" were used to obtain the fragility curves.

Experimental Program and Model Structure

SMART 2008 Experimental Program

A reduced scaled model (scale of ¼th) of a nuclear reinforced concrete building was tested on the AZALEE shaking table at Commissariat à l'Energie Atomique (CEA Saclay, France). The loadings on the model ranged from very low seismic motions to five times the design level.

For validation of the model, three real and 10 synthetic accelograms were generated at AZALEE shaking table [15]. The details of the accelerogram sets are given in Table 1 and Figure 1. The earthquake motions were applied in both orthogonal directions. For vulnerability analysis 30 set of synthetic derived ground accelerograms were used as bi-directionally.

Model Structure

The plan and the mock-up pictures of the SMART 2008 specimen is displayed in Figure 2. Density of the concrete is used as 2460 kg/m^3 and Young Modulus of concrete is 32000 MPa as (a reference case) according to the SMART 2008 Phase 2 report given by CEA [16]. MKIN and CONCRETE are used for the concrete in the model. MKIN (Multi linear kinematic hardening), rate-depended plasticity is used. CONCRETE is a defined material model in ANSYS for Willam–Warnke material model. For this material type open shear transfer coefficient, 0.2 and closed shear transfer coefficient, 0.8, are used. Uniaxial cracking stress is 2.4 MPa.

The model developed for this study in Figure 3 consists of 28740 SOLID65 (3-D Reinforced concrete elements) and 5282 MASS21 (Structural mass) element types. Also, the model has 43179 nodes for calculations. Shaking table and foundation is not modeled and basement is assumed as fixed supported as proposed in [15]. Seismic excitations applied at basement level in the analytical model.

No		Real Earthquakes	M	Dist.	Acc.(g)
1	REA 1	UMBRO-MARCH(AS)	5.2	23	0.05
2	REA 2	MANJIL(AS)	4.4	14	0.05
3	REA 3	UMBRO-MARCHIGIANO	5.9	81.4	0.05
		Synthetic Earthquakes			
4–13		Derived according to the response spectrum and scaled from 0.1g to 1.0g			

Table 1 — Real and synthetic accelerogram sets

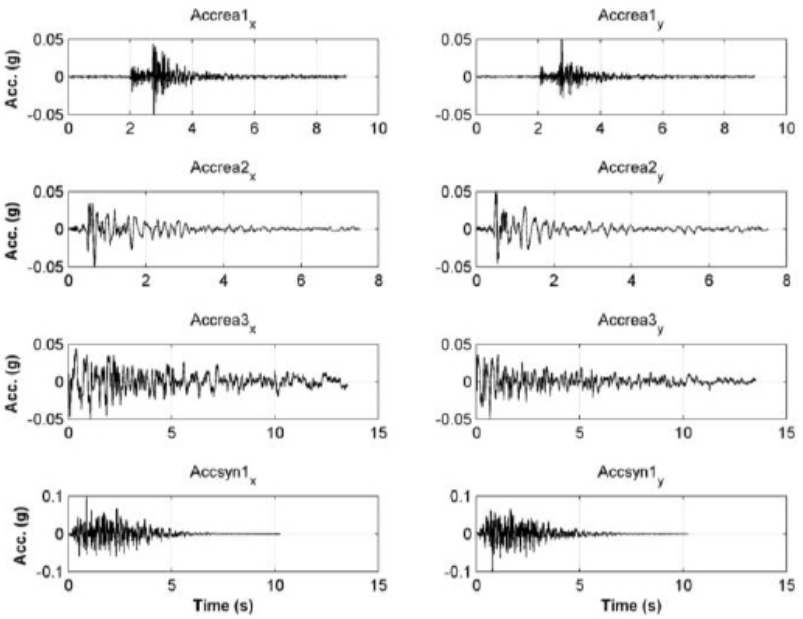

Figure 1 — Ground motion data used in the experiments

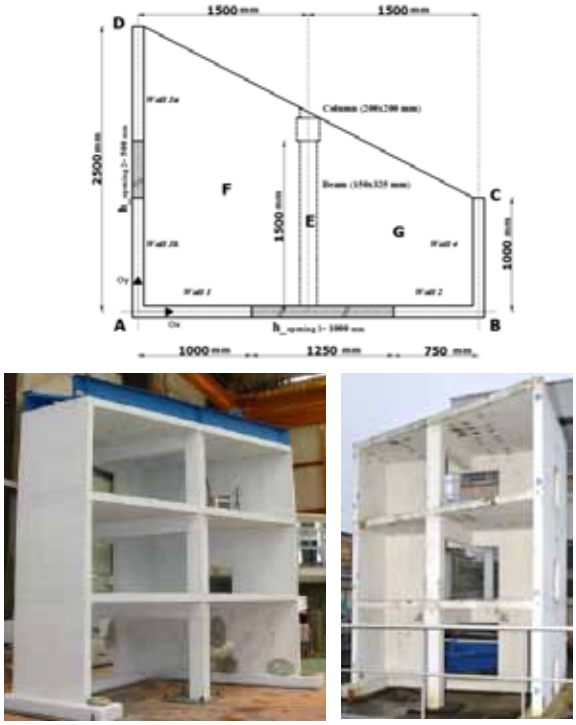

Figure 2 — The Identification of locations where results have to be computed, SMART 2008 specimen before and after tests

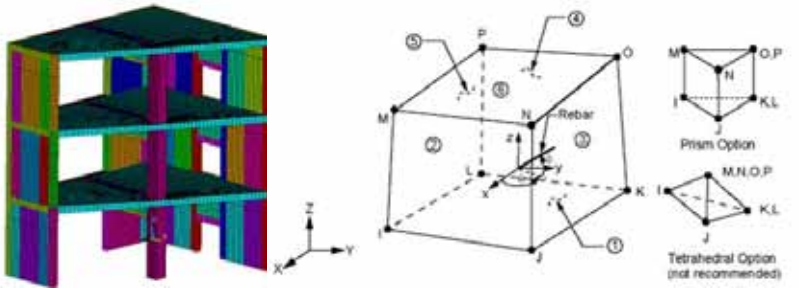

Figure 3 — Numerical model of SMART 2008 mock-up and SOLID 65 element type

Model Verification and Fragility Analysis

Model Verification

The verification of the model was done by comparing the experimental results with the calculated ones. In Table 2, these results were compared in terms of relative percentage errors.

	Ax	Ay	Bx	By	Cx	Cy	Dx	Dy
Accsyn 1	–0.84	–0.87	–0.88	–0.91	–0.87	–0.89	-0.85	-0.88
Accsyn 2	–0.40	–0.39	–0.45	–0.03	–0.46	0.14	-0.26	-0.42
Accsyn 3	–0.65	–0.75	–0.61	–0.69	–0.62	–0.67	-0.67	-0.74
Accsyn 4	–0.05	0.33	–0.05	0.05	–0.10	0.10	-0.20	0.36
Accsyn 5	0.18	0.26	0.36	0.07	0.07	0.14	-0.15	0.34
Accsyn 6	0.24	0.32	0.26	0.18	0.23	0.32	-0.04	0.33
Accsyn 7	0.22	0.37	0.28	0.31	0.05	0.36	-0.03	0.37
Accsyn 8	0.39	0.38	0.42	0.55	0.23	0.69	0.14	0.44
Accsyn 9	0.11	0.33	0.15	0.35	0.19	0.42	0.02	0.35
Accsyn 10	0.17	0.12	0.08	0.35	0.12	0.43	0.07	0.20

Table 2 — Relative Error Percentages between calculated and measured data according to absolute maximum displacements

Negative values in Table 2 mean that calculated values are smaller than the experimental results. Increase in the level of the seismic excitation, results in decrease in error percentages. Detailed analysis results for verification of the model can be obtained from [1] and [13].

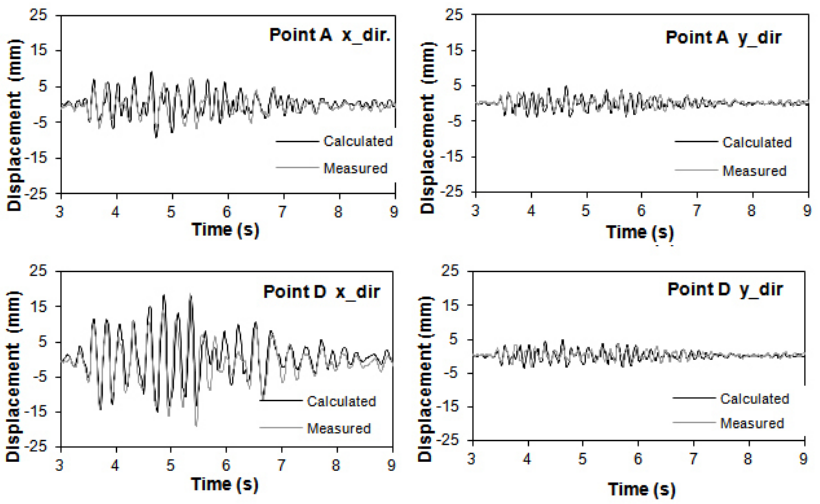

Figure 4 — Displacement comparisons of the experimental results and analytical results at the 3rd floor level for Run 10 (Accsyn–0.7 g)

Fragility Analysis

One of the main objectives of this study was to obtain the fragility curves for this structural type to develop the behavior of shear wall buildings under different seismic excitations with torsion effects. The thresholds which were defined by the project team are given in Table 3, [16].

Maximum inter-story drifts were used as a damage indicator (Table 3). To investigate the local effects of the damage, the fragility curves were calculated at specified points shown in Figure 2. These damage levels are used as the criteria for the fragility analysis. H is the story height and equals to 1.2 m.

Damage Levels	Drift Ratio
Light Damage	H / 400 = 3
Controlled Damage	H / 200 = 6
Extended Damage	H / 100 = 12

Table 3 — SMART 2008 Damage levels defined for maximum inter-story drifts

Thirty bi-directionally applied time-history analyses were performed for the fragility analysis. According to the results of the fragility analysis, the log-normal distribution was assumed for the distribution of the structural response indicators and then the fragility curves were obtained according to median capacity, A_m and standard deviation, $\square$ of this distribution.

The probability of failure P_f of a structure or component conditioned on seismic ground motion level "a" is expressed by fragility curves as given in Equation (1).

$$P_f \equiv P\left(Failure \middle| a\right) = P\left(A < a\right) \tag{1}$$

Failure occurs if the actual capacity of the structure is inferior to the seismic demand, that is the given ground motion level "a". The failure probability conditioned on ground motion parameter "a" given by the cumulative distribution function of capacity A_m is calculated from Equation (2).

$$P_f = \Phi\left(\frac{\ln(a) - A_m}{\beta}\right) \tag{2}$$

To obtain the fragility curves from the probability density functions, we need to define the acceptable median capacity and standard deviations for the limit states defined in Table 3 under different seismic excitations. One of the methods used to determine the median capacity and the standard deviation is the regression analysis. In Figure 5, the result of the regression analysis result for PGA versus maximum inter-story drift at point E in X direction is displayed.

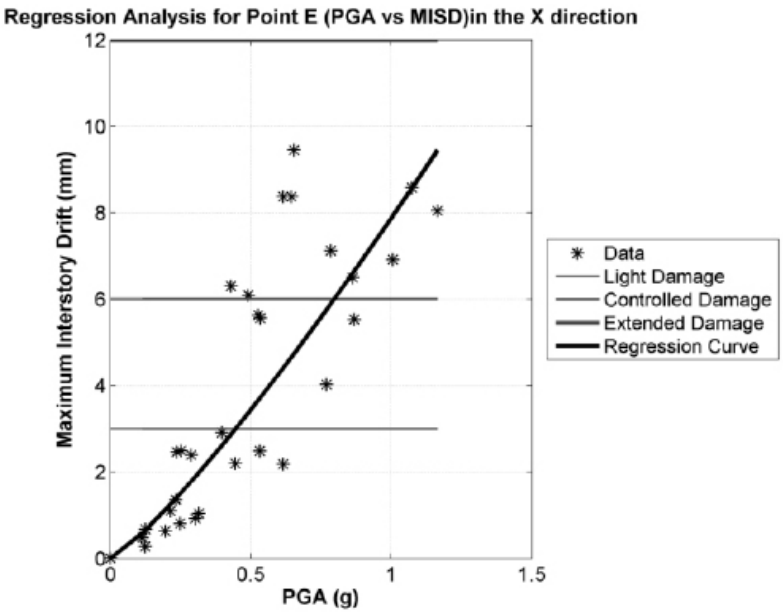

Figure 5 — Regression analyses for maximum inter-story drift at point E for PGA

To obtain the least error, the method of least squares is applied to the data in this study. Following regression analyses the needed median seismic capacity, Am and log-standard deviation,can be evaluated. For the evaluation of A_m, Y_{crit} value can be used as shown in Equation (3).

$$\ln(A_m) = \frac{\ln(Y_{crit}) - a}{b} \quad (3)$$

In Equation (3), Y_{crit} values were defined in the SMART 2008 Phase-2 report [16] as damage levels which were given in Table 3.

In this study, Point E is taken into account so as to represent the structural behavior. This point is close to the mass center of the system and, has the high correlation coefficients when the time history data is compared with the fitted curves as a result of the regression analysis. The correlation coefficients of fitted curves and time history analyses are given in Table 4. The correlation coefficient for PGA parameter for X and Y directions are respectively 0.89 and 0.91. These results were thought to have reasonably enough accuracy for the fragility curves.

Table 4 — Correlation coefficients for time history data versus fitted curves

	PGA x	PGA y	PGV x	PGV y	PGD x	PGD y	CAV x	CAV y
Point E	0.89	0.91	0.92	0.87	0.86	0.82	0.94	0.97

According to these regression analyses, the log-standart deviation coefficients and seismic median capacity coefficients for data are displayed in Table 5 and Table 6, respectively. The scatter of the fragility curves for the given damage levels changes under different seismic ground motion indicators as shown in Fig. 6. PGA and PGV have similar trends in shape; however the CAV and PGD differ.

The probabilistic scatters between the damage levels were slightly wider and the structure behaves well even under relatively higher seismic motions. In Figure 6, the probability of failure at the damage levels under PGA seismic motion indicator were nominal till 0.5 g. Our extensive calculations have shown a very good agreement between experiment and theory, supporting the power of the computational approach in obtaining far-reaching generalizations. The model was designed to experience significant coupled translation-torsion during its dynamic response, and the computations captured that well.

	PGA x	PGA y	PGV x	PGV y	PGD x	PGD y	CAV x	CAV y
Point E	0.46	0.41	0.45	0.49	0.73	0.80	0.73	0.62

Table 5 — β (Log-standard deviation) coefficients for data

	LD	0.45		LD	0.46
	CD	0.80		CD	0.82
PGA x	ED	1.42	PGA y	ED	1.48
	LD	0.22		LD	0.23
	CD	0.39		CD	0.40
PGVx	ED	0.66	PGV y	ED	0.70
	LD	0.08		LD	0.09
	CD	0.14		CD	0.15
PGD x	ED	0.25	PGD y	ED	0.26
	LD	7.09		LD	7.32
	CD	14.91		CD	15.37
CAV x	ED	31.36	CAV y	ED	32.27

Table 6 — A_m Seismic median capacity coefficients for data for Point E

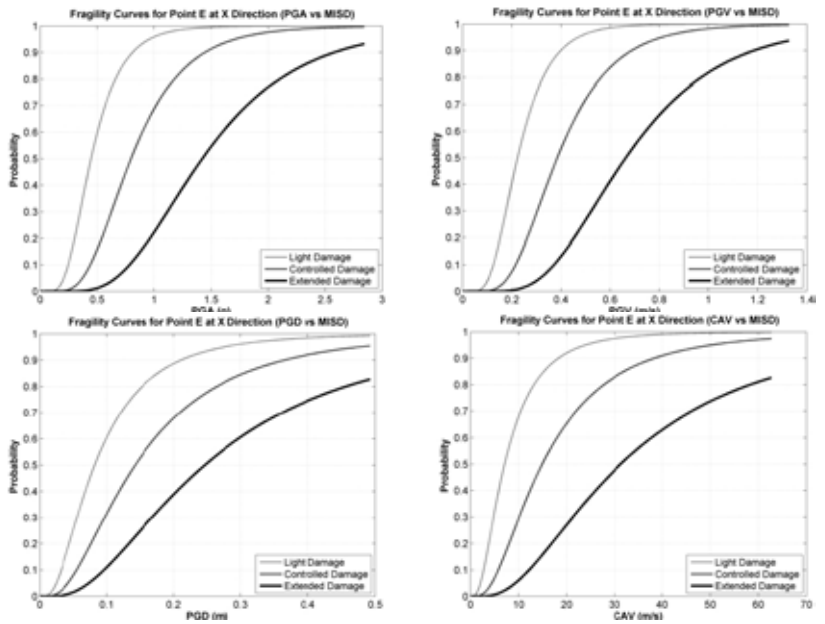

Figure 6 — Fragility Curves Comparisons of Point E for various seismic motion indicators at X direction

References

[1] *Akansel V. H., Kazaz İ., Yakut A. and Gülkan P. (2010). Modeling and simulation of the shear wall buildings' behavior under earth quake forces. Dicle Üniversitesi Mühendislik Dergisi. Vol.1, No.1, pp. 31–40.*

[2] *ANSYS R 12.1, Swanson Analysis System, 2011.*

[3] *Aziminejad A. and Moghadam A. S. (2009). Performance of asymmetric multistory shear buildings with different strength distributions. Journal of Applien Science. Vol.9, No.6, pp. 1080–1089*

[4] *Fischinger M. and Isakovic T. (2000). Benchmark analysis of a structural wall. 12th World Conference on Earthquake Engineering. 0416*

[5] *Ile N. and Reynouard J.M. (2003). Lightly reinforced walls subjected to multi – directional seismic excitations: Interpretation of CAMUS 2000-1 dynamic tests. Vol. 40, No. 2–4, pp. 117–135.*

[6] *Ile N. and Reynouard J.M. (2005). Behaviour of U-shaped walls subjected to uniaxial and biaxial cyclic lateral loading. Journal of Earthquake Engineering. Vol. 9, No. 1, pp. 67–94.*

[7] *Ile N., Nguyen X. H., Kotronis P., Mazars J. M. (2008). Shaking table tests of lightly RC walls. Journal of Earthquake Engineering. 12:6, pp. 849–878.*

[8] *Jeong S.–H. and Elnashai A. S. (2006a). New three-dimensional damage index for RC buildings with planar irregularities. Journal of Structural Engineering. Vol. 132, No.9, pp. 1482–1490.*

[9] *Jeong S.–H. and Elnashai A. S. (2006b). Fragility analysis of buildings with plan irregularities. 4th International Conference on Earthquake Engineering, Taipei, Taiwan*

[10] *Kazaz İ., Yakut A. and Gülkan P. (2006). Numerical simulation of dynamic shear wall tests: A benchmark study. Computers and Structures. Vol. 84, pp. 549-562.*

[11] *Kwak H.–G. and Kim D.–Y. (2004). FE analysis of RC shear walls subjected to monotonic loading. Magazine of Concrete Research. 56, No. 7, pp. 387-403.*

[12] *Moehle J. P. (1996). Displacement–based seismic design criteria. 11th World Conference on Earthquake Engineering. 2125, ISBN: 0 08 042822 3.*

[13] *Nazirzadeh S., Yakut A. Akansel V. H. and Kazaz İ. (2011). Numerical modeling of an unsymmetrical building tested on shaking table. Advances in Structural Engineering and Mechanics (ASEM 11) Conference.*

[14] *Palermo D. and Vecchio F. J. (2007). Simulation of cyclically loaded concrete structures based on the finite element method. Journal of Structural Engineering. Vol. 33, No. 5, pp. 728–738*

[15] *RAPPORT DM2S, (2007). Presentation of the Benchmark Contest– Phase 1 Project SMART 2008.*

[16] *RAPPORT DM2S, (2009). Presentation of the Benchmark Contest– Phase 2 Project SMART 2008. COMMISSARIAT A L'ÉNERGIE ATOMIQUE, SEMT/EMSI/PT/09-011/A*

[17] *Shinozuka M., Feng M. Q. Lee J. and Naganuma T. (2000). Statistical analysis of fragility curves. Journal of Structural Engineering. Vol. 126, No.12, pp. 1224–1231.*

[18] *Wallace J. W. and Moehle J. P. (1992). Ductility and detailing requirements of bearing wall buildings. Journal of Structural Engineering. Vol. 118, No.6, ASCE, ISSN 0733-9445/92/0006-1625.*

Vibration monitoring and structural identification of an historic masonry bell tower

CABBOI, Alessandro
University of Cagliari, Italy

Abstract

In this study, partial results of a long-term dynamic monitoring performed on an historic masonry bell-tower were carried out. The tower has significant structural problems, such as wide cracks on several façades. After a brief description of two previous ambient vibration tests, the paper focuses on the simple permanent monitoring system installed inside the tower (for several months) in order to investigate the variation of modal parameters. The experimental investigation is complemented by a 3D F.E. model and its subsequent vibration-based updating to get a first structural identification. The aim of this study is to assess how damage and environmental factors can influence the dynamic parameters.

Introduction

The preservation of historic masonry towers has gained an important role in Architectural Heritage conservation. In fact, these structures are affected by several issues due to the ageing of materials, damage and uncertain boundary conditions related to adjacent structures or to geotechnical problems. Another fundamental feature is their slenderness that confers a high sensitivity to dynamic actions such traffic-induced microtremors, bell swinging, wind and earthquakes. In this sense, ambient vibration testing and overall continuous dynamic monitoring seem to be ideal tools to evaluate the dynamic behavior under operational condition [1] and to validate F.E. models [2–3], crucial for successive safety assessment.

A further important application of dynamic monitoring is the evaluation of the influence of environmental factors on the modal parameters and its use for dynamics-based damage assessment. In the literature, damage identification (DI) methods can be categorised as non model-

based and model-based techniques [4, 5]. The first methods are based on the change of eigenfrequencies, mode shapes and its derivatives. Therefore, it becomes important to analyse the effects of environmental factors — since could mask the changes due to structural damages — on the modal parameter [6–7]. On the other side, the second DI methods need accurate numerical models. For these last methods, model updating is a fundamental step to enhance the quality of the model before it is used for damage assessment [8].

The paper details several main steps of the vibration-based damage assessment of historic bell towers, and involves both, experimental and theoretical modal analysis. The developed procedure starts by the research of the available information regarding: a) historical studies; b) the accurate survey of the tower geometry and of the crack pattern; c) previous ambient vibration testing and identification of the dynamic characteristics of the tower (June 2007–2008); d) the development of a first numerical tuned model [3]. Since the identified modal parameters of the tower highlight a clear non-linear behaviour caused by the bell-swinging excitation, a simple dynamic monitoring system was installed inside the tower for several months (2009–2010).

The frequencies tracked on the acquired data exhibit a significant dependence on temperature. Subsequently, in the theoretical part of the study, the identified natural frequencies were used to estimate some uncertain structural parameter of the F.E. model by using the simple Douglas-Reid method [9]. In addition, based on the information carried out from the dynamic monitoring and the numerical model, it is possible to assess how environmental factors and damage condition the dynamic behaviour of the tower.

The bell tower of San Vittore church in Arcisate

The investigated tower (Figure 1a), about 37.0 m high, is built in irregular stonework masonry on a square base and connected on the East side and partly on the South side to the San Vittore church (XI century) in Arcisate (Varese). The first historic document of the bell tower dates back to XVI century, even though it was probably built on a previous roman building and modified along the centuries.

The masonry tower exhibits 6 orders of floors, with 5 of them being defined by masonry offsets at the corners and by corresponding sequences of small hanging arches marking the floor levels. The two upper orders of floors were probably added in the XVIII century to host the bell trusses.

The accurate survey of tower geometry and crack pattern clearly reveals that the masonry texture appears often highly disordered, with local prevalence of continuous or little staggered vertical joints; in addi-

tion, it is difficult to distinguish between vertical cracks and insufficient stone interlocking because of erosion of the mortar joints. Along all sides, the tower exhibits long vertical cracks, most of them cutting the entire wall thickness and crossing through the keystones of the arched window openings. These cracks are mainly detected between the second/third order of the tower and the base of the belfry, showing a maximum aperture at the upper end (Figure 1b). Many superficial cracks are also diffused, particularly on the North and West fronts (Figure 1b), which are not adjacent to the church.

The masonry has been characterized through sonic tests; the results generally indicate a relatively compact masonry of fairly good execution.

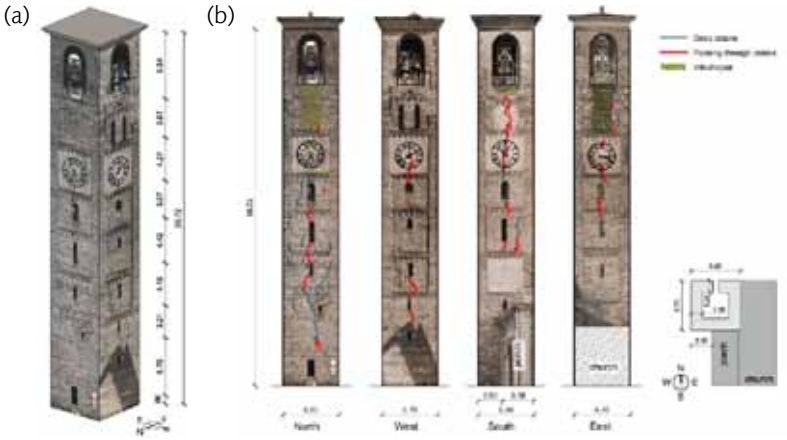

Figure 1 — (a) Axonometric view of the bell-tower; (b) crack pattern on the different fronts (dimensions in m)

Dynamic characteristics of the tower

Preliminary ambient vibration tests

Two ambient vibration tests were conducted on the tower: on June 2007 and June 2008. In both tests the response of the tower was measured in 15 selected points, according to the sensor layout shown in Figure 2a. For each test two different series of ambient vibration data were recorded: in the first series (AV1), the ambient excitation was only provided by the wind and the micro-tremors; in the second series (AV2), the excitation was provided by the swinging of bells. In both tests, the sampling frequency was 200 Hz and the time of acquisition was larger than 2000 times [10] the period of the structure's fundamental mode.

An example of the acceleration time-histories recorded in the test of June 2007 at the same channel for both test series is given in Figures 2b and 2c respectively. It should be noticed that the bell swinging (Fig. 2c) produced a significant increase of the vibration level associated with micro-tremors and other ambient excitations (Fig. 2b); it can be observed that the maximum amplitude of acceleration responses is increased of 10-20 times by the bell swinging. Similar results have been obtained in the test performed on June 2008.

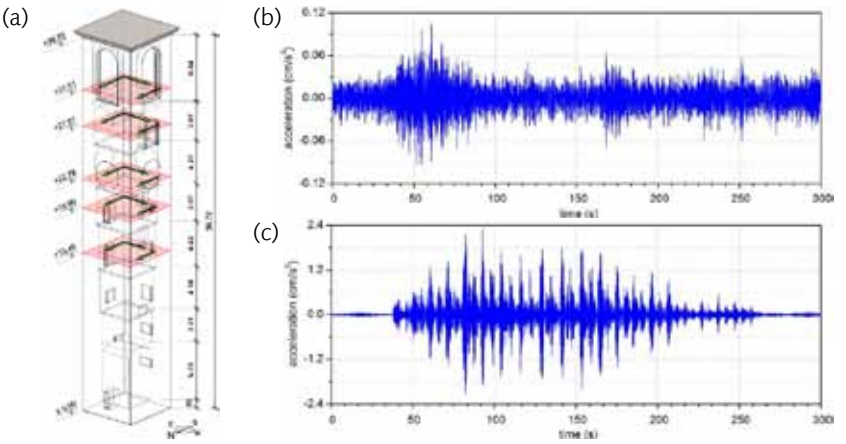

Figure 2 — (a) Sensor layout adopted in AVT of the tower (dimensions in m); Acceleration induced at the same point by: (b) micro-tremors and wind; (c) swinging of bells

The extraction of modal parameters was carried out by using two well-known and complementary techniques: the Frequency Domain Decomposition [11] and the data-driven Stochastic Subspace Identification [12]. In this paper, only the results obtained using the SSI technique will be reported, since this technique was used in the operational modal analysis (OMA) of monitoring's collected data. The application of SSI technique to the AV1 data recorded in June 2007 allowed the identification of 5 vibration modes in the frequency range of 0–6 Hz (Fig. 3a). Figure 3b shows the identified mode shapes: dominant bending (B) modes were identified at 1.21 (B1), 1.29 (B2), 3.98 (B3) and 4.14 Hz (B4) while only one torsion mode (T1) was identified at 3.56 Hz. The analysis of AV1 time series collected in June 2008 provided very similar results.

Since each test was conducted under different level of ambient excitation (Figure 2b and 2c), additional investigation was performed on the time invariance of resonant frequencies and mode shapes. This investigation was carried out by evaluating the corresponding average normalized auto-spectral (ANPSD) estimates [13] of the accelerations acquired on June 2007. The ANPSDs obtained from each test are plotted in Figure 4 and reveals that all natural frequencies tend to decrease at the higher level of ambient excitation; the decreases approximately range from 1.7% (mode B1) to 2.7% (mode B3). It has to be further noticed that differences were detected between the mode shapes as well. Those difference generally tend to increase as the mode order increases.

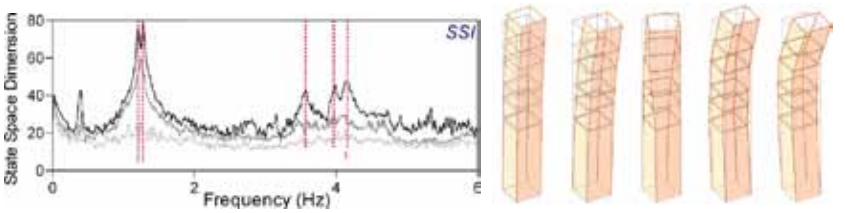

(a) (b)

Figure 3 — (a) Stabilization diagram (SSI technique); (b) Vibration modes

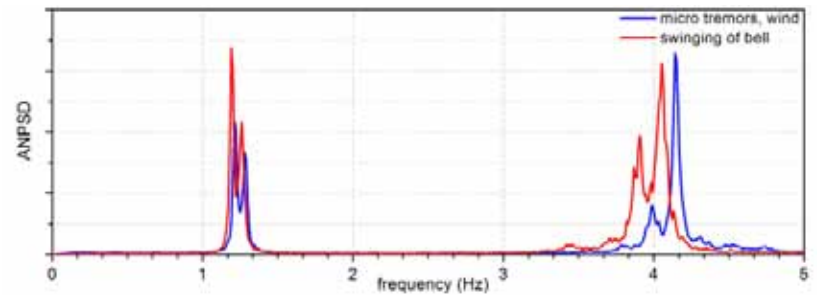

Figure 4 — ANPSD of the accelerations acquired on June 2007 under different levels of ambient excitation

Vibration monitoring

From June 2009 until March 2010 a continuous dynamic monitoring system operated inside the tower in order to better investigate the time variance of resonant frequencies (Figure 4). The instrumentation consisted of 3 uni-axial Dytran 3191A1 piezoelectric accelerometers (10 V/g), a 4-channel data acquisition system (NI 9234) and a local PC for the management of the continuous acquisition and the data storage (Figure 5). The sampling frequency was 200 Hz. The choice of instrumented level was based on the information collected in the previous ambient vibration tests, so that all previously identified modes are observable at that level.

In addition, averaged temperature data were recorded by a static monitoring system previously installed on the tower and managed by Politecnico di Milano [14], as well: 8 thermocouples measured internal and external temperature at different levels of the tower.

The OMA of collected accelerations was performed in two main steps. The first step, performed by a powerful tool developed in LabView [15], involved the following tasks: a) the creation of a database with the original data for subsequent developments; b) detrending, automatic recognition and extraction of the time series associated to swinging of bells (the responses induced by the swinging of bells do not comply with some basic hypothesis of OMA, such as white noise and stationarity of input); c) statistical analysis; d) low-pass filtering and decimation of the data containing the response to micro-tremors and wind only; e) creation of a second database with essential data

Figure 6 — General arrangement of the dynamic monitoring system

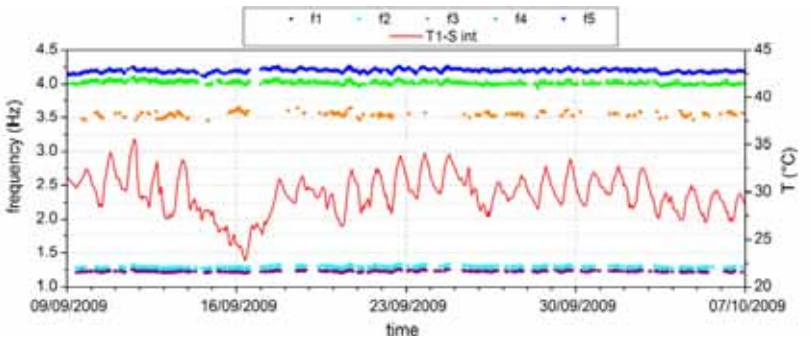

Figure 7 — Identified natural frequencies of the first five modes and internal temperature at the first level of the south side masonry between Sept 09 and Oct 07, 2009

records. The second step consisted in the modal identification using the data driven automatic SSI method [12] available in the commercial software ARTeMIS.

The inspection of Figure 7 reveals that the bending modes are much more frequently identified than the torsion mode, probably as a consequence of the low level of ambient actions that generally excite the tower. Since only the response to low level excitation (micro-tremors and wind) has been considered, the cyclic frequency variation is likely to be related to temperature. In order to clearly point out this aspect the frequency variation and the correlation with temperature are better illustrated in Figure 8.

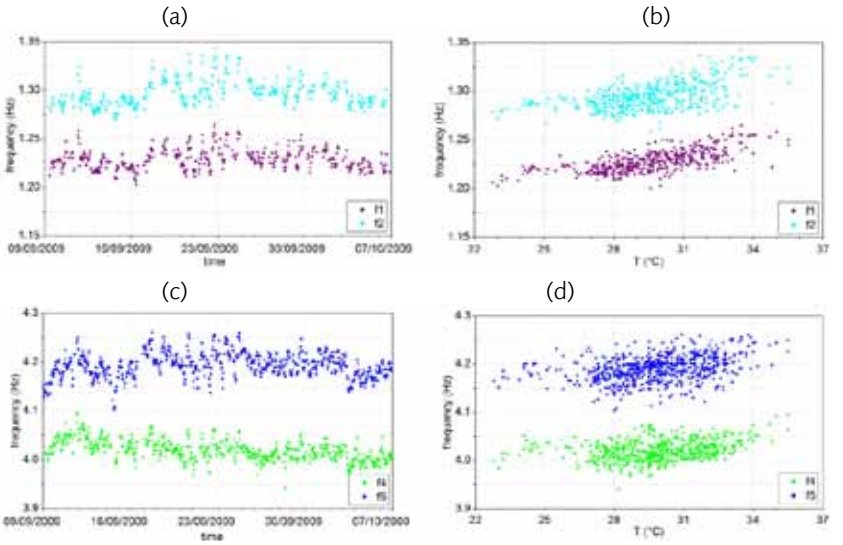

Figure 8 — Identified frequencies of bending modes f1, f2, f4 and f5 versus: (a,c) time and (b–d) temperature recorded between September 09 and October 07, 2009

A linear trend is clearly detected between frequency and temperature data: more specifically, the inspection of Figures 8b–d reveal that the natural frequencies increase as temperature increases. This behaviour can be explained through the closure of superficial and deep cracks induced by the thermal expansion of materials; furthermore, the stone interlocking of irregular stonework masonry conceivably tends to increase as the temperature increases. The natural frequencies of the lower bending modes exhibit higher percent variations: the mode

frequencies f1–f2 daily oscillates of about 0.05 Hz (around 4% of the average values), whereas the mode frequencies B3–B4 exhibit daily variation of about 0.1 Hz (around 2.4% of the average frequency). It is further noticed that the internal south side masonry temperature were ranging between 22.8–35.5 °C during the investigated period, with a mean value of 29.8 °C.

	Monitoring (26/06/09 - 31/07/09)				Monitoring (09/09/09 - 07/10/09)			
Mode Id.	f_m [Hz]	$\square_f$	f_{min} [Hz]	F_{max} [Hz]	f_m [Hz]	$\square_f$	f_{min} [Hz]	F_{max} [Hz]
$B_1 - 1$	1.249	0.0138	1.198	1.282	1.229	0.0107	1.203	1.265
$B_2 - 2$	1.319	0.0190	1.258	1.367	1.297	0.0134	1.270	1.343
$T_1 - 3$	3.524	0.0574	3.365	3.688	3.551	0.0394	3.457	3.655
$B_3 - 4$	4.056	0.0329	3.941	4.163	4.020	0.0209	3.941	4.095
$B_4 - 5$	4.247	0.0442	4.094	4.383	4.193	0.0249	4.104	4.261

Table 1 — Natural frequencies identified during the investigated period of monitoring

Table 1 presents the mean values, the standard deviations and the range of variation of natural frequencies estimated during the investigated period of monitoring and compares these values with the ones obtained around July 2009 (studied in a previous work [16]). The mean values of natural frequencies of the current period are lower than ones obtained during July. It can be also observed a decrease of the standard deviations from July to September. These differences can be explained by the temperature effect, since the weather in July was warmer ($T1\text{-}S_{int,mean}$ = 33.5 °C). Therefore, higher temperature induced higher thermal expansion of materials that closed superficial and deep cracks, increasing the global stiffness of the tower.

Hence, the dynamic characteristics of the tower are clearly dependent on the environmental factors, due to the very low amplitude of ambient excitation in the time series collected during the monitoring. After all, to better understand how damage influences the modal parameters, it becomes necessary to develop a finite element model and update the latter in agreement with the experimental response of the structure.

F.E. modeling and structural identification

Finite element model and sensitivity analysis

The F.E. program Straus 7 was used to create the numerical model. The tower was modelled by using 8-node brick elements. A relatively large number of finite elements have been used in the model, so that regular distribution of masses could be obtained and all the openings in the load-bearing walls could be reasonably represented. The model

consist of 3475 solid elements with 17052 active degrees of freedom. The geometry of the tower was accurately checked; the main uncertainties are related to the boundary conditions and the characteristics of the material. The following assumptions were introduced in order to reduce the number of uncertainties in the model calibration: (a) the weight per unit volume of the masonry equal to 17.0 kN/m³; (b) constant Poisson's ratio of the masonry equal to 0.15; (c) fixed tower footing to account for the fact that the soil-structure interaction is hardly involved at the low level of ambient vibrations that existed during the tests. The F.E. model was firstly refined in 4 steps of systematic manual tuning. The correlation between the dynamic characteristics of the F.E. model and the experimental results was evaluated via the maximum absolute frequency discrepancy $D_{F,max}$:

(1) $$D_{F,max} = max\,(D_{F,i})$$

(2) $$D_{F,i} = 100\left|\frac{f_{FEM,i} - f^{exp}_{mean,i}}{f^{exp}_{mean,i}}\right|$$

and the average frequency discrepancy J:

(3) $$J = \frac{1}{M}\sum_{i=1}^{M} D_{(F,i)}$$

The mean values of the identified natural frequencies regarding the period around September are assumed as reference experimental values inasmuch show a smaller variation in time.

In the first dynamic analysis (FEM1) the Young's modulus of stone masonry was assumed equal to 3.00 GPa (value suggested by engineering judgement and the results of sonic tests). The comparison between theoretical and experimental modal parameters shows highly imperfect correlation: a) the model is much stiffer than the tower; b) the torsion mode T1 of the model does not follow the experimental sequence; c) the mode shapes of FEM1 bending modes involve motion along N-S and E-W directions while the experimental tower modes involve bending along the diagonals (Fig. 4b). The poor quality of correlation clearly indicates that the assumptions on the isotropic behaviour of stone masonry and on the connection with neighbouring building need to be revised. Hence, an orthotropic elastic behaviour (FEM2) was assumed for the stone masonry; the average characteristics of the material were E = 3.00 GPa, $G_{13} = G_{23} = 0.3$ GPa. The orthotropic model improved the correlation with the experimental results: a) the stiffness of the model significantly decreased: b) the torsion mode T1 of FEM2 correctly follows the experimental sequence. Subsequently, a third model (FEM3) was developed, by accounting for the connection between the tower and the church through a series of linear (nodal) springs of constant stiffness k. An initial stiffness of

B1 = 1.198 Hz B2 = 1.234 Hz T1 = 3.375 Hz B3 = 4.280 Hz B4 = 4.359 Hz

Figure 9 — Mode shapes of FEM4

springs was assumed equal to k = 4* 10⁴ kN/m. After the correction, the bending modes are fully consistent with experimental data. Finally, based on a preliminary sensitivity analysis, the uncertain parameter were assumed as follows (FEM4): E = 3.00 GPa; G13 = G23 = 0.4 GPa; k = 3* 10⁴ kN/m. The latter model improve the correlation with the experimental setup (Fig. 9). In Tab. 2 are reported the evaluated frequency discrepancies of the main steps carried out.

In order to assess the most sensitive parameters of the F.E. model and to select the minimum number of uncertain parameters for the inverse problem of structural identification, the base F.E. model (FEM4) was checked through a sensitivity analysis. The sensitivity coefficients s_{ik} (Fig. 9) are computed — by a perturbation technique — as the rate of change of a particular response of the model $f_{i,}^{FEM}$ with respect to a change in a structural parameter X_k (1). If sensitivity coefficients for different types of parameters are to be compared and normalized with respect to the base response value, then s_{ik} can be calculated as percentage like (2). The k^{th} parameter X vary into a range defined by an upper and lower bound (3); the responses $f_{i,}^{FEM}$ are respectively computed at these limit values (4).

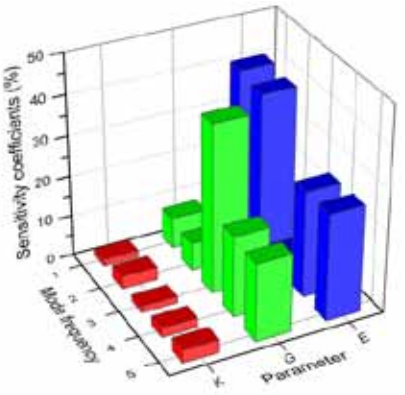

Figure 10 — Sensitivity coefficients

$$s_{ik} = \frac{\Delta f_i^{FEM}}{\Delta X_k} \quad (1)$$

$$s_{ik} = 100 \frac{X_{b,k}}{f_{b,i}^{FEM}} \frac{\Delta f_i^{FEM}}{\Delta X_k} \quad (2)$$

(3) $$\Delta X_k = X_k^U - X_k^L$$

(4) $$\Delta f_i^{FEM} = f_i^{(FEM,U)} - f_i^{(FEM,L)}$$

The inspection of the sensitivity coefficients clearly reveals that: a) the bending modes, above all lower order modes, are significantly affected by E; b) the shear modulus G mostly influence the torsion mode and affected considerably the higher order bending modes; c) the stiffness constant of springs k weakly conditions the dynamic characteristics. Therefore, E and G are good candidates to be selected as updating parameters in a structural identification approach, since they do not affect the inverse problem by ill-conditioned states.

On the other hand the influence of constant k deserves more careful regards. Comparing the sensitivity coefficients between the first — second and third — fourth bending mode, it seems that this parameter conditions them differently. K is the only parameter able to regularize the correct distance between the bending modes. From Tab. 2, it appears that the computed bending modes from FEM3 and FEM4 are spaced between them in a different way compared with the experimental results SSI_{mean}. Therefore, a further variation of the constant k was necessary in order to tune the correct spacing between the bending modes. It was assumed a new value of k equal to $8^* 10^4$ kN/m. After that point, the model FEM5 can be chosen as "base" model for a structural identification process, containing only two uncertain parameters: the elastic modulus E and the shear modulus G.

Structural identification procedures and damage assessment

The uncertain parameters E and G were estimated by minimizing the objective function (3). According to the Douglas-Reid approach [9], the relationship between any response (natural frequencies and mode shapes) of the model and the structural parameters X_k of the model is approximated around the current values of X_k by the following expression:

(5) $$f_i^*(X_1, X_2, \ldots, X_N) = \sum_{k=1}^{N} [A_{ik} X_k + B_{ik} X_k^2] + C_i$$

To satisfy the expression and solve the problem, (2N + 1) constant (A_{ik}, B_{ik} and C_i) must be calculated before to compare each f_i^* to its experimental counterpart. In order to calculate the coefficients, structural base parameters X^B_k, upper X^U_k and lower X^L_k values were estimated with engineering judgement. When those (2N + 1) parameters are defined, the constants on the right hand side of (5) can be computed by satisfying the equation with frequencies obtained for defined parameters. Thus, the equations stated above will be obtained:

$$
\begin{aligned}
f_i^*(X_1^B, X_2^B, \ldots, X_N^B) &= f_i^{FEM}(X_1^B, X_2^B, \ldots, X_N^B) \\
f_i^*(X_1^L, X_2^B, \ldots, X_N^B) &= f_i^{FEM}(X_1^L, X_2^B, \ldots, X_N^B) \\
f_i^*(X_1^U, X_2^B, \ldots, X_N^B) &= f_i^{FEM}(X_1^U, X_2^B, \ldots, X_N^B) \\
f_i^*(X_1^B, X_2^B, \ldots, X_N^L) &= f_i^{FEM}(X_1^B, X_2^B, \ldots, X_N^L) \\
f_i^*(X_1^B, X_2^B, \ldots, X_N^U) &= f_i^{FEM}(X_1^B, X_2^B, \ldots, X_N^U)
\end{aligned}
\tag{6}
$$

The first choice of the structural parameters corresponds to the base values; then, each of them is varied one at time from the base value to the upper and lower limit respectively. Once the coefficients A_{ik}, B_{ik} and C_i have been computed, the approximation (5) is completely defined and it can be used to update the structural parameters. In order to obtain the optimal parameters, the average frequency discrepancy (3) was minimized through an unconstrained optimization algorithm, well known as Nelder-Mead simplex method. The optimizing iterative procedure identified the uncertain values concerning the material properties used in the updated model as follows: E = 3.00 GPa; G = 0.43 GPa. Table 2 summarizes the main results obtained for the updated process.

	B1	B2	T1	B3	B4	J	$D_{f,MAX}$
SSI_{mean}	1.229	1.297	3.551	4.020	4.193	–	–
FEM3	1.171	1.218	2.992	4.031	4.144	5.600	15.742
FEM4	1.198	1.234	3.375	4.280	4.359	4.553	6.468
FEM5	1.218	1.285	3.426	4.394	4.544	4.603	9.303
FEM_{ott}	1.226	1.292	3.534	4.468	4.610	4.440	11.144

Table 2 — Correlation between the experimental results and computed frequencies in [Hz]

The correlation between theoretical (FEM_{ott}) and experimental behaviour (SSI_{mean}) is satisfactory for the first three modes. In addition, physical constraint like spacing between the modes shapes was achieved. On the other hand the $D_{f,max}$ for the higher bending modes remains quite high (11.14% for the fourth mode). Probably this discrepancy could be due to the following reasons: a) as a consequence of the simplified distribution of the model elastic properties; b) damage has a considerably influence on the higher modes that are characterized by more complex mode shapes, suffering much more the physical and mechanical properties alteration of the material.

A future development of this work is to improve the numerical model, simulating the most damaged areas of the tower and the parts that were built or modified along the centuries by a non-homogeneous distribution of the Young's modulus. To limit the number of structural parameters in the structural identification procedure, the tower could be divided in three regions assuming different masonry Young's modulus as constant within each zone. Once the model will be satisfactory

tuned on the experimental data, it will form a helpful tool for damage identification and numerical analysis for successive safety assessment. As a final remark, if we add the information carried out from long-term dynamic monitoring, the dynamic-based damage assessment methodology outlined in the paper seems a powerful tool for diagnosis of historic structures. It is worth underlining that long term monitoring is mandatory to distinguish between the cyclic (temperature) and the irreversible (damage) effects on the global dynamic characteristics [7]; in this sense, it will become important to apply a pattern recognition technique on the experimental data.

Conclusions

An experimental and theoretical dynamic investigation of a historic masonry tower is described in the paper. The following conclusions can be drawn from the study: a) notwithstanding the very low level of vibration during the dynamic monitoring, operational modal analysis has proved to be effective tools for modal identification of masonry towers; b) within the frequency range 0–6 Hz, 4 dominant bending and 1 torsion modes were clearly identified from ambient vibration data; c) the dynamic behaviour of the investigated tower is significantly affected by the temperature variation (the natural frequencies identified increases as the temperature increases) and by the amplitude of bell swinging excitation; d) it becomes important to investigate the time-history of identified modal parameters by pattern recognition techniques in order to distinguish between cyclic and irreversible effects on the global dynamic characteristics.

Furthermore, the comparison between measured and predicted modal parameters was used to verify the assumptions adopted in formulating a F.E. model of the structure. The correlation between theoretical and experimental modal parameters provides partially accurate verification of the model main assumptions. One of them regards the hypothesis of orthotropic elasticity, that seems more suitable when modelling stone masonry structures.

Although this part of the study cannot be considered concluded due to excessive lack of information on the mechanical characteristics of materials and to the too simplified assumptions adopted for the numerical model, dynamic-based damage assessment methodology seems a promising approach to monitor and evaluate damage in historic structures.

References

[1] *Schmidt, T. (2009). FE Comparison of the dynamic behavior of 16 historical twin bell towers. Proceedings of 3th Int. Operational Modal Analysis Conference (IOMAC-I), Portonovo/Italy, S. 483–490.*

[2] *Ivorra, S., Pallares F. J. (2006). Dynamic investigation on a masonry bell tower. Engineering Structures 25(5), S. 660-667.*

[3] *Gentile, C., Saisi, A. (2010). FE modeling of an historic masonry tower and vibration-based systematic model tuning. Proceedings of 7th Int. Conf. on Structural Analysis of Historic Constructions (SAHC), Shanghai/China, S. 435-430.*

[4] *Fritzen, C.P. (2005). Vibration-based structural health monitoring concepts and application. Proceedings of the DAMAS 2005, Key Engi neering Materials, Trans Tech Publications, Zürich/Switzerland, S. 3-20.*

[5] *Maeck, J. (2003). Damage assessment of civil engineering structures by vibration monitoring. PhD Thesis, K.U. Leuven/Belgium.*

[6] *Ramos, L. F., Marques, L., Lourenço, P. B., De Roeck, G., Campos-Cost,a A., Roque, J. (2010). Monitoring historical masonry structures with operational modal analysis: two case studies. Mechanical Systems and Signal Processing 24, S. 1291-1305.*

[7] *Magalhães, F., Cunha, A., Caetano, E. (2012). Vibration based structural health monitoring of an arch bridge: From automated OMA to damage detection. Mechanical Systems and Signal Processing 28, S. 212-228.*

[8] *Gentile, C., Saisi, A. (2007). Ambient vibration testing of historic masonry towers for structural identification and damage assessment. Construction and Building Materials 14(4), S. 1311-1321.*

[9] *Douglas, B. M., Reid, W. H. (1982). Dynamic test and system identification of bridges. Journal of the Structural Division 108(10), S. 2295-2312.*

[10] *Cantieni, R. (2005). Experimental methods used in system identification of civil engineering structures. Proceedings of 1st Int. Operational Modal Analysis Conf. (IOMAC'05), Copenaghen/Denmark, S. 249-260.*

[11] *Brincker, R., Zhang, L. M., Andersen, P. (2000). Modal identification from ambient responses using Frequency Domain Decomposition. Proceedings of 18th Int. Modal Analysis Conference (IMAC-XVIII), San Antonio/Texas/U.S.A., S. 625-630.*

[12] *Van Overschee, P., De Moor, B. (1996). Subspace identification for linear systems: Theory, implementation, applications. Kluwer Academic Publishers.*

[13] *Felber, A.J. (1993). Development of a hybrid bridge evaluation system. Ph.D. Thesis, University of British Columbia/Canada.*

[14] *Binda, L., Condoleo, P., Tiraboschi, C. (2012). On-site investigation and crack monitoring of an ancient bell-tower. Proceedings of Structural Faults & Repair-2012 (in print).*

[15] *Gentile, C., Saisi, A., Busatta, F. (2011). Dynamic testing and permanent monitoring of an historic iron arch bridge. Proceedings of 8th Int. Conference on Structural Dynamics (EURODYN), Leuven/Belgium, S. 1186-1193.*

[16] *Gentile, S., Saisi, A., Cabboi, A. (2012). Dynamic monitoring of a masonry tower. Proceedings of 8th Int. Conf. on Structural Analysis of Historic Constructions (SAHC), Wroclaw/Poland, (in print).*

Knowledge based structural assessment of Mallorca cathedral

ELYAMANI, Ahmed
Technical university of Catalonia, Spain

CASELLES, Jose Oriol
Technical university of Catalonia, Spain

CLAPES, Jaime
Technical university of Catalonia, Spain

ROCA, Pere
Technical university of Catalonia, Spain

Abstract

The paper presents the current state of an on-going research on Mallorca cathedral. The cathedral is an audacious Gothic structure built in the island of Mallorca in Spain during XIV–XVI centuries, characterized for its large dimensions and slender structural members. So far, experimental and numerical modal analysis, in addition to tentative model updating and seismic analysis were performed. The dynamic identification were carried out by ambient vibration testing, and then the frequency domain decomposition (FDD) technique was used to obtain the modal parameters. A 3D Finite Element (FE) model was used to determine the vibration modes. The model was updated to improve the matching between experimental and numerical modal parameters. Once updated, the model was utilized to study the seismic response of the cathedral using non-linear static pushover analysis. The results of a continuous dynamic monitoring system currently installed in the building are also presented.

Introduction

Even though Mallorca Cathedral is located in a low-to-medium seismic region, its seismic behaviour is of concern due to the vulnerability which may result from its audacious structural features, as in particular the long-span and very high central nave vaults and very slender nave piers. Moreover, the structure shows significant deformation and some cracking can be observed in piers, vaults and walls [1], [2].

The island of Mallorca has been struck by three moderate earthquakes (with intensity higher than VI on the Mercalli scale) in the last 400 years with epicentre in Campos-Palma (1660), Selva (1721) and Palma-Marratxí (1851). This last event, with estimated maximum

intensity of VIII in the MSK scale, is considered as the major earthquake having occurred in Mallorca in the last four centuries [3].

In the current research the dynamic identification tests were carried out as one of the tasks planned to assess the seismic performance of Mallorca cathedral. Those tests are useful to characterize the main modal parameters (natural frequencies, mode shapes and damping ratios) which represent the structure's dynamic behaviour as a result of physical or mechanical properties (as the elastic modulus of the masonry composite) that may be difficult to obtain [4]. The extracted modal parameters were then used to tune a FE model. The tuned model was used for the seismic assessment by means of nonlinear static pushover analysis.

Another aspect of the research is the dynamic monitoring of the cathedral. It was instrumented with a network of critically located high-sensitivity accelerometers. This system has allowed the capture of the dynamic response for ambient vibration and also in the occasion of some seismic events with different epicentre distance to the building location.

Mallorca cathedral

The construction of Mallorca Cathedral (Figures 1 and 2) started around the year 1300. The Trinity Chapel (part A in Figure 2) was completed in year 1311 while the Royal Chapel (part B in Figure 2) was finished around the year 1370.

It was then decided to modify the design from that of a single nave building to a three-nave one. Unfortunately, the reason behind this dramatic change is not known with certainty. The imposing main large nave (part C in Fig. 2) and the west facade were completed by the year 1601.

Figure 1 — General view of Mallorca cathedral showing south facade and apse

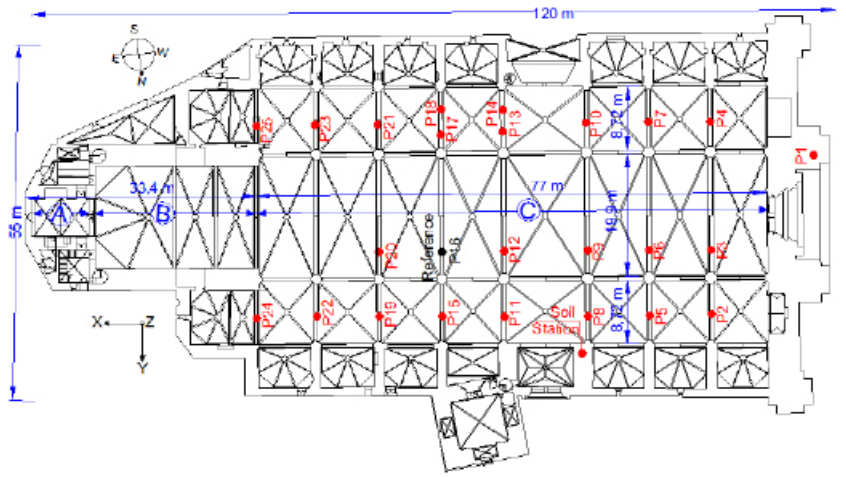

Figure 2 — Plan of the cathedral indicating the main parts and the measured points in the dynamic identifications tests

The main nave is composed of a central nave and two lateral naves surrounded by a series of lateral chapels built between the buttresses. The central nave spans 19.9 m and reaches 43.9 m at the vaults' keystone. The two lateral naves span 8.72 m each and reach a height of 29.4 m. The naves are sustained on octagonal piers with a circumscribed diameter of 1.6 or 1.7 m and a height of 22.7 m to the springing of arches. The bell tower is 45 m high and has a square cross section with side length of 12.5 m.

The building has been subjected to important repairs throughout its history. During the XVIII and XIX centuries a significant number of vaults of the central nave were repaired or even reconstructed. The west facade was totally demolished and reconstructed in the XIX century [5].

Dynamic identification tests

Description of tests

Three tri-axial force balance accelerometers were used to carry out the ambient vibration dynamic tests. Two of them correspond to the CMG-5T model with dynamic range of 140 dB for 0.005 to 0.05 Hz and 127 dB for 3 to 30 Hz, bandwidth ranging from DC to 100 Hz, full scale from 0.1 to 4 g, and weight of 2.7 kg. The other one is Titan model with dynamic range of 166 dB for 1 Hz and 155 dB for 3 to 30 Hz, bandwidth ranging from DC to 430 Hz, full scale from 5 V/g to 80 V/g, and weight of 960 gm.

Acceleration records were measured in 25 points in 15 different setups; see Table 1 and Figure 2. The test time was chosen to be approximately 1000 times the fundamental period of the cathedral [6]. The fundamental period was found analytically and experimentally by [3]. The recording time for each setup was 15 minutes with 100 samples per second. A 9-channel Digital to Analogue Converter was used for data acquiring.

Setup	1	2	3	4	5	6	7	8
Points	P3	P6	P20	P9, P12	P1	P2, P4	P5, P7	P8, P10
Setup	9	10	11	12	13	14	15	
Points	P11, P13	P15, P17	P19, P21	P22, P23	P24, P25	P14, P18	P23, P25	

Table 1 — measured points in each setup (p16 is measured in all setups)

Results of tests

The Frequency Domain Decomposition (FDD) technique [7] was used for determining the modal parameters (natural frequencies and mode shapes). In this technique the Power Spectrum Density (PSD) matrix is firstly evaluated then decomposed with the Singular Value Decomposition (SVD) method.

The recorded signals were processed by a decimation of 1 (Nyquist frequency of 50 Hz), the number of lines between 0Hz and the Nyquist frequency is 1024, and the Hanning window overlap is 66,67%. The peaks related to resonant frequencies were picked (Figure 3), and then the corresponding mode shapes were defined.

It was not possible to identify all the modes. The identified modes in each individual setup and in all setups processed together were investigated. Based on that, it was concluded that the fourth, fifth, sixth, seventh and eighth modes were reasonably identified. Those modes were considered for the modal matching and the updating process of the FE model. It is noteworthy that the identified frequencies were confirmed by the long term monitoring of the cathedral, performed for nine continuous months just after the dynamic identification tests, [8].

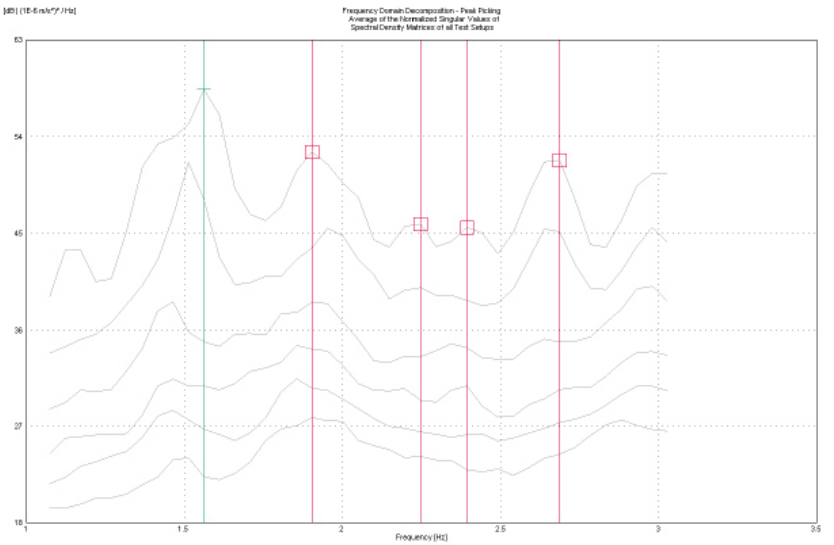

Figure 3 — FDD of all set-ups processed together and picked peaks

Model updating

The FE model previously used by [9] was used. The same properties of materials were also used as initial values in the updating process. The model was built in Diana code [10].Vaults were modelled using T15SH elements, three-node triangular isoparametric curved shells. The rest of the cathedral was modelled using TE12L elements, four-node three-side isoparametric solid pyramid. The model includes 149248 nodes and 491851 elements with 490789 degrees of freedom (Figure 4).

In the model updating process, experimental and numerical frequencies and mode shapes were compared. The mode shapes were compared using the Modal Assurance Criterion (MAC) [11], defined as:

$$MAC_{(e,n)} = \frac{\left| \sum_{i=1}^{n} \varphi_i^e \ \varphi_i^e \right|^2}{\sum_{i=1}^{n} (\varphi_i^e)^2 \sum_{i=1}^{n} (\varphi_i^n)^2} \qquad (1)$$

In which φ^e and φ^n are the experimental and numerical mode shape vectors, respectively. A MAC value less than 0.40 is considered a poor match while MAC value greater than 0.80 is considered a good match [12].

So far, two updating steps have been carried out. In the first step, we introduced springs to compensate for un-modelled parts. Those parts include mainly the vaults of lateral chapels, the adjacent building to the tower and the trinity chapel. In the second step, the Young's moduli (E) of different materials were modified. Figure 5 shows the comparison between numerical and experimental mode shape with

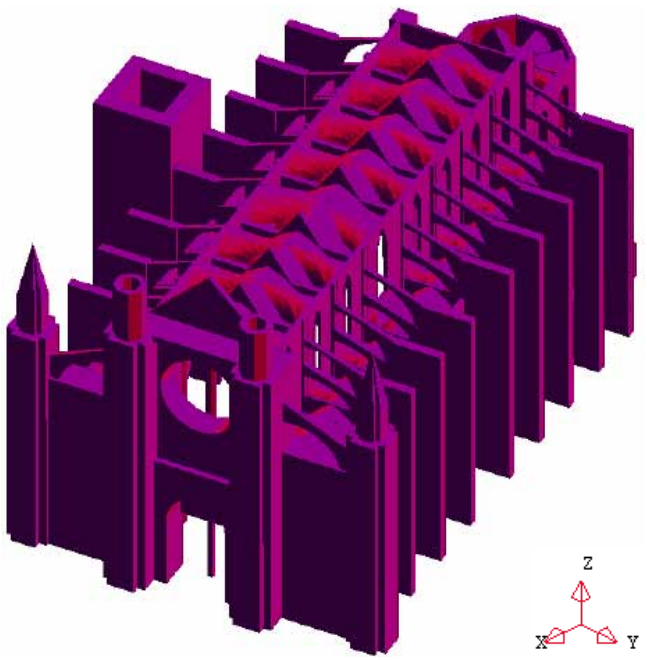

Figure 4 — FE model of Mallorca cathedral

the highest MAC value. Table 2 summarizes the updating process results. In terms of frequency difference, the updating is sufficient, but in terms of MAC values more updating steps are required.

Seismic analysis

The seismic analysis was carried out by the static nonlinear pushover method. In this method, a monotonically increasing horizontal load is applied under constant gravity load. The horizontal load distribution adopted was a uniform load proportional to the structural elements' masses. The cathedral was subjected to seismic loads in the longitudinal (X-direction) and transversal (Y-direction) considering both positive and negative sings (see Figure 4 for axes directions).

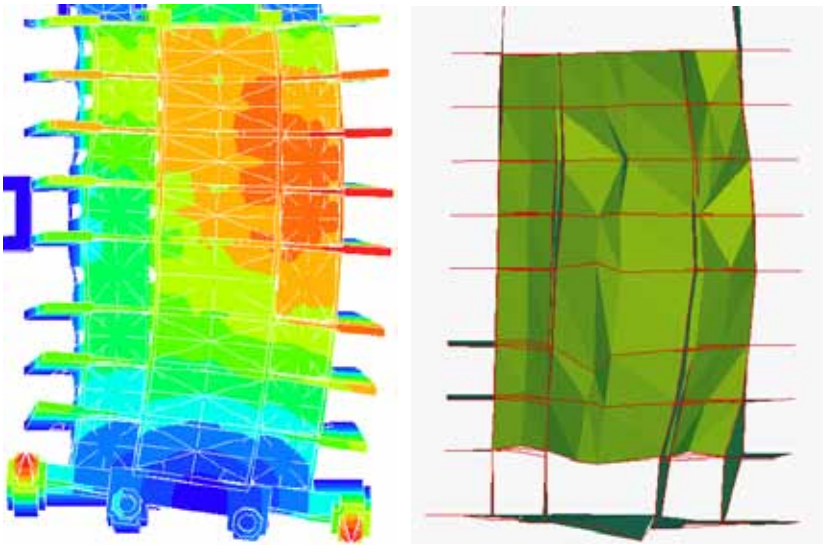

Figure 5 — Comparison between second num. mode (left) and fourth exp. mode (right)

The expected spectral acceleration is about 0.1 g according to [9]. The procedure is well known and is both proposed by Eurocode 8 and the Spanish seismic code (NCSE-02); it has also been applied previously to historical structures, e.g. [13] and [14].

Num. mode no.	Exp. mode no.	F (Hz)	Initial model F (Hz)	Error %	MAC	Last Step F (Hz)	Error %	MAC
2	4	1,563	1,592	1,9	0,697	1,624	3,9	0,713
3	5	1,904	1,694	11,0	0,363	1,868	1,9	0,248
7	6	2,246	2,116	5,8	0,137	2,263	0,8	0,308
9	7	2,393	2,446	2,2	0,326	2,372	0,9	0,378
10	8	2,686	2,638	1,8	0,467	2,576	4,1	0,498
			Aver-age	4,54	0,398	Aver-age	2,32	0,429

Table 2 — Model updating results

To simulate nonlinear behaviour of masonry, both cracking (tensile regime) and crashing (compressive regime) were considered in the material model. Tensile regime was modelled using tension cut-off with multi-directional fixed crack model (smeared cracking). The previous model was accompanied by isotropic plastic Drucker-Prager model in compressive regime. The nonlinear properties of materials were guided by the values previously used by [9] and [15].

The updated values of Young's moduli (E) were also used. The tensile strength (f_t) was assumed as 5% of compressive strength (f_c). The cohesion (C) was calculated from angle of internal friction (ø) and angle of diltancy (ψ) assuming associative plasticity. The materials parameters are specified in Table 3.

Structural elements	E (GPa)	γ (Density) kg/m³	f_c (MPa)	ε_u Ultimate strain	C (MPa)	ψ = ø
Columns and flying arches	13,6	2400	8	0,1%	3,36	10°
The rest of the cathedral	3,4	2100	2	0,4%	0,84	10°

Table 3 — Properties of different materials used in nonlinear seismic analysis.

Seismic response of the cathedral

The structure shows different seismic capacity depending on the direction of the applied seismic forces. When the seismic forces are in the transversal direction, the building can resist it with eight frame-like structures including imposing buttresses. These frames show large capacity because the forces are applied in its more resistant (in plane) direction. On the other hand, when seismic forces are applying in the longitudinal direction the structure shows a lower seismic capacity because of the loading of buttresses in a direction perpendicular to their plane and the large windows in the clerestory walls.

Figure 6 shows the capacity curves obtained. In both X and Y directions the structure behaves linearly up to seismic load about 0.05 g with clear higher stiffness for an earthquake in the Y-direction, which is the stronger direction of the structure. The collapse occurs at seismic load of 0.08 g in X-direction and 0.12 g in Y-direction. The curves are saw-tooth like. This can be related to the number of insufficient integration points through the thickness (1 point for solids and 3 points for shells were utilized), the usage of relatively coarse mesh in the damaged regions, and the opening of several cracks. This type of saw-tooth curves have also been obtained in other studies [16] and [17] on historical structures.

The damage experienced by the structure under seismic forces applied in the transverse +Y direction, at the last step of analysis, is described includes the following aspects:

– The pillars are showing cracks at their bases, at both the compressed the tensioned sides and the springing of arches (Fig. 7).

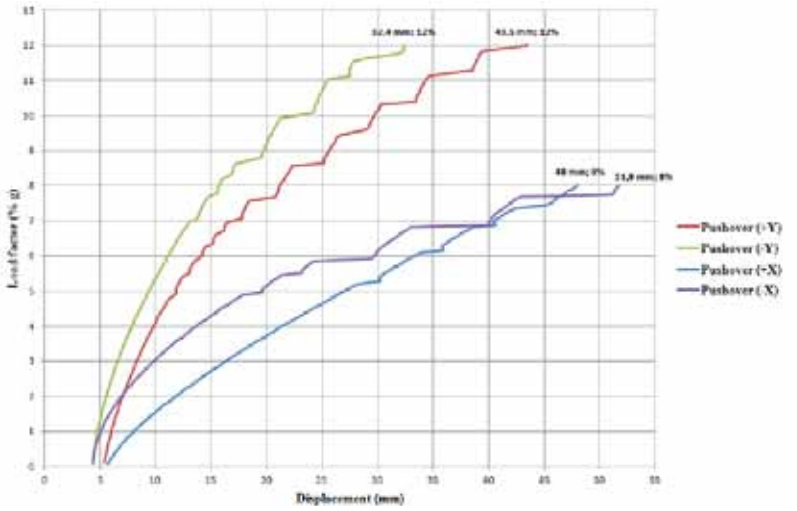

Figure 6 — Capacity curves under seismic loads in different directions

– Diagonal cracking in southern buttresses, starting from most tensioned zones and passing through windows openings. Compression damage also appears on the other side of the buttresses in the most compressed zone. Northern buttresses are showing also diagonal cracks around windows (Figure 7).

– Cracking along the full span of flying arches. The cracks are more intensive at the connections with buttresses and clerestory walls (Figure 7).

– Intensive cracks in vaults of lateral and central naves. This finding is matched with historical documentation of several collapses and reconstruction of vaults.

For the case of seismic load in +X-direction, and at the last step of analysis, the damage is characterized by:

– Diagonal cracks passing around windows' openings in upper clerestory walls connected to pillars, and lower clerestory walls conected to buttress (Fig. 8). Diagonal cracking in apse walls (Fig. 8).

– Cracks at pillars bases and at its connection with clerestory wall.

– There are intensive cracks in vaults like the earthquake in +Y direction.

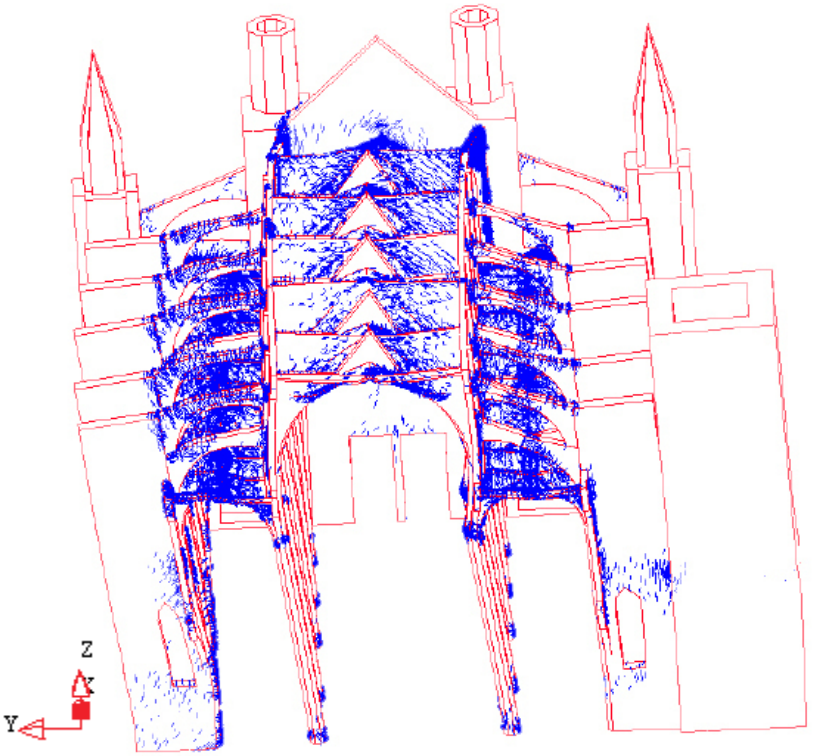

Figure 7 — Crack patterns (in blue) in buttresses, pillars and flying arches (case of +Y earthquake)

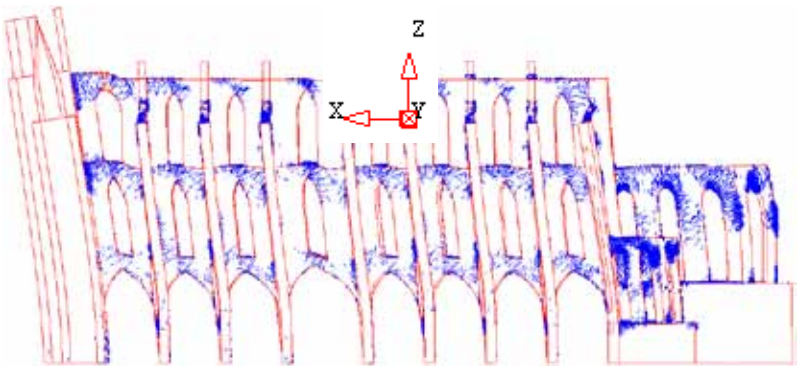

Figure 8 — Crack patterns (inblue) at apse walls and frame of buttresses and lower clerestory wall (case of +X earthquake)

Continuous dynamic monitoring

The monitoring system was chosen to continuously measure, record, and wirelessly transfer the records of the accelerations without having to set up an activating threshold. It was decided to implement this type of monitoring because the amplitude of the seismic motion expected in the island of Mallorca is low to moderate and may be similar in magnitude to frequent wind effects. The system is composed of digitizer, data acquisition system, GPS antenna, an internet router and the three tri-axial accelerometers previously used in dynamic identification. Two accelerometers were kept above two arches of the main nave: the first (called S1 Station) was kept at point P6, and the other at point P16 (called 145 Station), see Figure 2. The third accelerometer (called Soil Station) was kept as shown in Figure 2. The system worked from 17th December 2010 to 13th September 2011.

Response during recorded earthquakes

The website of European-Mediterranean Seismological Centre (http://www.emsc-csem.org/) has been checked periodically for the occurrence of any earthquake with significant magnitude that might produce a recordable effect to the cathedral. From following some seismic events, it has been noticed that regional earthquakes with magnitude higher than 4, and teleseismic earthquakes with magnitude higher than 8 are of interest. For this purpose, the time-frequency distribution of each channel has been computed (Figures 9 and 10) to determine whether the earthquake arrived with enough energy.

In the post-processing of the information for any earthquake, the time-frequency distributions are calculated by 100 seconds Hanning windows, which is considered enough to obtain appropriate frequency resolution and to avoid side lobes. Power spectral densities, coherence and two transfer function estimators (H1 and H2) for different combinations of pairs of channels of (S1 Station-Soil Station) and (145 Station-Soil Station) are computed before, during, and after the considered seismic event. Frequencies with coherence higher than 0.8 are considered for calculations of transfer function.

During the monitored period it has been possible to capture one local seismic event, corresponding to the recent Menorca earthquake (31/7/2011), and six regional earthquakes with epicentre in Lorca (11/5/2011), Alagüeña (10/7/2011), Gulf of Lion (2/7/2011 and 7/7/2011) and Northern Italy (17/7/2011 and 25/7/2011). Also, it has been possible to register the teleseismic earthquake of Honshu occurred in Japan (11/3/2011).

Considering the range of interest of natural frequencies of the cathedral, it was found that the effective duration of regional earthquakes is less than 250 seconds and for the local ones is less than 100 seconds. Also, It was noticed that only the teleseismic earthquake of Honshu arrived with very low range of frequency contents (less than 1,5 Hz), whereas all the other captured regional and local earthquakes had frequency contents able to excite the range of interest of natural frequencies of the structure (Figure 9).

Some effects observed in the dynamic response, even for very low amplitude motion, are attributed to the non-linear response of the building. Hence, the appearance of multiple close peaks for the same mode in the spectral diagrams is believed to be due to a breathing behaviour caused by existing cracks [18]. This phenomenon can be seen, for instance, in the 4th mode during the occurrence of the Menorca earthquake (Figures 10 and 11). Due to the short effective duration of the captured earthquakes, the uncertainty in the power spectral densities is greater than the shift experienced by the peaks. The change of frequencies produced by earthquakes is less than 1%.

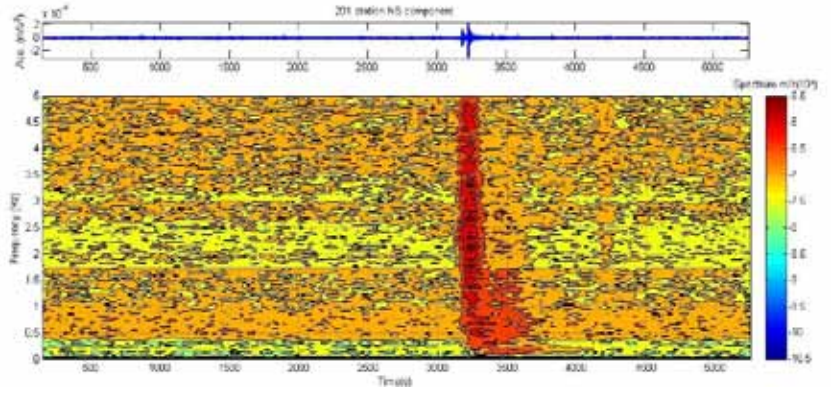

Figure 9 — time-frequency distribution of the NS component at Soil Station for the Gulf of Lion earthquake

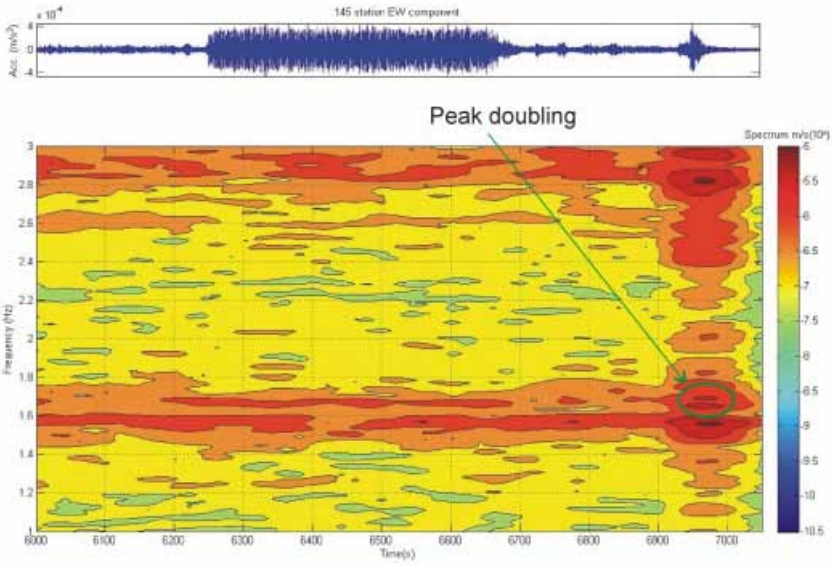

Figure 10 — Time-frequency distribution of the EW component at 145 Station for Menorca earthquake

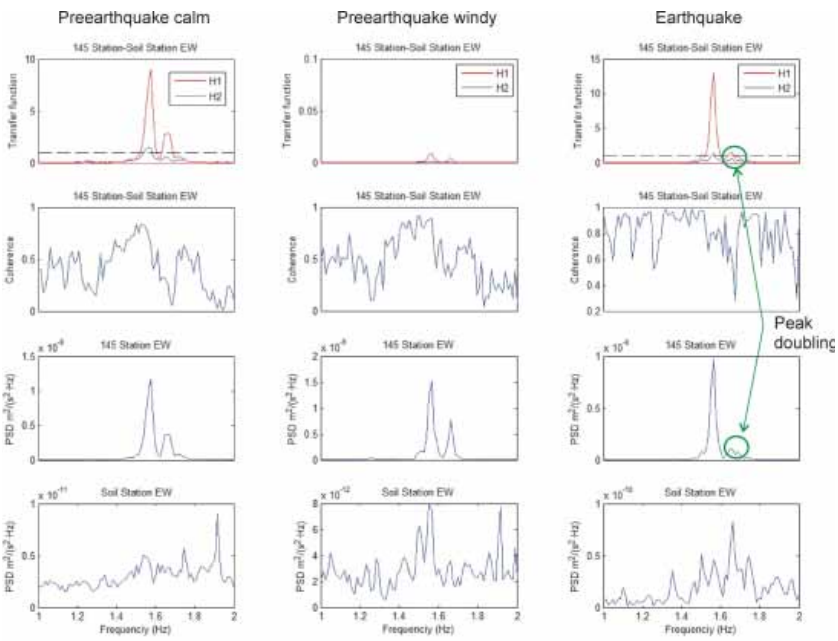

Figure 11 — Transfer function, coherence and power spectral densities of EW component at 145 Station for Menorca earthquake, before earthquake with calm wind and windy, and during earthquake

Conclusions

The paper presents an application of ambient vibration dynamic identification tests on a complex structure. Only well identified mode shapes and frequencies were used for the purpose of updating the global FE. The modal shape of each associated pair of experimental and numerical modes was visually compared to assure an adequate correspondence. In terms of frequencies, the updating process was sufficient and satisfactory. In terms of MAC values, it can be considered only acceptable. Many effects may be affecting the obtained MAC values, among which the soil-structure interaction, not considered so far in the modal, and the existing cracks. In addition to include the influence of the soil, it is intended to improve the model by simulating the main existing cracks as discontinuities in the FE mesh.

The tuned model was subjected to seismic loads in both the transversal and longitudinal directions using nonlinear static pushover analysis. The curves showed that the cathedral has higher resistance in transversal direction than in longitudinal one. The resisted acceleration in transversal direction is a little higher than the expected spectral one, whereas in the longitudinal direction it is slightly lower.

The use of a long term dynamic monitoring in Mallorca Cathedral has provided a better understanding of the dynamic behaviour in spite that only very low motion earthquakes registered since its implementation in December 2010. For the very low motion earthquakes registered, the only non-linear effect so far observed is the doubling of some frequency peaks. This peak doubling is probably due to a breathing crack effect. It is expected that the capture of higher motions in the near future may allow a better characterization of the dynamic response including such non-linear effects.

Acknowledgements

This research has been carried out within the project "New Integrated Knowledge based approaches to the protection of cultural heritage from Earthquake-induced Risk-NIKER" funded by the European Commission (Grant Agreement n° 244123), whose assistance is gratefully acknowledged.

References

[1] *Roca P. (2001) Studies on the structure of Gothic Cathedrals. In: Proc. 3rd Int. Seminar on Historical Constructions Guimarães, Portugal, University of Minho, 71–90.*

[2] *González R., Caballé F., Domenge J., Vendrell M., Giráldez P., Roca P. and González J.L.(2008) Construction process, damage and structural analysis. Two case studies. In D'Ayala D. and Fodde E. (ed) Structural Analysis of Historical Construction. CRC Press Balkema, 643–651.*

[3] *Martinez G., Roca P., Caselles O. and Clapés J. (2006) Characterization of the dynamic response for the structure of Mallorca cathedral. In Lourenço P., Roca P., Modena C. and Agrawal S. (ed) Structural Analysis of Historical Constructions. Macmillan Advanced Research Series.*

[4] *Ramos, L.F., Alaboz, M., Aguilar, R. and Lourenco, P.B. (2011). Dyanmic identification and FE updating of S.Torcato Church, Portugal. Dynamics of Civil Sturctures. Volume 4, 71–80.*

[5] *Domenge J., (1999). L'obra de la Seu. El process de construcció de la Catedral de Mallorca en el tres-cents. Institu d'Estudis Balears, Palma de Mallorca (in Catalan).*

[6] *Ramos, L. F. (2007). Damage identification on masonry structures based on vibration signatures. PhD thesis, University of Minho, Portugal.*

[7] *Brincker, R., Zhang, L. and Andersen, P. (2000). Output-only Modal Analysis by Frequency Domain Decomposition. 25th International Conference on Noise and Vibration Engineering. Vol II.*

[8] *Elyamani, A, Caselles,J,O, Clapes,J, & Roca,P, Assessment of Dynamic Behavior of Mallorca Cathedral, 8th internation conference of structural analysis of historical constructions, 15–17 Oct, 2012, Wroclaw, Poland,*

[9] *Martínez, G. (2007) Seismic vulnerability for middle and long span masonry historical buildings (in Spanish). PhD thesis, Technical University of Catalonia, Barcelona,Spain.*

[10] *TNO DIANA BV 2005. DIANA-Finite Element Analysis, The Netherlands.*

[11] *Allemang, J. R. (2003). The modal assurance criterion — twenty years of use and abuse. Sound and Vibration 37:8,14–21.*

[12] *Gentile, C. and Saisi A. (2004) Dynamic-based F.E. model updating to evaluate damage in masonry towers. Proc. of 4th Int. Seminar on Structural Analysis of Historical Constructions pp. 439–449.*

[13] *Betti, M. and Vignoli, A. (2008). Modelling and analysis of a Romanesque church under earthquake loading: assessment of seismic resistance. Engineering Structures 30:2, 352–67.*

[14] *Elyamani, A. (2009). Wind and earthquake analysis of spire of cimborio of Barcelona cathedral. MSc thesis, Technical university of Catalonia, Barclona.Spain.*

[15] *Clemente,R. (2006). Structural analysis of historical buildings using localized crack models (in Spanish). PhD thesis, Technical University of Catalonia, Barcelona,Spain.*

[16] *Rots, J.G. (2001). The role of structural modelling in preserving Amsterdam architectural city heritage. 3rd International Seminar on Historical Constructions. 685–696.*

[17] *Trujillo,A. (2009) Stability analysis of Famagusta Churches: St. George of the Latins. MSc thesis, University of Minho, Guimarães. Portugal.*

[18] Chondros T. G., Dimarogonas A. D., and Yao J. (2001) Vibration of a beam with a breathing crack. Journal of Sound and Vibration, 239(1): 57–67.

Seismic Strengthening of Masonry Infilled Reinforced Concrete Frames

GRUBIŠIĆ, Marin
Faculty of Civil Engineering,
J. J. Strossmayer University
of Osijek, Croatia

SIGMUND, Vladimir
Faculty of Civil Engineering,
J. J. Strossmayer University
of Osijek, Croatia

Abstract

Structural frames are often filled with masonry panels for architectural purposes as divisional walls or cladding. There has been much work conducted into the seismic behaviour of infilled frame buildings (e.g., Abrams, 1994–1996; Chrysostomou et al, 1992; Žarnić and Tomažević, 1984). However, the most significant outcome is perhaps the general consensus that brickwork infill can have a beneficial effect on the overall seismic performance of the building if it is properly tied into the rest of the building.

The purpose of the present study was to investigate possible seismic strengthening options for use in the seismic upgrade of a infilled frame structures with an emphasis on strengthening brick masonry infill walls. In order to test the numerical models and to define a simple method for analysing the behaviour of reinforced concrete frames with infill in earthquake regions, we have done a series of tests with the aim to investigate the behaviour of strengthened infills of r/c frames under seismic loads.

Model frames represent part of a model structure, designed according to the EN 1998. Here we consider six one story — one bay specimens, built in a scale 1:2.5; infilled with two types of masonry (hollow and solid clay masonry units) and three types of strengthening methods, tested under constant vertical and cyclic in–plane lateral loads. Presented is the relationship between drift capacity and properties of the frame–wall system controlling drift capacity.

Keywords: reinforced concrete (r/c) frame, masonry infill, seismic strengthening, infilled r/c frame, experimental testing

Introduction

Infilled frame structures

As mentioned, in many countries situated in seismic regions, reinforced concrete frames are usually infilled by brick masonry panels. For seismic design and evaluation of existing buildings, the contribution of infill walls is usually neglected although it can be — and usually is beneficial. Its contribution is of special importance also for seismic strengthening of r/c frame buildings. Until today, a large number of seismic strengthening projects have been documented and provide an excellent database for practising engineers. The strengthening methods used naturally reflect the state-of-the art at the time. A selection of case studies encompassing a wide range of strengthening options, of which are most commonly referred and discussed, are beam–column joint and connection strengthening, column strengthening and many types of frame bracing. Therefore, we can see that strengthening methods of masonry infill are not sufficiently investigated, especially experimentally, and the investigation of these is necessary.

The complex nature of the interaction between concrete frames and masonry infill wall panels is reflected perhaps in the large number of experimental studies conducted on this topic. The results of previous work suggest that the brickwork can be accurately modelled using "equivalent struts", but still is a common principle of structural analysis that often regards the masonry infill as a non-structural (architectural) element. So, moment frame members are designed for the full lateral loads while the contribution of infill masonry panels is usually neglected, and this approach may represent a major threat considering different mechanisms of the response and seismic loads transmission for moment resisting bare frame and fully masonry infilled frame, shown in Figure 1.

Since the nonlinear behaviour is in close relation with the connection between the frame and infill, it is very difficult to predict it by analytical methods if the analytical models are not supported and verified by the experimental data. Due to the complex behaviour of such composite structures, experimental research is of great importance to determine the strength, stiffness and dynamic characteristics at each stage of loading.

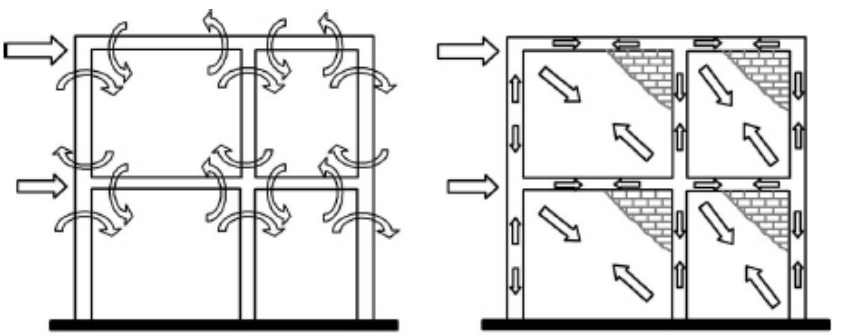

Figure 1 — Mechanisms of response and seismic loads transmission for moment resisting bare frame and fully masonry infilled frame.

Strengthening of Masonry Infills

In multi-story construction, the most important attribute of the structure is its capability to retain its integrity at interstorey drifts ranging from 1.5% to 2.0%. The results of neural-network analysis (Sigmund, V., Kalman, T., 2009) based on approximately 100 tests of one bay — one story infilled frames have demonstrated that interstorey drifts of that magnitude can be achieved by a reinforced concrete frame with solid infill walls provided the columns have the ability to sustain the required shear force under reversals of shear and axial forces.

There has been a substantial increase in the topic of seismic retrofit or strengthening of existing buildings in recent years as evidenced by the growing number of research papers published in this area. The overall aim of many projects was to identify the optimal combination of strengthening options that would enable the building to meet the present–day "life-safety" performance criteria for buildings subject to a design magnitude earthquake. Today we have growing need for strengthening of existing structures, and infills contribution is of special importance for seismic strengthening of r/c frame buildings.

Often mentioned out-of-plane strength of unreinforced masonry infill walls is well-recognised as being one of the major weaknesses of these types of infills with regard to seismic actions. However, masonry infill walls must not fail in the out-of-plane direction if they are to maintain their in-plane load capacity. Aničić (1995) reports that horizontal ties, tie beams and/or columns and "rigid" floor diaphragms are normally effective at preventing out-of-plane collapses of masonry walls provided the span-height ratio and height-thickness ratio are kept within normal design limits. Therefore, we have observed only in-plane strengthening methods.

Where the masonry infill is susceptible, it can be strengthened in a wide variety of ways. While recent research trends are towards the use of advanced fibre composites, energy dissipation devices and seismic isolation schemes for the seismic strengthening of buildings, the more traditional methods should not be neglected when considering which system(s) to employ. Within the scope of our research, we have planned to investigate possible strengthening methods, of strong and weak frames, by application of the masonry infill. Up to now, following strengthening methods of the strong r/c frame, were investigated and shown in Figure 2:

a) Masonry infill anchored to the surrounding r/c frame (Type 1/I – hollow, Type 1/II – solid),
b) Reinforced masonry infill anchored to the surrounding r/c frame (Type 2/I – hollow, Type 2/II – solid), and
c) Masonry infill wall with additional confining element (Type 3/I – hollow, Type 3/II – solid).

Figure 2 — Seismic strengthening methods applied on six test specimens

Tests were performed at the Laboratory for experimental mechanics at the Faculty of Civil Engineering in Osijek, Croatia. The results of strengthened specimens are compared to the previous experiments when the r/c frame was without infill (Model TYPE 0) and with infill with no connection to the frames (Model TYPE 1). The main goal of this experiment was to determine the contribution of each method of strengthened infill to the carrying capacity of infilled frames under horizontal actions and the actual behaviour of the infill panel itself.

Description of the prototype

In order to separate the experimental infilled frame model, a reinforced concrete frame structure with ground plan dimensions of 16.00 m x 17.50 m was used, as shown in Figure 3.

When calculating and designing the prototype, weight of infills are taken into account using the appropriate line load, but infills alone was intentionally not modelled. Dead weight of all the structural elements was taken into account by Radimpex Tower 6 in the physical spatial 3D design model, so we obtain the internal forces and design of frame members. Modal analysis, seismic analysis and design of r/c elements were made according to latest EN 1992 and EN 1998 standards. Selected sections and reinforcement amounts of frame columns and beams are given in Figure 4.

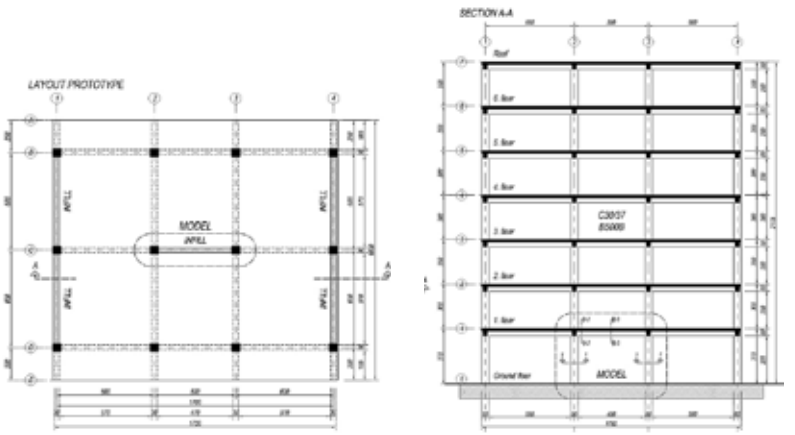

Figure 3 – Model of the prototype frame building

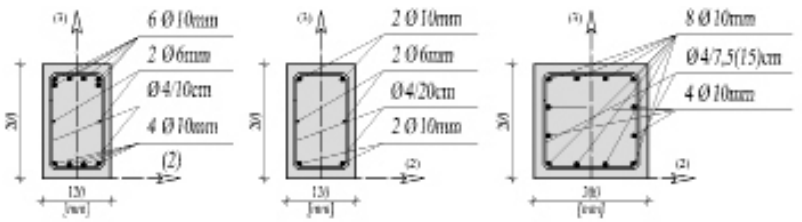

Figure 4 — Selected dimensions, cross sections and reinforcement of the frame building members, columns (1–1) and beams (2–2 and 3–3)

Test specimens

Within the research project a total of six r/c frame models with strengthened infill, one bare r/c frame model (without infill) and one frame with infill who has no connection to the frames — were constructed and tested through in-plane cyclic loading. The specimens are a scaled part of a model 7-story building (middle frame of the "Tsukuba" building) located in the ground floor and constructed in a scale 1:2.5 as shown on Figure 5. Two types of infill walls with different strength properties were used: the high strength solid bricks (Opeka Osijek), medium strength hollow brick blocks (Sladojevci). Mechanical properties of the infill blocks were tested on three samples each. The compressive strength of concrete was obtained by testing the cube size 15 x 15 x 15 cm, and the compressive strength of the infill elements can be found in [3]. Comparison of the results obtained by testing the r/c infilled frame models with two different infill types and those obtained by testing the r/c bare frame model was made. The test models were 2,2 m wide and 1,5 m high, with columns and beam cross section of 20 x 20 cm and 12 x 20 cm, respectively. Materials used were concrete of class C 30/37 and reinforcement of type B500B.

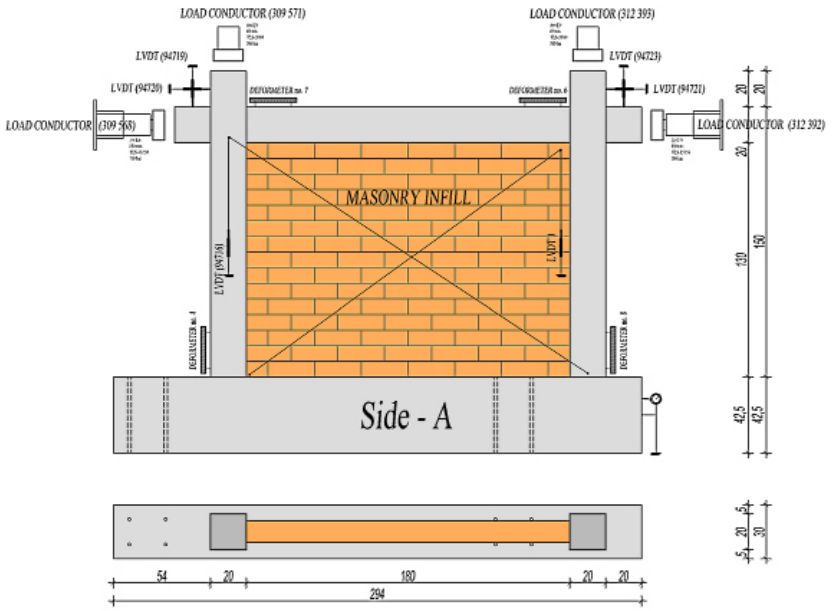

Figure 5 — Selected dimensions and the position of the instruments on the test model

R/C columns rebar percentage is 2,36%, while the rebar percentage of r/c beams are 1,31% in the middle of the beam span and 3,27% at its ends. Masonry panels were built subsequently, i.e. frame elements were made first and then the masonry infill walls were added with frame and infill in close connection without spacing. They after the r/c frame was done and hardened, and they were made by the cement-lime mortar (cement-lime-sand in volume proportion 1:1:5 and nominal strength of 3 MPa) with thicknesses of horizontal joints of 1 cm and completely filled vertical joints in a manner typically used in Croatia. After 28 days infilled frames have been tested under vertical and reversed in-plane cyclic loading. Test models are designed according to EN 1992 and EN 1998 standards and according to the common practice while their experimental results were analysed and compared as follows.

Test setup and procedure

Before testing, we set the measuring devices and hydraulic presses as shown in Figure 5. We continue to set four load converters, eight LVDT to measure drift, and four deformeters (extensometers) to measure deformations of columns and beams, and of course — all the measuring instruments are connected to the computers and monitored by software Dewetron DeweSoft 6.6.7. Columns of the test specimens were loaded with constant vertical load that replaced the stories above. Scaled load applied at the column tops was 365 kN in each column. Horizontal loading has been applied in-plane as reversed cyclic load, and it steadily increased by increment of 10 kN as shown on Fig. 6. Vertical load are slightly oscillated during the test due to the additional moment introduced to the frame by horizontal load. During the test measured were: loads at each point, vertical and horizontal displacements at the top of the frame, sliding of foundation and extension/shortening of diagonals, deformations in the columns and beams.

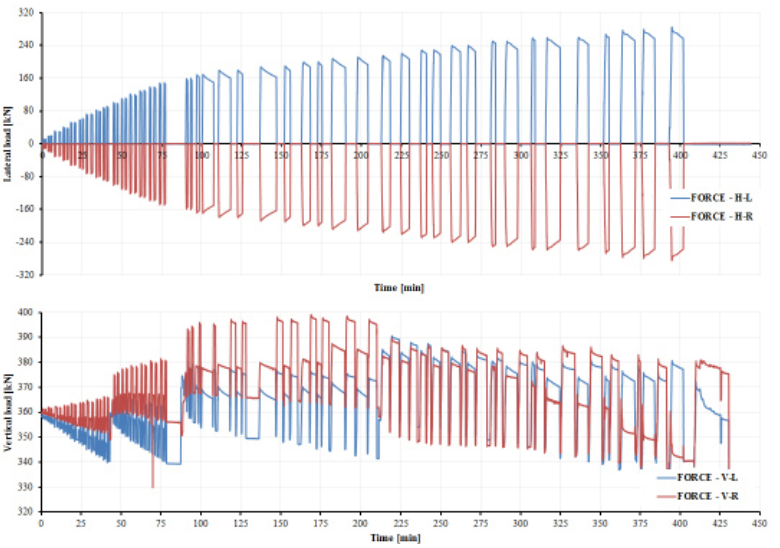

Figure 6 — Example of applied lateral cyclic loading and changes of vertical forces due to specimen rotation for one frame

Figure 7 — View of the experiment in progress and associated samples of masonry and mortat

Model TYPE 1

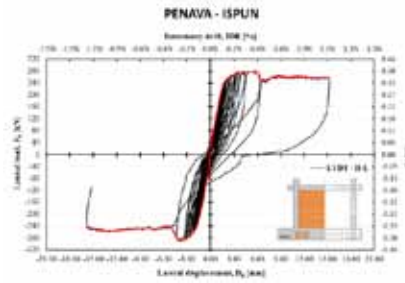

Model TYPE 1-II

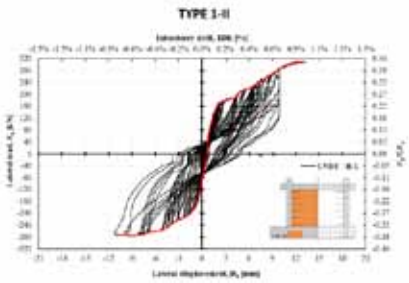

Model TYPE 2-I

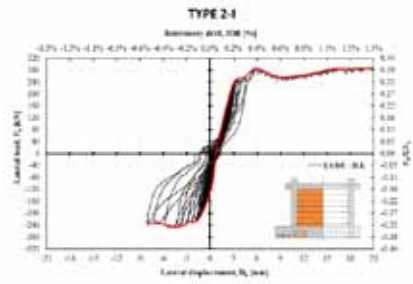

Model TYPE 2-II

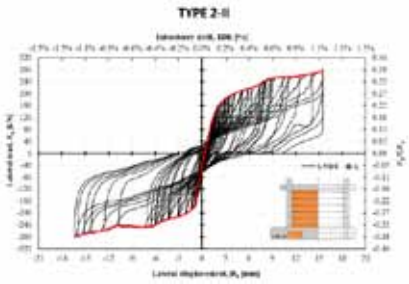

Model TYPE 3-I

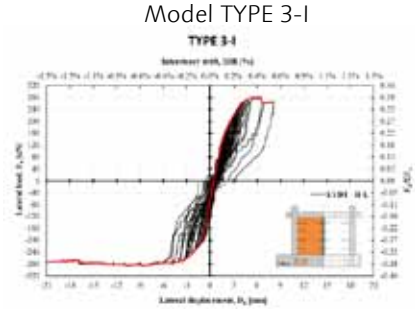

Model TYPE 3-II

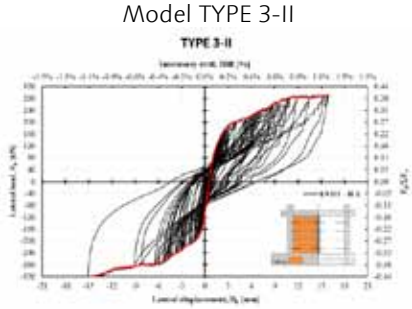

Model TYPE 0 (Bare frame)

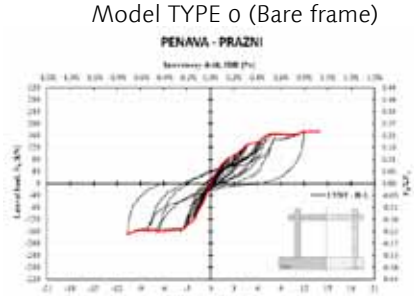

Envelopes of all models

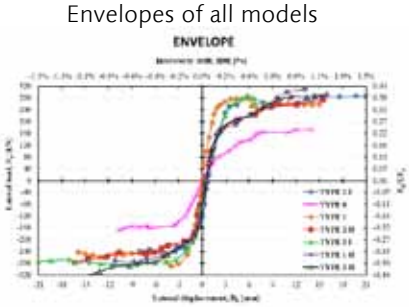

Figure 8 — Review of hysteretic curves and their envelopes for all models

Results

Part of the measured results is present in a form of base shear vs. horizontal displacement of the frame for three types of strengthened frames with two types of infills. The hysteretic curves and envelopes are presented in the following Figure 8.

Conclusions

The behaviour of the infilled frame under seismic loading is difficult to predict by analytical methods unless the analytical models are supported and revised by the experimental data. Within the scope of a larger project we have tested six r/c frames infilled with two types of masonry infill, solid and hollow brick units. The frames were made with standard materials and procedures as used in Croatia. From the measured results could be observed that any strengthening method enhances the initial stiffness of a composite structure and allows larger drifts with less loss of stiffness compared with models without any strengthening.

Thus strengthening models can withstand much greater interstorey drifts at almost maximum lateral load level, while infill panels will reach their deformation capacity and lose their load carrying ability at much larger displacements, where we can see model TYPE 3-I that can withstand up to 2.6% IDR. Increase in the load carrying capacity depends on the strengthening method and brings from 5 to 15% in the increase. It is important to notice that much larger energy dissipation is prominent in the models which infills contains solid brick elements, and thus we observe much better effect of mortar sliding with regard to out-of-plane face dropping of hallow clay blocks.

Acknowledgements

The research presented in this full paper is a part of the research project "Seismic design of infilled frames", No. 149-1492966-1536, supported by the Ministry of Science, Education and Sports of the Republic of Croatia and its support is gratefully acknowledged.

References

[1] *Griffith M.: Seismic Retrofit of RC Frame Buildings with Masonry Infill Walls: Literature Review and Preliminary Case Study, JRC European Commission Report, JRC 44166. 2008.*

[2] *Kalman, T., Sigmund, V.: Seismic capacity of infilled frames using neural networks, 6th ICCSM Proceedings, Croatian Society of Mechanics, Zagreb, 2009.*

[3] *Matošević, Đ., Sigmund, V., Zovkić, J.: Experimental Testing of Masonry and Masonry Piers, 6th ICCSM Proceedings, Croatian Society of Mechanics, Zagreb, 2009.*

[4] *Sigmund, V., Zovkić, J., Sigmund, Z.: Experimental Tests of R/C frames with Masonry infill, 14ECEE, Ohrid, Macedonia, 2010.*

[5] *El Gawady, M., Lestuzzi, P., Badoux, M.: A Review of Conventional Seismic Retrofitting Techniques for URM, 13th International Brick and Block Masonry Conference, Amsterdam, July 4–7, 2004.*

Time dependent analysis of steel-concrete composite beams

HEGYI, Péter
University of Technology and Economics, Budapest

Abstract

In this paper the phenomenon of the creep of steel-concrete composite beams is investigated. Some of the available material models are briefly introduced, including the Dischinger-theorem and the ageing linear viscoelasticity theorem. Based on these material models different structural models were developed of which five are involved in this paper: the Fritz-method, a finite element approach, numerical integration methods for both material models and the codified formulae of the Eurocode. Analyses were carried out considering a three-step load sequence of a simply supported beam with the assumption of the Bernoulli-Navier hypothesis. Calculations were performed for different widths of concrete slab to get information about the behaviour of each model. The results were compared to the values based on the Eurocode.

Introduction

A steel-concrete composite structure consists of a steel girder and a composite slab, connected with shear connectors along the girder, so both of the components contribute to the load-bearing capacity of the composite girder. These structures became frequently used after the Second World War based on the several advantages (e.g. higher stiffness than steel structures, less self-weight as concrete structures, unpropped construction) which make them very competitive and economic in different parts of the building industry. One of the disadvantages is that the modelling and analysis of a composite girder is more complex than in the case of a homogenous structure. The cases of some bridges show that the time dependent behaviour of the concrete should be included in the analysis accurately. In Palau [1] a prestressed box girder bridge (main span 240 m) was built, which produced 1.2 m deflection after 13 years of service, and it was predicted

in a detailed analysis that an additional 0.9 m deflection will develop over the next 100 years. Another example is in Turku (Finland) [2], where a slender 90 m long beam leg bridge was built in 1975, which produced twice the deflection that was estimated during the design. The concrete cracked in the support zone so the strengthening of the bridge became necessary. The aforementioned and also some further examples show the importance of the time dependent behaviour of concrete on the structural response, therefore, it is necessary to take it into consideration during the analysis. This makes the modelling of the composite structures even more difficult.

In this paper different methods of analysis are presented which take into consideration the time dependent behaviour of the concrete slab. Some of these methods were developed with significant amount of simplification to reduce the computational requirements which made them suitable in the practical calculations. Apart from these methods, more accurate solutions are also introduced. Calculations are carried out on the case of a simply supported beam to compare these methods to each other.

Time dependent behaviour

The time dependent behaviour causes two problems, which are interrelated but frequently considered independent during the analysis [3]:

– material behaviour: the prediction of creep and shrinkage strains;
– structural behaviour: the determination of the structural response.

To treat with these problems different models have been developed. This paper deals with mainly the structural problem.

Dischinger-theorem

The first basic models describing the creep behaviour were developed in the 1930s, including the Dischinger-theorem [4]. In this model one single creep coefficient-curve is determined taking into consideration the age of concrete at the first loading time ($\varphi(t)$). Then the creep strains are calculated based on this one curve. (see Fig. 1 and Eq. (1)):

$$\varepsilon_{cr}(t, t_0) = \varphi(t, t_0) \cdot \varepsilon_{el}(t_0) = (\varphi(t) - \varphi(t_0)) \cdot \varepsilon_{el}(t_0) \quad (1)$$

where: t_0 is the time of the loading, and t is the actual time;
ε_{el} $(t_0) = \sigma_c (t_0) / E_c$ is the elastic strain caused by the imposed σ_c stress at t_0;
$\varphi(t, t_0)$ is the creep coefficient at time t for a sustained constant load imposed at time t_0;
ε_{cr} (t, t_0) is the creep strain at time t from the ε_{el} elastic constant strain imposed at time t_0.

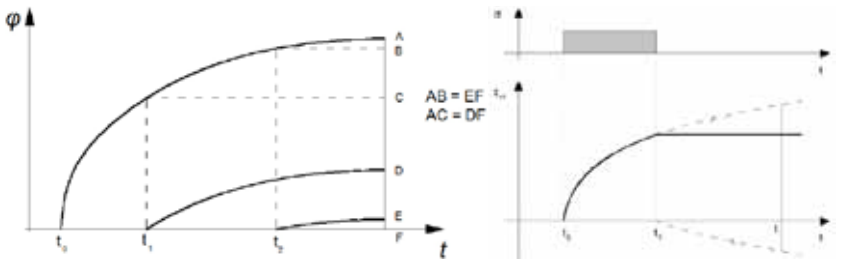

Figure 1 — The Dischinger-theorem

With the use of the Dischinger-theorem the creep strain is considered permanent after unloading. This behaviour does not coincide with the experimental results, which shows a creep recovery after unloading. On the contrary, this formulation allows the usage of simple methods for calculating the creep response of structures.

Ageing linear viscoelasticity (ALV)

As the computational capacity increased, the ageing linear viscoelasticity (ALV) theorem was adopted to describe the behaviour of the concrete. This theorem already considers the ageing of the material. With the application of this more realistic theorem new creep prediction methods were developed, which differs from one another in the parameters which they take into account to determine the creep coefficient. These methods include parameters such as the relative humidity, notional size, cement type, cross sectional shape, aggregate content, compressive strength of concrete, etc. Different methods can lead to rather different results, as shown in Figure 2.

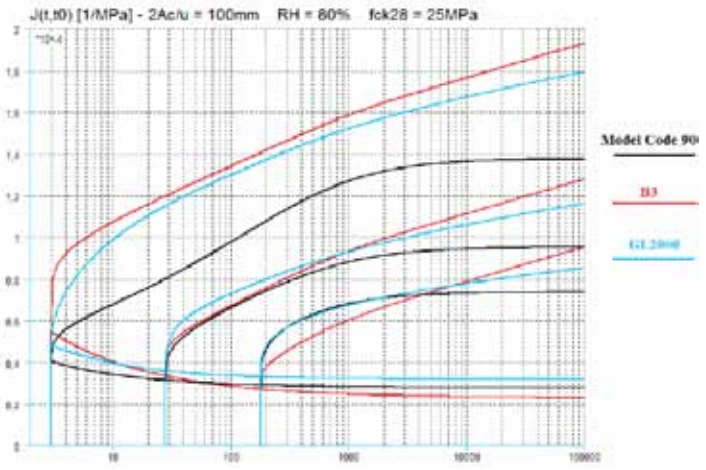

Figure 2 – Different compliance functions

The main equations of the ALV material behaviour are shown in Eq. (2) (for creep) and Eq. (3) (for relaxation):

$$\varepsilon_{\sigma}(t) = \int_{0}^{t} J(t,\tau) \cdot d\,\sigma_{c}(\tau) \qquad (2)$$

$$\sigma_{c}(t) = \int_{0}^{t} R(t,\tau) \cdot d\,\varepsilon_{\sigma}(\tau) \qquad (3)$$

where: σ_c is the total stress;
ε_σ is the total stress dependent strain (including elastic and time-dependent strain);
$J(t,\tau)$ is the compliance function (strain response at time t to a unit imposed stress applied at time τ);
$R(t,\tau)$ is the relaxation function (stress response at time t to a unit imposed strain applied at time τ).

This material model fits to the experimental results better than the previous models. To solve these integral equations a variety of methods were developed, which will be described in chapter 3.2.

Analysis methods

Dischinger-theorem

Traditional methods

As the steel-concrete composite structures came into general use, several methods were developed to consider the long term behaviour of the structural type based on the Dischinger-theorem. The most accurate among these methods is the Fröhlich-method, which is an analytical approach and uses exponential-type equations [5]. Since this method was found too complicated to use in the practical calculations, Sontag applied a simplification. He stated that the bending stiffness of the concrete slab is negligible, so the bending moment of the concrete slab can be eliminated from the equilibrium equations. By this simplification a more simple equation could be obtained, however, it was still deemed rather complex.

Fritz described the effective modulus of the concrete with the aid of a correction factor (φ), which was defined based on Sontag's results:

$$E_{(c,eff)} = \frac{E_c}{1 + \psi \cdot \varphi(\infty)} \tag{4}$$

where the reduction factor for permanent load is

$$\psi = \frac{e^{\alpha_v \cdot \varphi(\infty)} - 1}{\alpha_v \cdot \varphi(\infty)} \tag{5}$$

and

$$\alpha_v = \frac{1}{1 + \frac{E_c \cdot A_c}{E_a \cdot A_a} + a^2 \cdot \frac{E_c \cdot A_c}{E_a \cdot I_a}}$$

where the subscription '*a*' stands for steel and '*c*' for concrete, whilst a is the distance between the centroid of the steel and concrete.

To simplify the calculations the stiffness-dependent correction factor was replaced with a constant coefficient. This was determined for permanent load as 1.1 considering average stiffness properties (for shrinkage it was defined as 0.52). These values can be found in the corresponding Eurocode (EC4 1–1). This is the most generally used method in the manual calculations and was widely used before the FEA softwares became capable of taking into consideration time dependent behaviour.

Numerical integration

Since the values of the Fritz-method are average values they do not describe the real behaviour of the cross sections. To identify the actual behaviour a numerical approach was established for the case of a simply supported beam. It is based on the Dischinger-theorem to ensure the comparability with the Fritz method.

The basic differential equation of Dischinger is shown in Eq. (6):

$$\varepsilon_{\sigma}'(t) = \frac{\sigma_c'(t)}{E_c} + \frac{\sigma_c(t)}{E_c} \cdot \frac{\partial}{\partial(t)} \varphi(t, t_0) \qquad (6)$$

where: ε_{σ} id the total stress dependent strain at the centroid of the slab;
σ_c is the stress at the same fibre;
E_c is the elastic modulus of the concrete at the age of 28 days;
$\varphi(t, t_0)$ is the creep coefficient.

The time interval $[t_0; t]$ can be represented with sufficient amount of time steps (t_i) and so $\varepsilon_{\sigma}(t_n)$ can be expressed from Eq. (6) by replacing the integral with a summation using Eq. (1):

$$\varepsilon_{\sigma}(t_n) \cong \frac{\sigma_c(t_n)}{E_c} + \sum_{i=1}^{n} \frac{\sigma_c(t_{i-1})}{E_c} \cdot (\varphi(t_i) - \varphi(t_{i-1})) \qquad (7)$$

Supposing that the history of the strains and stresses is known until time step tn-1, this equation contains two unknowns. Thus another equation has to be formed, based on the compatibility and equilibrium assumptions (built upon the Bernoulli-Navier hypothesis):

$$\sigma_c(t) = \frac{A}{2 \cdot C} \cdot \varepsilon_{\sigma}(t) - \sqrt{\frac{D \cdot \varepsilon_{\sigma}(t) + \frac{A^2}{4 \cdot C} \varepsilon_{\sigma}^2(t) - B \cdot \varepsilon_{\sigma}^2(t)}{C}} \qquad (8)$$

A, B, C, and D are constants, which contain the stiffness properties of the steel (subscript 'a') and concrete (subscript 'c') part and also the bending moment (M_{Ed}) acting on the cross section:

$$A = A_c \cdot a^2 + I_a \frac{A_c}{A_a} + I_c \qquad C = \frac{I_c \cdot A_c}{E_a \cdot A_a}$$

$$B = E_a \cdot I_a \qquad D = -M_{ed} \cdot a$$

The calculations can be performed based on Eq. (7) and (8).

ALV-theorem

Age Adjusted Effective Modulus method

The ALV methods are more complex than those based on the Dischinger theorem so their usage is more elaborate. Different solution methods were developed for this theorem, including Age Adjusted Effective Modulus (AAEM) method which can well be used in the conceptual and preliminary design stages [3]. The phenomenon of ageing is taken into account through an ageing coefficient (i.e. $\chi(t, t_0)$), which can be calculated based on the J and R functions and the elastic modulus at time t_0. Using this ageing coefficient the age adjusted effective modulus can be defined as follows:

$$E_{c,adj}(t, t_0) = \frac{E_c(t_0)}{1 + \chi(t, t_0) \cdot \varphi(t, t_0)} \tag{9}$$

where $E_c(t_0)$ is the elastic modulus of the concrete at the loading time t_0. With the aid of this modulus a quasi-elastic analysis can be performed, which makes the AAEM method efficient for preliminary calculations:

$$\varepsilon_\sigma(t) = \frac{\sigma_c(t_0)}{E_{c,eff}(t, t_0)} + \frac{\sigma_c(t) - \sigma_c(t_0)}{E_{c,adj}(t, t_0)} \tag{10}$$

where

$$E_{c,eff}(t, t_0) = \frac{E_c(t_0)}{1 + \varphi(t, t_0)}$$

Its formulation is quite similar to the Fritz method but its approach is different: the AAEM method describes the behaviour of an ageing material under varying loads, whilst the Fritz method describes the behaviour of a composite structure with an imposed permanent load.

Apart from AAEM, numerical solutions are also feasible for solving the equations. One possible method is the time-history integral, where the basic equations of ALV are solved by means of numerical integration. This method uses great computational efforts, since the whole history of stresses and strains have to be stored during the calculation (see 3.2.2.). A more efficient numerical method is based on rate-type creep laws. Using this method only the results of the last time step

should be stored, so this means a more efficient computation. This method is also efficient to adapt to FEM softwares, which makes this method the most powerful tool in the design process because of its adaptability. Some of the modern finite element softwares can deal with the time dependent behaviour of concrete such as MIDAS, SOFiSTiK, etc. With these softwares even the most complex structures can be analyzed in a more accurate and detailed way than with the Fritz method.

Time-history integral

To solve Eq. (2) a similar numerical procedure was established as in the case of the Dischinger-theorem. From Eq. (2) the incremental stress dependent strain can be expressed as follows:

$$\varepsilon_c'(t) = \frac{\sigma_c'(t)}{E_c} + \frac{\sigma(t_0)}{E_c} \cdot \frac{\partial}{\partial t} \varphi(t, t_0) + \int_{t_0}^{t} \left[\frac{\sigma_c'(t)}{E_c} \cdot \frac{\partial}{\partial t} \varphi(t, \tau) \right] d\tau \qquad (11)$$

It can be observed that this equation shows some similarity to Eq. (6). It is also clear that the creep strain increment depends on the actual stress in Eq. (6), however, in the ALV-theorem it depends on the whole history of the stress. Likewise in the case of Eq. (6), $\varepsilon_c(t)$ can be expressed from Eq. (11), and the time interval can be replaced with sufficent amount of time steps:

$$\varepsilon_\sigma(t_n) \cong \frac{\sigma_c(t_n)}{E_c} + \frac{\sigma_c(t_0)}{E_c} \cdot \varphi(t_n, t_0) + \sum_{i=1}^{n-1} \frac{\sigma_c(t_i) - \sigma_c(t_{i-1})}{E_c} \varphi(t_n, t_i) \qquad (12)$$

Since the compatibility and equilibrium assumptions are no different than in 3.1.2., the same expression (Eq. (8)) can be adopted to this analysis.

Analysing a simply supported beam

Analysis strategy

The purpose of the analysis was to compare the results of the different models. A simply supported beam was used with a length of 30 metres. The cross section can be seen in Figure 3. To get information about the behaviour depending on various stiffness ratios, the analysis was performed using several slab widths namely: 0.5 m, 1.0 m, 2.5 m, 5.0 m and 10.0 m. To take into account the effect of loading, a loading process was considered with three load steps at age 14 days, 60 days and 3,000 days, with loads 22.222 kN/m, 11.111 kN/m and 11.111 kN/m respectively. This means a total bending moment of 5,000 kN/m at the centre of the span. The steel is S235 type according to Eurocode, the concrete is C 20/25. The Eurocode was also used to describe the creep phenomenon. The basic parameters for the calculation of the creep coefficient were determined as relative humidity: 80%; and cement type: normal.

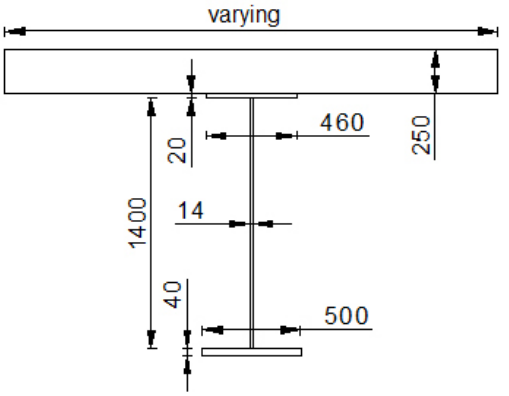

Figure 3 — The investigated cross section (dimensions in mm)

The calculations were carried out by obtaining the procedure of the Eurocode (a Fritz method using $\psi = 1.1$), and also with the original ψ factor of Eq. (5), determined by Fritz. These results were then compared to those obtained by the numerical integration described in chapter 3.1.2. The Dischinger-based models were compared to the ALV-methods too, using AAEM method and a time-history integral (as per chapter 3.2.2.). The numerical integration was carried out assuming that $t_1 = 10^{-4}$ days after the first loading, as the end of the first time step. Every following step's length equals the previous multiplied by 1.005. The last day of the integral was over 200,000 days (540 years) in order that the creep coefficients would be within 0,1% range of their final values. The results were also compared to a finite element model of MIDAS/Civil software, which is fully capable to consider steel-concrete composite sections and time dependent material behaviour.

Results

ψ factors

At first, analyses were carried out on single load steps to compare the ψ factors of the models. Based on the results of the numerical integration the ψ factor could be easily expressed for every considered beam. These values are summarized in Figure 4 and 5.

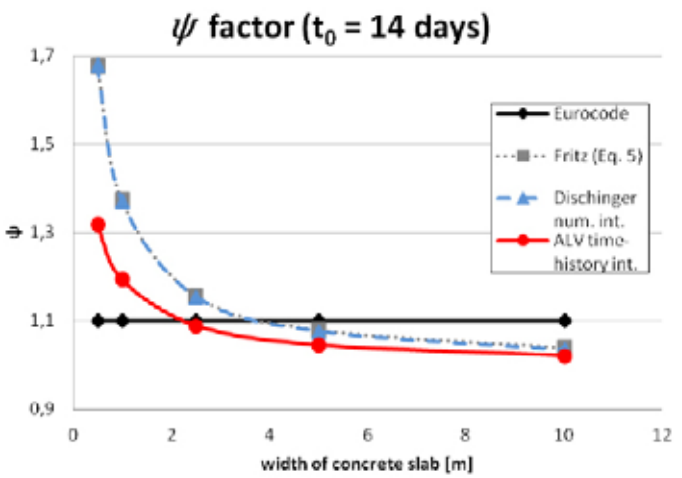

Figure 4 — ψ factors for loading at age 14 days

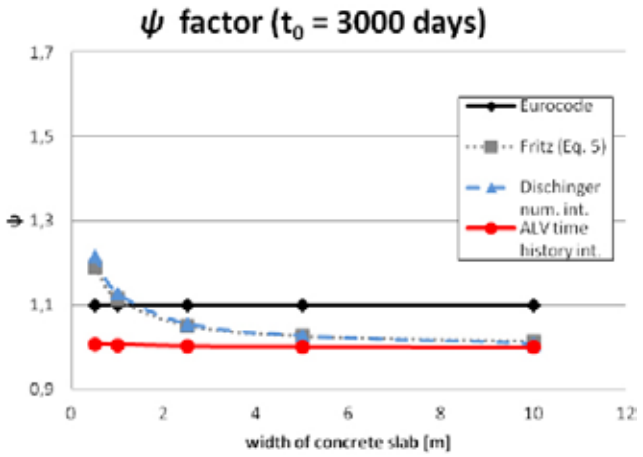

Figure 5 — ψ factors for loading at age 3,000 days

It can be observed that the numerical integration results of the Dischinger-theorem agree well with those obtained by Eq. (5), in fact the difference is negligible. In the case of small concrete slabs the difference between the Eurocode factor and the Fritz value may become significant. It is also shown that the increasing of loading time decreases the ψ factor. In the case of t_0 = 3,000 days, the actual value of ψ remains mostly under the Eurocode value.

It is clear that the ψ factors obtained by the ALV time-history integral are less than the ones obtained by the Dischinger-theorem. In the case of t_0 = 3,000 days it can be considered as 1.0 without any notable loss of accuracy. Based on these figures the ψ factor can be decreased not only in the case of high age loading but also when stiff concrete slabs are used.

Altogether the value of the reduction factor ψ depends on the adopted material theorem, the age of concrete when imposing the load and the stiffness ratio of the cross section. These dependences are neglected by the Eurocode in favour of a simple calculation method.

Inner forces

During the design process the inner forces have greater importance than the ψ factors. The bending moment which acts on the composite cross section can be divided into three components (see Fig. 6): bending moment of the slab (M_c), bending moment of the girder (M_a) and axial force (N) (an equal force in the girder and the slab).

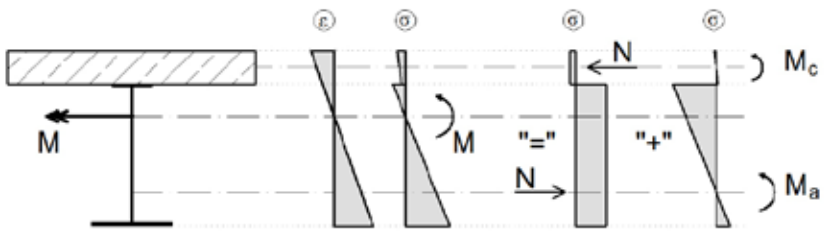

Figure 6 — Inner forces

Although the difference in the values of M_c was significant, their contribution to the global bending moment is negligible. So in this study only the bending moment of the girder and the axial force are discussed. The results of these inner forces are summarized in Figure 7 and 8, respectively. The values were compared with the results obtained by the Eurocode.

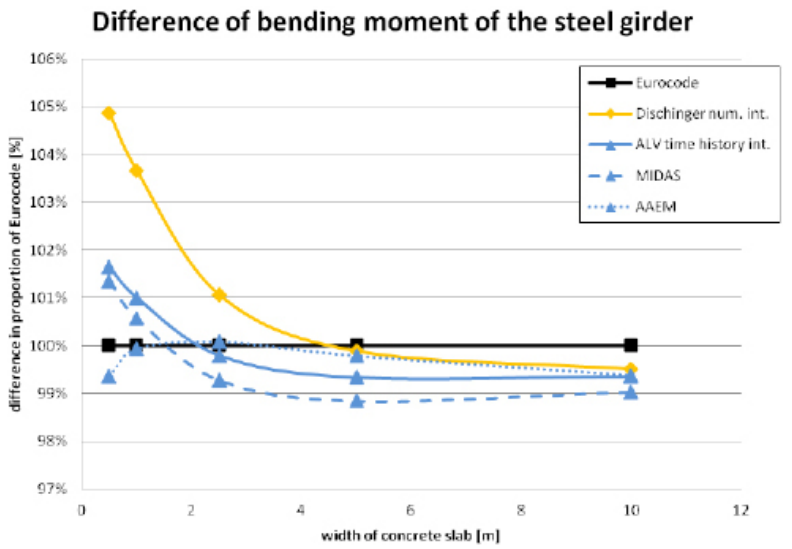

Figure 7 — Bending moment of the girder

Based on both figures it is clear that the tendency of inner forces is analogous to the ψ factors (Figure 4). In the case of the bending moment it can be observed that each model produces less than 5% difference from the Eurocode. Moreover, the difference is around 1% in the case of normal-width concrete slabs (between 2 and 8 metres). The Dischinger-based numerical integral produces greater differences with small slab width than the ALV-based ones. It can be also observed that the time-history integral shows the same behaviour as the FEM results (calculated with MIDAS/Civil), their difference is about 0.5%. This similarity is more evident in the case of the normal forces.

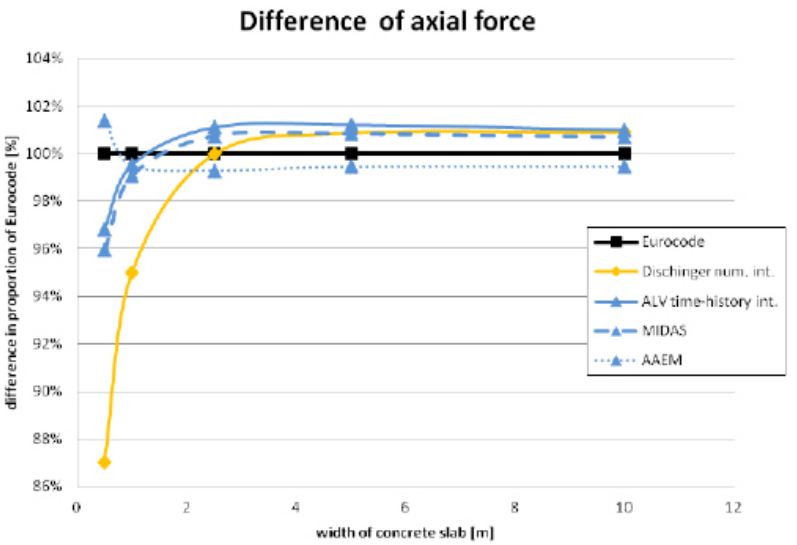

Figure 8 — Axial force

Based on Figure 7 and 8 it can be said that the time-history integral and the finite element model yield to the same result. The third ALV-method (i.e. AAEM) shows different behaviour than the previous ones but its results are slightly closer to the values of the Eurocode. It can be observed that all the models produce greater differences in the case of axial force than of the bending moment; the maximum difference is 13%, in the case of normal slab width it reduces to 2–3%.

Both figures show that the Dischinger-theorem provides results with different behaviour than the other models. The ALV-methods are more complex and in the case of small slab widths they can produce closer results to the Eurocode procedure. However, above 2 metres of slab width the Dischinger-theorem is nearer to the results according to EU Standards. Still, in the case of normal concrete slab width all methods produce maximum 3% difference, which is quite small, particularly according to the differences in the material models predicting the creep coefficient. Although, in the case of a statically determinate structure the difference is small for each model, the usage of the finite element software is recommended because of its greater adaptability.

Conclusion

In the design phase of a steel-concrete composite girder the long-term behaviour of concrete plays an important role. In this paper some available material models were discussed in order to take into account the creep behaviour of the concrete. Structural models were also introduced including the method suggested by the Eurocode, the Fritz-method, the Age Adjusted Effective Modulus method and calculations based on numerical integration and finite element analysis. These were compared to each other.

In the case of the reduction factor (ψ) it was found that the value of ψ reduces if the structure is loaded at high age. It was shown that the ψ factor also depends on the stiffness ratio of the cross section. The difference between the actual value of ψ and that is to be found in the Eurocode may become significant. The trend of the inner forces is influenced by the ψ factor, although, the magnitude of differences are significantly smaller. The time-history integral and the finite element model produced almost equal results. The AAEM method showed different behaviour and it also provides a slightly smaller difference compared to the results of the Eurocode. In the case of normal slab width each model produces around 1% difference at the bending moment of the girder and 3% at the axial force. This difference is quite small, particularly according to the differences in the material models predicting the creep coefficient.

Acknowledgement

The previous researches which laid the foundation of this paper were carried out along with Balázs Somodi and with the aid of Prof. László Dunai and Dr. Tamás Kovács as consultants. Their part in the work is gratefully acknowledged.

References

[1] *Burgoyne, C.J. and Scantlebury, R.C.: Why did Palau Bridge Collapse?, The Structural Engineer, 84/11, 30–37, June 2006.*

[2] *Aarne Jutila: Vasbeton hidak Finnországban, Vasbetonépítés, XIII/1, p. 14–25, 2011/1 (in Hungarian)*

[3] *Analisys of Creep and Shrinkage Effects in Concrete Structures, reported by ACI Committee 209 (ACI 209.3R-XX, March 2th, 2011.)*

[4] *Chiorino, Mario: Analysis of creep and shrinkage effects in concrete structures, Advanced Professional Training, CISM Training, May, 23–27., Udine, 2011.*

[5] *Platthy Pál: Vasbeton lemezzel együttdolgozó acéltartók, Műegyetem Kiadó, Budapest, 1983. (in Hungarian)*

Multi-filament yarns testing for textile-reinforced concrete

KADĚROVÁ, Jana
Institute of Structural Mechanics, Faculty of Civil Engineering, University of Technology, Brno

VOŘECHOVSKÝ, Miroslav
Institute of Structural Mechanics, Faculty of Civil Engineering, University of Technology, Brno

Abstract

The present paper copes with an experimental study of multi-filament yarns made of AR-glass which are used for textile-reinforced concrete. The behaviour under tensile loading was investigated by laboratory tests. A high number of yarn specimens (over 300) of six different lengths ranging from 1 cm to 74 cm was tested to obtain statistically significant data which were subsequently corrected and statistically processed. The behaviour of the yarn was predicted by the studied numerical model of the multi-filament bundle that was applied also for the later results interpretation. The model of n parallel filaments describes the behaviour of a bundle with varying parameters representing different sources of disorder of the response. The aim of the carried experiment was to validate the model presumptions and to identify the model parameters to fit the real load-displacement curves. Due to a distortion of the measured displacements caused by the unstiff experiment device, only the maximal load values were statistically evaluated and the identification of the model parameters was not successful. The effect of the specimen length on its strength was demonstrated and the size effect curve did not exclude the existence of spatial correlation of material mechanical properties modifying the classical statistical Weibull theory.

Introduction

Textile-reinforced concrete is a developing composite material with a high potential of application in civil engineering structures and also in other industrial branches. The material combines a cementitious matrix providing the compressive strength and a tensional reinforcement made by multi-axial fabrics.

The advantages compared to usual steel-reinforced concrete are the reduction of thickness and subsequently of weight of the structural elements and a wide shape variability.

The fibers used for the textile reinforcement have to meet several criteria: high fibre tenancy, breaking elongation and modulus of elasticity much higher than the modulus of the concrete matrix, so that the stiffness of a building component is not drastically reduced by occurring cracks. The most common material of fibers is alkali resistant glass (AR-glass). Filaments are combined to yarns. One yarn composes of several hundreds up to thousands of single filaments with diameter measured in tens of micrometers. The fineness of the yarn is defined by the unit "tex" (gram per 1,000 meters) and depends on the average filament diameter, the fibre material density and the number of filaments. Yarns are subsequently combined into textiles. Historically, the textile-reinforced concrete developed from fiber-reinforced concrete with short filaments of random orientation by aligning the filaments in the direction of the tensile stresses similarly to classical steel reinforcement, which led to better effectiveness of the reinforcement, increased load-bearing capacity and cost reduction. The material is a subject of an intensive research in many institutions [1].

Numerical model of a bundle

The yarn structure is a system made by many parallel filaments with random properties. These properties vary randomly over the length of the yarn as well as within each cross-section due to imperfections from the production process. To describe the complex behaviour of the bundle, definition and study of each individual property and the influence of its randomization on the overall performance is essential. Statistical approach is applied as the most convenient way to capture the yarn behaviour under tension. The presented project studied the computational model introduced in [2] and [3].

This model consists of a set of parallel fibers with no interaction among them. Each filament is considered to act independently and the response of the whole bundle during displacement-controlled tensile loading can be evaluated in an analytical and numerical approach. Parameters used for the bundle model can be divided into two groups: those describing the separate filament and those describing the yarn

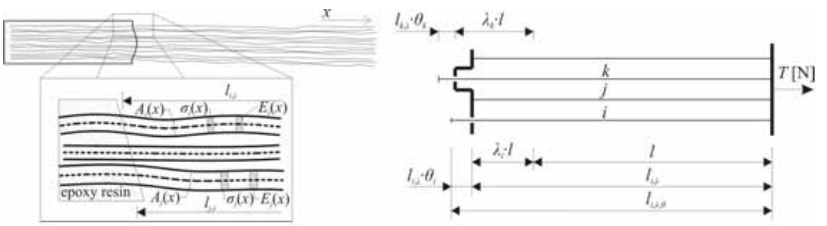

Figure 1 — Left: Filaments in the bundle and their elementary characteristics varying over the length. Right: Filament lengths.

(a set of filaments). Parameters appointed to i-th filament can be used regardless of the composition of the bundle. For AR-glass, where linear brittle fracture behaviour is considered, these parameters are the Young's modulus of elasticity E_i, the cross-section area A_i and the filament strength σ_i. For cases where the filament parameters are randomized within the cross-section, no variability in these parameters over the filament length is considered.

Parameters appointed to the bundle describe the variability of filaments within the bundle. Each of the filament parameters is randomized and described by a probability distribution function — $G_E(E_i)$, $G_A(A_i)$, $G_\sigma(\sigma_i)$. Differences in filament lengths from the nominal length l of the bundle are captured by two extra parameters: parameter λ for the different distance of fixing points of each filament and parameter θ for the different global activation strain of each filament due to waviness of filaments in the bundle (slack). The total length of i-th filament is then $l_{i,\lambda,\theta}$ — see Figure 1 Right.

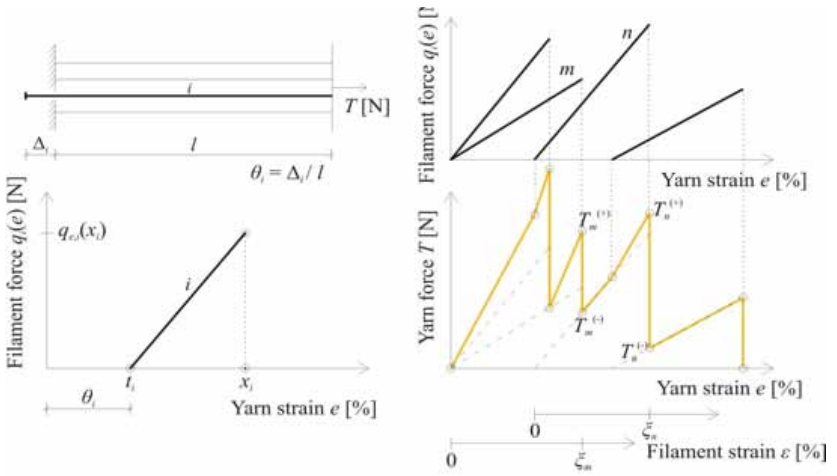

Figure 2 — Left: Load-strain diagrams of one filament. Right: the whole yarn.

The above mentioned parameters are featured in the load–strain diagram equation of the i-th filament made of linear–elastic brittle material: $q_{\varepsilon,i}(\varepsilon_i) = E_i A_i \varepsilon_i H(\varepsilon_i) H(\xi_i - \varepsilon_i)$ using the Heaviside (unit step) function: $H(x) = 1$ for $x \geq 0$ and $H(x) = 0$ elsewhere, which zeros the filament stress out of the filament's possible strain interval.

The overall response in form of the load–strain diagram of the bundle during tensile loading can be obtained numerically simply by summing up the contributions of all filaments at each level of global strain. In practical applications the number of the bundle filaments is very high (several hundreds to thousands). For such a high number of filaments n the bundle mean response $M(e)$ can be solved analytically as n-multiple of the mean filament response $\mu(e)$: $M_\theta(e) = n\ \mu_\theta(e)$:

$$\mu_\theta = \int_\theta q_e(e;\theta)\, dG_\theta(\theta) \quad \text{where } \theta_i\{A_i, E_i, \sigma_i, \theta_i, \lambda_i\}$$

Experiment

The material selected for the tensile tests was the AR-glass yarn produced by Saint Gobain Vetrotex with brand name Cem-FIL Direktroving LTR 5325, 2400 tex. The experiment was focused on the observation of effect of size (resp. length) on the yarn strength [4]. Consequently, a wide range of yarn lengths was desired with emphasis on production of the longest possible specimen length, so that the behavior in this region can be mapped. Six length groups were suggested with equal distribution of their logarithms, as the size effect curve is visualized in the double-logarithmic scale: 1, 2.5, 6, 13, 31 and 74 cm (the longest possible specimen length with regards to the testing equipment). The most problematic part of tensile testing was to deal with the anchoring of glass yarns into the machine. Basically, there are two ways how to create bundle supports: endings can be either directly coiled up on a cylinder or poured into anchoring blocks and clamped. Anyway, both techniques show certain deficiencies. As the testing machine is equipped with self–locking holders, yarn endings were poured into 75 mm long anchoring blocks made of epoxy resin. The total number of tested samples was 317 pieces.

Tensile tests were performed using the machine Z100 Zwick/Roell equipped by two load cells measuring the force (20 and 2.5 kN) and mechanical tensile clamps (jaws) of combined type (self-locking with pre-stressing screws). The displacement was measured at the top edge of the upper jaw by deflection extensometer. Samples were loaded by displacement-increments of the cross-head with the constant rate and the reaction force was measured by the load–cell. The test speed was chosen to correspond to 1.1% elongation of the nominal length per a minute. Force–displacement curves obtained from experiment are plotted in Fig. 5. Different colours represent different length groups of samples. "Raw" curves plotted in the figure are obtained directly from experimental device without any modification.

Before it could be proceeded to the evaluation of experimentally obtained results, some modifications of the data set had to be made. Firstly, the number of samples was reduced by elimination of samples either with strength value extremely differing from the corresponding length group's average, or due to serious imperfections caused in the production (such as the sample damage, epoxide penetration into the yarn, etc.). The number of these outliers was 37. These samples were excluded from further evaluation; they are marked with a cross in the graphs (Figure 6).

Also the displacements measured during the tensile loading embodied some harmful patterns. While the force reaction induced by displacement loading can be measured without any errors, the objective measurement

of sample deformation is much more challenging. In the presented experiment, the deflection extensometer was placed on the upper side of the top jaw, which caused an inaccuracy of the measured displacements.

By placing the extensometer on the mentioned position the read deformation did not belong only to the yarn elongation, it was a sum of deformations of all the device parts under the extensometer. Furthermore, the unstiff behaviour of jaws developed other additional more complicated displacement distortion. After several unsuccessful attempts to subtract these parasite deformations by finding the proper calibration curve, the statistical evaluation of the experiment had to be reduced to interpretation of the maximal force with respect to the sample's length.

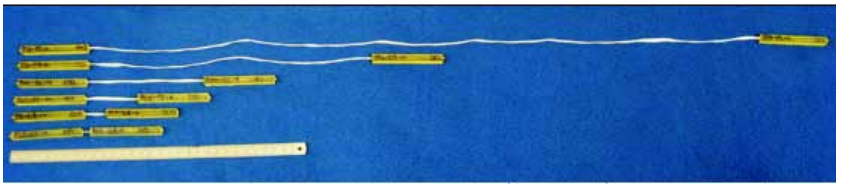

Figure 3 — Specimens' length groups.

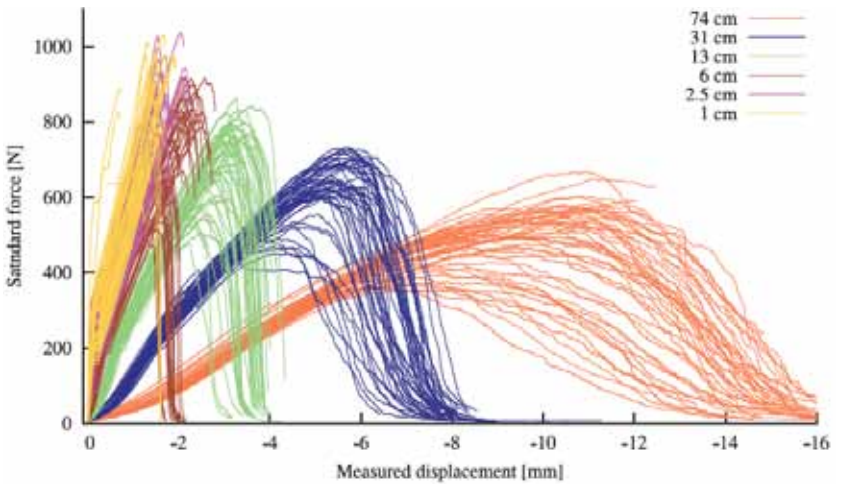

Figure 4 — Unmodified force–displacement curves (all samples).

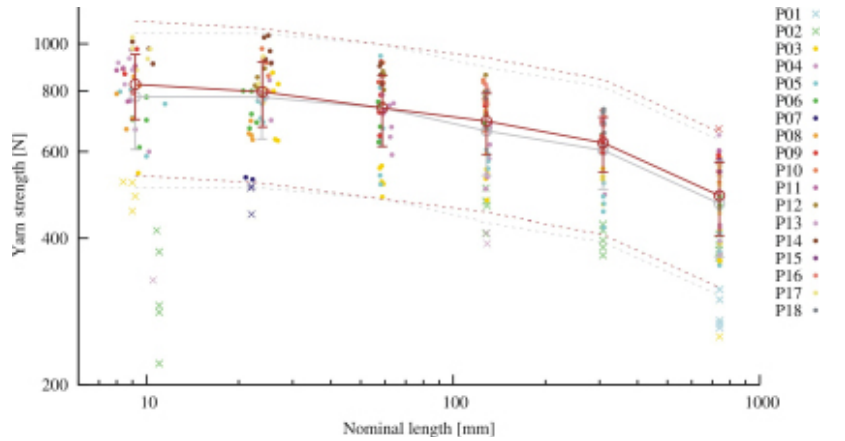

Figure 5 — Yarn strengths vs. yarn lengths of tested sample groups and the size-effect curve as an average ± std of modified (red) and original (grey) data set.

Conclusion

By knowing the true load–displacement diagrams from the experiment, the parameters of the computational model and their distribution could be identified so that the model would fit the reality. Unfortunately, this intention was not fulfilled as the test-curves' adjustment was not successful. Consequently, the only objective information obtained from the experiment were the bundle strengths (maximal load value). The strength of each yarn was plotted versus its length in a double-logarithmic scale – Figure 6. The obtained size-effect curve was intuitively fitted by the equation of modified Weibull size effect with the spatial strength autocorrelation. Although those two curves show a good agreement, it should be stated that the sample strength could be influenced also by other effects, e.g., effects of unequal length of the filaments, individual activation strain of each filament in the bundle, friction among filaments of the longer lengths, or with other unpredictable factors (as the local conditions or the human factor). Without knowing the correct load–deformation curves, these statements are only hypothetical. More detailed information about the experiment can be found in [4].

Acknowledgment

The work has been supported by the Czech Science Foundation under project no. P105/10/J028 and also by the Junior project no. FAST-J-12-21.

References

[1] *RILEM (2006). Textile Reinforced Concrete. State-of-the-Art Report 36, RILEM Technical Commitee, Aachen, Germany*

[2] *Chudoba, R.; Vořechovský, M.; Konrad, M. (2006). Stochastic modeling of multi-filament yarns I: Random properties within the cross-section and size effect. International Journal of Solids and Structures (Elsevier), volume 43, nr. 3–4, pages 413–434*

[3] *Vořechovský, M.; Chudoba, R. (2006). Stochastic modeling of multi-filament yarns II: Random properties over the length and size effect. International Journal of Solids and Structures (Elsevier), volume 43, nr. 3–4, pages 435–458*

[4] *Kaděrová, J., Vořechovský, M. (2012). Multi-filament yarns testing for textile-reinforced concrete. Master thesis, Institute of Structural Mechanics, Faculty of Civil Engineering, Brno University of Technology*

Seismic response of short columns affected by brick/tile aggregate concrete wall infills

KRAUS, Ivan
Faculty of Civil Engineering,
J. J. Strossmayer University
of Osijek,Croatia

MILIČEVIĆ, Ivana
Faculty of Civil Engineering,
J. J. Strossmayer University
of Osijek, Croatia,

Abstract

Various post-earthquake reports indicate that short columns are vulnerable structural members and significant source of serious earthquake damage. Observation that non-structural partial brick infills, comparatively to partial concrete infills, have less harmful effects on short columns put a new perspective on the use of recycled brick/tile as concrete aggregate with the additionally benefit of providing a sustainable management of such material. This paper discusses a numerical study on the influence of brick/tile aggregate concrete infills on the response of short concrete columns. In addition, this paper presents an approach for the analysis and design of short columns, similar to that of tie beams. Linear elastic analysis was carried out on four- and seven-story three-bay concrete frames using modal response spectrum analysis. Mechanical properties of brick and tile aggregate concretes determined by laboratory testing at Faculty of Civil Engineering Osijek are described and used in this study.

Introduction

Various post-earthquake reports indicate that short columns are vulnerable structural members and significant source of serious earthquake damage (see Figure 1). Nevertheless, it is not uncommon to find short columns even in new buildings, for instance in buildings on sloping ground; buildings with partially buried basements; or buildings with frames having partial infills, [1].

As described in [4], short columns are those that fail in shear having height-to-depth ratio $\alpha_s \leq 3$. In addition, columns of a depth equal to 75 cm with a clear height of 230 cm, which is not uncommon for industrial buildings, can also be designated as short, [4].

Figure 1 — Examples of short column failure: a) 5-story building, built in 1997 according to the new Greek Seismic Code, [2]; b) Ø10 mm at 10 cm transverse reinforcement did not prevent heavy damage, [3]

Post-earthquake field investigations have shown that non-structural, or better to say "non-intentional structural", partial brick infills, comparatively to partial concrete infills, have less harmful effects on short columns, [1]. This observation put a new perspective on the use of recycled brick/tile as concrete aggregate with the additionally benefit of providing a sustainable management of such material. A numerical study on the influence of brick/tile aggregate concrete infills on the response of short concrete columns and an approach for the analysis and design of short columns, similar to that of tie beams are presented and discussed in this paper.

Bi-diagonal reinforcing of short columns

An extensive theoretical and experimental research conducted provided efficient principles for analysis and design of tie beams for walls with openings. Due to similarities in behaviour of short columns and tie beams when subjected to earthquake action ([4]) the same principles were used in this study.

The procedure for calculating the amount of bi-diagonal reinforcement used here is illustrated by Figure 2 and given by the following expressions, [4]:

(1) $$F_s = F_c = \frac{V_{Ed}}{2\,sin\,\alpha}\; A_s \cdot f_{yd}$$

or

(2) $$A_s = \frac{V_{Ed}}{2\,sin\,\alpha \cdot f_{yd}}$$

where

(3) $$tg\;\alpha = \frac{h_c - d_1 - d_2}{L_s}$$

and

(4) $$f_{yd} = \frac{f_y}{\gamma_s}$$

where F_s is tensile force, F_c is compressive force, V_{Ed} is design shear force, α isangle between longitudinal and diagonal reinforcement, A_s is cross sectional area of reinforcement of one diagonal steel-bar cage, f_{yd} is design yield strength of reinforcement, d_1 is the distance of the centre of the compression reinforcement from the extreme compression fibres, d_2 is the distance of the centre of the tension reinforcement from the extreme tension fibres and L_s is the clear length of column.

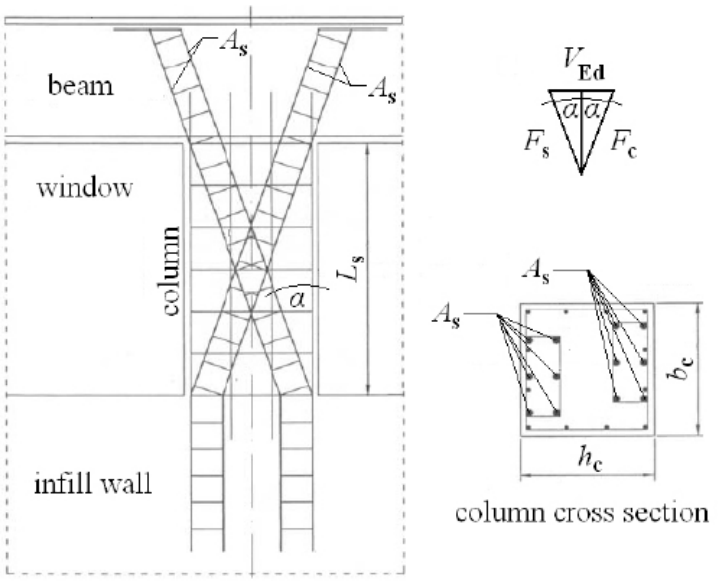

Figure 2 — Bi-diagonal reinforcing of short column, [4] (edited by the authors)

The transversal reinforcement of the bi-diagonal steel-bar cages should be calculated and placed in the same manner as recommended for ordinary columns, [4].

Horizontal and vertical reinforcement of the short column (see Fig. 2) has the role to keep the crushed concrete in its place during strong earthquakes, [4].

Numerical models

2D linear elastic analysis was carried out on four- and seven-story three-bay facade frames using modal response spectrum analysis. In order to concentrate on the effects induced from both column slenderness and the type of material used in infill walls, the frames were taken from buildings regular in plan and elevation. It is assumed that the buildings are located in seismically active area on ground type B defined according to Eurocode 8 ([5]). Also, it is assumed that the buildings are fixed at the ground level. The basement is not included in the analytical model.

The numerical analysis was performed using structural analysis program SAP2000, [6]. Beams and columns were modelled using frame elements while infill walls were modelled using four-noded quadrilateral shell elements.

Materials

The frame elements and floor and roof slabs were made from normal conventional C 30/37 concrete with characteristic compressive cylinder strength at 28 days f_c = 30 N/mm², secant modulus of elasticity E_{cm} = 330,00 N/mm² and density ρ_c = 2,400 kg/m³. Only infill walls were made from different types of concrete described in Table 1. Mechanical properties of brick and tile aggregate concrete (BTAC) were determined by laboratory testing conducted by the authors.

Table 1 — Types of concrete used in infill walls

Concrete		f_c (N/mm²)	E_{cm} (N/mm²)	ρ_c (kg/m³)
C 12/15	Eurocode 2	12	27,000	2,400
C 16/20	Eurocode 2	16	29,000	2,400
BTAC 9	Laboratory test	9	10,500	1,800
BTAC 15	Laboratory test	15	21,500	2,000

Table 2 shows percentage of replacement of fine and coarse dolomite aggregate with crushed brick and tile in BTAC mixtures.

Table 2 — Brick and tile aggregate concrete mixtures

Concrete mixture	Brick		Tile		Dolomite	
	0–4 mm	4–16	0–4 mm	4–16	0–4 mm	4–16
BTAC 9	50%	50%	25%	25%	25%	25%
BTAC 15	50%	0%	25%	25%	25%	75%

Poisson's ratio is taken equal to 0,2 for all types of concrete.

Structural elements were reinforced with B500B steel bars with characteristic yield strength f_y = 500 N/mm² and modulus of elasticity E_s = 200,000 N/mm². It is assumed that all of the reinforced concrete structural elements were reinforced with normal percentage of reinforcement which adds 100 kg/m³ to concrete density values, as recommended in [7].

The partial safety factors for materials for ultimate limit state were adopted according to [8]: γ_c = 1.5 for concrete; and γ_s = 1.15 for reinforcing steel.

Geometry

Geometry of structural elements is provided in Table 3. Floor and roof solid reinforced concrete slabs were 18 cm thick thus satisfying the provision for concrete diaphragms, [5]. Wall thickness is equal to one-half of the column cross sectional height. As noted in [9], the minimal thickness of the partial infill wall should not be less than 12 cm. The concrete cover is taken equal to 3 cm.

Element	Geometry (cm)
Beam b_b/h_b	40/50
Beam length (*CL to CL*)	600
Column b_b/h_b	50/50
Column height at the 1st level (*CL to CL*)	375
Column height at higher levels (*CL to CL*)	300
Slab thickness	18
Wall thickness	25

Table 3 — Geometry of structural elements

Height of the first level infill walls is a function of the captive column height-to-depth ratio which varies from 1 to 3 with step size of 0.5. Infill walls at higher levels have fixed height equal to one-half of the story height.

Loading on frames

The vertical load includes both dead and live load and was added to the frames as described in [10]. The structural analysis program ([6]) calculates the self weight of the structural frames and weight of infill walls. The weight that includes wall partitions and ceilings was taken into account by uniformly distributed load equal to 3.35 kN/m² as suggested in [11]. The weight of perpendicular beams were added to frames as described in [10].

The live load for floors was taken equal to 3 kN/m², which is the normative value for school buildings ([7]), while the live load for roof is taken equal to 2 kN/m² as suggested in [12].

Seismic loading is applied by using modal response spectrum method. Four horizontal design response spectrums of type 1 were made by combination of two earthquake intensities and two ductility classes in accordance with Eurocodes (see Figure 3). Behaviour factors were calculated in accordance with [5] for multi-storey, multi-bay frames or frame equivalent dual systems. It is assumed that the stories have correlated occupancy. Load combinations were made as described in [10] and in accordance with Eurocodes.

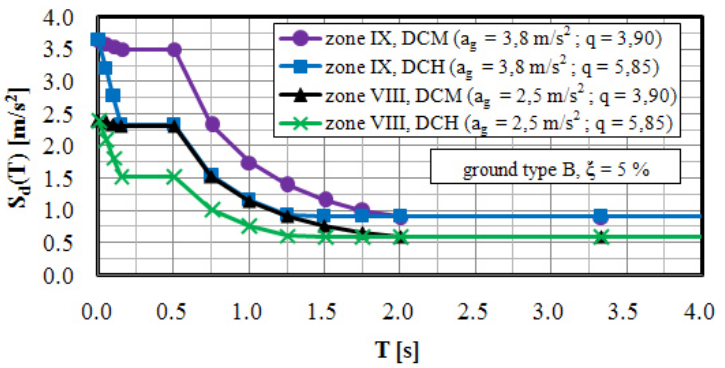

Figure 3 — Design response spectrums used in analysis

Results and discussion

Results provided here concerns the inner columns of the first story of the frames defined in this paper.

Figure 4 shows reduction in the design shear force V_{Ed} to design shear resistance of the member without shear reinforcement $V_{Rd,c}$ ratio which goes up to 5% for the four-story frames and up to 15% for the seven-story frames when the conventional concrete is replaced with BTAC.

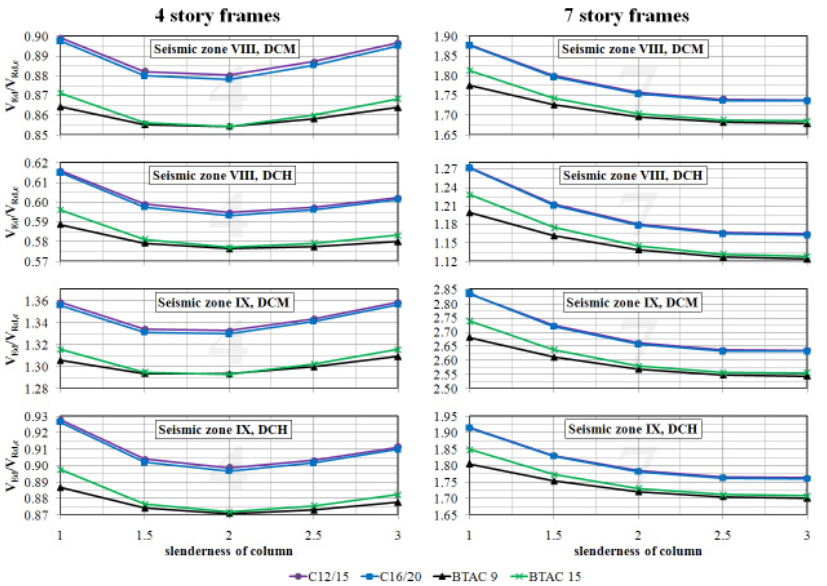

Figure 4 — V_{Ed}/V_{Rd}, c-slenderness of column relationships for different types of concrete

By inspecting Figure 4 and Table 1 it was observed, and as expected, that the density of the concrete influences the magnitude of the shear forces the most. Furthermore, it is observed that compressive strength of concrete and modulus of elasticity of concrete significantly influences the magnitude of shear force of columns having height-to-depth ratio equal to 1. Significant influence of compressive strength of concrete and modulus of elasticity of concrete on the magnitude of the shear force is also observed for columns having height-to-depth ratio equal to 3 and relatively low normalised axial force (average values of normalised axial forces $v_{d,av}$ are provided in Figure 5).

Figure 5 shows reduction in the amount of required bi-diagonal reinforcement up to 3.80% for the four-story frames and up to 4.60% for the seven-story frames when the conventional concrete is replaced by BTAC. This reduction is also mostly influenced by the relatively low density of BTAC, while the influence of compressive strength of concrete and modulus of elasticity of concrete are negligible.

Small influence of compressive strength of concrete and modulus of elasticity of concrete on reduction of required bi-diagonal reinforcement is observed for columns having height-to-depth ratio equal to 1 and relatively high normalised axial force (see Figure 5).

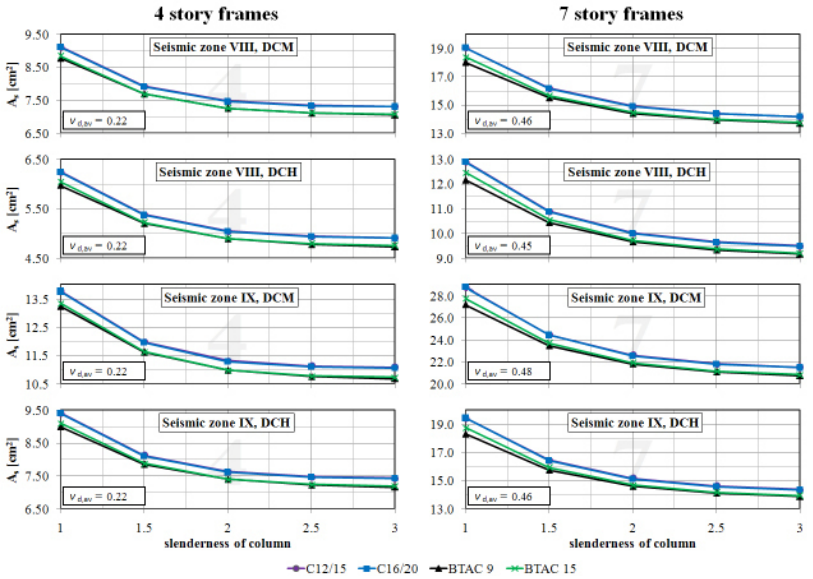

Figure 5 — As-slenderness of column relationships for different types of concrete

Conclusion

Numerical study on the behaviour of short columns subjected to seismic action was conducted on four- and seven-story frames having partial infills made of different types of concrete. Two types of conventional concrete and two types of non-conventional brick/tile aggregate concrete, all having relatively small compressive strength, were used in this study. The use of brick/tile aggregate concrete in partial infills reduces the magnitude of shear forces in the short columns thus reducing the amount of required reinforcement. Among others, due to relatively small density of brick and tile, when compared to the density of natural stone, brick/tile aggregate concrete has relatively lower specific weight. This observation gives additionally benefit on the use of brick/tile aggregate concrete in buildings located in seismically active zones thus providing a sustainable management of such material. Further research on brick/tile aggregate concrete should be conducted to inspect its mechanical and physical properties and to prove its usage as building material. Moreover, an experimental research should be performed to verify the results of this study.

References

[1] *Guevara, L. T., Garcia, L. E. (2005). The captive- and short-column effects. Earthquake Spectra 21 (1), pp. 141–160, [online] Available at: http://15wceess.blogspot.com/2012/05/captive-and-short-column-effects.html [Accessed 11 May 2012]*

[2] *Multidisciplinary Center for Earthquake Engineering Research (MCEER) at University of Buffalo, 1999. Failure of column, due to short column effect, of a 5-storey building in Ano Liosia. [image online] Available at: http://mceer.buffalo.edu/research/Reconnaissance/greece9-7-99/fig_5.asp [Accessed 26 July 2012]*

[3] *Fierro, E., 2001. Short column at another school in Camana, [image online] Available at: http://www.eeri.org/2001/06/southern-peru/ [Accessed 26 July 2012]*

[4] *Tomičić, I. (2009). Analysis and design of short reinforced-concrete columns. Građevinar 62 (8), 717–722, [online] Available at: http://www.casopis-gradjevinar.hr/arhiva/article/279 [Accessed 11 May 2012]*

[5] *CEN — European Committee for Standardization (2004). Eurocode 8 — Design of structures for earthquake resistance — Part 1: General rules, seismic actions and rules for buildings*

[6] *SAP2000, version 14.1.0. Structural analysis program. Pacific Earthquake Engineering Research Center, University of California, Berkeley, California*

[7] *CEN — European Committee for Standardization (2002). Eurocode 1 – Actions on structures — Part 1–1: General actions — Densities, self-weight, imposed loads for buildings*

[8] *CEN — European Committee for Standardization (2004). Eurocode 2 — Design of concrete structures — Part 1–1: General rules and rules for buildings*

[9] *Tomičić, I. (1996). Betonske konstrukcije (3rd edition), Društvo hrvatskih građevinskih konstruktora, Zagreb*

[10] *Kraus I., Morić, D. Netinger, I. (2011). Comparison in seismic response of reinforced concrete buildings made of non conventional concrete. The Electronic Journal e-GFOS, Number 3 — December, [online] Available at: http://e-gfos.gfos.hr/en/index.php/archive/number-3 [Accessed 23 May 2012]*

[11] *Konstantinidis, A. (2008). Earthquake resistant buildings from reinforced concrete, Volume A — The art of construction and the detailing. Athens, [online] Available at: http://www.pi.gr/CMSnew/index.php [Accessed 23 May 2012]*

[12] *Sigmund, V., et al (2000). Comparison in the application of Croatian regulations and Eurocode 8. Građevinar 52 (7), 379–388, [online] Available at: http://www.casopis-gradjevinar.hr /arhiva/article/77 [Accessed 17 July 2012]*

Experimental research on thermo-creep behavior of soft sedimentary rock

KURIMOTO, Yuhei
Department of Civil Engineering, Nagoya Institute of Technology, Japan

ZHANG, F
Department of Civil Engineering, Nagoya Institute of Technology, Japan

XIONG, Y
Department of Civil Engineering, Nagoya Institute of Technology, Japan

NISHIMURA, Tomohiro
Department of Civil Engineering, Nagoya Institute of Technology, Japan

Abstract

In Japan, nuclear electricity generation has occupied about 30% of total power generation. On the other hand, we are faced with a serious problem of how to manage the nuclear waste disposal, especially the disposal of high-level radioactive waste (HRW). Until now, deep geological disposal is regarded as one of the most viable and the safest ways of permanent disposal of HRW. The soft sedimentary rock is one of the host rocks that are suitable for the geological disposal of the nuclear waste. The half-decay period of many nuclear elements, however, is very long and the amount of the thermal energy generated during the half-decay period is huge enough to make troubles. It is known that temperature and its change may affect the mechanical behaviors of the rock, especially the long-term stability. Therefore, it is necessary to study carefully the interacting factors related to the mechanical properties of host rock, especially the thermo-mechanical properties. Author conducted the thermal triaxial compression tests and thermal triaxial creep tests under different constant temperatures. From these tests, it is known that: (1) peak strength of soft rock decreases as the temperature increases; (2) creep failure occurs more quickly as temperature increases.

Introduction

It is commonly known that deep geological disposal is regarded as one of the most viable and the safest ways of permanent disposal of HRW [1]. On the other hand, there are so many problems to be resolved. The half-decaying span of many nuclear elements is very long and the amount of the thermal energy generated during the radioactive decaying period is so huge. Therefore, it is natural that

shielding material like rock mass for deep geological disposal should be stable in a long time under high temperature conditions. So, it is necessary to study carefully the interacting factors related to the mechanical properties of host rock, especially the thermo-mechanical properties. In this paper, in order to grasp the mechanical properties of host rock under high temperature conditions, author conducted the thermal triaxial compression tests and thermal triaxial creep tests under 4 different constant temperatures.

Test device and specimen

Test device

Figure 1 shows the temperature-controlled triaxial compression and creep test device. It consists of a load controlling unit for cell pressure and axial load, and a temperature controlling unit, as shown in Figure 2. Performances of test device are listed in Table 1.

Figure 1 — Temperature-controlled triaxial compression and creep test device.

Figure 2 — Temperature controlling unit.

Control method	PC
Maximum temperature [°C]	90
Maximum confining pressure [MPa]	10
Maximum axial pressure [MPa]	25
Maximum back pressure [MPa]	1

Table 1 — Performances of test device.

Heating system

The heating system includes a heater, a mixer and a temperature sensor that is installed within the pressure cell chamber and connected to the temperature controlling unit. To reduce the difference of temperature of the water inside the triaxial cell chamber, an inclined propeller (45°) was installed within the cell to keep the temperature of water distributed uniformly and quickly, as shown in Figure 3. Besides, the rotating speed of the inclined propeller is adjustable. During the test, for safety, the highest temperature within the chamber was set at 90°C.

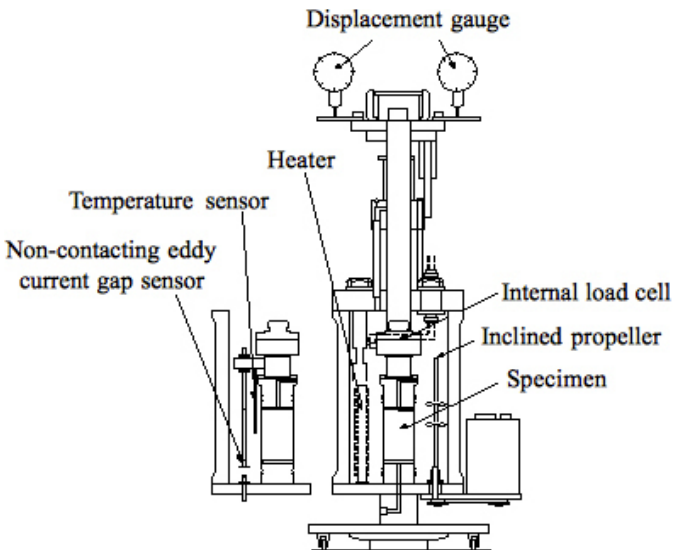

Figure 3 — Schematic illustration of pressure cell chamber.

Specimen

It is known that the homogeneity of the test samples is a very important factor to acquire reliable test results, especially for studying thermo-mechanical properties of soft sedimentary rocks. Ohya stone, a typical green tuff, is distributed widely in the northeastern part of Japan and used as the test specimen in this experiment. The stone is a typical soft volcanic tuff formed in Miocene age, and is widely used in laboratory tests for their mechanical properties in Japan. Ohya stone usually has a uniaxial compressive strength of around 10 MPa, and some of its basic physical properties are given in Table 2.

The cylindrical test specimen of Ohya stone is 100 mm in height and 50 mm in diameter, as shown in Figure 4. To obtain a satisfactory degree of saturation (more than 95%) for the specimens in the test, saturation using vacuum pump was conducted.

Soil particle density ρ_s [g/cm³]	2.56
Moisture content ω [%]	19.54
Wet density ρ_t [g/cm³]	2.05
Dry density ρ_d [g/cm³]	1.71
Initial void ratio e_0	0.49

Table 2 — Some physical properties of Ohya stone.

Figure 4 — Soft sedimentary rock specimen.

Test procedure and results

Thermal triaxial compression test

Based on the test specification [2] of the Japanese Geotechnical Society, the thermal triaxial compression tests were conducted under the room temperature (20°C), 40°C and 60°C, 80°C respectively. The procedures include three stages:

(1) Heating stage. The temperature was increased at a rate of 0.5 °C/min to the target temperature under drained condition and then was kept constant.

(2) Consolidation stage. Isotropic consolidation was conducted for 24 hours under the prescribed confining pressure and the target temperature.

(3) Compression stage. Shearing was conducted under drained condition and the constant target temperature.

The detailed thermo-mechanical conditions are listed in Table 3.

Temperature [°C]	20, 40, 60, 80
Effective confining pressure [MPa]	0.49
Strain rate [%/min]	0.002
Drainage condition	Drainage

Table 3 — Conditions of compression tests.

Figure 5 shows the stress difference-axial strain relations of the tested soft rock subjected to compression under different constant temperatures. From Figure 5, it is known that Ohya stone shows strain softening and peak strength of soft rock decreases as the temperature increases. Figure 6 shows the relations between the volumetric strain and the axial strain. It can be seen that the volumetric strain in all tests first contracts and then expands (dilatancy characteristics).

Moreover, in spite of residual stress, volumetric strain is not constant. This cause is that failure surface is very rough (roughness is indexes of discontinuity plane), as shown in Figure 7.

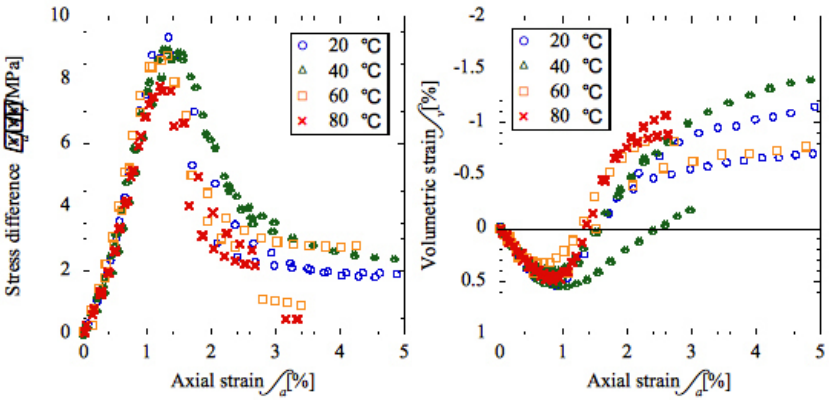

Figure 5 — Stress difference vs. Axial strain.

Figure 6 — Volumetric strain vs. Axial strain.

Figure 7 — Specimen after thermal triaxial compression tests.

Thermal triaxial creep test

The thermal triaxial creep tests were conducted under the room temperature (20°C), 40°C and 60°C, 80°C respectively with constant creep load. In the creep tests, instead of abrupt loading, the axial creep load was applied at a constant rate until the specified creep stress was reached. The specified creep stress, which is defined as the percentage of the peak strength obtained from the drained compression tests of 80°C, is listed in Table 4.

Temperature [°C]	20, 40, 60, 80
Creep stress [MPa]	7.37 (95%)
Effective confining pressure [MPa]	0.49
Rate of loading [kN / min]	0.05
Drainage condition	Drainage

Table 4 — Conditions of creep tests.

The axial strain was plotted against time on a logarithmic scale, as shown in Figure 8. From Figure 8, the creep failure time is largely dependent on the temperature. Figure 9 shows the relations between the axial strain rate and time on a logarithmic scale. The general characteristics of creep behavior, such as the transient creep, the steady creep and the accelerating creep can be clearly observed. Moreover, the higher the temperature is, the faster the creep rupture will occur.

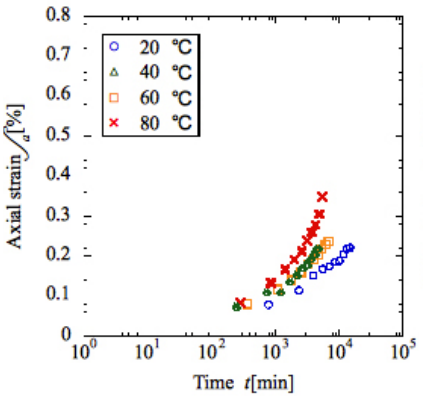

Figure 8 — Axial strain vs. Time.

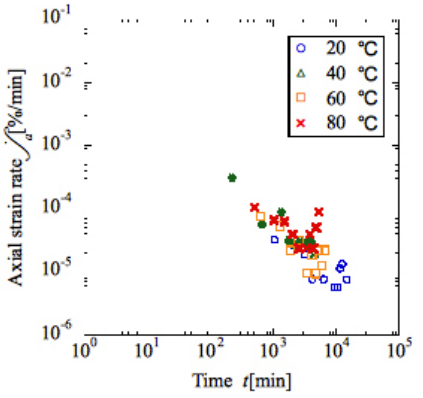

Figure 9 — Axial strain rate vs. Time.

Conclusions

In this paper, the thermal triaxial compression tests and thermal triaxial creep tests were conducted under different constant temperatures. From these tests, the following conclusions can be drawn:

(1) The temperature does influence the peak strength of the soft rock. In the triaxial compression tests, peak strength of soft rock decreases as the temperature increases and the volumetric strain in all tests first contracts and then expands.
(2) In the triaxial creep tests, the creep failure time is largely dependent on the temperature. In other words, the creep failure occurs more quickly as temperature increases.

References

[1] *Okada T. Mechanical properties of sedimentary soft rock at high temperatures (part1) — evaluation of temperature dependency based on triaxial compression test. Chiba, Japan: Central Research Institute of Electric Power Industry, 2005 (in Japanese).*

[2] *Japanese Geotechnical Society. (2000). Field study and testing me thod for rock. [S.l.]: JGS-Soft, in Japan.*

Bridge-Wizard: Expert system for FE modeling and post — processing of Bridges

LESGIDIS, Nikolaos D.
Aristotle University of Thessaloniki, Department of Civil Engineering, Greece

Abstract

Experience is essential at the process of structural modeling, especially in case of large scale structures. Modern Finite Element software provides advanced capabilities related to complex constitutive laws, geometry and loading patterns; however, many pre- and post-processing tasks still require a high level of engineering judgment while others are significantly time consuming. To this end, a bridge analysis expert system called Bridge-Wizard has been developed. Bridge-Wizard is an interactive front-end software that applies a step by step logic in the process of modeling and post-processing and consults the user in two different ways, i.e., by providing (a) conceptual assistance in developing the FE model in an open source program environment (OpenSees) through the user's description of the structure and (b) expert advice with respect to the simulation of the components expected to exhibit nonlinear response (particularly, deck, piers, bearings and abutments). The software also provides interactive modeling of the boundary conditions considering the effect of soil-structure interaction at both the abutments and the middle piers. Bridge-Wizard also offers in depth visualization of the results of the non linear response history analysis, through a set of graphs, thus providing a spherical overview of the analysis results. It is deemed that the development of Bridge Wizard improves the efficiency and robustness of the finite element of complex structures with the use of OpenSees.

Introduction

Similarly to every other scientific area, the technological breakthrough of the last two decades has greatly affected structural engineering as well. The use of advanced finite element software is increasing in popularity day by day making it a vital part in the structural engineer's every day work. Nonetheless there is still room for improvement by

eliminating difficulties the user may encounter. Such difficulties are the large amount of time consumed in the construction of an analysis or the error possibility due to the user's misjudgement. The development of an expert system named Bridge wizard is an improvement attempt in the field of bridge computer analysis. Bridge wizard copes with the difficulties mentioned above by counseling the user in his modeling decisions and offering him automated solutions.

Bridge wizard is capable of performing time history (linear or non linear), modal and static analysis of a bridge structure that belongs in the category of beam bridges. Since Bridge Wizard does not include an analysis algorithm the open source software OpenSees was selected to complete that task. Thus a cooperation takes place were bridge wizard is exporting the structure's data to Opensees and importing the analysis results from it. In the following pages the structure, the applied methods and the general image of Bridge wizard will be discussed and in the conclusion the results and the objectives accomplished will be commented.

Structure of Bridge Wizard

Bridge Wizard is a windows form application created in Microsoft Visual Studio 2008. The main program is written in Visual Basic but knowledge of tcl was needed for the exchange of data between OpenSees and Bridge Wizard.

Since Bridge Wizard is a front to end wizard software, there is a specific path the user can follow as depicted in the main algorithm figure (Figure 1). In order for the user to start and complete the modeling of a structure, a seven step process must be followed. In each step the software obtains information from the user in order to complete a sufficient description of the structure. This information is carefully stored into a large number of Matrixes and waited to be used in the final step of the process. In the first step the user is asked to supply general information on the geometry of the Bridge. During the four following steps the software asks for more specific information corresponding on the four parts the structure is divided (Deck, Piers, Abutments, Pier-Deck connection). At the 2 final steps the users supplies the software with the details of the static, modal and time history analysis.

By the end of the 7th step a tcl data file is created and all the data obtained in these 7 steps, combined with other preset information, are organized and printed in that file according to an Opensees input file template. The Opensees software initializes and runs an analysis according to the directions of the tcl data file. The tcl data file consists of a repeated three part process. The first part directs the creation of the model of the structure while the second part declares the selected methods of analysis. Finally the third part organizes the location and format of the post processing output data. The process repeats itself

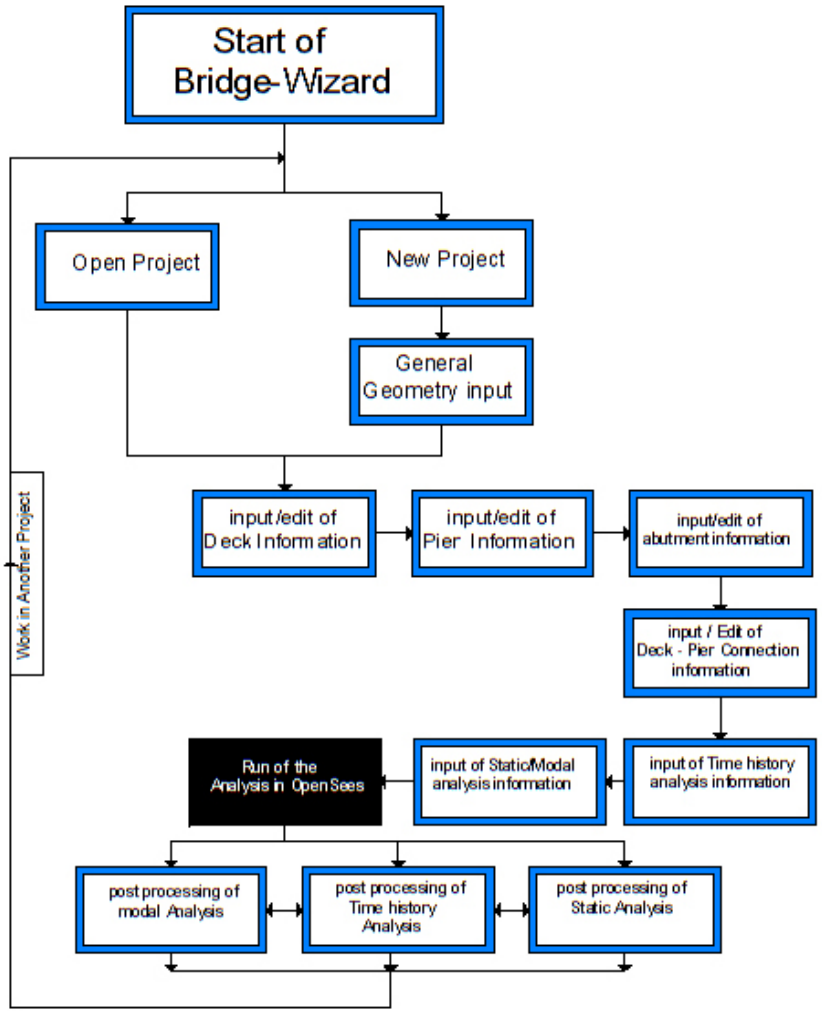

Figure 1 — Main Algorithm of Bridge Wizard

in the data file for each loading combination respectively. By the end of the analysis OpenSees terminates automatically and all the data results of the analysis are stored and organized by Bridge Wizard.

By the end of the seven step procedure the user has the opportunity to check the results of the analysis either in a graphical manner through the software Bridge Wizard or by the output files produced from OpenSees. For the graphical depiction of the results Bridge wizard has in its possession a small number of tools. These tools are a component named Ms Chart specialized in the creation of visual charts and a 2D graphics algorithm created for Bridge Wizard. The component is used in the visual display of stress or displacement to time charts of a specific node of the structure where the graphics algorithm is used in the depiction of the stress or displacement of the overall structure for a specific moment of time. The user has the ability to leap from one method of post processing to the other. Finally, if the user wishes to analyze a different structure or change details on the current structure, there is the option of repeating the whole procedure from the first step.

Modeling and Analyzing Methods

As expected from an expert system, Bridge Wizard has the ability to input information from the user and based on that information lean on the correct decisions regarding the modeling and analysis of a bridge structure. For these decisions Bridge wizard follows a number of methods stored in its memory. There are modeling methods selected for every structural part of the bridge (Deck, Piers, Abutments, Bearings, Gaps) and analyzing methods for every analysis available in Bridge Wizard.

Deck: The finite elements used for the simulation of the deck are stick elements. The use of shell or solid elements is avoided due to 2 main reasons. Firstly with a different selection from the stick model, the number of finite elements are greatly increased resulting to a more complicated differential equation system for OpenSees to solve, while the accuracy of the results remain the same. Secondly, due to the complexity and lack of regularity of the section's geometry, modeling the deck with shell or solid elements could be considered as a significant geometrical challenge. Bridge wizard's main objective is to be able to solve the majority of the structural cases addressed by the user, an objective reached only by the use of stick model's simple geometry.

Regarding the stress — strain curve simulated for the deck material, Bridge wizard considers the curve linear. The reason of the selection of an elastic material for the simulation of the deck is the capacity design of the deck itself in an earthquake load combination. Since the deck is not considered as a dissipative mechanism of the structure, the design is calculated in way of not exciting the yielding stress of the deck and thus making unnecessary the use of a nonlinear simulation of the stress-strain curve. Considering the meshing technique used, every span of the bridge is divided in 10 finite elements. The meshing technique used may cause small inaccuracies if the bridge analyzed consists of highly unequal span lengths.

Piers: For the simulation of the piers, the finite elements used are also stick elements. The reasons of the stick element selection are the ones mentioned on the deck section with the addition of the necessary compatibility between deck and piers. Foundations of the piers are modeled with either a hinged or fixed connection depending on the user's preferences. The height of the deck's section is simulated through rigid finite elements extending from the piers. Considering the meshing technique used, every Pier of the bridge is divided in 10 finite elements excluding any rigid finite elements.

In contrast to the deck, piers are frequently used as dissipative mechanisms of a bridge due to their ductile formation of plastic hinges in their end, making the non linear simulation of the piers an ideal solution. However, due to simplicity the user's only option is the linear stress — strain curve simulation for the piers material.

Bearings: Bridge wizard bearings simulation can be either linear or non linear (bilinear). The option of non linearity applies only to the horizontal displacements (Ux, Uy) of the bearing, leaving every other (Uz, Rx, Ry, Rz) with a default option of elastic simulation. For the modeling process of the bearings, OpenSees offers a finite element object called "elastomeric bearing element", an object capable to supply all the perquisites named by Bridge Wizard.

Bridge wizard offers the option to add any number of bearings in one pier with the only request of being identical. However, adding different bearings from pier to pier is a possible action. In contrast to the common way of modeling a bearing connection, Bridge wizard encounters the problem with a more simplified method. Instead of using one object for each bearing connected to the pier, only one individual object is used with characteristics defined in a way to create a modeling equal. In order to calculate these characteristics, Bridge wizard follows the equations below.

(2.1, 2.2) $$K_{Ux,el}^{ind} = \sum_{n} K_{Ux,el}^{i} \quad , \quad K_{Ux,pl}^{ind} = \sum_{n} K_{Ux,pl}^{i}$$

(2.3, 2.4) $$K_{Uy,el}^{ind} = \sum_{n} K_{Uy,el}^{i} \quad , \quad K_{Uy,pl}^{ind} = \sum_{n} K_{Uy,pl}^{i}$$

(2.5) $$K_{Uz,el}^{ind} = \sum_{n} K_{Uz,el}^{i}$$

(2.6) $$K_{Rx,el}^{ind} = \sum_{n} K_{Rx,el}^{i} + \sum_{\frac{n}{2}} i^2 \cdot K_{Uz,el}^{i} \cdot l^2$$

(2.7) $$K_{Ry,el}^{ind} = \sum_{n} K_{Ry,el}^{i}$$

(2.8) $$K_{Rz,el}^{ind} = \sum_{n} K_{Rz,el}^{i} + \sum_{\frac{n}{2}} i^2 \cdot K_{Ux,el}^{i} \cdot l^2$$

Like every other simplified method the bearing modeling method has its disadvantages. As long as the bearings are linear there is no difference in the results from the analytical method. However, in the case of multiple non linear bearings at one pier, the overall rotational stiffness K_{Rz}^{ind} becomes also non linear due to geometrical affection of the non linear stiffness K_{U}^{x} (the geometrical affection is obvious in the equation 2.8). This affection may result in a miscalculation of the overall rotational stiffness K_{Rz}^{ind} making the model unrealistic.

Abutments: Bridge Wizard offers the user two possible options for the modeling of the abutments. On the first method the node corresponding to the location of the abutment can have its degrees of freedom fixed according to the user's selections.

The second method refers to abutments using bearings to connect with the deck and optionally gaps in the horizontal directions. The modeling of abutment bearings follows the exact same method explained in the previous "bearings" subchapter. For the simulation of a possible gap in the horizontal direction Bridge Wizard uses a uniaxial

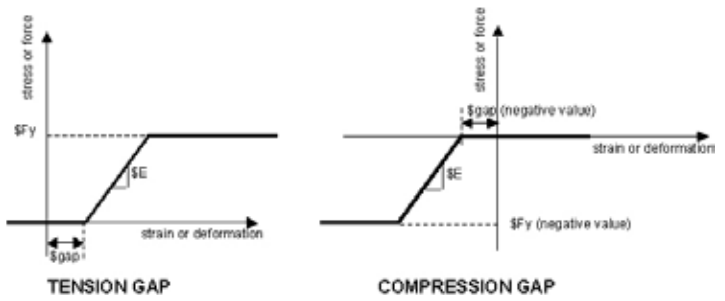

Figure 2.1 — Stress and strain curve of OpenSees gap object

material object from OpenSees with the name "Elastic perfectly Plastic Gap Material". A clearer picture can be obtained from the stress-strain curve of the gap element (Figure 2.1). The material is used through a zero-length element.

Time history analysis: The time history analysis can be either linear or non linear depending on the user's preferences. The method used for the solution of the differential equation system in both linear and non linear case is the numerical integration method "Newmark-Beta". For the solution algorithm object which determines the sequence of steps taken to solve the non-linear equation, Bridge wizard has a default selection of the Newton algorithm.

Presentation of Bridge Wizard

In order to achieve a decent presentation of a modern software, it is essential for the reader to take a tour in the software mechanics from the perspective of the user. The presentation can be divided in 2 subchapters. The topic of the first subchapter is the seven step process the user follows from the initiation of the software to the last point of modeling and analysis of the structure. In the second subchapter Bridge Wizard's main tools of post-processing are introduced to the user.

Initiation of the software: The user's first contact attempt with the software is through its main window as shown in figure 4.1. By the startup of the main window almost every possible action is locked leaving the user with the only options of creating a new project, loading an existing project or starting the help guide. By clicking the "New project" button the user initiates the modeling and analysis process of a bridge structure.

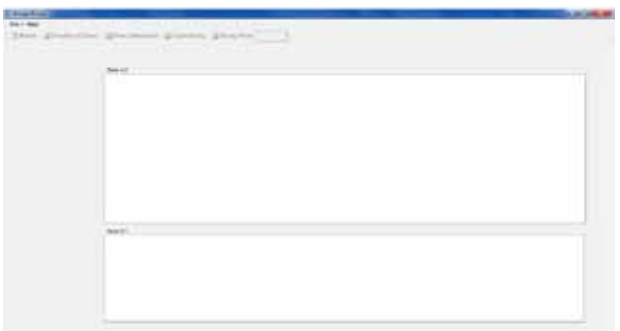

Figure 4.1 — Main Window after initiation

First step — General geometry: On the first step of the modeling process, the software collects preliminary information describing the number of spans and piers of the structure as depicted in figure 4.2.

Second step — modeling of the Deck: The software navigates the user to the deck configuration window as depicted in figure 4.3.a giving him the option to select a span and edit its properties. The user imports material, geometry and section properties of the selected span through a section window of his choice (an example of a section window is depicted in figure 4.3.b).

Third step — modeling of the Piers: The software navigates the user to the Piers configuration window as depicted in figure 4.4.(a) giving him the option to select a Pier and edit its properties. The user imports material, geometry and section properties of the selected Pier through a section window of his choice (an example of a section window is depicted in figure 4.4.(b)).

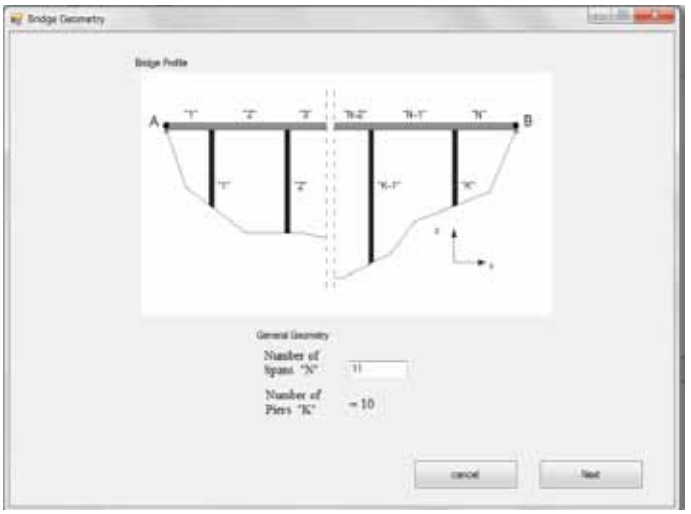

Figure 4.2 — Bridge geometry Window

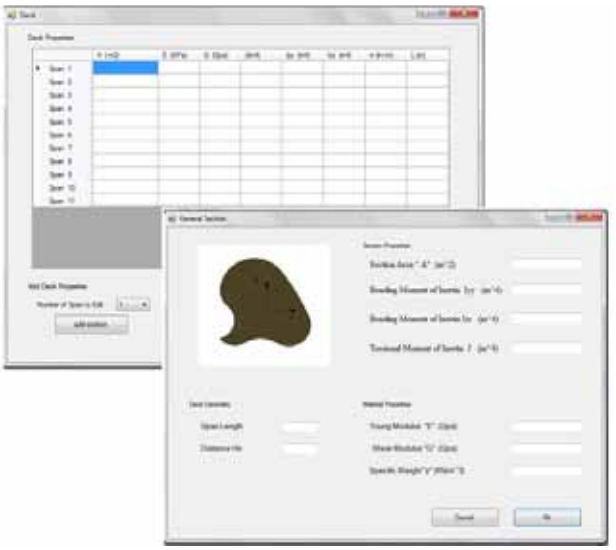

Figure 4.3 — (a) Deck configuration window (b) General section Window (deck)

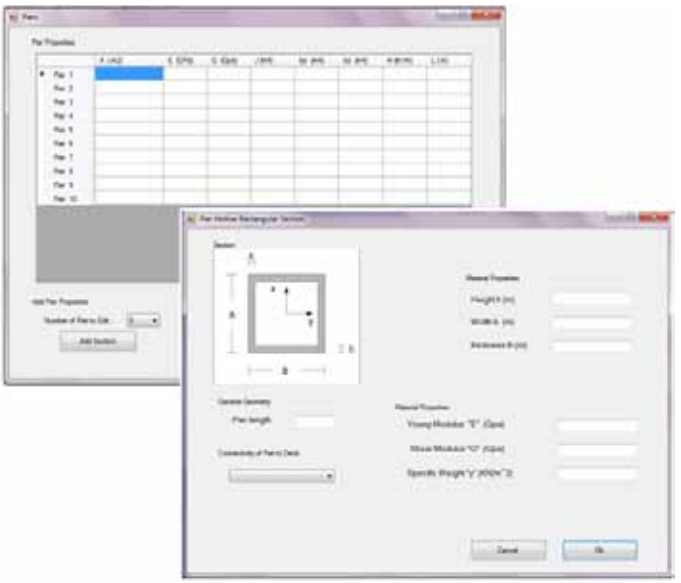

Figure 4.4 — (a) Pier configuration window (b) Rectangular Hollow section Window (Pier)

Forth step — modeling of the Abutments: The software navigates the user to the abutment configuration window as depicted in figure 4.5. If the simplified option is selected, the user can assign the restrains on the abutment node DOFs from the abutment configuration window. If the "abutment with bearings" option is selected the user imports the bearing connection properties through a bearing configuration window of his choice (example given in fig. 4.6.(a). Then the user may proceed to the optional gap configuration window as depicted in figure 4.6.(b), were gaps at the horizontal directions of the abutment can be assigned.

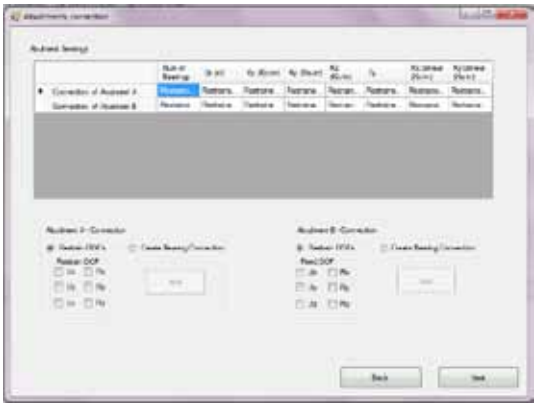

Figure 4.5 — Abutment configuration window

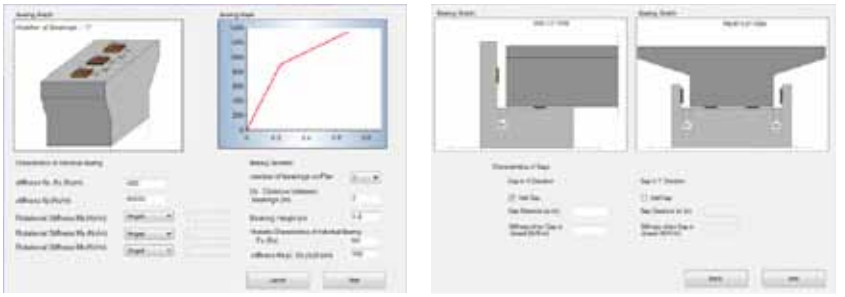

Figure 4.6 — a) Bilinear bearing configuration window b) Gap configuration Window

Fifth step — modeling of the pier-deck connections: The software navigates the user to the "pier-deck connection window" were the user proceeds to import the bearing properties to every non monolithic pier-deck connection. For the bearing connection the process followed is identical to the one described in the "abutments modeling" subchapter with the exception of the gap configuration step.

Sixth step — Time history analysis preferences: The step is initiated with the display of the "time history analysis" window depicted in figure 4.7.a, were the user can define the directions affected by the earthquake and import the analysis properties. For every affected direction the user must import its ground acceleration record through the "ground acceleration window" depicted in figure 4.7.b. The record must be in NGA format. With the record imported the software presents the graphs of the acceleration — time curve and its response spectrum to the user.

Seventh step — Static/Modal analysis preferences: on the final step of the procedure the software navigates the user to the "modal/Static analysis window" where he can provide to the software the modal and static analysis details. Opensees initiates and completes the analysis and the user returns to the main window with the post processing options unlocked.

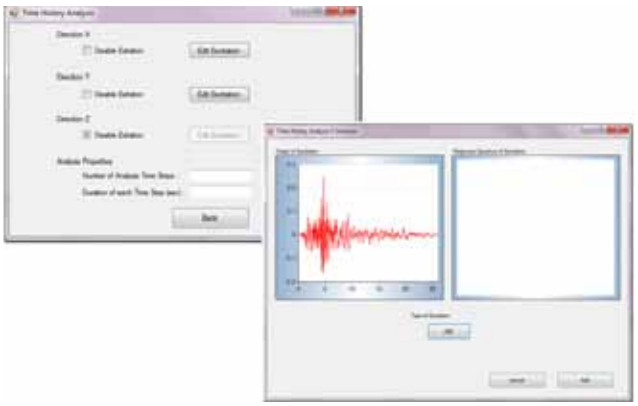

Figure 4.7 — a) Time History Analysis Window b) Ground Acceleration Window

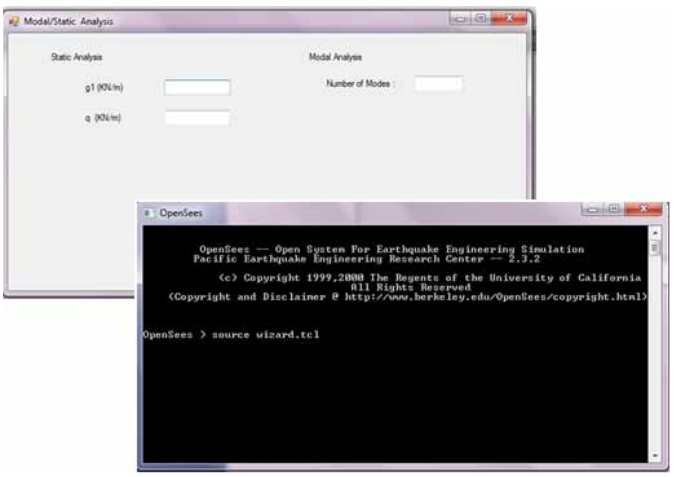

Figure 4.8 — a) modal/Static analysis window b) Opensees starting Window

Post-Processing analysis results: Bridge wizard can offer to the user two different post processing tools in order to evaluate the analysis results. The first tool consists of two plane screens located in the main window representing a side view and an overview of the bridge as depicted in figure 4.9. With that tool the user has the ability to view the deformation, the stresses and the modes of the overall structure in both planes for a given moment of time for any load combination.

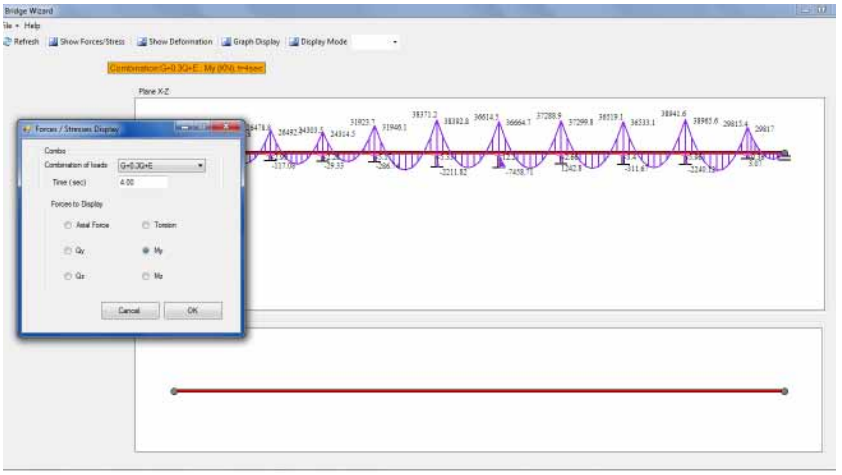

Figure 4.9 — a) Main window — Moment y from loading combination G + 0.3Q + E (t = 4.0sec)

The second tool is located in the graph display window as depicted in figure 4.10. The user can process the deformation or stress results of a specific node of the structure through time. The selected node can be located as a red dot through a screen depicting the structures sketch.

Conclusions

The basic scope of the development of bridge wizard was the creation of an expert system capable of eliminating the error possibility due to user's misjudgement and simultaneously greatly decrease the time needed to complete the modeling process of the structure. In order to verify a possible success in the first objective a number of comparison tests have taken place. The tests compared various analysis results (stress, deformation, modes) of a bridge analyzed once manually with SAP2000 and afterwards with Bridge Wizard. The results

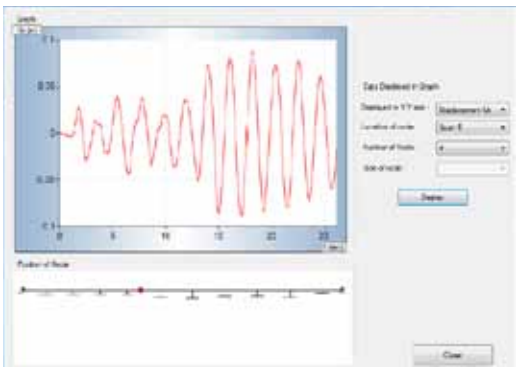

Figure 4.10 — Graph display window

of the comparison were quite pleasing as the deviation between the results didn't exceeded the 5% while the average deviation was estimated around 2%. In reference to the second objective an important increase in the speed of modeling process is expected since a great number of user's decisions are now made by the software itself, however no concrete proof can be provided what so ever.

References

[1] *Chopra, A. K. (2001) "Dynamics of structures: Theory and applications to earthquake engineering 2nd Edition" Prentice Hall, Englewood Cliffs, N.J.*

[2] *Sextos, A. and Katsanos, E. (2009) 'Programming Techniques and use of specialized software for structural engineering', Aivazis Publications, Thessaloniki*

[3] *Fardis, M., Kolias V., Panagiotakos T., Katsaras C., Psychogios T., (2012). 'Guide for bridge design with emphasis on seismic aspects', university of Patras, Patra*

[4] *Opensees Ver 2.3.2 ,User's documentation, Berkeley, California, U.S.*

[5] *SAP 2000 Ver. 14.0, User's Reference Manual, Berkeley, California, U.S.*

Experimental and numerical assessment of the dynamic behaviour of a railway viaduct with precast deck

MALVEIRO, Joel
Department of Civil Engineering, Faculty of Engineering, University of Porto, Portugal

RIBEIRO, Diogo
Department of Civil Engineering , Polytechnic Institute of Porto, Portugal

CALÇADA, Rui
Department of Civil Engineering, Faculty of Engineering, University of Porto, Portugal

Abstract

This paper describes the experimental and numerical work developed in order to evaluate the dynamic behaviour of a railway viaduct with precast deck. The experimental work consists on an ambient vibration test and a dynamic test under railway traffic. The ambient vibration test allows the identification of the modal parameters (natural frequencies, modal configurations and damping coefficients) related to global and local modes of vibration. These modal parameters were used to calibrate the numerical model using an iterative methodology based on a genetic algorithm. The dynamic test under railway traffic allows obtaining the dynamic response in terms of displacements, accelerations and deformations at different deck locations for the passage of Alfa Pendular train. The calibrated model was validated based on a comparison between numerical and experimental responses and a very good correlation was obtained.

Introduction

Railway bridges and viaducts are structures subjected to high intensity moving loads, where the dynamic effects can reach significant values. These effects have assumed greater importance due to the increase of the circulation speed, especially in high speed lines. In these lines the dynamic effects tend to increase considerably as a result of the resonance phenomena that occur due to the passage of trains composed by regularly spaced groups of axles. The dynamic analyses are usually based on finite element numerical models of the structure that involves assumptions and simplifications that may cause errors. These errors are basically related to the inaccuracy in the FE model discretisation, uncertainties in geometry and boundary conditions and variation in the material properties. Therefore, the accuracy of the FE model strongly depends on the experimental validation of the numeri-

cal results that is usually performed by means of dynamic tests. Thus, this paper describes the experimental and numerical work developed in order to evaluate the dynamic behaviour of a railway viaduct with precast deck. The experimental work consists on an ambient vibration test and a dynamic test under railway traffic. The numerical model was calibrated using an iterative methodology based on a genetic algorithm. The calibrated model was validated based on a comparison between numerical and experimental responses and a very good correlation was obtained.

Alverca railway viaduct

Alverca railway viaduct is located in the Northern line of the Portuguese railway network that establishes the connection between Lisbon and Porto (Figure 1). The viaduct supports only one railway track and consists in 47 successive simply supported spans, with lengths of 16.5 m, 17.5 m and 21 m.

(a) (b)

Figure 1 — Alverca railway viaduct: (a) side view and (b) bottom view

Each span is composed by a prefabricated "U" beam connected by an upper slab cast in situ, forming a single-cell box-girder deck. The deck is directly supported in the piers by elastomeric reinforced bearings. These bearings are fixed at one of the extremities of each span and guided in the transverse direction at the other extremity. The track is continuous between successive spans and is composed by 30 cm of ballast, monoblock sleepers and UIC60 rails.

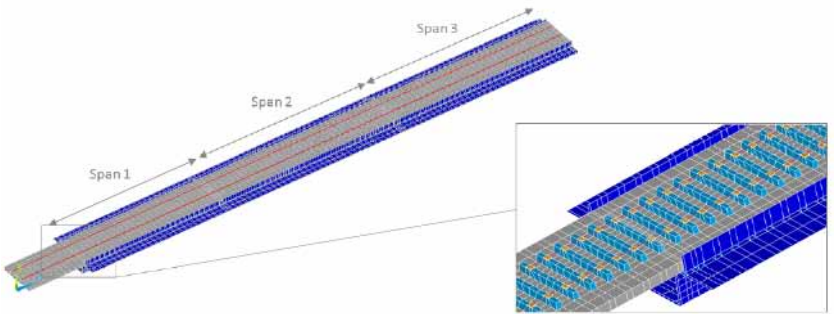

Figure 2 — Numerical model of the Alverca railway viaduct: overview and a detail

Numerical model

For the dynamic analysis of the viaduct, a three-dimensional numerical model was developed with the software ANSYS [1]. Figure 2 shows an overview of the model and also a detailed cross section [2]. In this model three simply supported spans were considered, adjacent to the north abutment, one of them with 16.5 m (span 1) and two spans with 21 m (spans 2 and 3). It was also modelled 6 m of track beyond the abutment to simulate the effect of the track on the adjacent embankment.

The density adopted for concrete and ballast was respectively 25 and 20 kN/m^3. The modulus of elasticity of concrete corresponds to the average correction to 28 days for the average value at the time of experimental test. As the bridge was built to 13 years ago, the values considered for the modulus of elasticity of concrete C 30/37 (upper slab) and C 45/55 (prefabricated beam) were respectively 35.4 GPa and 40.9 GPa. The structural bearings were considered flexible in the vertical direction and with stiffness equal to 5,200 x 10^6 N/m.

Ambient vibration test

The ambient vibration test allowed the identification of the modal parameters of the structure, namely its natural frequencies, mode shapes and damping coefficients. This test was performed in two different phases: the first was focused on the identification of the global modal parameters and the second allowed the characterization of the local dynamic behaviour of the upper slab of the box-girder section.

Both tests were performed using a technique with fixed reference points and using 12 piezoelectric accelerometers (PCB model 393A03). The dynamic response was evaluated in several setups, in terms of accelerations in the vertical and longitudinal directions. The acceleration series were measured during 4 minutes with a sampling frequency of 2,000 Hz and decimated to frequencies of 100 Hz for global modes and 200 Hz for local modes of vibration. The data acquisition system was the NI cDAQ-9172®, including IEPE analog input modules (NI 9233®).

An external excitation was applied to the structure by a group of people jumping randomly in time and space. This excitation technique increased the signal-to-noise ratio and consequently increased the coherence of the measured signals. Figure 3 shows an overview of the instrumented spans as well as details of the accelerometers, the excitation technique and the acquisition system.

The identification of the modal parameters was performed using the stochastic subspace identification method (SSI-DATA), variant UPC, available in the commercial software ARTeMIS® [3].

(a) (b) (c)

Figure 3 — Ambient vibration test: (a) instrumented spans; (b) external excitation; (c) acquisition system

Phase 1

In this phase of the ambient vibration test 57 measurement points distributed along the three spans in analysis, with particular emphasis in the intermediate span of 21 m (Figure 4a), were considered. The accelerometers were placed on the ballast retaining walls, on the vertical direction, through metal plates bonded to the concrete surface (Figure 4b). Attending that these walls are monolithically connected to the upper slab and deviate from the symmetry axis of the deck, the measured responses at these locations allowed the identification of the modes of vibration associated to the bending and torsion movements of the deck.

Additionally, there were also some accelerometers positioned near the structural joints between decks of 21 m span, at two distinct levels: in the webs of the prefabricated beam nearby the bearings (Figure 4c) and at the same vertical alignment but at the level of the ballast retaining walls (Figure 4d). The data obtained from these accelerometers allowed the characterization of the relative rotation between these two successive spans in order to characterize the structural continuity provided by the track, namely by the rails and the ballast layer.

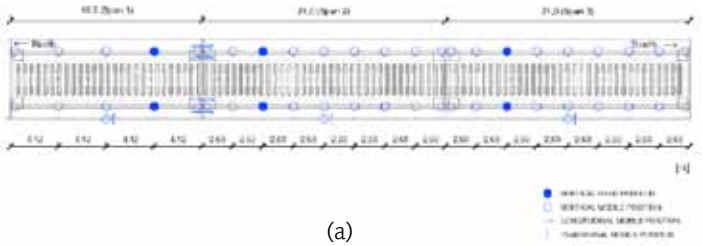

(a)

(b) (c) (d)

Figure 4 — Ambient vibration test — phase 1: a) location of measurement points; b) accelerometer in the ballast retaining wall; c) and d) accelerometers nearby the joint between the successive spans

Mode	Type of mode	Frequency (Hz)	Damping coefficient (%)
1G	Vertical bending	6.76	1.63
2G	Vertical bending	6.95	3.56
3G	Vertical bending	9.65	2.39
4G	Torsion	13.04	4.99
5G	Vertical bending	20.94	3.46

Table 1 — Natural frequencies and modal damping coefficients of global modes

Table 1 shows the values of natural frequencies and damping coefficients for the global vibration modes identified by the application of SSI-DATA method. Figure 5 shows the mode shapes in correspondence with the identified natural frequencies.

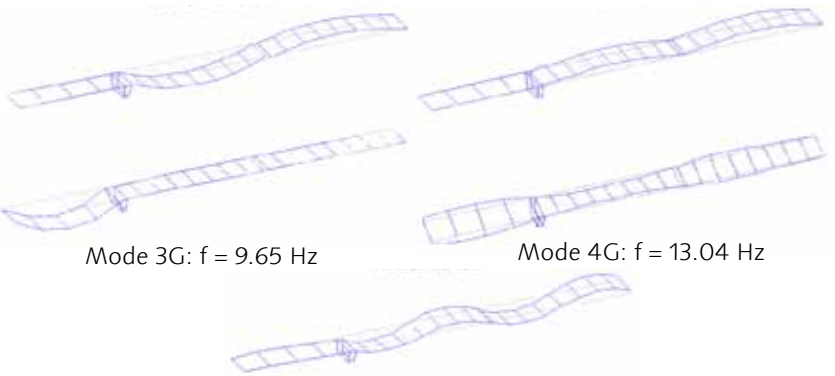

Figure 5 — Global experimental modes of vibration

Phase 2

In this phase of the ambient vibration test 84 measurement points located in the intermediate span of 21 m, with particular incidence in half of that span, were considered (Fig. 6a). The accelerometers were placed on the sleepers, on the ballast retaining walls, on the precast girders located in the extremity of the footway cantilever and on lower slab of the deck, through metal plates bonded to the concrete surface. The accelerometers placed on the sleepers allowed the identification of the local modes of vibration of the upper slab, once it was impossible to access directly to the slab either internally, trough the box-girder deck or externally, by removing the ballast layer. Figure 6b and c shows the installation process of accelerometers on the sleepers.

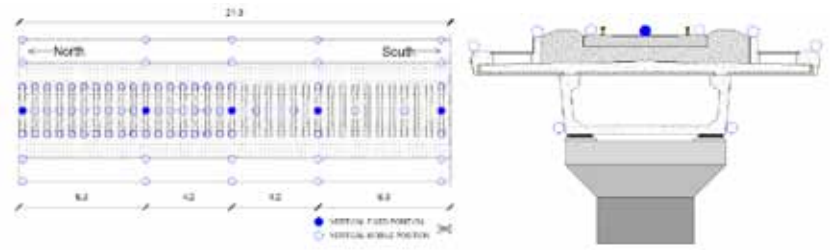

(a)

Figure 6 — Ambient vibration test – phase 2: (a) location of measurement points; (b) installation process of the accelerometers on the sleepers; (d) accelerometer on the sleep-er edge

(b)

(c)

belongs to Figure 6

Table 2 shows the values of natural frequencies and damping coefficients for the local modes of vibration identified by the application of SSI-DATA method.

Mode	Frequency (Hz)	Damping coefficient (%)
1L	25.48	2.16
2L	27.41	2.13
3L	53.18	4.47
4L	60.18	3.35
5L	74.60	4.81

Table 2 — Natural frequencies and modal damping coefficients of local modes

As shown in the table above, the values of the damping coefficients are higher than those obtained by applying the EN1991-2 (2003) standard for this type of structures and spans. Figure 7 shows the mode shapes in correspondence with the identified natural frequencies.

Dynamic test under railway traffic

The dynamic test under railway traffic allowed obtaining records of displacements, accelerations and deformations on the middle span section of the second span (Figure 8).

Figure 9a shows an acceleration record obtained for the passage of the Alfa Pendular train at 185 km/h. Figure 9b shows the frequency content related to the temporal response. The dynamic response is dominated by frequencies associated to the train action, especially to the passage of regularly spaced groups of axles with a spacing of 25.9 m.

Mode 1L: f = 25.48 Hz Mode 2L: f = 27.41 Hz Mode 3L: f = 53.18 Hz

Mode 4L: f = 60.18 Hz Mode 5L: f = 74.60 Hz

Figure 7 — Local experimental modes of vibration

Calibration of the numerical model

The calibration of the numerical model of the viaduct was performed taking account the modal parameters obtained in the ambient vibration tests. This process involved two phases: the sensitivity analysis and the optimization technique. The technique adopted for the mode pairing between experimental and numerical modes is also discussed.

Phase 1: Mode pairing

The mode pairing criteria establishes the correspondence between each experimental and numerical mode of vibration. In this work, that correspondence is done by the application of the modal assurance criterion MAC [41] for global modes and of the energy-based modal assurance criterion EMAC [42] for local modes of vibration. This last criterion enhances the traditional modal assurance criterion MAC by the relative modal energy of a certain cluster of numerical degrees-of-freedom related to a numerical mode.

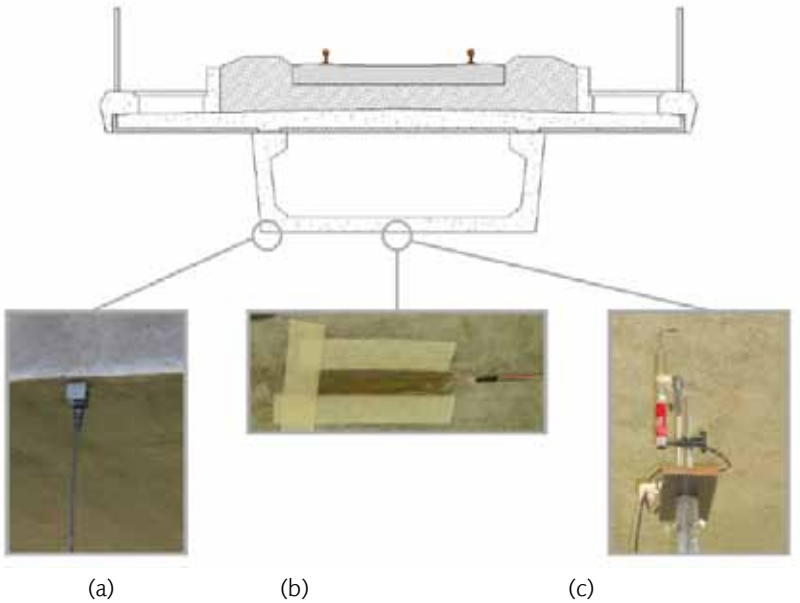

(a) (b) (c)

Figure 8 — Dynamic test: (a) accelerometer, (b) strain gage and (c) LVDT

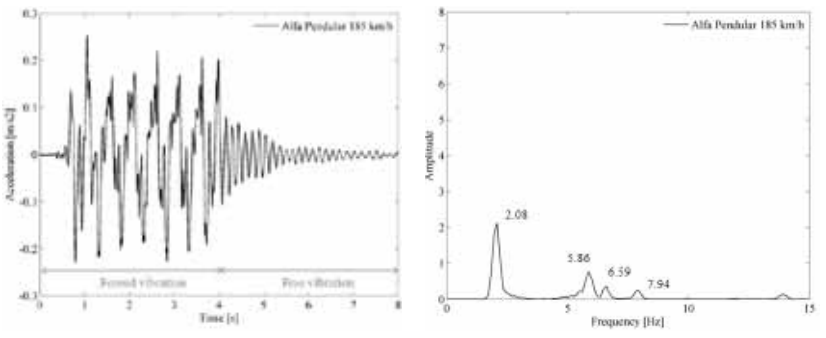

(a) (b)

Figure 9 — Dynamic response: (a) acceleration record and (b) frequency content

The clusters reflect the information obtained from the distribution of experimental measurement points and their directions in ambient vibration test. These clusters were related to the translational degrees-of-freedom according to Figure 10. Figure 11 shows the MAC and EMAC correlation matrices between experimental and numerical modes of the initial finite element model.

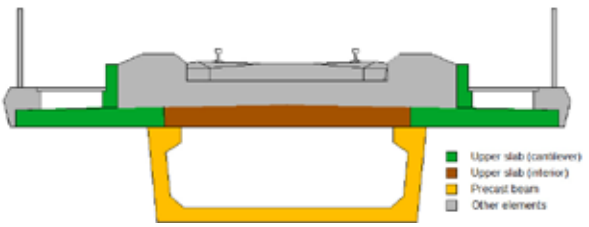

Figure 10 — Clusters used in the mode pairing

(a) (b)

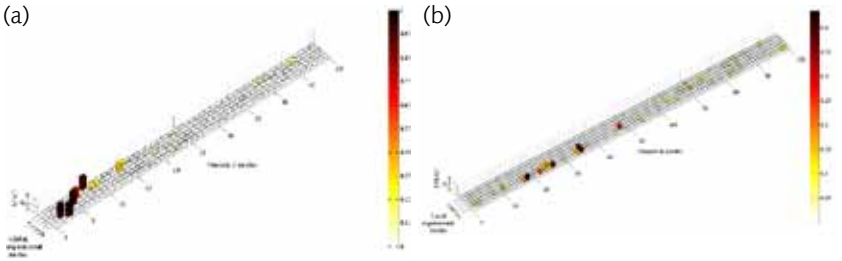

Figure 11 — Mode pairing: (a) MAC and (b) EMAC correlation matrices

Phase 2: Sensitivity analysis

The sensitivity analysis allows the selection of the parameters that most influence the frequencies and MAC values of the global and local modes, and consequently should be included in the subsequent optimization phase.

The sensitivity analysis showed that the modulus of deformability of the prefabricated beam, the density of the concrete and the horizontal stiffness of the supports have a significant influence on frequencies and MAC values of the global modes. On the other hand, the modulus of deformability of the upper slab influences the frequencies and MAC values of the local modes of vibration.

Phase 3: Optimization

The optimization phase allowed obtaining the parameters values that minimize the differences between the numerical and experimental modal responses, and involved the definition of an objective function and the application of an optimization technique based on a genetic algorithm. The objective function (f) comprises two terms, one related to the natural frequencies of global and local modes, and other related to the MAC values of global and local modes:

$$f = a \sum_{i=1}^{n\ mod\ es} \frac{\left| f_i^{exp} - f_i^{num} \right|}{f_i^{exp}} + b \sum_{i=1}^{n\ mod\ es} \left| MAC\ (\phi_i^{exp}\ ,\ \phi_i^{num}) - 1 \right| \quad (3)$$

where f_i^{exp} and f_i^{num} are the experimental and numerical frequencies for mode i, ϕ_i^{exp} and ϕ_i^{exp} are the vectors containing the experimental and numerical modal information regarding the mode i, a and b are weighing factors of the terms of the objective function, assumed in this case equal to 1.0, and *nmodes* is the total number of modes.

Figure 12 shows the flowchart [6] with the iterative process of calibration of the numerical model, using three commercial software packages.

In Figure 13 are presented the optimization results in terms of ratio between the experimental and numerical frequencies (Figure 13a) and the MAC values (Figure 13b), for the three independent optimization runs (GA1 to GA3).

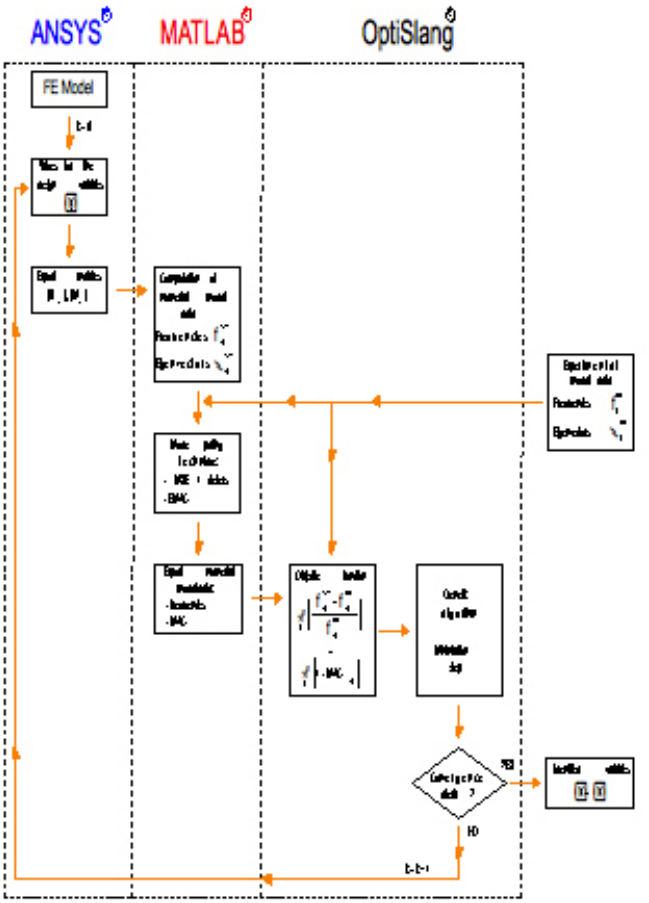

Figure 12 — Flowchart of the iterative optimization process

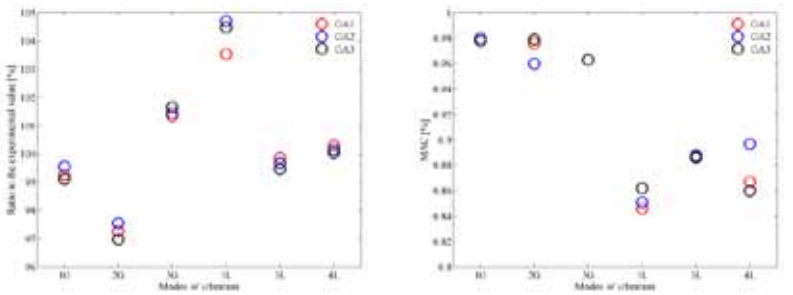

(a) (b)

Figure 13 — Response values for runs GA1 to GA3: (a) frequencies and (b) MAC

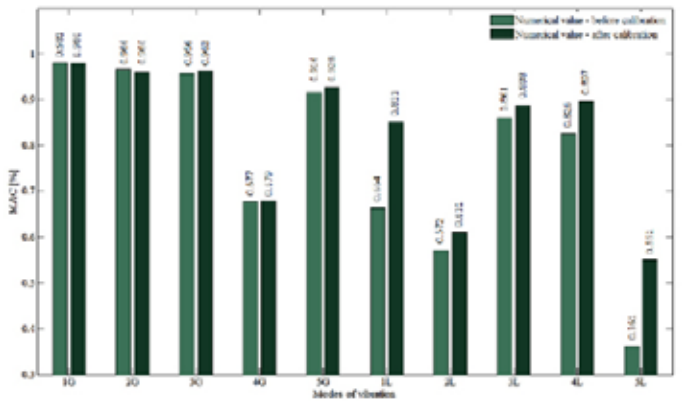

Figure 14 — MAC values, before and after the model calibration

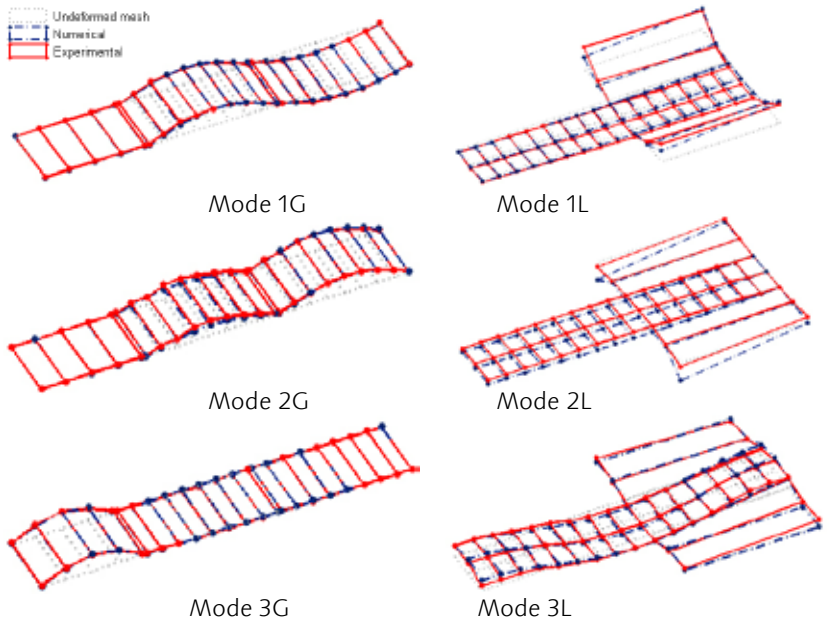

Figure 15 — Comparison between the experimental and numerical mode shapes after the calibration process

Figure 14 shows the MAC values of global and local modes of vibration, before and after the calibration of the numerical model.

Figure 15 presents a comparison between numerical and experimental mode shapes after the model calibration, for the first three global and local modes of vibration.

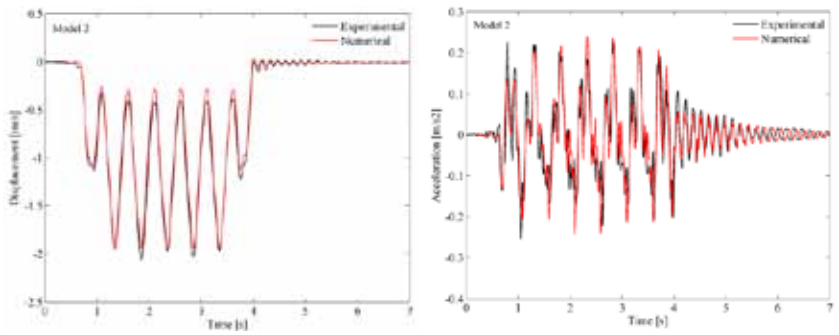

(a) (b)

Figure 16 — Experimental and numerical dynamic responses of the deck: (a) vertical displacement and (b) vertical acceleration

Validation of the numerical model

The validation of the numerical model was performed based on a dynamic test under railway traffic that consisted in the measurement of the dynamic response in terms of displacements and accelerations of the deck. The dynamic analyses were performed by the modal superposition method, using a moving loads methodology, considering the modes of vibration with frequencies up to 30 Hz and an integration time increment equal to 0.002 s. The modal damping coefficients adopted were those obtained experimentally.

Figure 16 shows the comparison between the experimental and numerical dynamic responses for the passage of Alfa Pendular train at 185 km/h. The records were filtered based on a Chebyshev (type II) low-pass digital filter with a cut-off frequency equal to 30 Hz.

Conclusions

This paper aimed to describe the experimental and numerical work developed in order to evaluate the dynamic behaviour of a railway viaduct with precast deck.

The ambient vibration test allowed the identification of the modal parameters of the structure, not only associated to the global modes of vibration but also to the local modes associated to the vibration of the upper slab of the deck. This test also allowed verifying that certain modes involve the vibration of adjacent spans, although all the spans of the viaduct are simply supported, due to the continuity established by the track.

The optimization of the numerical model was performed using a genetic algorithm and involved 11 numerical parameters and 12 modal responses. The results of 3 optimizations runs, based on different initial populations, led to very similar values of frequencies and MAC values, for example, above 95% for global modes and between 85% and 90% for local modes of vibration.

The dynamic test under railway traffic allowed obtaining a database of displacements, accelerations and deformations of the structure. The comparison between numerical and experimental dynamic responses due to the passage of Alfa Pendular train revealed an excellent agreement after the model calibration.

References

[1] *ANSYS. Structural Analysis Guide - Release 11.0. In: ANSYS, editor. 2007.*

[2] *Horas, C. (2011). Dynamic behavior of bridges with precast deck on high-speed rail lines (in Portuguese), MSc Thesis. Porto: Faculdade de Engenharia da Universidade do Porto.*

[3] *ARTeMIS. (2009). ARTeMIS Extractor Pro — Academic Licence. User's Manual. In: SVS A, editor. Aalborg, Denmark.*

[4] *Allemang, R. J. (2003). The modal assurance criterion — twenty years of use and abuse. Journal of Sound and Vibration, 37: 14–21.*

[5] *Brehm, M., Zabel, V., Bucher, C. (2010). An automatic mode pairing strategy using an enhanced modal assurance criterion based on modal strain energies. Journal of Sound and Vibration, 329: 5375–92.*

[6] *Ribeiro, D., Calçada, R., Delgado, R., Brehm, M., Zabel, V. (2012). Finite element model updating of a bowstring-arch railway bridge based on experimental modal parameters. Engineering Structures, 40: 413–435.*

Running Safety Evaluation of Trains Moving Over Bridges shaken by Earthquakes

MONTENEGRO, Pedro Aires
University of Porto, Faculty of Engineering, Portugal

CALÇADA, Rui
University of Porto, Faculty of Engineering, Portugal

VILA POUCA, Nelson
University of Porto, Faculty of Engineering, Portugal

Abstract

This paper shows the development of a wheel-rail contact model for running safety evaluation of trains moving over bridges subjected to earthquakes. A contact point search methodology is presented and validated with results from commercial softwares. The algorithm is prepared for three dimensional situations where the wheelset yaw angle can have a significant influence in the position of the contact point. This research also includes the implementation and validation of two algorithms for computing the contact forces: FASTSIM and USETAB.

Introduction

The running safety analysis of railway vehicles during earthquakes is one of the major concerns in railway engineering. This problem assumes larger proportions if the train is moving over a bridge subjected to such actions. Several statistics elaborated in Japan concluded that 25% of the derailments in railway bridges were caused by transverse vibrations of the deck originated by earthquakes that did not provoke significant structural damage [1]. Such facts suggest that the running safety can be compromised not only for intense shakings, but also for service earthquakes with a higher probability of occurrence.

Hence, in order to take into account the effects of the transverse vibrations in the running safety of railway vehicles, it is necessary to develop a suitable train-structure interaction model capable of describing the wheel-rail contact behavior. The present paper describes a research focused on the relative motion between the wheelset and rails. With such methodology, it is possible to store all the characteristics of the contact points (relative position between the gravity center of the wheelset and the rails, position of the contact points, contact angles, body curvatures in each contact point, among others, necessary for

computing the normal forces by the Hertz theory) in a lookup table (offline calculation) to be later used and interpolated in the dynamic analysis, resulting in a considerable reduction in computation time. Although it is possible to make an interaction model with an online contact point search, i.e., determining the contact point in each time step during the dynamic analysis [2,3], many authors proved the efficiency of an offline calculation supported by pre-calculated values stored in a lookup table [4,5]. Santamaria et al [5], showed that an offline calculation could be up to 10 times faster than an online calculation. In this paper, a methodology for three dimensional wheel-rail geometrical problems is shown and validated with results obtained with different commercial software packages. Such results were obtained in the Wheel-Rail Contact (WRC) Manchester Benchmark [6] and published in [7]. This benchmark had the objective of comparing the efficiency of different multi-body dynamic codes in the analysis of train-track interaction.

The contact information presented in the lookup table is used to compute the contact forces associated with wheels and rails. These forces are subdivided into normal and tangential forces, being the former computed according to the Hertz Theory [8]. The tangential wheel-rail creep forces, which are dependent on the normal contact tensions, are computed with Kalker's Simplified Theory [9], throughout FASTSIM algorithm, and through USETAB algorithm, based on results given by Kalker's Exact Theory [10]. FASTSIM algorithm is a compromise between efficiency and accuracy (the deviation in the results is not larger than 10% compared to those obtained with the Exact Theory). USETAB consists on a table-based program, using pre-calculated values obtained with the Exact Theory, for the creep-spin force/moment law and it is 8 times faster than FASTSIM. For this reason, FASTSIM and USETAB, with some modifications to improve its accuracy, were implemented in this work.

Methodology for evaluation of the contact geometry

Assumptions and coordinate systems

In a wheel-rail contact model, the geometrical problem is a crucial point in order to achieve good results during the dynamic analysis. The geometrical problem consists of searching the contact point through the wheel and rail surface to get all the geometrical information in that same point (rolling radius, curvature radius in both longitudinal and lateral directions, among others) to be subsequently used in the computation of the contact forces. For achieving this, the following assumptions were made:

- There is only one contact point for each wheel-rail pair;
- There is always contact between the wheel and the rail;
- Both the wheels and rails are considered to be rigid;

– At a contact point, the vertical distance between the wheel and the rail is null (no penetration allowed), and is greater than zero at non-contact points.

The searching contact point algorithm depends on the relative displacements of the wheelset with respect to the centerline of the track. Unlike other simpler where the assumption of a total compatibility of movements between structure and vehicle is made, in a complete wheel-rail interaction model, relative movements between these two bodies are permitted. However, considering the previous assumptions, the six degrees-of-freedom (DOF) of the wheelset can be reduced to two independent DOFs: the relative lateral displacement, y_g, and the yaw angle, ψ. In these cases, the problem is considered three dimensional.

Some simplification can be made if the influence of the yaw angle is neglected, which is allowable in certain situations, for instance for trains running on straight tracks or curves with large curvature radius. In such cases, all the DOFs of the wheelsets are dependent only on the lateral displacement and the contact point search is restricted to a two dimensional section called main cross-section. Wheel-rail coordinate systems are the basis for wheel-rail relationships. Figure 1 summarizes all the coordinate systems used in the present work that could be described as follows:

– G-XYZ: Global inertial coordinate system, which has origin at the center of gravity of the wheelset and moves with it at constant forward speed. The X axis is longitudinal, the Y axis is directed to the right side and the Z axis is vertical, pointing downwards;
– G-$X_gY_gZ_g$: Wheelset coordinate system, which follows the wheelset motion and has origin in its gravity center. The Y_g axis is positioned along the wheelset axle directed to the right side, the X_g axis is longitudinal and Z_g forms a Cartesian coordinate system, pointing downwards;
– CP_r-$X_{cr}Y_{cr}Z_{cr}$: Right contact patch coordinate system, with its origin in the right contact point. The X_{cr} axis is longitudinal, while Y_{cr} and Z_{cr} are located in the right tangent contact plan defined by the right contact angle, γ_r;
– CP_l-$X_{cl}Y_{cl}Z_{cl}$: Left contact patch coordinate system, which has its origin in the left contact point. Its definition is analogous to the right contact patch coordinate system.

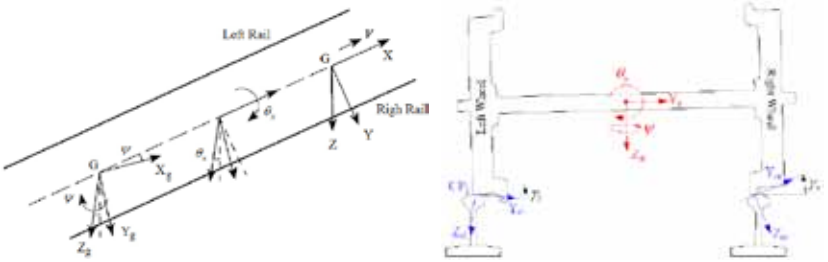

a) Wheelset coordinate systems b) Contact patch coordinate systems

Figure 1 — Definition of the coordinate systems

Wheel-rail geometrical contact problem

Algorithm implementation

Considering that the wheelset can displace perpendicularly to the track, its relative movement with respect to the track can be totally described by four components: the lateral displacement, y_g, the vertical one, z_g, the roll rotation, θ_x and the yaw rotation, ψ. However, these four DOFs can be reduced to two independent DOF, y_g and ψ. Hence, when the yaw angle is take into account, mandatory when the train is passing in a tight curve, the contact point can shift in the X_g direction, which implies the wheel and rail meshing and. The rail surface is obtained by means of an extrusion of the rail profile along the X axis, while the wheel surface is generated through a revolution of its main cross-section around the Y_g axis.

In order to build an efficient algorithm for this purpose, the geometry of the surfaces from both wheel and rail have to be known. Since these surfaces are not provided by simple analytical functions, a series of control points were considered to define both sections with a spline parameterization scheme. All the following algorithms were programmed with the commercial software MATLAB.

The search for the contact points is accomplished by the calculation of the minimal vertical distances between wheels and rails in the left, Δz^l_{min}, and right, min Δz^r_{min} , sides of the wheelset. The two points are considered to be the left and right contact points if the following condition is met:

$$\Delta Z^l_{min} = \Delta Z^r_{min} \tag{1}$$

Otherwise, the condition is violated and the roll angle has to be adjusted. The number of iterations needed to find the contact points is substantially reduced if the roll angle adjustment, , takes the following value [11]:

$$\Delta \theta_x = \frac{\Delta Z^l_{min} - \Delta Z^r_{min}}{y^r_{min} - y^l_{min}} \tag{2}$$

where y^l_{min} and y^r_{min} is the lateral location of both left and right points with minimum vertical separation between wheel and rail. The search ends when condition (1) is fulfilled, with a tolerance value of 10^{-3} mm (enough from the engineering point of view). When this point is reached, it is possible to know the values of the dependent DOFs of the wheelset, such as the roll angle, θ_x, and the relative vertical displacement, z_g (see Figure 1):

$$\begin{aligned} \theta_x &= \theta^0_x + \sum_{i=1}^{k} \Delta \theta^i_x \\ z_g &= mean\left(\Delta z^l_{min}, \Delta z^r_{min}\right) \end{aligned} \tag{3}$$

where θ_X^0 is the initial roll angle (considered equal to zero in this work) and k is the number of iterations needed to fulfill condition (1). The longitudinal displacement and wheelset rotation are constraints of the problem. The search algorithm can be resumed by the flow chart presented in Figure 2.

Results

Figure 3 presents the relation between the lateral displacement of the wheelset and its dependent DOFs. The shape profile of the sections of the wheels and rails are S1002 and UIC60, respectively, with an internal gauge of 1.360 m, a wheel nominal radius, r_{w0}, of 0.460 m and a rail inclination of 1:40 (these profiles and geometry were the same as those used in the WRC Manchester benchmark [6]). In order to clarify the relative movement between the wheelset and the track, an example of the wheel-rail contact for a lateral displacement of 10 mm and a yaw rotation of –5° is also presented. Note that, for a lateral displacement larger than 6 mm, the contact in one of the wheels takes place in the flange, which leads to a sudden rise of the roll angle of the wheelset and the position of its gravity center.

Validation with WRC Manchester Benchmark results

In 2006, the Rail Technology Unit at Manchester Metropolitan University coordinated a benchmark for assessing the impact of modelling assumptions for the wheel-rail contact on the simulation of railway vehicle dynamics [6]. A significant number of multi-body dynamic codes were tested in order to investigate the effects of different wheel-rail contact models. One of the tests consisted on evaluating

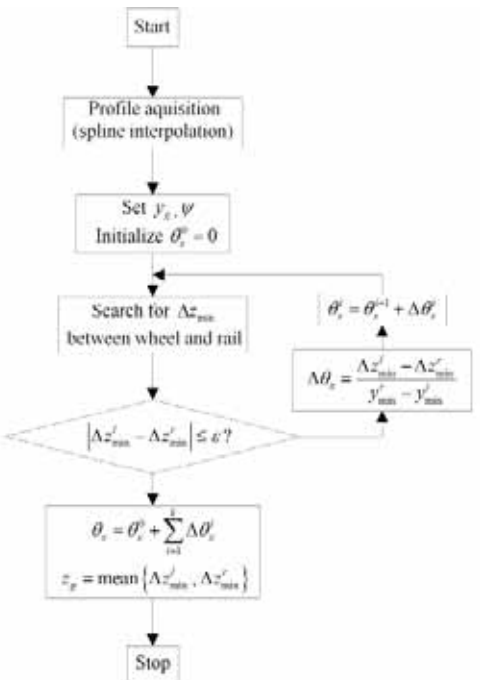

Figure 2 — Flow chart for the wheel-rail contact point search procedure

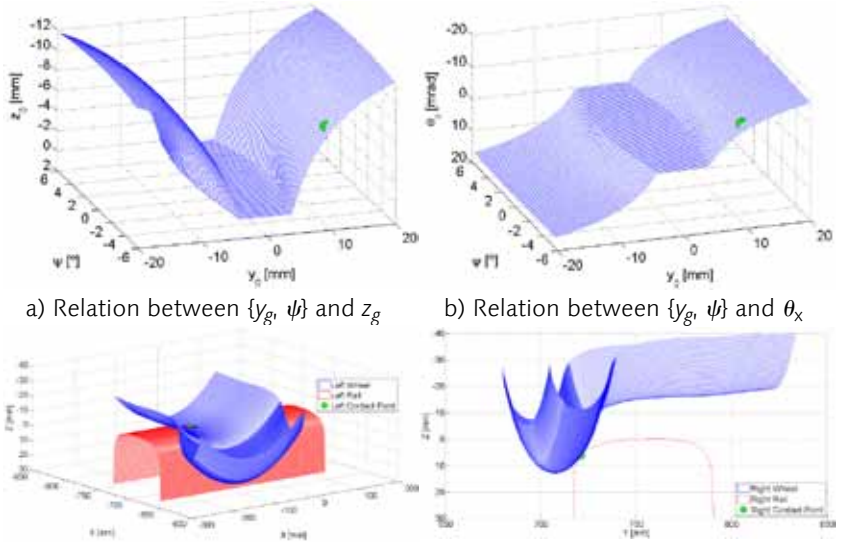

a) Relation between $\{y_g, \psi\}$ and z_g b) Relation between $\{y_g, \psi\}$ and θ_x

c) Left contact (y_g = 10 mm; ψ = –5°) d) Right contact (y_g = 10 mm; ψ = –5°)

Figure 3 — 3D wheel-rail contact case results

the contact conditions of a single wheelset subjected to a prescribed motion. Based on this test, it was possible to validate the contact point search algorithm with results obtained by various commercial software packages. Such results were published by Shackleton and Iwnicki [7]. In order to compare the results from the present work with the ones obtained in the benchmark, the same local coordinate systems were adopted:

– $X_wY_wZ_w$: Local wheel coordinate system with origin in the point with nominal radius. The X_w axis is located along the rolling direction and the Z_w vertically down. The Y_w axis makes a right-hand Cartesian for the right wheel and a left-hand Cartesian for the left wheel;
– $X_rY_rZ_r$: Local rail coordinate system with origin in the highest point of the inclined rail profile. The axis orientation follows the same principle as the local wheel coordinate system.

One of the main variables needed for solving the normal and tangential problem described in the next section is the contact point position. Figure 4 compares the contact point position, referred to the wheel coordinate system, obtained in the present work and with the commercial software packages tested in [7]. The wheelset was displaced laterally from 0 mm (central position) to 10 mm at 0.5 mm increments. The results obtained in the present work are consistent with the ones shown in [7].

When the wheelset displaces laterally in respect to the track, the wheel radius and contact angle changes due to the characteristics of the wheel profile. Figure 5 and Figure 6 compare the differences of the rolling radius of the wheel, between the right and left wheel, and contact angles obtained in this research and in [7]. For the computation of the contact angles, the wheelset was subjected not only to a lateral

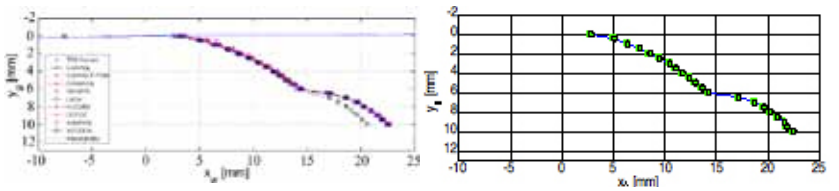

a) Left wheel contact position [7] b) Left wheel contact position (present)

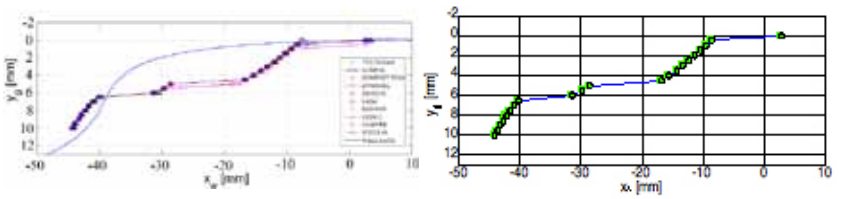

c) Right wheel contact position [7] d) Right wheel contact position (present)

Figure 4 — Contact positions according to the wheel' coordinate systems

displacement, but also to a yaw rotation. The lateral displacement sequence mentioned above was accompanied by a yaw angle increment of 1.2 mrad from 0 mrad to 24 mrad (negative values). The results show a good agreement, even when the yaw angle is taken into account.

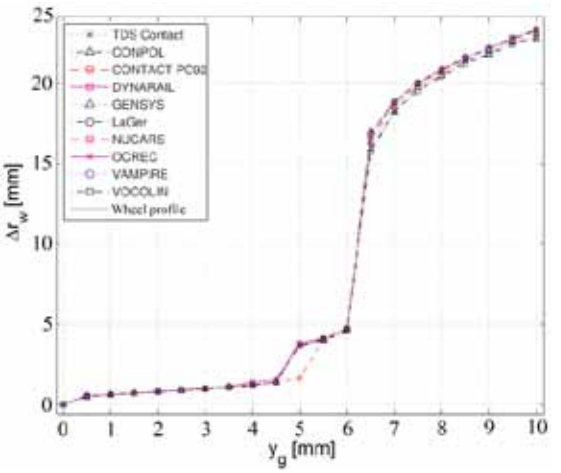

a) According to [7]

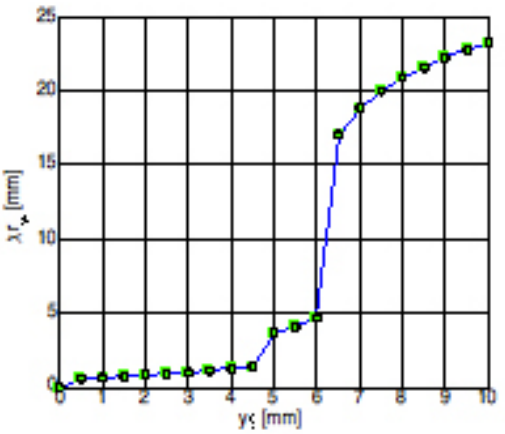

b) Present algorithm

Figure 5 — Rolling radius difference between right and left wheel for a lateral displacement of the wheelset

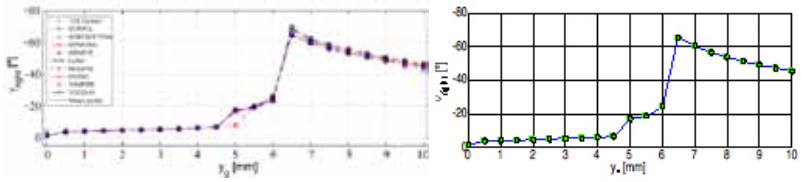

a) According to [7] b) Present algorithm

Figure 6 — Contact angle for the right wheel with a lateral displacement and yaw rotation of the wheelset

Contact forces computation

The contact forces are divided in two groups: the normal forces and the tangential forces. Such forces are projected in the contact patch coordinate systems presented in Figure 1, in which the normal force lies on Z_{ci} axis while the tangential ones are in the X_{ci} (longitudinal) and Y_{ci} (lateral) axis. In this work, Hertz theory is used to solve the normal problem, while the tangential problem is solved by FASTSIM [9] and USETAB [12] routines.

Normal problem

The normal contact problem consists on determining the contact surface dimensions and the normal stresses produced on it when two bodies are compressed to each other. In this research, the shape of the contact surface is elliptical and it is calculated by means of Hertz theory. This model is only valid if the following assumptions are made [8, 13]:

- The contact area is small when compared to the curvature radius of the bodies;
- The curvatures inside the contact patch are constant;
- The deformations arising from the normal contact are elastic;
- Both bodies in contact have smooth surfaces.
- The semi-axes *a* and *b* of the ellipse can be computed using the following expressions proposed by Iwnicki [13]:

$$a = m \sqrt[3]{\frac{3}{2} F_N \frac{1-v^2}{E} \frac{1}{A+B}} \tag{4}$$

$$b = n \sqrt[3]{\frac{3}{2} F_N \frac{1-v^2}{E} \frac{1}{A+B}} \tag{5}$$

where E and v are the combined elasticity modulus and Poisson's ratio from both materials, F_n the normal contact force, A and B the combined curvatures from both bodies (wheel and rail) in direction X_g and Y_g, respectively, and m an n two non-dimensional coefficients dependent of the curvatures (detailed in [13]).

Tangential problem

The wheel-rail contact is a rolling friction contact that differs from the Coulomb's sliding friction theory because, unlike the last one, the contact patch is divided into an area of adhesion and an area of slip which appears progressively as the slip speed increases. In the present research, two methods for solving the tangential contact problem were implemented: FASTSIM algorithm [9] and USETAB routine [12].

FASTSIM algorithm

FASTSIM uses the simplified theory of elasticity for relating the deformations in the contact patch with the tangential stresses. In this algorithm, the contact ellipse is discretized in strips parallel to the rolling direction, each one divided into the same number of elements. The stresses are computed in the center of each element through a numerical integration method, where the tangential stress in one element depends on the tension of the previous element in the strip. The main inputs in a rolling contact theory are the relative velocities between the two bodies (wheel and rail in this specific case), which are called creepages. The creepages are divided in three components: the longitudinal creepage, ξ, the lateral creepage, η, and the spin creepage, ϕ. Generically, these can be computed by the following expressions:

$$\xi = \frac{v_{xc,1} - v_{xc,2}}{V} \tag{6}$$

$$\eta = \frac{v_{yc,1} - v_{yc,2}}{V} \tag{7}$$

$$\phi = \frac{\omega_{zc,1} - \omega_{zc,2}}{V} \tag{8}$$

where $v_{xc,i}$, $v_{yc,i}$ and $\omega_{zc,i}$ are the longitudinal, lateral and spin velocities of body i projected in the contact patch coordinate system and V the imposed translation speed of the train.

Thus, taking advantage of the simplified theory of elasticity (the relation between displacements and stresses is linear), the tangential stress in both directions, τ_x and τ_y, in a point of the contact patch with coordinates (x_c, y_c) can be related with the stress on a previous point in the same strip $(x_c + \Delta x_c, y_c)$through the following expression:

$$\begin{matrix} \tau_x(x_c, y_c) \\ \tau_y(x_c, y_c) \end{matrix} = \begin{matrix} \tau_x(x_c + \Delta x_c, y_c) \\ \tau_y(x_c + \Delta x_c, y_c) \end{matrix} - \frac{\Delta x_c}{L} \begin{matrix} \xi - \phi\, y_c \\ \eta + \phi\, x_c \end{matrix} - \frac{\Delta x_c}{L} \begin{matrix} s_{xc} \\ s_{yc} \end{matrix} \tag{9}$$

where s_{xc} and s_{yc} are the relative displacements between the two bodies in direction x_c and y_c, respectively, and L is a flexibility parameter described, for example, in [9].

As previously mentioned, the algorithm is nonlinear, since the tangential tension cannot overcome the Coulomb's friction limit given by:

$$\tau(x_c, y_c) \quad \mu.\sigma\,(x_c, y_c) \qquad (10)$$

where μ is the friction coefficient and $\sigma\,(x_c, y_c)$ is the normal tension. Therefore, in a first iteration, the current point is considered to be in adhesion, which implies that the last term in equation 9 is equal to zero. The computed stresses are called hypothetical tensions, τ_H, and are compared to the Coulomb's friction limit. If τ_H overcomes such limit, the point is in slip condition, otherwise the assumption is correct and the hypothetical tension coincides with the real tension.

USETAB algorithm

The USETAB routine consists of a table with four entries (creepages and ellipse semi-axis ratio) and three outputs (longitudinal and lateral creep forces and spin moment). This table, proposed by Kalker [12], contains pre-calculated values from creep forces for a large number of cases, computed with the software CONTACT [14] which solves rolling contact problems with Kalker's Exact Theory. Such routine cannot be used directly in a railway dynamic code due to its high computational cost; instead, it is possible to build a table and then linearly interpolate its values during the dynamic analysis. For solving each rolling contact problem, USETAB is 8 times faster than FASTSIM and gives more accurate results.

The table uses a smart layout, taking advantage of all creepage symmetries in order to reduce the number of cases and to normalize it. So, the table is made exclusively for railroad dynamics, with a Poisson's ratio of 0.28 (typical for steel) and can be used only with elliptical contact areas. According to Kalker's work exposed in [12], the USETAB routine is constructed with the following normalized quantities:

- Shear modulus of rigidity, G, equal to 1;
- Coulomb's friction limit, $\mu.F_N$, equal to 1;
- Square root of the ellipse semi-axis product, $\sqrt{a.b}$, equal to 1;

Finally, in order to obtain the correct values of creep forces, F_x and F_y, and spin moment, M_z, the outcome is multiplied by:

$$F_x = F_x(G.a.b.\mu.F_N) \qquad (11)$$

$$F_y = F_y(G.a.b.\mu.F_N) \qquad (12)$$

$$M_z = M_z \quad G.(a.b)^{3/2}.\mu.F_N \qquad (13)$$

Kalker proposed a table with 115,000 entries, transforming the range $0<q<$ into $0<q<1$ and $0<1/q<$, where q is one of the table entry, with 7 interpolation intervals each. However, for high creepages or

high ellipse semi-axis ratios, the interpolation intervals become large (the interpolation is made with the inverse value of the entry for $q>1$), which implies a loss of accuracy. Therefore, in order to overcome such limitation, the original table was replaced by a larger one, with 288,000 entries, where the range $q>1$ is no longer interpolated through inverse values. Instead, the interval $0<1/q<$ is replaced by $0<q<15$ with 10 interpolation intervals (the value 15 was chosen in order to double the accuracy limit provided by the original table, which is 7).

Hence, although the USETAB routine is valid for almost all cases, when the input value is beyond the table boundaries (rarely attendant), FASTIM is called during the dynamic analyses for solving these exceptions.

Validation of the tangential algorithms

In the present sections, the two implemented algorithms for solving the rolling contact problem are validated through a comparison with results given by the Exact Theory implemented in the commercial software CONTACT. The following graphics show the evolution of the contact forces for different creepage combinations. The creepages were scaled through the following expressions:

$$\xi = \frac{abG}{3\,\mu\,F_N}\,c_{11}\,\xi \tag{14}$$

$$\eta = \frac{abG}{3\,\mu\,F_N}\,c_{22}\,\eta \tag{15}$$

$$\phi = \frac{(ab)^{3/2}\,G}{\mu\,F_N}\,c_{23}\,\phi \tag{16}$$

where c_{11}, c_{22} and c_{23} are the Kalker's coefficients that can be found in [10]. For this validation, a Poisson's ratio of 0.28, a Young's modulus of 210 GPa and a normal force of 100 kN were considered.

Figure 7 compares the evolution of the tangential contact forces, normalized by Coulomb's friction limit, $\mu.F_N$, with $\mu = 0.3$, among the exact solution, the original USETAB, the implemented FASTSIM and the modified USETAB with a larger number of entries, for equal semi-axes of the ellipse and two combinations of creepages. The original USETAB provides good results for creepages until 1.0, but after that the accuracy starts to decreases. This happens because, for creepages above 1.0, the interpolation intervals start to be too large, resulting in a loss of accuracy for such cases. Analyzing the modified USETAB results, the accuracy achieved by this routine is better, since the number of entries in the table is much higher, resulting in smaller interpolation intervals. As for FASTSIM, as previously mentioned, the results follow the tendency of the exact theory but with errors that can reach 10% for very high creepages.

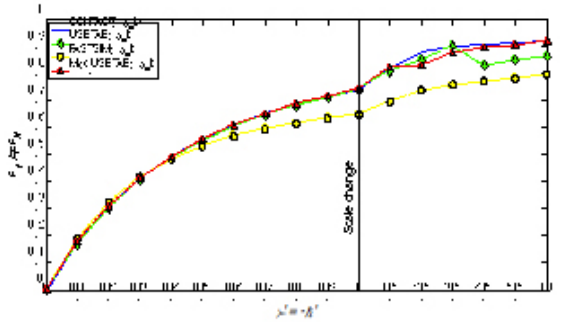

a) Lateral contact force for $\phi = -\eta$

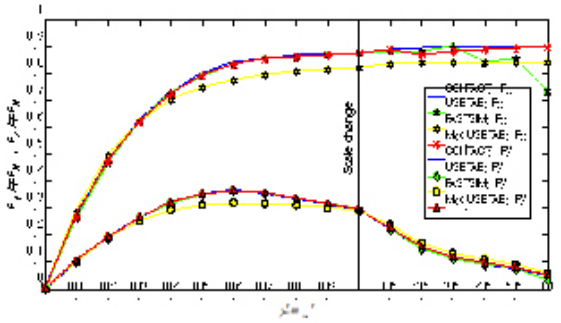

b) Tangential contact forces for f $\phi = \xi$

Figure 7 — Comparison of the contact force obtained by different algorithms

Conclusions

A wheel-rail contact model for evaluating the contact position in 2D and 3D applications is presented and properly validated with results from commercial software packages obtained in the WRC Manchester Benchmark. When several contact characteristics, namely the position of the contact point, the instantaneous rolling radius of the wheel, the wheel-rail contact angle, among others, obtained with the proposed contact search algorithm are compared with the ones obtained with commercial programs, the agreement among them appears to be sufficiently accurate. Therefore, the pre-processor is suitable to make a lookup table for the wheel-rail interaction in a railroad dynamic code. The proposed three dimensional version of the algorithm is appropriate, not only for vehicles running in straight tracks, but also for cases where the yaw angle of the wheelset can have a significant influence in the final results.

For the computation of the tangential contact force, two algorithms were implemented with successful results when compared to the exact solution given by the commercial software CONTACT developed by Kalker. A more accurate version of Kalker's USETAB routine is also proposed. The contact search algorithm, as well as the contact force computation routines, will be used in a railroad dynamic code with the intention of evaluating the running safety of trains passing over bridges subjected to vibrations imposed by service state earthquakes.

Acknowledgments

The present work has been funded by the Portuguese Foundation for Science and Technology (FCT), in the context of the doctoral grant number SFRH/BD/48320/2008. The authors would also like to thank Prof. Simon Iwnicki and Prof. Philip Shackleton (Manchester Metropolitan University) for the permission to use figures from their paper referenced in [7].

References

[1] *Matsumoto, N., M. Tanabe, M. Sogabe and H. Wakui — "Running safety analysis of vehicles on structures subjected to earthquake motion", Quarterly Report of Railway Technical Research Institute (Japan), 45 (3), 116–122, 2004.*

[2] *Shabana, A., K. Zaazaa, M. Tobaa and H. Sugiyama — "On the computer formulations of the wheel/rail contact problem", Nonlinear Dynamics, 40 (2), 169–193, 2005.*

[3] *Pombo, J., J. Ambrosio and M. Silva — "A new wheel-rail contact model for railway dynamics", Vehicle System Dynamics, 45 (2), 165–189, 2007.*

[4] *Antolín, P., A. Alonso, J.M. Goicolea and M.A. Astiz, A methodology for analysing lateral coupled behavior of high speed railway vehicles and structures, in 9th World Congress on Computational Mechanics and 4th Asian Pacific Congress on Computational Mechanics 2010: Sydney, Australia.*

[5] *Santamaria, J., E.G. Vadillo and J. Gómez — "A comprehensive method for the elastic calculation of the two-point wheel-rail contact", Vehicle System Dynamics, 44 (1), 240–250, 2006.*

[6] *Shackleton, P. and S. Iwnicki — "Wheel-Rail Contact Benchmark Report", Version 3.0, Manchester Metropolitan University, Manchester, U.K., 2006.*

[7] *Shackleton, P. and S. Iwnicki — "Comparison of wheel-rail contact codes for railway vehicle simulation: an introduction to the Manchester Contact Benchmark and initial results", Vehicle System Dynamics, 46 (1), 129–149, 2008.*

[8] *Wriggers, P. and T. Laursen — "Computational Contact Mechanics", SpringerWienNewYork, Udine, Italy, 2007.*

[9] *Kalker, J. J. — "A fast algorithm for the simplified theory of rolling contact", Vehicle System Dynamics, 11 (1), 1–13, 1982.*

[10] *Kalker, J. J. — "The computation of three-dimensional rolling contact with dry friction", International Journal for Numerical Methods in Engineering, 14 (9), 1293–1307, 1979.*

[11] *Li, Z. — "Wheel-Rail rolling contact and its application to wear simulation", Ph.D. Thesis, Delft Technical University, Delft, The Netherlands, 2002.*

[12] *Kalker, J. J. – "Book of tables for the Hertzian creep-force law", in I. Zobory (Ed.) Proceedings of the 2nd Mini Conference on Contact Mechanics and Wear of Wheel/Rail Systems, Budapest, Hungary, 1996.*

[13] *Iwnicki, S., J.–B. Ayasse and H. Chollet — "Chapter 4: Wheel-Rail Contact", in Handbook of Railway Vehicle Dynamics, CRC Press, Boca Raton, FL, USA, 2006.*

[14] *CONTACT 11.1 — "User guide for CONTACT, J.J. Kalker's variational contact model", VORtech Computing, 2011.*

Numerical and experimental study of the vertical interfaces behaviour of interconnected structural masonry walls

OLIVEIRA, Luciane Marcela Filizola
School of Engineering of São Carlos, University of São Paulo

CORRÊA, Márcio Roberto Silva
School of Engineering of São Carlos, University of São Paulo

Abstract

The shear strength of the vertical interfaces is a key parameter to guarantee the flange contribution to shear walls and the possibility of shear force transference between interconnected walls. In this regard, this research presents the results of an experimental and numerical investigation to study the behaviour of vertical interfaces of interconnected concrete blockwork masonry walls. H-shaped test specimens were used, constructed in running bond. A uniformly distributed pressure was vertically applied on the web of the specimens. The experimentally obtained shear strengths are compared with the Brazilian code. Numerical analysis was also carried out in DIANA® finite element program to simulate wall behaviour focusing on the shear at the vertical interfaces and their ability to transfer shear forces from web to flanges. The shear strength of the vertical interface was obtained with a good correlation to the theoretical analysis and Brazilian code can be very strict.

Introduction

When the walls are connected and subjected to different loads, there is interaction between them. The interaction is dependent on the shear capacity of the interface. In practical situations, many walls are stiffened due to flanged sections which increase their shear strength. Tests on H-shaped walls have revealed that more studies and improvement are needed in shear strength in interconnected masonry walls area.

The type of connection between the walls influences the way interaction occurs. The supporting flanges are usually linked to the web through the running bond. In that case, interaction might be higher because the interface plane crosses units which may be consid-

ered common to the connected walls. Alternatively, the connection between the walls is through metal shear connectors embedded in the bed joints and extended across the shear plane with the vertical joint filled with mortar at the interface. The present study used the running bond connection type.

Masonry walls with flanges have already been studied by some researchers (Lissel et al. [1]); Camacho et al. [2]; Yoshimura et al. [3]; Modena et al. [4]; Maurício [5]; Capuzzo Neto et al. [6]; Bosiljkov et al. [7]). However, these types of specimens need special testing apparatus.

Lissel et al. [1] tested shear walls with flanges and observed the influence of the type of connection on their behaviour and strength. The tests indicated that bonding pattern of the web-flange connection affect the shear strength of masonry. Bonding the web-flange connection with brickwork clearly increases the shear strength of this joint. Hence, a series of specimens with H-shaped cross sections was tested in an attempt to determine the effect of bond pattern on the strength of the web-flange intersection. A nominal compressive force approximately equivalent to a normal floor load was applied to the flanges to stabilize the specimen during and after the test. According to Lissel et al. [1], the results of these tests indicate that the mechanical interlock of a bonded web-flange connection provides a significant structural advantage over a tied connection. The forces applied on the specimens with bonded wall are three times the forces applied on specimens with tied connection.

Capuzzo Neto et al. [6] conducted new studies at the School of Engineering of São Carlos (University of São Paulo), contributing towards the understanding of the wall interaction phenomena. The author strived for a better representation of possible stress trajectories along the building structure, including proposing an H-shaped specimen to evaluate the shear strength of the vertical interface. These specimens were used in this work to obtain the shear strength through experimental tests. The computational modelling of masonry structures can focus on micro-modelling of individual components or macro-modelling of masonry as a composite (Lourenço and Rots [8]). According to Lourenço [9], it is possible to use one of these strategies, depending on the level of accuracy and the simplicity desired.

In the detailed micro-modelling units and mortar in the joints are represented by continuum elements whereas the unit-mortar interface is represented by discontinuous elements. In simplified micro-modelling expanded units are represented by continuum elements whereas the behaviour of the mortar joints and unit-mortar interface is lumped in discontinuous elements. Macro-modelling represents units, mortar and unit-mortar interface smeared out in the continuum. (Figure 1)

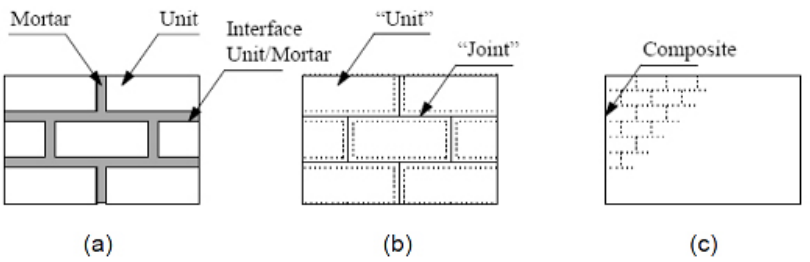

Figure 1 — Modelling strategies for masonry structures (Lourenço, 1996) [9]: (a) detailed micro-modelling; (b) simplified micro-modelling; (c) macro-modelling.

It is well known that both approaches provide satisfactory results. Macro-models are applicable when the dimensions of the analysed structure are sufficiently large so that the stresses across or along a macro length will be essentially uniform. Besides, the low computational cost supports its use on the analysis of large structures. On the other hand, micro-models are applicable in very specific problems where local failures should be analysed. Even though micro-modelling includes all the basic failure mechanisms that characterize masonry and enables the detailed representation of resisting mechanisms of the walls, the macro-modelling approach was chosen since the research is in the calibration phase, and this approach is enough for preliminary analyses.

Experimental Details

For the physical and mechanical characterization tests, concrete hollow blocks were used for the construction of the masonry specimens. They had a percentage of holes equal to 55. The mortar utilized for bed joints was a mixture of cement, hydrated lime and sand. The thickness of the bed joints was approximately 10 mm. Face shell bedding was used on the construction of the specimens.

Uniaxial compression tests were carried out on 12 blocks, 12 mortar specimens, 12 prisms and 6 wallets (about 790 x 1000 x 140 mm of dimension), according to EN 772-1 [10], NBR 13279 [11], NBR 15812-2 [12] and EN 1052-1 [13], respectively. Tests in 12 units were carried out to determine the splitting tensile strength of masonry units according to ASTM C1006 [14]. Plus, triplet specimens were built with the same materials to characterize the shear behaviour of concrete unit-mortar through initial shear tests carried out according to EN1052-3 [15] (Figure 2).

However, due to the difficulty of obtaining mode I fracture energy and the shear stiffness of the unit-mortar interface, this mechanical property could not be used in the numerical model. Table 1 summarises the material characterization tests results.

Figure 3 shows the compressive strength tests and splitting tensile strength tests of blocks, and the compressive strength tests of wallets. Figure 4 shows the stress-strain diagram results of all compressive tests.

Material	Physical and mechanical characteristics				
Blocks	Dimension (mm)	Weight (kg)	Mean comp. strength (N/mm²)	Elastic modulus (N/mm²)	Splitting tensile strength (N/mm²)
	390x190x140	12.70	10.21	9,910	0.91
Mortar	Composition (C:L:S) in volume 1:1:6	Composition (C:L:S) in weight 1:0.66:8.21	Mean comp. strength (N/mm²) 3.52	Elastic modulus (N/mm²) 6,800	
Wallets	Compressive strength, (N/mm²) 4.88	Elastic modulus (N/mm²) 7,900			

Table 1 — Characteristics of the materials

H-shaped specimen was used for the shear tests. All the tests were carried out in the Structures Engineering Laboratory at the School of Engineering of São Carlos, University of São Paulo. The specimen was prepared by a professional mason and were cured in laboratory condi-

Figure 2 — Initial shear tests

(a) (b) (c)

Figure 3 — (a) Units in compressive strength and (b) splitting tensile strength tests. (c) Wallets in compressive strength tests.

tions for 28 days before testing. The type of bonding used was running bond. Face shell bedding was used on the construction of the specimens. (Figure 5)

As shown in Figure 6, the relative vertical displacements between the web and the flanges (due to shear deformations along the flange-web interface) were measured using LVDTs located in the sample and connected to the actuator at a rate of 0.001 mm/s (Figure 6).

The web in H-shaped test specimens was 990 mm in height and 810 mm in length. The length of the flanges was 940 mm. Prior to applying a shear load to the H sections, a small pre compressive stress of 0.5 MPa was applied to each flange to stabilize the specimen and simulate a typical level of preload. According to Bosiljkov [7], the level of pre-compression in the flanges also influenced the shear resistance,

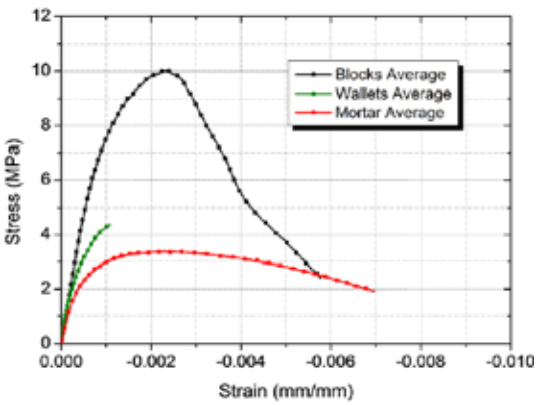

Figure 4 — Stress-strain diagrams of the specimens in compressive strength tests.

Figure 5 — Construction of the Specimens.

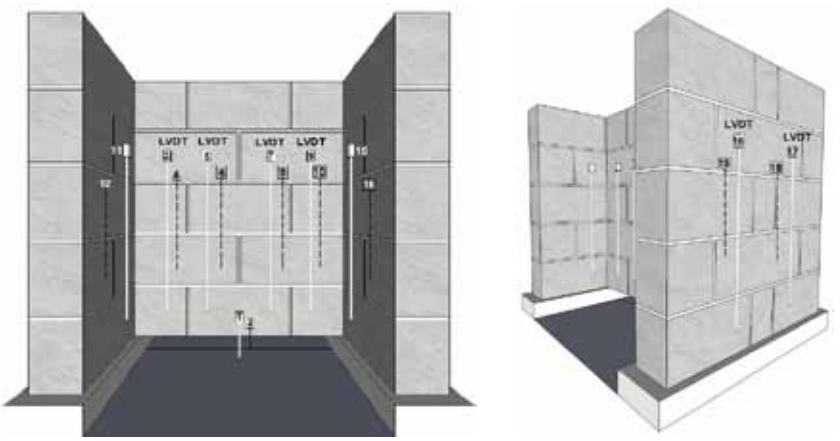

Figure 6 — Instrumentation of the specimens.

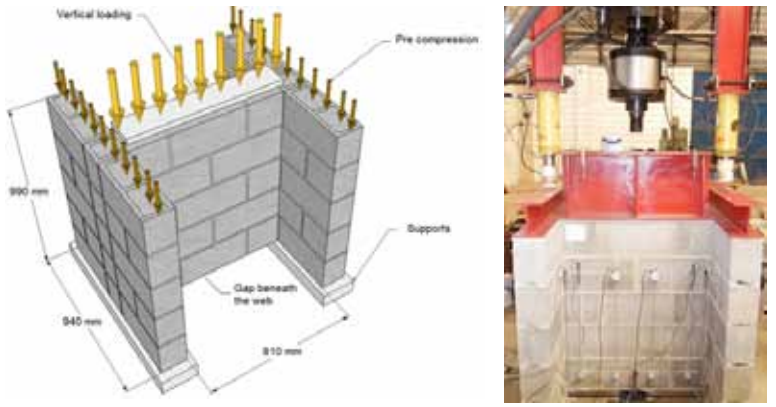

Figure 7 — Geometric specification of the specimens.

but only up to a certain limit (of approximately 0.5 MPa). A compressive load has been applied on the top web of the sections under displacement control to produce shear in the flange-web interface. The load was applied monotonically to failure (Figure 7).

Numerical Modelling

The numerical model applied to study masonry walls was defined using the DIANA® finite element program. The macro-modelling approach was chosen due to the reasons previously described. Some mechanical properties used in the description of the material models were obtained through experimental tests carried out on materials and masonry assemblages. Others were adopted from current research, due to the difficulty of obtaining them. The mesh was composed of continuum elements representing the masonry units and the masonry joints as a composite.

It is common to model potential cracks in units in order to avoid an overestimation of the collapse load and stiffness. Thus, potential cracks placed at the web-flange intersection were considered. Interface elements with a discrete cracking model were used to represent the interlocking of units located in the connection of the flanges with the web wall. The stiffness of these interfaces was defined by fitting the numerical to the experimental results obtained in the masonry walls. An exponential softening behaviour was adopted for the tensile of these interfaces. The tensile strength (ft = 0.91 MPa) was obtained through tensile tests performed on the concrete units. The mode I fracture energy (Gf I = 0.047 N/mm) was obtained from the experimental results in Mata (2011) in concrete blocks with a similar composition of raw materials. The constitutive law for discrete cracking

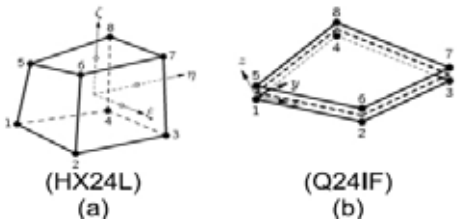

Figure 8 — Elements used in 3-D numerical modelling (DIANA®)

in DIANA® is based on a total deformation theory, which expresses the tractions as a function of the total relative displacements. Eight-node isoparametric solid brick elements with Gauss integration scheme were adopted to represent the walls (HX24L-DIANA®). An interface element between two planes in a three-dimensional configuration was adopted to represent the interface at the flange-web intersection (Q24IF-DIANA®) (Fig. 8).

Monotonic loading was applied to the specimens in the numerical analysis. Similarly to the experimental tests, the flanges have firstly been subjected to a vertical uniformly distributed load p = 0.5 MPa which was maintained constant, in addition to the self weight. After that, vertical load were imposed on the web until failure. The boundary conditions considered were fixed bottom walls to simulate the experimental tests. The bottom concrete slabs were not included since their consideration does not influence the masonry wall behaviour.

Results and Discussion

The ultimate capacity of interlocked specimens was 169 kN. The shear strength of interlocked wall intersection was 0.61 MPa. The test exhibited little deformation and some cracks before failure and almost pure shear failure could be achieved at the flange-web intersection. It can be seen that the vertical head joint at the flange-web intersection broke clearly away from the flanges at the same time as shearing of the intersecting block occurred (Figure 9).

The numerical load versus displacement curve is plotted in Figure 10 and compared with the experimental one. A reasonably good agreement has been found. However, the results presented linear behaviour until the experimentally obtained ultimate load. This indicates that it is necessary to calibrate the properties of the interface for the model represents its behaviour correctly.

Conclusions

In the experimental test, masonry walls failed under shear and the shear strength of interlocked wall intersection was 0.61 MPa. From previous research on the same materials (Mauricio [5]), the shear strength of interlocked wall intersection found was 0.88 MPa. Both results are larger than the Brazilian code indicates, 0.15 MPa. It indicates that Brazilian code can be very strict. Results pointed out some aspects and indicators in the behaviour of flanged walls that should be numerically and experimentally confirmed in order to clarify the behaviour of these structures and to allow the development of accurate design models.

Figure 9 — Failure mode of specimen.

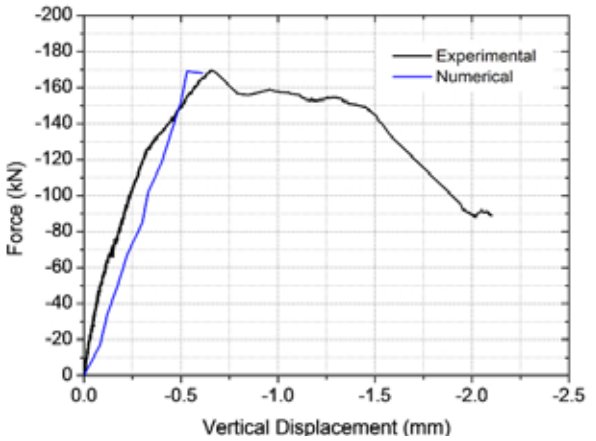

Figure 10 — Vertical web displacement.

References

[1] *Lissel, S. L., Shrive, N. G., & Page, A. W. (2000). Shear in plain, bed joint reinforced, and posttensioned masonry, In : Canadian Journal of Civil Engineering, Vol. 27 , No. 5, pp. 1021–1030.*

[2] *Camacho, J. S., Ramalho, M. A.; & Andolfato, R. P. (2001). An experimental study of the interaction among walls submitted to vertical loads, In: Amc — 6th Australian Masonry Conference, Adelaide: Griffith, Vol. 1, pp. 95–104.*

[3] *Yoshimura, K., Kikuchi, K., Kuroki, M., Nonaka, H., Kim, K.T., Matsumoto, Y. Itai, T., Reeznag, W., Ma, L.. Experimental study on reinforcing methods for confined masonry walls subjected to seismic forces, Proceedings of 9th North American Masonry Conference, Clemson, South Carolina, USA, 2003.*

[4] *Modena, C., Porto, F., Valluzzi, M.R., Reinforced and rectified clay block masonry, Proceedings of 6th National Congress of Seismology and Seismic engineering, Guimarães, Portugal, 2004, pp. 155–177*

[5] *Maurício, R. M. (2005). Theoretical and experimental study of direct stretcher bond connections between walls of concrete blocks in real and small-scale 1:4, Msc Thesis, Engineering College of Ilha Solteira, Ilha Solteira, São Paulo, Brazil. (in Portuguese).*

[6] *Capuzzo Neto, V., Corrêa, M. R. S., & Ramalho, M. A. (2007). Shear strength of vertical interfaces of intersecting walls, In: 10th North American Masonry Conference, Saint Louis, Boulder, The Masonry Society, Vol. 1. pp. 872–883*

[7] *Bosiljkov, V., Page, A. W., Simundic, M. S. G., & Zarnic, Roko (2010). Shear capacity of the Flange-Web Intersections of Brick Masonry Nonrectangular Sections, Journal of Structural Engineering, Vol. 136, No. 5, May, pp. 574–585.*

[8] *Lourenço, P.B.; Rots, J.G. (1997). Multisurface interface model for analysis of masonry structures, Journal of engineering mechanics, V. 123(7), 660–668*

[9] *Lourenço, P.B. (1996). Computational strategies for masonry structures, PhD Thesis, Delft University of technology, Delft, The Netherlands. ISBN 90-407-1221-2.*

[10] *EUROPEAN STANDARD. EN 772-16, Methods of tests for masonry units — Part16: Determination of dimensions, 2000.*

[11] *ASSOCIAÇÃO BRASILEIRA DE NORMAS TÉCNICAS (ABNT). NBR 13279, Mortars applied on walls and ceilings — Determination of the flexural and the compressive strength in the hardened stage. Rio de Janeiro, 2005. (in Portuguese)*

[12] *ASSOCIAÇÃO BRASILEIRA DE NORMAS TÉCNICAS (ABNT). NBR 15812-2, Structural masonry — Clay blocks Part 2: Execution and site quality control. Rio de Janeiro, 2010. (in Portuguese).*

[13] *EUROPEAN STANDARD. EN 1052-1, Methods of test for masonry: Part 1 — Determination of compressive strength, 1999.*

[14] *ASTM C1006, Standard Test Method for Splitting Tensile Strength of Masonry Units (1996).*

[15] *EUROPEAN STANDARD. EN 1052-3, Methods of test for masonry: Part 3 — Determination of initial shear strength, 2002.*

Low cycle performance of T-stub components of bolted moment beam-to-column connections

POP, Ana-Maria
Politehnica University of Timisoara, Romania

GRECEA, Daniel
Politehnica University of Timisoara, Romania

CIUTINA, Adrian
Politehnica University of Timisoara, Romania

Abstract

The present research represents the numerical investigation used to characterize the behaviour of bolted steel beam-to-column joints in low-cycle fatigue. The study is based on existing experimental investigation on T-stub components performed at the Politehnica University of Timisoara, using mild and high strength steel. First a calibration of numerical results is performed based on the monotonic experimental response. The challenge of the numerical investigation is represented by the calibration of cyclic curves, using adequate FEM techniques.

Introduction

In the seismic design of steel structures, the Moment Resisting Frames (MRF) are recognized as highly dissipative structures. In consequence, the seismic input energy is dissipated through plastic deformations concentrated in specific locations, whose behaviour has to be predicted by proper design. According to the Eurocode 8 rules, the dissipative zones could be located either in elements or in beam-to-column joints [1]. As shown by previous studies, the end-plate connections could prove adequate rotation capacity if special measures are taken, e.g. use of relatively thin end-plates, avoiding brittle failure of welds and bolts etc. From this point of view, the T-stub element (see Fig. 1) represents the key-macro-component of the connection behaviour.

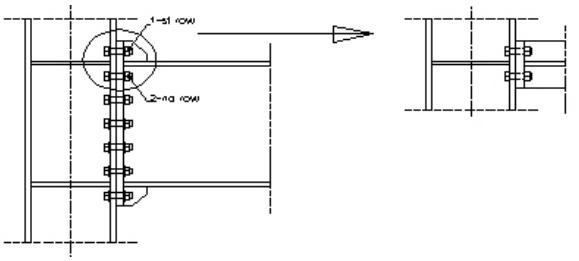

Figure 1 — End-plate connection: T-stub element

Globally the T-stub macro-component can lead to 3 types of failure modes, depending of the connection component characteristics (see Figure 1 and Table 1). Mode 1 is represents generally a very ductile behaviour and is characteristic to thin end-plates, but cannot be considered a real solution to strength demands in case of seismic resistant structures. On contrary, the Mode 3 leads usually to a good T-stub resistance, while the failure mode is fragile in nature by bolt rupture. In consequence, the Mode 2 could answer well to both strength and ductility demands.

From this point of view, the Dual Steel (DS) concept can be extended to connections, based on the same philosophy used in structures: using High Strength Steel (HSS) in non-ductile components that should poses over-strength and Mild Carbon Steel in ductile components in order to achieve both ductility and robustness criteria.

Figure 2 — Types of T-stub failure modes

Based on this principle, a large experimental research program was carried out at the CEMSIG Research Centre of the "Politehnica" University of Timisoara, in order to study the performance of dual-steel configuration for beam-to-column joints under monotonic and cyclic loading. The experimental study was considering full joint specimens, T- stub and weld detail specimens [2], [3], [4]. The present research focuses on the numerical investigation (by FEM) of the T-stub elements, through parametric studies and low-cycle fatigue interpretations of the results. The parametric study also shows the borders for T-stub macro-component failure mode 2 –> 1 and 2 –> 3 with careful classification of element behaviour.

Results of experimental investigation

Summary of testing program

The main objective of the experimental program was to study the performance of welded and bolted end-plate beam to column joints realized from two different steel grades. For this purpose, the experimental program integrated experimental investigation on materials, welded components, T-stub components, and beam to column joints. In this way the main sources of ductility were investigated, in local (material and components) and global (joint tests) manner. Although the entire research is much larger, this paragraph describes only the investigations performed on T-stub components, chosen for numerical study. Previous papers by the same authors already summarized the results on materials, welded components, weld details and beam-to-column joints (Dubina et al. 2008 a, b, c). Both monotonic and alternating cyclic tests were performed on T-stub components obtained by welding S 235 web plates to S 235, S 460 and S 690 end-plates, using

K bevel full-penetration welds. MAG welding was used, with G3Si1 (EN 440) electrodes for S235 to S235 welds, and ER 100S-G/AWS A5.28 (LNM Moniva) for S235 to S460 and S690 welds. T-stubs were connected using M20 gr. 8.8 bolts. The EN 1993-1.8 was used to obtain the design strength of T-stubs and failure modes. From the experimental program, for the numerical modelling was set a T-stub type A (Table 1).

Table 1 — T-stub characteristics

T-stub type	Label	Web	End-plate	Design failure mode
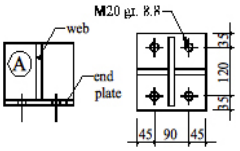	TST-12A-S235	S235 t = 15 mm	S235 t = 12 mm	2
	TST-20A-S235		S235 t = 20 mm	2 -> 3
	TST-10A-S460		S460 t = 10 mm	2
	TST-16A-S460		S460 t = 16 mm	2 -> 3
	TST-8A-S690		S690 t = 8 mm	2
	TST-12A-S690		S690 t = 12 mm	2 -> 3

T-stub performance on monotonic an cyclic loading

Table 2 shows the measured average values of yield stress f_y, tensile strength f_u and elongation at rupture A. It has to be recognized that the value of elongation for S460 is surprisingly large. Bolts were tested in tension as well, showing an average ultimate strength of 862.6 N/mm².

Table 2 — Material properties

Nominal steel grade	f_y, N/mm²	f_u, N/mm²	A, %	Actual steel grade
S235	266	414	38	S235
S460	458	545	25	S460
S690	831	859	13	S690

Loading was applied in displacement control under tension and force control under compression. Compressive force was chosen so as to prevent buckling of the specimen. In general a good ductility was observed for all specimens. However, thicker end-plate specimens, even for S235 show a smaller ductility. The conclusions of the experimental study proves the fact that the choice of thickness associated with steel grade is important in the conception of a proper connection, for obtaining a good balance between strength, stiffness and ductility of components. Figure 3 shows as example the experimental results under the form of force-displacement relationships of T-stub specimens, while the photos in the same figure show two types of failure modes (mode 2 and 1 respectively). No significant differences in force values between failure modes of monotonic and cyclic specimens were recorded. Also, both results agreed with the analytical predictions computed according to EN 1993-1.8. Cyclic loading reduced the maximum resistance of the T-stub specimens, though the reduction was not significant. The ductility of the T-stub specimens was quantified through the ultimate displacement Du. Under monotonic loading,

ultimate displacement was smaller for specimens with thicker end-plates that failed in modes 2 and 3 involving bolt failure. Cyclic loading reduced significantly ultimate displacement of specimens with thinner end-plates that failed in mode 1. This behaviour is attributed to low-cycle fatigue that generated cracks in the HAZ near the welds, along yield lines. On the other hand, cyclic loading did not affect much ultimate displacement for specimens with thicker end-plates that failed in modes 2 and 3, governed by bolt response. It is to be emphasized that specimens realized from high-strength end plates (S460 and 690, with lower elongation at rupture), had a ductility comparable with the one of specimens realized from mild carbon steel (S235). The parameters governing the ductility of T-stubs were type of loading (monotonic / cyclic) and failure mode (end-plate or bolts) [5], [7], [8].

Numerical analysis

Calibration of T-stub FEM response

The first step in the FEM analyses was the calibration of T-stub responses presented in Figure 4, using ABAQUS computer code [6]. T-stubs modelling passed the following steps: choose of the FEM, mashing, define of the material properties. The used FEM was continue solid element (brick element) C3D8R, with reduced integration. For material, it was used a stress-displacement real curve. Between all the elements a normal "hard contact" law was defined, with the surfaces separation possibility. To calibrate the numerical model developed in ABAQUS, an analysis was made in order to compare behaviour curves of some T-stubs of the experimental program with curves obtained by numerical simulation with real characteristics of steel obtained by tests. The results are presented in the following figures. Reference numbering should be placed between brackets and left aligned. The text is to be 7.5 mm indented from the left margin, as presented in the following example.

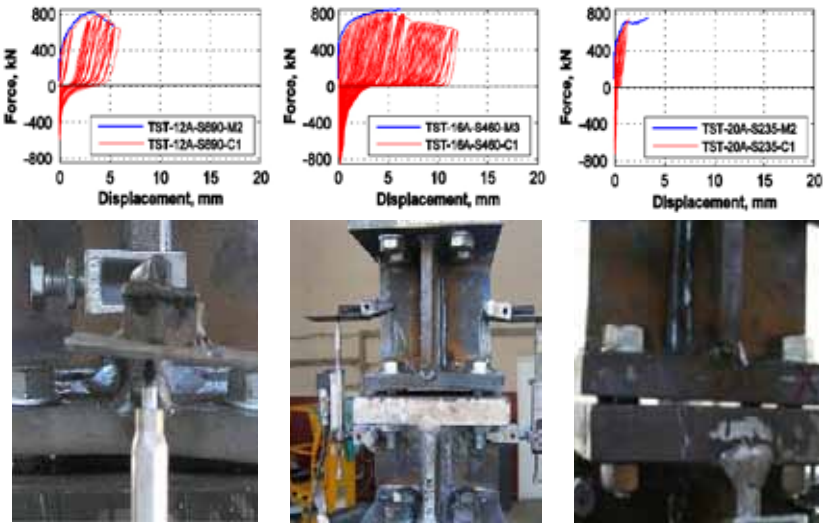

TST-12A-S690
Failure mode 2

TST-16A-S460
Failure mode 2

TST-20A-S235
Failure mode 1 ® 2

Figure 3 — Examples of failure modes of T-stub specimens

Conclusions

The strength and ductility of the bolted end-plate beam-to-column joint is highly influenced by the T-stub behaviour. The FE model of some previously tested T-stubs show good agreement response under the form of Force-Displacement curves, both in monotonic and cyclic response.

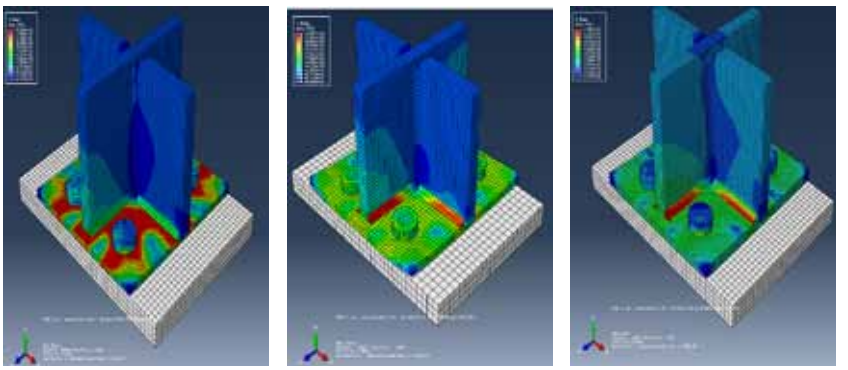

TST-12A-S690-C1
Failure mode 2

TST-16A-S460-C1
Failure mode 2

TST-20A-S235-C1
Failure mode 1 –> 2

Figure 4 — T-stub behaviour and failure mode according to numerical analysis

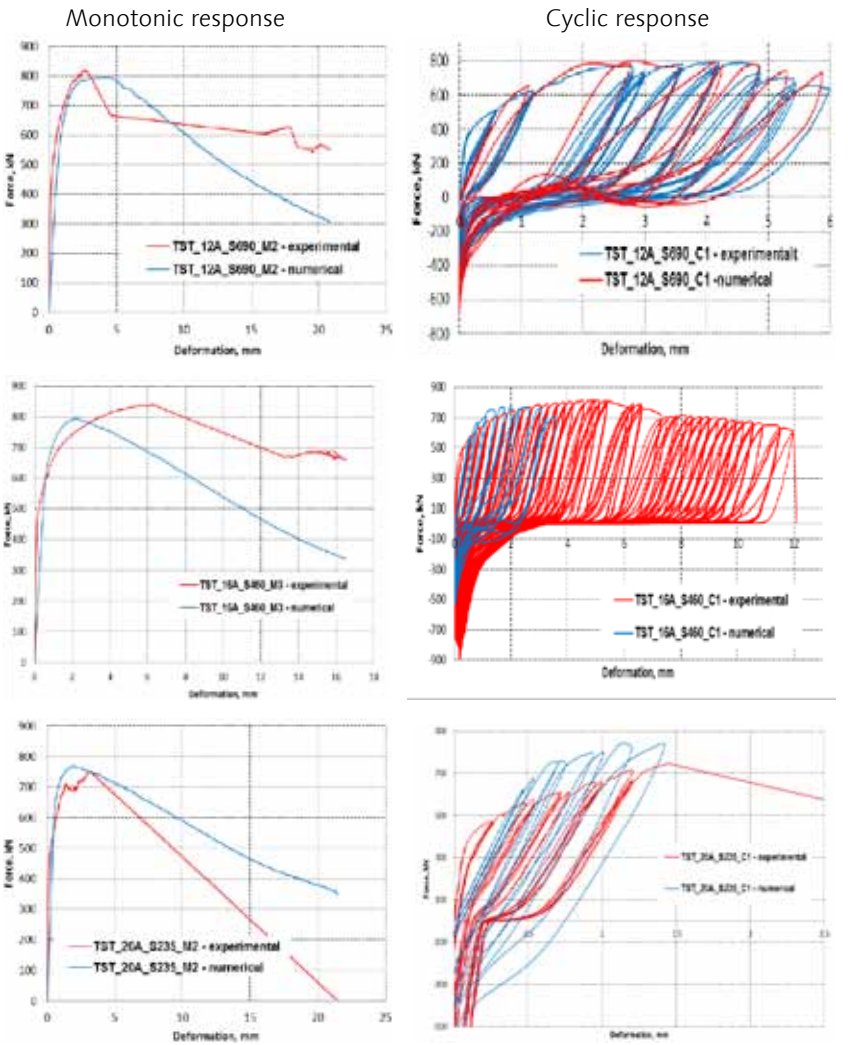

Figure 5 — T-stub behaviour according to numerical analysis

Acknowledgments

This work was partially supported by the strategic grant POSDRU 107/1.5/S/77265, inside POSDRU Romania 2007–2013 co-financed by the European Social Fund — Investing in People

References

[1] *EN 1993-1.8. 2003. Design of steel structures. Part 1–8: Design of joints, European standard.*

[2] *Dubina, D, Stratan, A, Muntean, N, Grecea, D, "Dual-steel T-stub behaviour under monotonic and cyclic loading", ECCS/AISC Work-shop: Connections in Steel Structures VI, Chicago, Illinois, USA, 23–55, 2008.*

[3] *Dubina, D, Stratan, A, Muntean, N, Dinu, F, "Experimental program for evaluation of Moment Beam-to-Column Joints of High Strength Steel Components", ECCS/AISC Work-shop: Connections in Steel Structures VI, Chicago, Illinois, USA, June 23–55, 2008.*

[4] *Dubina, D, Muntean, N, Stratan, A, Grecea, D, Zaharia, R, "Testing-program to evaluate behaviour of dual steel con-nections under monotonic and cyclic loading", Proc. of 5th European Conference on Steel and Composite Structures – Eurosteel 2008, 3–5 September, Graz, Austria, 609–614, 2008.*

[5] *Dubina, D, Grecea, D, Stratan, A, Muntean, A., "Performance of dual-steel connections of high strength components under monotonic and cyclic loading", STESSA 2009, Behaviour of Steel Structures in Seismic Areas, Taylor & Francis Group, London, 16–20 Aug. 2009, Philadelphia, USA, 437–442, 2009.*

[6] *ABAQUS Inc. "ABAQUS analysis user manual", version 6.10, 2010.*

[7] *Dubina, D, "Dual-steel frames for multistory buildings in seis-mic areas", Keynote lecture, Proceedings of SDSS'Rio 2010 International Colloquium Stability and Ductility of Steel Structures, 8–10 September, Rio de Janeiro, Brazil, 59–80, 2010.*

[8] *Muntean, N, Grecea, D, Dogariu, A, Dubina, D, "Strength and ductility of bolted T-Stub macro-components under mono-tonic and cyclic loading", Proceedings of SDSS'Rio 2010 International Colloquium Stability and Ductility of Steel Structures, 8–10 Sept, Rio de Janeiro, Brazil, 223–230, 2010.*

Dynamic safety assessment of a small span high-speed railway bridge

ROCHA, João Miguel
University of Porto, Faculty of Engineering, Portugal

HENRIQUES, António Abel
University of Porto, Faculty of Engineering, Portugal

CALÇADA, Rui
University of Porto, Faculty of Engineering, Portugal

Abstract

The main purpose of this work is to evaluate the sensitivity of small span bridges in high speed railway lines to the resonance phenomena bearing in mind the real variability of the parameters that influence the bridge dynamic response. As a case study, the railway bridge of Canelas, located in the Northern line of the Portuguese railway, was selected. Simulation techniques, namely the Monte Carlo and Latin Hypercube methods, were applied as they allow an accurate consideration of the randomness of structural parameters that influence the bridge dynamic response. The influence of the train-bridge interaction effects on the dynamic response was also studied. Furthermore, a safety assessment of the bridge was done based on the results obtained in the simulations in order to define the train speed limit on the bridge.

Introduction

The dynamic effects caused by high speed trains crossing a bridge is one of the most relevant facts to take into account during the design stage and for the selection of the proper structural solution. Excessive vibrations have a higher tendency to occur for speeds higher than 200 km/h as a consequence of resonant effects [1].

During the design stage it is common that several aspects are not entirely known, leaving the designer to deal with these uncertainties. Unfortunately, these uncertainties may be responsible for unexpected dynamic response of railway bridges. In short span bridges this variability can be due to structural-related parameters as well as train-related parameters [2]. The current work intended to take these aspects into account and to analyze how the dynamic response of bridges is affected by the variability of these parameters. To do so, two different simulation techniques were applied, Monte Carlo and Latin

Hypercube methods, and scenarios with different sample sizes and different train speeds were analysed. When the dynamic properties of the train are taken into account, train-bridge interaction needs to be included in the analysis. The interaction effects take particular importance when analysing the dynamic response of short span bridges [2, 3]. The European standards allow not taking into consideration the train-bridge interaction, suggesting, however, that an additional damping is added to the bridge damping coefficient [1].

As a case study, a bridge with six simply supported spans was selected. The goal of the present work is to perform a safety assessment of the bridge and compare the differences in the dynamic response when different methods, namely the moving loads method and methods which include train-bridge interaction, are applied, allowing the assessment of the influence that the train-bridge interaction has in the dynamics response.

Case Study – Canelas bridge

The case study used in this paper is Canelas Bridge, located in the Northern line of the Portuguese railway. The bridge has six simply supported spans of 12 m each, leading to a total length of 72 m. The bridge deck is a composite structure consisting of two half concrete slab decks with nine embedded rolled steel profiles HEB 500. This kind of structural system is called filler beam and is a very common structural solution for small span bridges in the European high-speed railway lines, especially in France and Germany [4, 5]. A general view of the bridge used as case study, as well as the typical cross section of the bridge deck is shown in Figure 1.

As it can be seen in Figure 1b, due to the existence of a longitudinal expansion joint between the decks throughout the entire structure, the bridge has two separate and independent decks, each one supporting a single railway. However, the columns and the abutments are unique, supporting both decks. Each deck has a total width of 6.2 m, where 4.5 m correspond to the width of the concrete slab with a height of 0.7 m and 1.7 m is the width of the cantilever with a variable height from 0.3 to 0.5 m. Embedded on the concrete slab with a spacing of 0.475 m are the referred nine rolled steel profiles HEB 500.

(a) General view

Figure 1 — Canelas Bridge

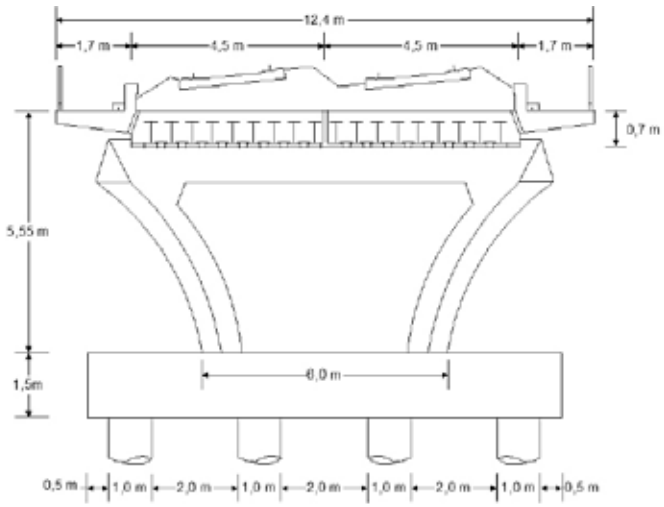

belongs to Figure 1

(b) Typical cross section

Cement plates were placed underneath the concrete slab, between the steel profiles, to be used as formwork during the concreting of the slab. It should also be pointed out that the deck has small ballast retention wall placed on the top of the slab and right before the beginning of the cantilever, corresponding to a beam with 0.6 m of height and 0.3 m of width.

Numerical models

Dynamic model of the bridge

A 2D beam model of the bridge was developed using a FEM program [6]. The numerical model was defined according to the design drawings.

Along with the deck, the model included the ballast, the rail and the bearings. The deck and the rail were modelled as beams, positioned at the corresponding centre of gravity, whereas the bearings were modelled as springs. The connection to the bearings is positioned at the corresponding centre of rotation. The laminated neoprene elastomeric bearings are placed under each rolled steel profile HEB 500. Due to the existence of steel plates between each neoprene layer, each layer acts as an individual spring so the bearing, as a whole, works as a system of series-connected layers. Horizontal springs were used to reproduce the frictional behaviour of the ballast. According to [2] the ballast has a linear elastic range until a relative horizontal displacement, u_0, of 0.002 m is reached, followed by a plastic phase. In this paper a load, k, of 20 kN/m, corresponding to an unloaded track, was considered. Since the relative displacements are very small (smaller than the u_0 limit), the ballast stiffness was computed in accordance with the elastic range. The connection between the track elements and the deck elements, and the connection between the deck elements and the bearings was accomplished by means of rigid beams. A schematic view of the bridge model used can be seen in Figure 2. Despite the

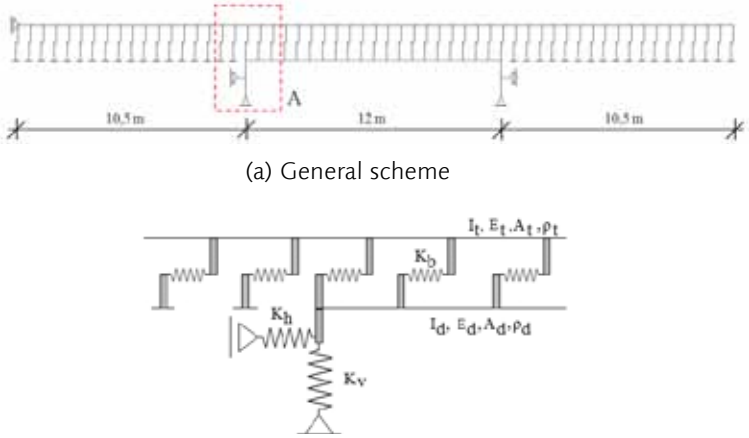

(a) General scheme

(b) Detail A

Figure 2 — Bridge model

structural system of the bridge consisting of simply supported beams, the rail is continuous and this continuity affects the dynamic response of the bridge. This was included in the numerical model by extending the rail 10.5 m in both directions over the length of the bridge.

Dynamic model of the train

In this paper two models were used to reproduce the train, corresponding to two different applied methods. For the moving loads method, the simplest used method, the train consists in a series of concentrated loads, representing each axle of the train. For this model, only the value of the load per axle is required. Prior to the analysis, the time history of the loads must be defined for each axle. For each time step the axle loads are converted into equivalent nodal forces.

The other used method took into consideration the train-bridge interaction. For this analysis a dynamic model of the train is required. The axle positioning as well as the load per axle are the same in both models. The car bodies and bogies are simulated by rigid bodies with mass, M_c and M_b, and rotational inertia, I_c and I_b, respectively. The primary and secondary suspensions are simulated by a spring-damper set with stiffness, K_p and K_s, and damping coefficient, c_p and c_s, respectively. The wheelset is simulated by a concentrated mass, M_e, whereas the wheel-rail contact stiffness is simulated by a spring with stiffness K_h. It should be mentioned that the dynamic properties of the train were defined according to [2]. A scheme of the model used can be observed in Fig. 3.

Random variables

In an early stage of this work several variables that might have non-deterministic properties and whose variation might lead to a relevant variability on the structural response were selected. This required the definition of variables related to the structure, the train, the track and also the wheel-rail contact.

The random variables used in the current paper can be divided into two separate groups. One group related with the structural and track variables and the other related with the train variables. The bridge-related and track-related variables selected, as well as their correspondent distribution and variability [7, 8], are presented in Table 1.

The train-related variables are presented in Table 2. The variability of these parameters was defined according to information provided by the manufacturers. A uniform distribution was assumed for all the parameters. It should also be mentioned that the variation of the car body mass was defined according to the occupancy of the train. The values of load per axle referred in [2] were assumed for a train operating at full capacity.

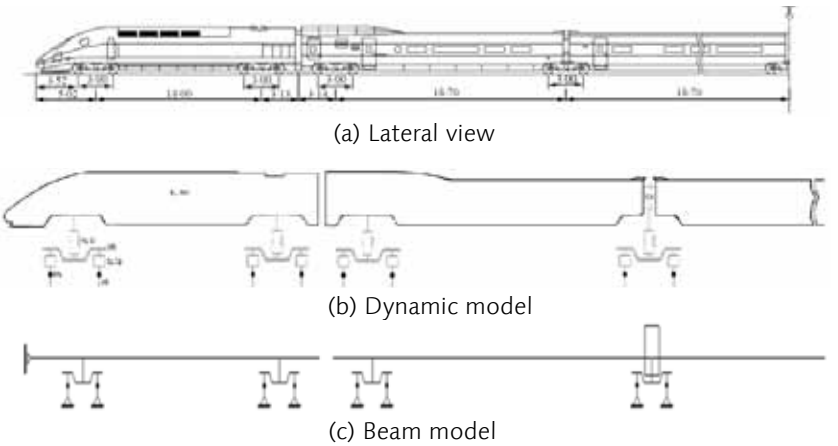

(a) Lateral view

(b) Dynamic model

(c) Beam model

Figure 3 — Train model

Variable [simulation]	Distribution	Mean (Gaussian) or Min. (Uniform)	Standard deviation (Gaussian) or Max. (Uniform)
Concrete density weight (1, 2)	Gaussian	2,5 t/m³	0.1 (CV = 4%)
Ballast denisty weight (3, 4)	Uniform	17 kN/m³	21 kN/m³
Ballast area (5, 6)	Uniform	1.48659 m²	2.76081 m²
HEB 500 area (7, 8)	Gaussian	nominal area	0.04 x nominal area
Elasticity modulus concrete (9, 10)	Gaussian	36.1 GPa	2.888 (CV = 8%)
Concrete weight (geometrical variation) (11, 12)	Uniform	minimum area	maximum area
Concrete height (13, 14)	Gaussian	nominal value	10 mm
Concrete width (18, 19)	Gaussian	nominal value	5 mm
Shear modulus neoprene (16, 17)	Uniform	0.75 MPa	1.18 MPa
Elasticity modulus neoprene (15, 20)	Uniform	420 MPa	600 MPa

Table 1 — Bridge random variables, distribution functions and variability

Variable	Variation (%)
Primary suspension stiffness	± 10
Primary suspension damping	± 15
Secondary suspension stiffness	± 10
Secondary suspension damping	± 15
Carbody mass	± 15
Wheel-rail contact stiffness	± 15

Table 2 — Train-related variables and variability

Dynamic properties of the numerical models

In this section the properties of the dynamic models developed, both the bridge and the train, are presented.

In both cases the obtained results correspond to an analysis where the average values were assigned to all the random variables previously defined.

In Figure 4 the first two bending modes of the bridge are illustrated. It can be seen that the first natural frequency of the bridge has a particularly high value, but is within the typical range of values for this type of structure.

In Fig 5 the dynamic properties of the train are presented with the illustration of the global modes of the train. It can be observed that the values obtained in the modal analysis are in agreement with the literature.

Variable screening procedure

Due to the large number of variables used in the analysis, a variable screening procedure was performed. The goal of this procedure is to assess the importance of each variable on the dynamic response, allowing to check if any of the used variables can be considered as

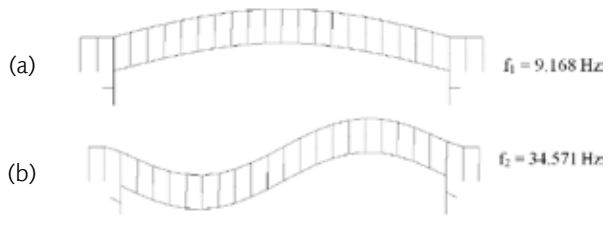

Figure 4 — Schematic view of the bending modes of the bridge

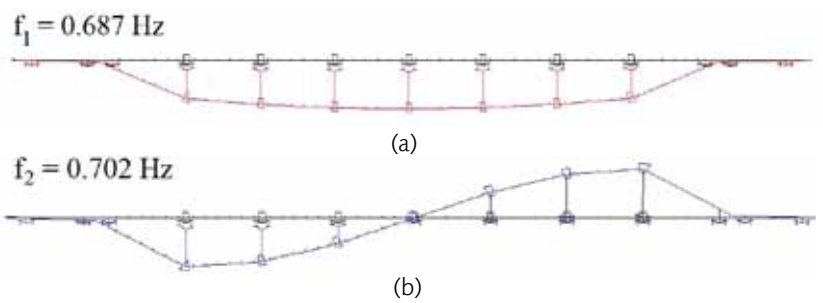

Figure 5 — Train modal analysis (only one half of the train is presented)

deterministic in the following analysis. The variable screening procedure was also divided into two separate analysis. The method used for the screening procedure is similar to one presented in [9].

Procedure

The first stage of the procedure corresponds to the selection of the random variables that allow the definition of the problem. Afterwards, a structural analysis is performed adopting the mean values for all the variables. At next step, the bridge dynamic response is computed keeping all the variables with their mean values except for the "tested" variable which is changed from its mean value (about two times the standard deviation). This step is repeated for all variables allowing the evaluation of the sensitivity coefficients and the importance indicators for each variable.

The sensitivity coefficients and the importance indicators are obtained by comparing the difference between the reference results (correspondent to the analysis where all the variables have their mean values) and the results obtained for each "tested" variable, as expressed on Equations 1 and 2:

$$b_k = \frac{(\Delta y_k / y_m)}{(\Delta x_{ik} / x_{im})} = \frac{(\Delta y_k / y_m)}{(h \cdot \sigma_{xk} / x_{im})} \quad (1)$$

$$(b\sigma)_k = b_k \cdot CV \quad (2)$$

where Δy_k is the difference between the structural response reference results and the results obtained for each "tested" variable, Δx_{ik} is the difference between the mean value of the "tested" variable and the value used in the analysis and ym and x_{im} are the structural response reference value and the "tested" variable mean value, respectively.

After analysing these coefficients for all variables, the maximum importance indicator is determined and the relative importance for each variable is established by comparing to the maximum value obtained. Variables which relevance is smaller than a pre-established value (10%) are considered irrelevant for the bridge dynamic response and in further analysis are considered as deterministic. In these cases the variables values used on the analyses will be their mean value.

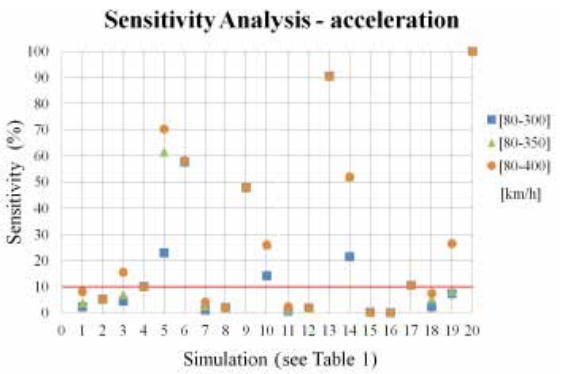

Figure 6 — Results of the sensitivity analysis for the accelerations

Results

Bridge-related and track-related variables

Some of the results obtained from the variable screening procedure for the bridge-related and track-related variables can be seen on Figure 6. It should also be pointed out that in this work four distinct response parameters were analysed: natural frequencies, displacements, accelerations and reactions.

The variables with higher influence on the dynamic response were the inertia variation due to the variation of the section height, the ballast area, the elasticity modulus of the concrete and the stiffness of the bridge bearings. On the other hand, the geometrical variation of the rolled steel profiles and the shear modulus of the neoprene had a very small influence on the response and could be taken as deterministic variables.

Train-related variables

In order to assess the influence of the train-related variables on the dynamic response, the acceleration on the bridge and inside the coaches was analysed. Consequently, the influence of the train-related variables can be split into two different analysis: one concerning the bridge response and the other related with the train response. However, this work is focused on the variations of the bridge response. In Figure 7 some of the obtained results are presented.

It could be observed that the bridge response is practically unaffected by the changes on the train properties. The only exception occurs when the carbody mass and the wheelset mass are changed. All the other parameters can be kept as deterministic on dynamic analysis focused on the bridge dynamic response.

Simulations

Initially, the structure and track variables are analysed, keeping the train properties constant. On this stage the dynamic response is analysed by the moving loads method.

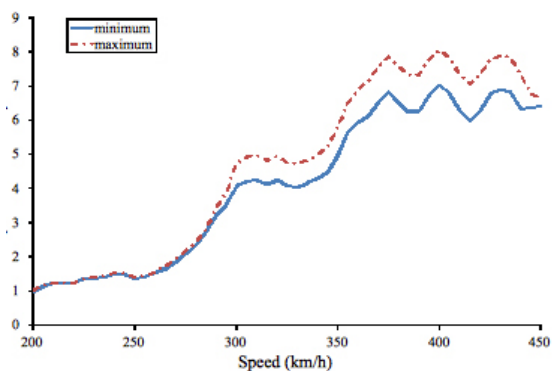

Figure 7 — Influence of the carbody mass on the dynamic response

Two different simulation methods were used: the Monte Carlo method, which is the basis of most of the simulation methods, and the Latin Hypercube method, which is a variation of the previous method. The bridge dynamic behaviour was analysed for the crossing of a train with the same characteristics of the type B train presented in [1] with a variable speed ranging from 200 km/h to 450 km/h in steps of 5 km/h. For the Monte Carlo method four different sample size simulation scenarios were analyzed: 5,000, 2,500, 2,000 and 1,000 simulations. For the Latin Hypercube two different scenarios were analyzed with 500 and 250 simulations, respectively.

Results

In this section some of the obtained results will be presented. In Fig. 8 histograms of the acceleration values for different train speeds obtained for the 5,000 Monte Carlo simulation are shown.

From the analysis of the histograms it can be seen that the structural response does not follow a Gaussian distribution. In Figure 8b a skewness in the distribution can be observed and in Figure 8a shows a combination of distributions. This is observed for several speeds, namely the speed range from 285 km/h to 305 km/h, and can be explained by the existence of two distinct structural responses (resonant and non-resonant response).Figure 9 shows the evolution of the mean values and the maximum values for the simulation scenarios analyzed when the speed of the train increases.

The obtained results in terms of mean values and standard deviation values are consistent for the different applied simulation methods and for the different sample sizes analyzed. However, when analysing the maximum response values obtained for the different simulation scenarios a higher scatter on the results can be observed. This turns out to be a key issue for the analysis since these are the values that have a higher importance in structural reliability problems.

Train-bridge interaction

Prior to the safety assessment, the influence on the train-bridge interaction effects on the dynamic response was analysed. A deterministic analysis was performed assigning the average value to all the random variables. A comparison between the results obtained from the moving loads method and the interaction method is shown in Figure 10.

From the observation of Figure 10 some significant differences can be noticed. The differences occur particularly in the resonant peaks, where a reduction in the acceleration values (~ 10%) is registered, confirming what was observed in the time history response. Non-resonant speeds do not show significant differences between both methods.

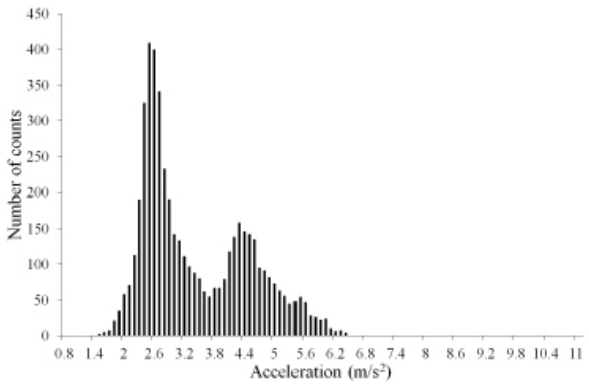

a) v = 285 km/h

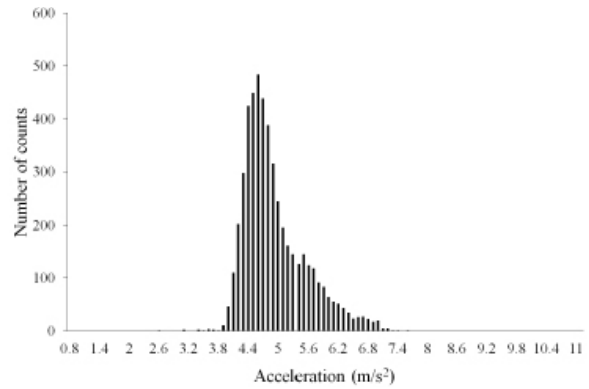

b) v = 320 km/h

Figure 8 — Histograms for different train speeds

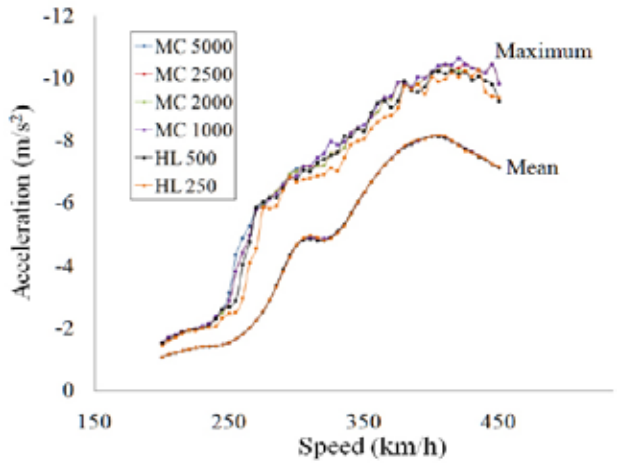

Figure 9 — Histograms for different train speeds

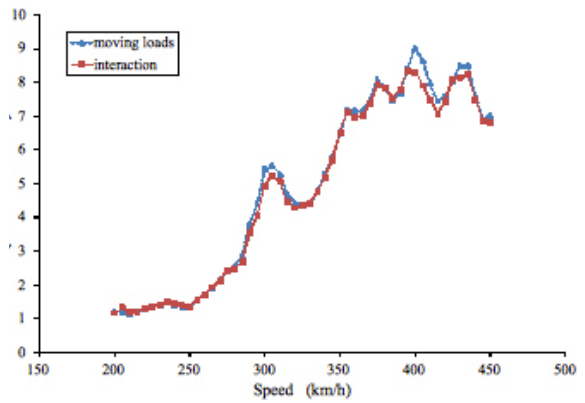

Figure 10 — Maximum acceleration comparison for different methods

Safety assessment

At this stage the safety of the bridge was only assessed taking the bridge and track variables into account. This analysis was based on the acceleration values registered at mid span of the bridge which turned out to be the most restrictive aspect of the response. The acceleration limit was considered to be 7 m/s² which is the value that some experimental tests confirmed to be the limit to the beginning of the ballast instability [10]. In the European standards, however, this limit is lower and the maximum acceleration allowed for ballasted track is 3,5 m/s² which comes from the use of a safety factor equal to 2 [1].

A curve was fitted to the upper extremity of the cumulative probability function in order to perform a safety assessment of the bridge. For this safety assessment several types of regression functions were used, namely sigmoidal and exponential functions. Taking into account the type of studied problem probability values up to 10–4 are considered to be acceptable to measure admissible failure due to the instability of the ballast layer. Analysing Figure 11 it can be seen that this value is not exceeded for speeds lower than 290 km/h, making this the train speed limit to be imposed on the bridge. It should also be pointed out that in the cases where less than 2,000 simulations were used, the obtained probabilities of failure are not accurate. This comes as a result of the misrepresentation of the interest zone in these cases due to the small number of points on the upper extremity of the structural response distribution, which had already been mentioned before, leading to an inadequate fit of the data.

Conclusions

This work intended to assess the influence that the variability of the train-track-bridge parameters have on the dynamic response. The Canelas railway bridge was selected as the case study and the identification of the parameters with higher importance on the bridge dynamic behaviour was done through a sensitivity analysis. This sensitivity analysis showed that the inertia, the area of the ballast layer,

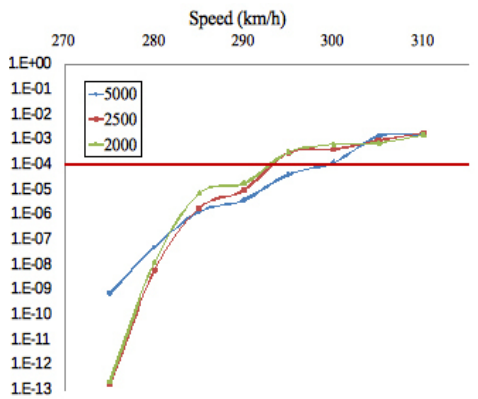

Figure 11 — Safety assessment for different sample size

the concrete elasticity modulus, the stiffness of the bridge bearings, the carbody mass and the wheelset mass are the parameters that most affect the bridge response.

By comparing the results from the two applied simulation methods it can be confirmed that the Latin Hypercube method is more efficient than the Monte Carlo method. However, the analysis of the maximum response values obtained for the two simulation methods shows a significant difference between them. Since these are the values that have a higher importance in structural reliability problems this turns out to be a relevant aspect and does not allow the applicability of the Latin Hypercube method to this problem due to the inadequate representation of the interest area when this method is applied.

The train-bridge interaction effects were analysed for a deterministic scenario where all the bridge variables were assigned their mean values. The comparison between the obtained results from the moving loads method and the interaction method showed important differences. These differences were, however, limited to the speeds that induced resonant effects on the bridge. The safety assessment of the bridge was based on the acceleration values registered at mid span of the bridge which were the most restrictive aspect of the dynamic response. The safety assessment concluded that the train speed limit on the bridge is 290 km/h in order to guarantee the running safety of the trains.

Acknowledgments

The present work has been funded by the Portuguese Foundation for Science and Technology (FCT), in the context of the Research Project FCOMP-01-0124-FEDER-007195 — Advanced methodologies for the assessment of the dynamic behaviour of high speed railway bridges (Ref. FCT PTDC/ECM/69697/2006). The authors also wish to acknowledge the information provided by REFER about Canelas Bridge.

References

[1] *Commité European de Normalisation (CEN) (2003) EN 1991 2 — Eurocode 1 — Actions on Structures — Part 2 — Traffic loads on Bridges. Brussels. CEN.*

[2] *European Rail Research Institute (ERRI) (1999) ERRI D-214/RP 9. Rail bridges for speeds > 200 km/h. Final report. Utrecht.*

[3] *Museros, P., Romero, M.L., Poy, A. & Alarcón, E. (2002) Advances in the analysis of short apsn railway bridges for high-speed lines. Computers and Structures 80: 2121–2132.*

[4] *Hoorpah, W. (2005) Dynamics calculations of high-speed railway bridges in France — some case studies. Dynamic of High-Speed Railway Bridges: 167–183. University of Porto — Faculty of Engineering: Porto.*

[5] *Martínez-Rodrigo, M., Lavabo, J. & Museros, P. (2010) Dynamic performance of existing high-speed railway bridges under resonant conditions retrofitted with fluid viscous dampers. Journal of Engineering Structures 32: 808–828.*

[6] *Azevedo, A. (2012) — "FEMIX 4.0 — Finite Element Analysis", http://www.alvaroazevedo.com/femix/.*

[7] *Joint Committee on Structural Safety (JCSS) (2001) Probabilistic Model Code — 12th draft. http://www.jcss.ethz.ch/.*

[8] *Wiśniewski, D.F. (2007) Safety formats for the assessment of concrete bridges — with special focus on precast concrete. Ph.D. Thesis. University of Minho. Guimarães.*

[9] *Henriques, A.A. (1998) Use of new safety concepts in the design of concrete structures (in Portuguese). Ph.D. Thesis. University of Porto — Faculty of Engineering. Porto.*

[10] *Zacher, M. & Baeßler, M. (2005) Dynamic behaviour of ballast on railway bridges. Dynamic of High-Speed Railway Bridges: 125-142. Porto.*

Comparative study of steel frame modelling levels and Eurocode based design methods

TÓTH, Adrienn
BME, Department of Structural Engineering, Hungary

JOÓ, Attila
BME, Department of Structural Engineering, Hungary

Abstract

In this paper a numerical study is presented which examines a steel frame with two different finite element programs. Stability failure is more frequent in a lot of cases than the strength failure hence it is important to focus on these failure modes: global, in-plane-, out-of plane-, lateral-torsional- and local buckling.

Three models were used with different elements such as shell elements and 7 DOF beam elements. 7 DOF beam elements were used in the first model, shell elements were used in the other two. The first of the shell models gave too much local buckling shapes therefore it was improved with local constraints and that is the third model where global buckling shapes can be examined.

There are three different procedures to calculate the resistance: (i) the general method, (ii) the method of the reduction factors and (iii) the simulation. The analysis results of the different programs and design methods were compared to each other and to the manual calculation based on the Eurocode 3 standards.

Introduction

The idea of the investigation of a frame came from a home work of an MSc class at BME Department of Structural Engineering. The connection of the column to the ground was hinged. The purlins and wall girts are not included in the finite element models, its effect is considered by lateral supports (see Fig. 1.).

By the design of steel frames it is very important to examine the stability failure modes. There are different types: the global, in-plane-, out-

of plane-, lateraltorsional- and local buckling. All of them have to be considered in the investigation of the frame.

The resistance of the whole frame can be calculated with the general method according to Eurocode 3 [2] standards. It is necessary to create a finite element model to obtain the collapse load factor related and the first buckling shape together with the critical load factor.

The resistance of the frame members can be also calculated according to the Eurocode 3, it is named manual calculation method. This is an approximation which is necessary because of the various height of the beam at the frame corner. The frame was divided into four members and reduction factors were used to calculate the resistances. These factors depend on the type of buckling. They were calculated to each member and to each buckling mode.

The resistance of the frame members can be obtained with the reduction factors and the help of the buckling shape of each member. The critical load factor of the first buckling shape related to the given member used for these calculations. The procedure is the same as the manual calculation method apart from the calculation of the critical force. The critical forces were determined by the finite element programs. The shell model provided only local buckling shapes which cannot be used to define the reduction factors. So this model was developed, the cross sections were constrained hence the local buckling cannot appear.

With the help of advanced finite element analysis we can have the resistance of the whole frame by numerical simulation. It has to be applied equivalent geometrical imperfections according to the buckling shapes of the members. On the imperfect finite element model the structural behaviour is simulated by Geometrical and Material Nonlinear Imperfect Analysis. [1]

The resistance and the utilization of the members were derived from each design method.

Models

7 DOF beam model (#1)
For the 7 DOF beam model the ConSteel [7] program was used. Each element with the 7 degrees-of-freedom can follow the behaviour of the lateral-torsional buckling, but the beam element is cannot provide local buckling which is considered as effective cross-section.

The internal flange bracings of the column and the beam were given as a lateral support on the internal flange of the members by the help of eccentric support as illustrated in Fig. 1.

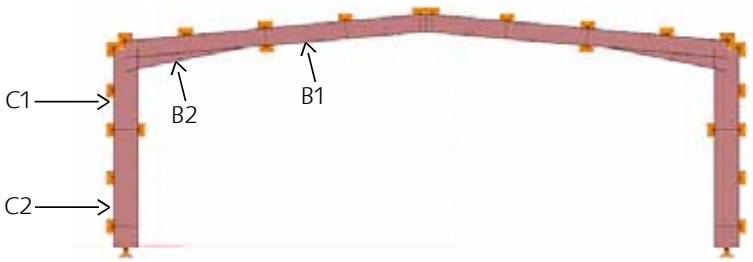

Figure 1 — 7 DOF beam model (ConSteel)

Shell model (#2)

Ansys [6] was used for the shell model. The applied shell element was SHELL181, what is a 4-node-element with six degrees of freedom at each node. The internal flange bracings of members were given as fix lateral support on one node of the internal flange. The purlins and wall girts are modelled as support on the outer flange.

The mesh was generated by free meshing method of Ansys with the maximum element length of 50 mm to be able to model local buckling at the frame corner. The full model and the details are illustrated in Fig. 2.

Figure 2 — a) Shell model (Ansys), b) Details of the shell model

The results of the linear instability analysis were local buckling shapes and this is a big disadvantage, because the global buckling shapes cannot be founded. To solve this problem the next model is developed.

Locally constrained shell model (#3)

The model #2 was modified to avoid the local buckling shapes. The column and the beam were divided into thin slices with the length of 50 mm which are perpendicular to the axle. This model will be the third one.

The nodes of the former mentioned divided sections are linked in the centre of gravity of each cross section and the section deformations are constrained. Because of these constraints the local buckling cannot come up. The constraints are displayed in Fig. 3. by pink colour.

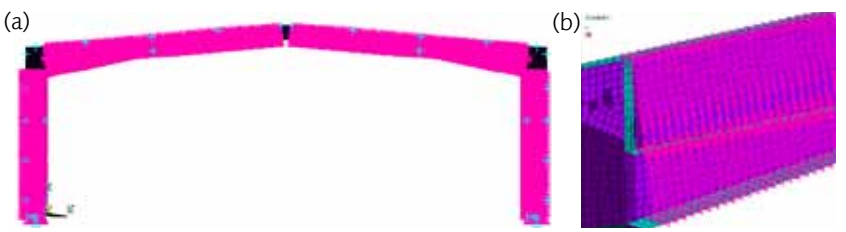

Figure 3 — a) Locally constrained shell model (Ansys), b) Constraints

By this modification of the model the critical forces of global buckling modes can be found to compare to the manual calculation and to the beam model. And later these modes can be used as the shapes of geometrical imperfections for the simulation.

Loading
Only one load step was applied which contains almost all loads according to the EC. The self-weight was applied as a steel density material property and gravity to the structure. Besides it the weight of the roof as permanent load and snow load as meteorology load was applied. Each of these was multiplied with the appropriate partial factors.

Analysis levels
Three different analysis levels were investigated. The first is the linear analysis to check the models. Chapter 3 shows more details. The next analysis is the linear instability analysis in Chapter 4. In Chapter 5 the nonlinear analysis is summarized which was necessary to perform a numerical simulation based design.

Linear analysis

The deflection of the centre point of the beam and the vertical reactions at the bottom of the columns were compared on the three models. There is a bit difference between the two different programs in the reaction force and in the deflections as well. The difference is about 5% in each case, which was accepted for further studies.

Table 1 — Results of the linear analysis

	Model #1	Model #2	Model #3
Deflection (mm)	40,60	38,44	38,38
Summa reactions (kN)	359,8	381,1	381,1

Linear instability analysis

Buckling shapes for manual calculation with reduction factors
The aim of searching the buckling shapes is to apply the critical load factors for manual calculation in case of model #1 and model #3. The column and the beam were divided into two parts so four members were investigated separately as former shown in Figure 1.

- C1: the part of the column, above the internal flange bracing
- C2: the part of the column, below the internal flange bracing
- B1: the part of the beam, right from the internal flange bracing (permanent cross-section)
- B2: the part of the beam, left from the internal flange bracing (variable height cross-section)

Different buckling shapes were searched. There were shapes which included more members and in a few cases and there were ones which were belonged to only one member. The in-plane, out-of plane and the lateral-torsional buckling were considered.

The critical internal forces (M_{cr}, N_{cr}) were calculated by the help of critical load factor related to the concerning buckling shape.

Buckling shapes for imperfections

For the nonlinear analysis it was necessary to know certain buckling shapes to apply them as geometrical imperfections according to the Eurocode 3 standards.

The shape of imperfections correspond to the shape of the related buckling modes of the model #3, and the size was chosen to reach the maximum amplitude defined by the Eurocode.

Model #1

The buckling shapes of the first model (the 7 DOF beam model) can be seen in Figure 4–5.

Model #3

Figure 6–8. illustrate the buckling shapes of the model #3 (the locally constrained shell model).T

he out-of-plane buckling shapes differ significantly from model #1. It is difficult to choose which shape should be compare to a beam model because each member has different shapes where the out-of-plane

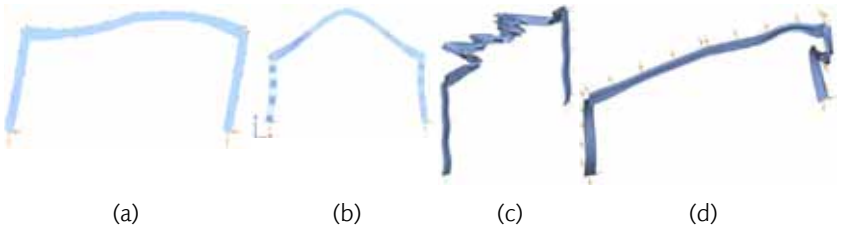

Figure 4 — (a) In plane B1, B2, (b) In plane C1, C2, (c) Out of plane C1, C2, (d) Lateral-torsional buckling C1, C2, B1, B2

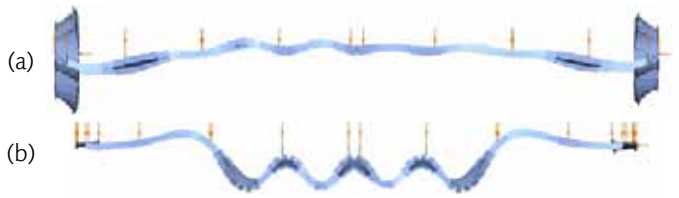

Figure 5 — (a) Out-of-plane B1, (b) Out-of-plane B2

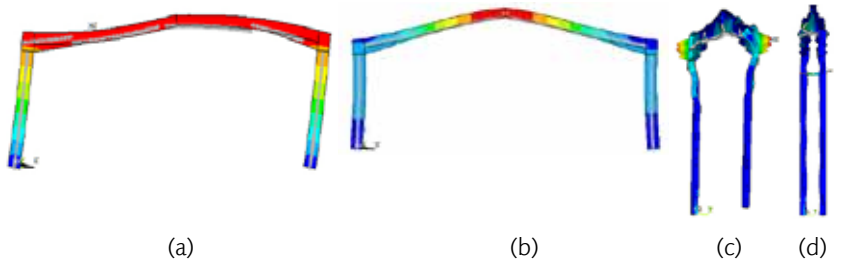

Figure 6 — a) In plane B1, B2, b) In plane C1, C2

deformation is the maximum. This can be a usual problem for practicing engineers as well if they use shell model. The critical load factors are compared between the two models, and later the utilization of the members as well to see the effect on design resistances.

Results of the linear instability analysis

The results of the critical load factors were summarized in Table 2. The values of in plane buckling were similar. The other types of buckling gave different results. The biggest difference was 129.97%. In case of out-of-plane buckling the shell model resulted higher values by each member than the 7 DOF beam model and were inversely in the case of lateral-torsional buckling. The results at the lateral-torsional buckling are the double by the beam model, because the internal nodes of the frame corner are stiffer in that case. The out-ofplane-buckling gave also big differences because these shapes were not clear modes and difference explained above.

Nonlinear analysis

Simulation

The Eurocode standards [3] allow perform calculation with advanced finite element analysis. The effect of non-perfect geometry is considered by the "equivalent geometry imperfection". The shape and the magnitude of these can be applied according to EC. In this case the assumed shapes of imperfections were derived from the elastic buckling mode of the whole frame and the members.

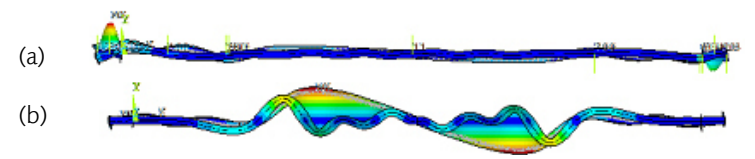

Figure 7 — (a) Out-of-plane B1, (b) Out-of-plane B2

Figure 8 — (a) Lateral-torsional buckling B, (b) Lateral-torsional buckling C

	In plane: B1, B2	In plane: C1, C2	Out-of-plane: B1	Out-of-plane: B2	Out-of-plane: C1	Out-of-plane: C2	Lateral-torsional buckling: B1, B2	Lateral-torsional buckling: C1, C2
Model #1	35.32	166.52	57.26	52.66	82.93	82.93	12.51	12.51
Model #3	38.07	164.11	109.55	92.11	177.06	190.71	5.68	7.55
Diff. [%]	7.79	1.47	91.32	74.91	113.51	129.97	120.25	65.70

Table 2 — Critical load factors

The result of this analysis is a force-displacement diagram, which shows the resistance of the frame. The material model was a bi-linear material model with nominal material yield stress 235 N/mm². The double of the design load was applied to the FE model for the simulation.The largest load step was the 1/10 of the design load; the minimum load step was 1/100 of the design load. If the analysis cannot find solution of the GMNI analysis by the smallest load step, the calculations stopped.

Results of the nonlinear analysis

The failure is shown in Fig. 9. This result came from the last converged load step. The red areas mean that the stress of the plate reaches the nominal yield point.

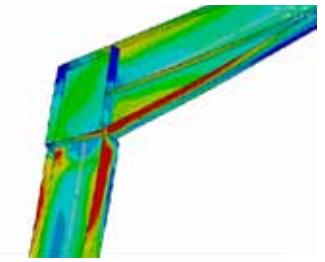

Figure 9 — Result of the simulation (detail: frame corner)

Evaluation of design resistance

The following calculations were compared:

- general method with model #1
- general method with model #3
- method of the reduction factors with model #1
- method of the reduction factors with model #3
- method of the reduction factors with manual calculation

Table 3–6 show that the discrepancies of reduction factors between the two finite element models are not so big as the discrepancies of the critical load factors. The maximum difference is between ±10 %.

	Model #1	Model #3	Manual	General method: Model #1	General method: Model #3
χ_y	0.947	0.947	0.998	–	–
χ_z	0.849	0.932	0.943	–	–
χ_{LT}	1.000	0.934	0.925	–	–
Utilization	0.586	0.618	0.620	0.633	0.638
%	94.8	100.0	100.3	102.4	103.2

Table 3 — C1 column

	Model #1	Model #3	Manual	General method: Model #1	General method: Model #3
χ_y	0.949	0.948	0.998	–	–
χ_z	0.852	0.940	0.943	–	–
χ_{LT}	0.929	0.818	0.816	–	–
Utilization	0.395	0.434	0.433	0.416	0.481
%	91.0	100.0	99.8	95.9	110.8

Table 4 — C2 column

	Model #1	Model #3	Manual	General method: Model #1	General method: Model #3
χ_y	0.669	0.690	0.699	–	–
χ_z	0.726	0.841	0.849	–	–
χ_{LT}	0.974	0.806	0.834	–	–
Utilization	0.463	0.547	0.529	0.477	0.574
%	84.6	100.0	96.7	87.2	104.9

Table 5 — B1 beam

	Model #1	Model #3	Manual	General method: Model #1	General method: Model #3
χ_y	0.584	0.608	0.843	–	–
χ_z	0.640	0.766	0.847	–	–
χ_{LT}	1.000	0.859	0.796	–	–
Utilization	0.538	0.626	0.639	0.561	0.617
%	85.9	100.0	102.1	89.6	98.6

Table 6 — B2 beam

The simulation provides a force-displacement diagram (Fig. 10). The displacement is the deflection of middle node of the beam. The end of the curve shows the resistance of the frame. The horizontal line in the diagram is the 100% resistance according to the manual calculation. The partial factors of model uncertainty and scatter of loading and resistance are chosen to 1.0 [1]. The result of the simulation shows that it satisfies the requirements of EC. The resistance is 3% higher than the load level correspond to 100% utilization.

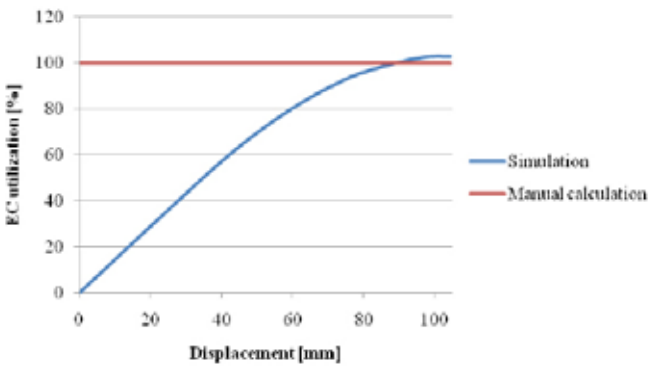

Figure 10 — Force-displacement diagram

Summary and conclusion

As it can be seen in Chapter 6 the magnitude of utilization is almost the same in model #3 and in the manual calculation. The values of model #1 are smaller in each case if only the method of the reduction factors is considered. We cannot declare that general method gives higher utilization value.

The non-linear analysis gave similar result to the manual calculation. As it was shown we can use also the GMNI analysis to design a frame but there were some uncertainties first of all at the out-of-plane buckling shapes. The linear instability analysis did not give clear shapes therefore the giving of the imperfections was also uncertain. The resistance is sensitive to the imperfection amplitudes. It was difficult to find the suitable imperfection shapes, because a small difference can create bigger discrepancy.

References

[1] *Joó, A, Dunai, L (2011). EUROSTEEL 2011 6th European Conference on Steel and Composite Structures (Volume C): Finite element simulation based design of steel frames*

[2] *EN 1993-1-1 (2005); Eurocode 3: Design of steel structures — Part 1–1: General rules and rules for buildings*

[3] *EN 1993-1-5 (2005); Eurocode 3: Design of steel structures — Part 1–5: Plated structural elements*

[4] *EN 1993-1-6 (2005); Eurocode 3: Design of steel structures — Part 1–6: Strength and stability of shell structures*

[5] *EN 1990 (2000): Basis of structural design*

[6] *ANSYS Finite Element Program; Documentation, Ansys Inc. (2003)*

[7] *ConSteel Finite Element Program; Documentation, (2012)*

Assessment of structure-tuned mass damper assemblies in an earthquake environment

TRIBUTSCH, Alexander
University of Innsbruck, Unit of Applied Mechanics, Austria

ADAM, Christoph
University of Innsbruck, Unit of Applied Mechanics, Austria

Abstract

In this paper the seismic performance of tuned mass dampers (TMDs) attached to multi-degree-of-freedom (MDOF) structures is assessed. In previous publications of the authors a wide range of single-degree-of-freedom (SDOF) systems was investigated, in particular focussing on the effect of detuned TMD-parameters. Design relations were derived to provide the engineering practice with response reduction coefficients for structures equipped with TMDs compared to structures without these devices.

Here, the consistency of these design equations is evaluated when applied to generic MDOF structures, represented by generic shear frames. If the effective TMD-structure mass ratio is kept constant, the seismic response of MDOF systems, which are dominated by the first vibration mode, and the TMD performance is almost independent from the position of the TMD. Nevertheless, a non-optimal attachment position results in an increase of the actual TMD mass. Additional results show that the application of a further TMD tuned to the second structural natural frequency hardly improves or even impairs the overall seismic response.

Finally, the paper presents a practical application of recently proposed "modified" response spectrum method considering the effect of a TMD on the seismic response. Planar frame structures with a varying number of stories, and both uniformly and non-uniformly distributed stiffness are considered. Estimated values provided by the proposed methodology are in good agreement with exact outcomes. It can be concluded that this methodology yields in an early design phase reasonable estimates of both the TMD space requirements and structural response quantities without performing costly time history analyses.

Introduction

Recent developments in material science, construction methods, and numerical simulations allow for the construction of tall and/or slender structures, which consequently may be prone to structural vibrations. Application of tuned mass dampers (TMDs) is one of the measures to reduce these structural vibrations. In the last decades various optimization strategies for optimal applications of TMDs have been proposed (see e.g. [1], [2], [3]). The positive effect of TMDs to mitigate periodic small-band induced vibrations (such as wind) is generally accepted, however still controversially discussed for seismic induced vibrations. Nevertheless, when located in an earthquake environment the seismic performance of a TMD (e.g. designed to protect the structure against wind) must be assessed, although mitigation of earthquake induced vibrations is not the primary objective of this TMD. This may result in larger space requirements or measures to limit the maximum TMD stroke.

Until recently, the seismic performance of TMDs could not be assessed reliably without performing computationally expensive time history analyses. The authors addressed the effect of TMDs on earthquake excited single-degree-of freedom (SDOF) structures in previous studies [4], [5]. Based on recorded ground motion sets, numerous time history analyses, statistical response evaluation, and subsequent multi-regression analyses analytical reduction coefficients have been derived to quantify the effect of a TMD. These coefficients allow for the estimation of important key parameters in an early design phase, such as the peak displacement reduction of the main structure and the TMD stroke (relative peak displacement of the TMD with respect to the attachment location of the main structure). Furthermore, an efficient methodology for the practical engineer is proposed to assess the seismic response reduction and TMD stroke of regular planar multi-degree-of-freedom (MDOF) high-rise structures [6].

Seismic response coefficients

Fundamentals

Response coefficients are appropriate to quantify the benefits of a TMD [7]. They are defined as the ratio of a response quantity from a structure with attached TMD to the corresponding quantity of the same structure without TMD. To account for the record-to-record variability the assessment is not based on the outcomes induced by single earthquake events, but on statistical response quantities such as quantiles and median values considering the ground motions of a complete set. The peak displacement reduction of the main structure is expressed by the coefficient.

$$P^{(i)} = \frac{\max \left| x^{(i)} \right|_{with\ TMD}}{max \left| x^{(i)} \right|_{without\ TMD}} \quad (1)$$

In Eq. (1) $x^{(i)}$ is the characteristic displacement of the considered structure with respect to the base (with and without TMD) subjected to a single earthquake record denoted by i. Corresponding statistical quantities are denoted as $P^{(med)}$, $P^{(16Q)}$ and $P^{(84Q)}$.

The limited deflection (stroke) of a mechanical TMD is considered by the response coefficient

$$D^{(i)} = \frac{max \left| x^{(TMD,i)} - x^{(i)} \right|_{with\ TMD}}{max \left| x^{(i)} \right|_{without\ TMD}} \tag{2}$$

which is defined as the maximum relative displacement of the TMD with respect to the attachment location, scaled by the maximum characteristic displacement of the stand-alone SDOF system. $D^{(med)}$, $D^{(16Q)}$ and $D^{(84Q)}$ are the corresponding statistical response quantities.

Seismic response coefficients for SDOF structures with attached TMD have been derived in previous studies of the authors [4], [5]. Three sets of real recorded ground motions from FEMA P-695 ("ATC63 project") [7] and [9] were utilized as seismic input. The first set, denoted as ATC63-FF set, contains 44 far-field records with a fault to rupture distance larger than 10 km, while the second set (ATC63-NFwP set) includes 28 near-field records with a strong pulse characteristic. All earthquake events show magnitudes ≥ 6.5 and have been recorded on NEHRP Site Class B (rock), C (soft rock/very dense soil), or D (stiff soil). A third set, denoted as LMSR-N, comprises 40 far-field records of moment magnitude between 6.5 and 7 and closest distance to the fault rupture between 13 km and 40 km on NEHRP site class D.

Analytically derived optimal TMD parameters for stationary white noise base excitation [2] are sufficiently accurate to provide the optimal performance of TMDs subjected to earthquake induced vibrations, as shown in [4], [5]. Accordingly, the optimal natural frequency ratio $\beta(= \omega_{TMD}/\omega_S)$ and the optimal viscous damping coefficient ζ_{TMD} of the TMD is [2]:

$$\beta_{opt} = \frac{\sqrt{1 - \mu/2}}{1 + \mu}, \quad \zeta_{TMD,opt} = \sqrt{\frac{\mu\,(1 - \mu/4)}{4\,(1 + \mu)\,(1 - \mu/2)}} \tag{3}$$

Here, $\mu(= m_{TMD}/m_S)$ denotes the mass ratio between TMD mass m_{TMD} and structural mass m_S. ω_S and ω_{TMD} is the natural circular frequency of the stand-alone SDOF structure and of the stand-alone TMD, respectively.

Exemplarily, in Figure 1 the median peak displacement reduction coefficient $P^{(med)}$ and the median TMD stroke coefficient $D^{(med)}$ are depicted for structural periods T_S between 0.05 s to 5.0 s, and mass ratios μ between 0.02 to 0.08.

To provide the evaluated results for the engineer in practice, analytical expressions of seismic response (reduction) coefficients were derived by multivariate regression analyses. They are listed in [10]. These analytical expressions are valid for optimally tuned TMD parameters, but also detuning is considered [5]. The range of admissible structural parameters, which enter the analytical expressions, is listed in Table 1.

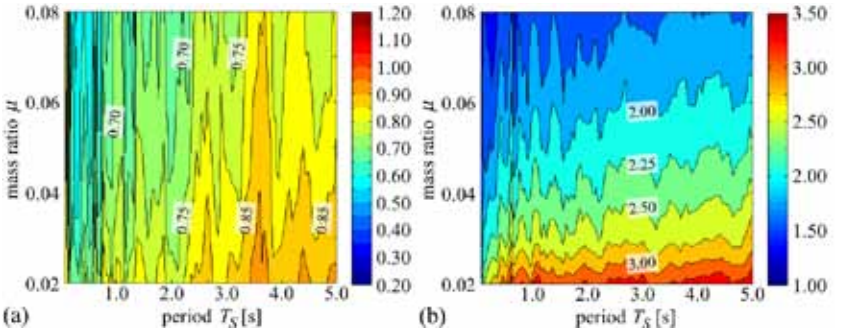

Figure 1 — (a) Median reduction coefficient $P^{(med)}$: structural peak displacement. (b) Median response coefficient $D^{(med)}$: TMD stroke. Optimal TMD parameters, structural damping $\zeta_S = 0.005$, ATC63-FF earthquake set.

Assessment of multi-degree-of-freedom structures

Considered structural models

A shear frame model is utilized for the investigation of multi-degree-of-freedom (MDOF) structures, as depicted in Figure 2. Mass and stiffness is distributed uniformly along the building height. Stiffness coefficient k_j^n denotes the stiffness in the j^{th} floor of a building with a number of n storeys. Here, stiffness coefficient is independent from the floor and tuned to fit a given first period of the main structure. Damping coefficients c_j^n are determined by the assumption of Rayleigh damping based on a selected damping ratio for the first and second structural mode.

Effective mass ratio

For the j^{th} mode of the n-story stand-alone structure, the modal mass ratio μ_j is defined [11] as:

Parameter	Variable	Min.	Max.
Period of the stand-alone SDOF structure	T_S	0.20s	5.00s
Mass ratio	$\mu(=m_{TMD}/m_S)$	0.005	0.08
Natural frequency ratio	$\beta(=\omega_{TMD}/\omega_S)$	0.86	1.04
Damping coeff. of the decoupled TMD	ζ_{TMD}	0.04	0.24
Damping coeff. of stand-alone structure	ζ_S	0.005	0.05
Ground motion sets	ATC63-FF, ATC63-NFwP, LMSR-N		

Table 1 — Range of structural parameters for analytical response coefficients

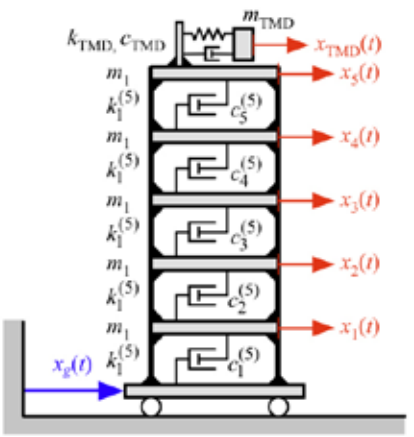

Figure 2 — MDOF shear frame structure with attached TMD at the roof.

$$\mu_j = \frac{\varphi_{jr}^2 \, m_{TMD}}{\varphi_j^T \, M \, \varphi_j}, \quad j = 1, \ldots, n \tag{4}$$

Here, M is the diagonal mass matrix (size n x n), and φ_j denotes the j^{th} mode shape of the structure without TMD. φ_{jr} is the r^{th} element (denoting the rth storey, where the TMD is attached) of φ_j.

According to Eq. (4) for a given TMD mass mass ratio μ_j increases with increasing φ_{jr}. In other words, in order to keep the fundamental mass ratio μ_1 constant, the TMD mass m_{TMD} must to be increased when the TMD is not located at its optimal position on top of the building. This effect is shown in Figure 3, where the seismic response (ATC-63FF record #1) of a five-storey building with inherent damping of 0.5% and a structural period of 1.0 s is plotted. It can be seen that the structural response of the third and the fifth floor is considerably reduced by the TMD, compare the red and blue dotted lines (stand-alone frame) with red and blue solid lines (coupled frame-TMD configuration). Note that in this example the TMD parameters are tuned optimally to the fundamental structural mode. Furthermore, it is readily observed that the structural response of structure-TMD assemblies with constant fundamental TMD mass ratios of 5%, but different TMD positions is almost identical, compare the solid lines (TMD at the 5th floor) and the dashed lines (TMD at the 3rd floor). The actual TMD mass is about 71% larger for the TMD attached to floor 3, compared to the mass of the TMD attached to floor 5. However, the response of the TMD itself is different. A TMD with a larger mass at a lower floor level results in a smaller TMD stroke.

The effect of an additional TMD tuned to the second mode is studied for medium height buildings (5 to 15 storeys). From the outcomes it can be concluded that their effect on the structural response is almost negligible. Exemplarily, Figure 4 shows a comparison of the structural response of configurations with one respectively two TMDs, attached

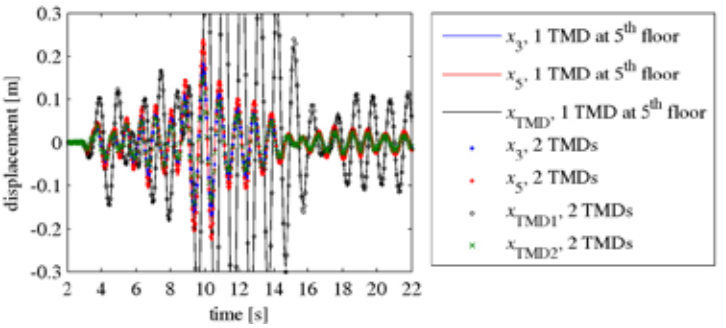

Figure 4 — Structural response. Frame equipped with one TMD tuned to the first mode versus frame equipped with two TMDs tuned to the first and second mode, respectively. Optimal TMD positions.

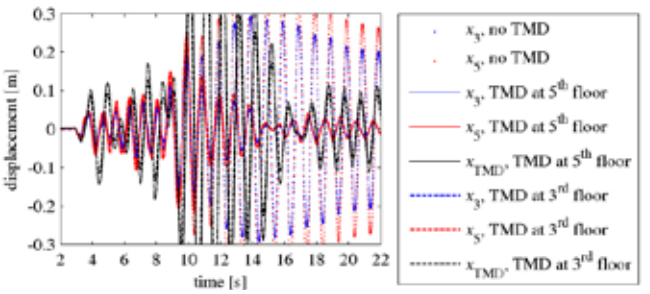

Figure 3 — Structural response without and with TMD attached at different storeys

to a five-story frame as described above. For all TMDs the mass ratio is 5%. The structural response is almost unaffected by the second TMD, compare e.g. the red solid line and with red dotted line. The optimal attachment location for the second mode TMD is at the second floor. These findings presented for a single earthquake were evaluated and confirmed to hold true also in a statistical sense based on the responses to complete sets of earthquake records.

Simplified assessment of multi-degree-of-freedom structures

Field of application

The proposed simplified assessment method applies to structures, whose seismic response is dominated by the fundamental mode. Consequently, the MDOF structure can be transformed into an equivalent SDOF system [12] without involving large errors by neglecting higher mode effects. For the equivalent SDOF system the response spectrum method [12] can be utilized to obtain the estimated seismic peak response.

Modified response spectrum methodology

A simple and time-saving procedure for estimating the performance and benefits of a TMD is proposed in [6]. It is based on the equivalent SDOF system approach, the derived analytical expressions for response coefficients (capturing the effect of a TMD), and displacement response spectra. Thereby, the engineer in practice obtains expected maximum seismic displacements, the TMD induced reduction of these displacements, and the TMD stroke (relative displacement of the TMD with respect to the attachment location) without time-consuming analyses appropriate for an early design phase.

The general approach is presented in [6] and can be summarized as follows:

- Transform the considered stand-alone MDOF structure into its equivalent SDOF system, and determine its period, damping coefficient, and modal participation coefficient.
- The maximum displacement of the equivalent SDOF system without TMD can be read from a displacement response spectrum (e.g. from design codes).
- Select the TMD mass and determine the modal mass ratio and optimum TMD parameters according to Eqs (4) and (3).
- Apply the derived analytical relations for the response coefficients to obtain the expected maximum structural displacement and stroke based on the equivalent SDOF system equipped with a TMD. Median values, as well as 16% and 84% quantiles can be determined.
- The maximum structural and relative TMD displacements of the MDOF structure are back-calculated from these outcomes.

Validation

The proposed methodology is based on several assumptions and simplifications, each of them leading to a deviation from the "exact" outcome:

1. Higher mode effects are not captured by the equivalent SDOF system.
2. The response spectrum method itself is a simplified approach for estimating maximum displacements of SDOF systems.
3. Analytical (smooth) response coefficients are an approximation of the actual coefficients.

Separating errors by these simplifications is a challenging task, and therefore, the results of the methodology are evaluated in a global approach.

10-storey shear frame structures with fundamental periods varying from 0.5 s to 5.0 s, fundamental modal mass ratios of 2%, 4%, and 5%, inherent damping of 0.5%, subjected to the 44 records of the ATC63-FF set, are subsequently utilized to assess the outcomes of the proposed methodology. For each earthquake record the corresponding response spectrum is calculated in advance. In Figure 5 maximum roof displacements ($i = 1,\ldots,44$) from time history analyses are plotted against the corresponding quantity based on the proposed simplified method. Red circles identify outcomes for stand-alone structures without TMD, while blue dots represent results for frames with attached TMD. Three distinct mass ratios are considered, thus, each red circle is connected (by green lines) to three blue dots.

An offset of the red circles from the diagonal dashed line results from the equivalent SDOF system approach. A green line pointing directly to the coordinate origin indicates a perfect approximation of the seismic response coefficient. For the utilized shear frame model in most of the considered cases the equivalent SDOF system with an assumed

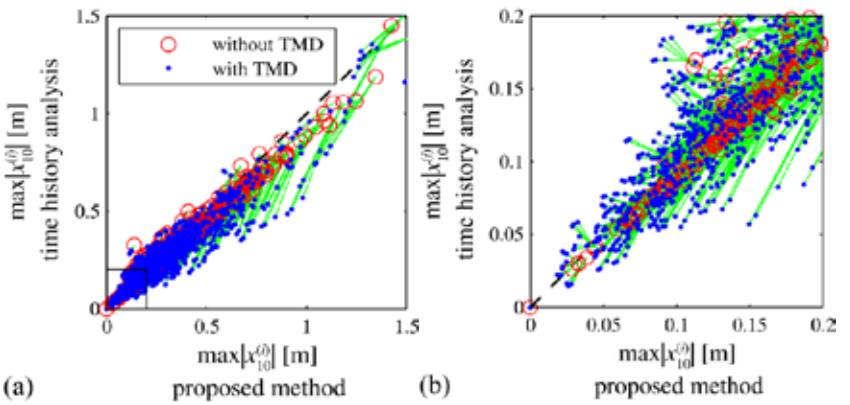

Figure 5 — Comparison of approximate and time history analysis results; individual outcomes of the peak displacement at top floor level for a 10-storey structure. (a) Full range. (b) Zoomed view.

linear first mode shape overestimates the structural peak displacement. For a small number of configurations the TMD even impairs the structural response, i.e. the green lines exhibit a negative slope. However, in a statistical sense the proposed approach provides appropriate response predictions.

Conclusions

After introducing seismic response coefficients the impact of a non-optimal TMD location in an MDOF structure was studied. A constant effective mass ratio requires a larger actual mass to provide the same efficiency.

A time-saving and easy-to-apply methodology for the engineer in practice was described to assess in an early design phase the seismic TMD performance for high-rise structures. It is based on the equivalent SDOF model of the structure, a displacement response spectrum, and analytical seismic response coefficients capturing the effect of a TMD. A global validation of the proposed approach shows that the results are in good agreement with the "exact" outcomes. The methodology provides absolute values of structural peak displacements and their reduction by a TMD. Moreover, the maximum relative TMD displacement is estimated to decide on space requirements or mechanical measures to limit the TMD stroke.

References

[1] *Den Hartog, J. P. (1956). Mechanical Vibrations. McGraw-Hill, New York.*

[2] *Warburton, G.B. (1982). Optimum absorber parameters for various combinations of response and excitation parameters. Earthquake Engineering and Structural Dynamics, 10 (3), 381–401.*

[3] *Hoang, N., Fujino, Y., Warnitchai, P. (2008). Optimal tuned mass damper for seismic application and practical design formulas. Engineering Structures, 30 (3), 707–715.*

[4] *Tributsch, A., Adam, C., Furtmüller, T. (2011). Mitigation of earthquake induced vibrations by Tuned Mass Dampers. Proceedings of EURODYN Conference, Leuven/Belgium.*

[5] *Tributsch, A., Adam, C. (2012). Evaluation and analytical approximation of Tuned Mass Damper performance in an earthquake environment. Smart Structures and Systems, accepted for publication.*

[6] *Tributsch, A., Adam, C. (2012). Simplified assessment of structure — Tuned Mass Damper assemblies under earthquakes. Proc. 5th European Conference on Structural Control (EACS 2012), Genoa/Italy.*

[7] Sadek, F., Mohraz, B., Taylor, A. W., Chung, R. M. (1997). A Method of Estimating the Parameters of Tuned Mass Dampers for Seismic Applications. Earthquake Engineering and Structural Dynamics, 26 (6), 617–635.

[8] *FEMA P-695 (2009). Quantification of Building Seismic Performance Factors. Federal Emergency Management Agency, Washington D.C.*

[9] *Medina, R.A., Krawinkler, H. (2003). Seismic demands for nondeteriorating frame structures and their dependence on ground motions. Report no. 144, The John A. Blume Earthquake Engineering Center, Stanford University.*

[10] *Tributsch, A., Adam, C. (2011). Application of Tuned Mass Dampers in an earthquake environment. Internal report, University of Innsbruck.*

[11] *Hochrainer, M. (2001). Control of vibrations of civil engineering structures with special emphasis on tall buildings. PhD thesis, Vienna University of Technology.*

[12] *Chopra, A. (2007). Dynamics of structures: theory and application to earthquake engineering. Third edition. Pearson Prentice Hall, New York.*

Performance-based evaluation of seismic demands for moment resisting steel frames using N2-method

TSONEV, Aleksandar
UACEG, Bulgaria

BONEV, Todor
UACEG, Bulgaria

KOLEVA, Tatyana
UACEG, Bulgaria

Abstract

Performance-based design approach is currently recommended in the modern seismic design and its regulations and provisions. The biggest advantages of N2 method in comparison to capacity spectrum method are summarized mainly in two items — there is no need to identify the elastic response and to define elastic-perfectly plastic capacity spectrum curve. Also, there is a good opportunity to control the solution through displacement ductility ratio.

Transformation of the original multi-degree of freedom system into equivalent single degree of freedom system is carried out on the basis of plastic mechanism reached in the process of loading. Performance point is found as intersection point considering two curves — capacity curve, being associated to inelastic response of the structure subjected to monotonically increasing lateral load and design spectrum curve, defined through design spectra provisions of Eurocode 8.

As a result on output inelastic displacement demand, internal force demand and interstorey drift demand are obtained and graphically presented and discussed.

Introduction to nonlinear methods

Nonlinear methods are usually used to estimate the structural capacity of buildings, designed on the basis of linear methods. Results of nonlinear analysis give us useful information, such as:

- Maximum reactions, which can be taken by specially designed structures.
- Maximum deformation of elements, which dissipate energy by inelastic behavior.

– The influence of the decreased resistance of some elements over the whole structural behavior.
– Plastic hinges formation and their location.
– Actual displacement between adjacent storeys and P-Δ effects.
– The most appropriate way for leading the load forces to the structure foundations.

Main methods in modern seismic design are dynamic nonlinear analysis and static nonlinear analysis. The first one is more precise but also difficult and time consuming. Therefore it is used for special studies. Some of static nonlinear methods are capacity spectrum method and N2 method.

N2 method

In recent years, simplified non-linear methods based on pushover analysis, equivalent single degree of freedom (SDOF) system and response spectrum approach have been implemented in guidelines, standards and codes for seismic resistant design of new buildings and evaluation of existing buildings. The methods have been developed for fixed base structures. One of simplified non-linear methods is the N2 method, which is based on extensive studies of inelastic response building structures performed by the Prof. P. Fajfar and his research team at the University of Ljubljana.

The method combines pushover analysis of a multi degree of freedom (MDOF) model with the response spectrum analysis of an equivalent SDOF model. Two main assumptions of the method are: the response of a structure is governed by one mode and this fundamental mode does not change significantly when the structure is subjected to different seismic intensities.

Pushover analysis is a nonlinear analysis carried out under conditions of constant gravity loads and monotonically increasing horizontal loads. It may be applied to verify the structural performance of newly designed and the existing buildings for the following purposes:

– To verify the overstrength ratio values.
– To estimate the expected plastic mechanism and the distribution of damage.
– To assess the structural performance of existing or retrofitted buildings.
– As an alternative to the design based on linear analysis which uses the behavior factor q.

In that case the target displacement should be used as the basis for the design.

Performance-based evaluation of seismic demands for moment resisting steel frames using N2-method

Structure modelling

The purpose of this paper is to examine the seismic response of a 3D steel frame structure in transverse direction. In this direction seismic loading is taken almost entirely by the steel frames. The whole construction fulfills the requirements of Eurocode 8, part 1, point 4.2.3 criteria for structural regularity. Therefore a planar model is used. It represents one typical steel frame.

Material definition

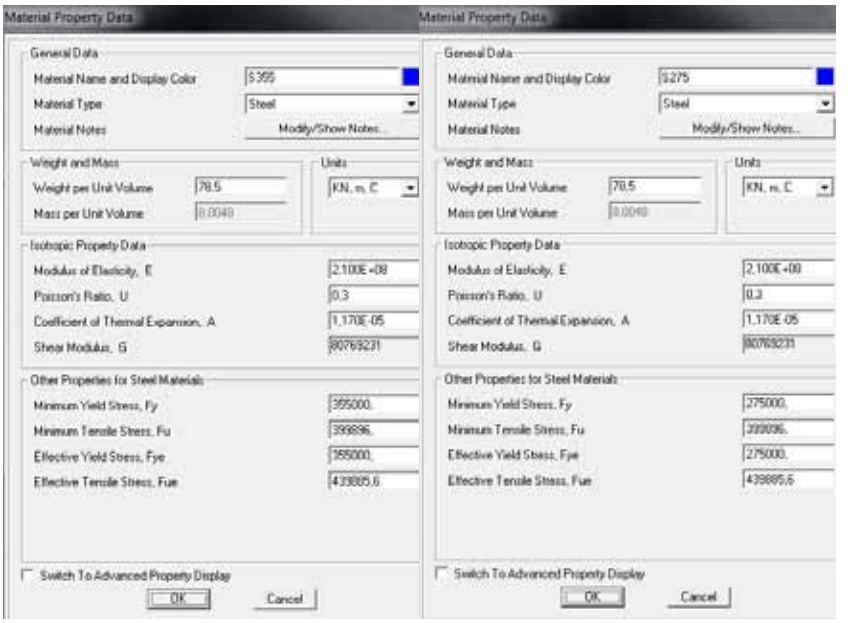

Figure 1 — Material definition for columns and beams

Transversal sections definition

Figure 2 — Column and beam section definition

Geometry definition and frame supports

Two spans l_1 = 7.2 m and between them one span l_2 = 6.0 m; floor heights $h_1 = h_2$ = 3.9 m; in transverse direction the frames are situated in intervals of b = 6 m; support conditions — moment resisting columns.

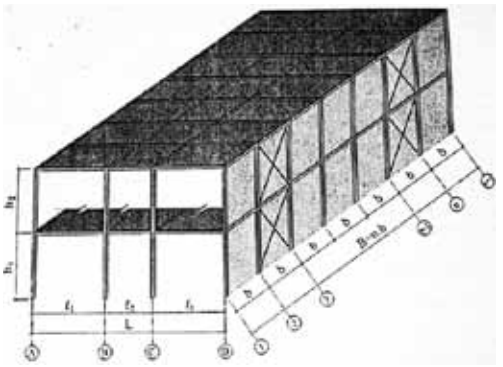

Figure 3 — Beam section definition

Seismic action parameters

γ_I = 1.0 — importance factor

a_{gR} = 0.25 — reference peak ground acceleration for Sofia, Bulgaria according to map of seismic districts of Bulgaria

soil conditions — soil type "C";

behavior factor q = 3.0 which transforms elastic acceleration spectrum into design spectrum

Defining and entering the loads in the design model

Loads in constructions are categorized in 2 groups: permanent and temporary. Temporary loads are 4 types — long term, short term, special and seismic. According to the way they change in time — dynamic and static. In this example every load is defined in its own load case with base normative values. To calculate their design values load coefficients γ_G и γ_Q are used.

Defining vertical static loads

- Self weight (DEAD) — includes main frame construction self weight
- Permanent weight (G) — includes weight of floor and roof construction, surroundings, coverings, isolations and instalations - gk,1, gk,2, gk,3;
- Serviceability loads on the floor construction — vk;
- Short term loads of snow — st.

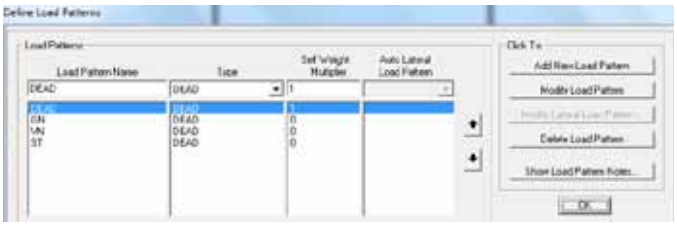

Figure 4 — Static normative load cases definition

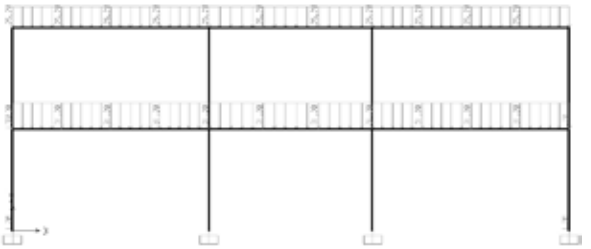

Figure 5 — Applied self-weight loads

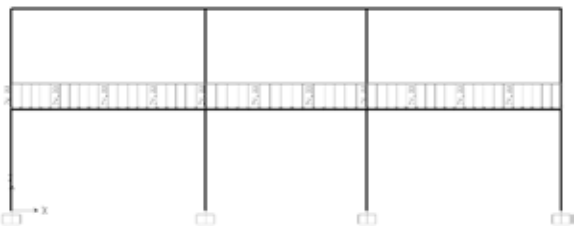

Figure 6 — Applied service-ability loads

Entering static loads in design model

To find linear distributed loads on the frame elements we have to multiply the given area load by the structure center distance.

Mass source definition

Concentrated masses in joints of construction are calculated automatically after defining mass sources. They have influence on dynamic behavior of the system — eigenvalues and forms.

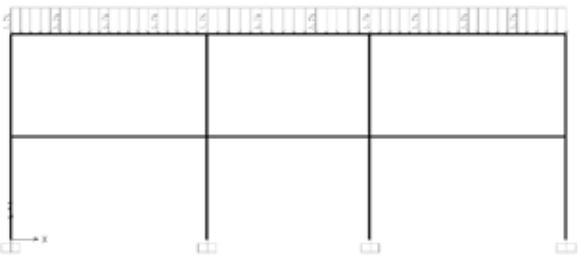

Figure 7 — Applied snow loads

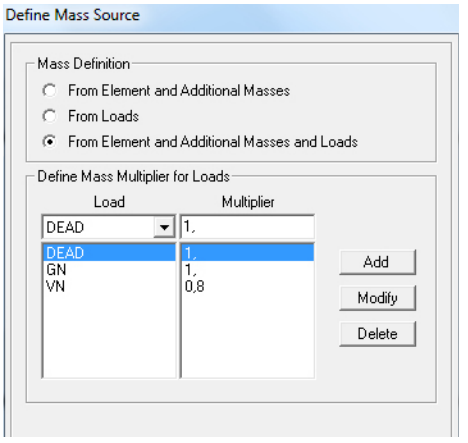

Figure 8 — Mass sources

Analysis case definition

Figure 9 — Analysis cases

Results

Eigenvalues

TABLE: Modal Participating Mass Ratios

Output Case	StepNum	Period	UK	UZ	SumUX	SumUZ
Text	Untiless	Sec	Untiless	Untiless	Untiless	Untiless
MODAL	1	1.726939	0.91604	0	0.91604	0
MODAL	2	0.644128	0.08184	0	0.99788	0
MODAL	3	0.512976	0	0.12615	0.99788	0.12615
MODAL	4	0.482115	0.0008	0	0.99868	0.12615
MODAL	5	0.401951	0	0.18409	0.99868	0.31024
MODAL	6	0.371829	0.00016	4.718E-20	0.99884	0.31024
MODAL	7	0.325506	0	0.23317	0.99884	0.54341
MODAL	8	0.244561	0	0.16149	0.99884	0.70489
MODAL	9	0.178429	0.00112	8.306E-18	0.99995	0.70489
MODAL	10	0.173827	0	0.00279	0.99995	0.70769
MODAL	11	0.135365	0.00003618	0	0.99999	0.70769
MODAL	12	0.131621	0.000005989	0	0.99999	0.70769

Table 1 — Eigenvalues from modal analysis

Definition of plastic hinges

N2 method considers the inelastic work of the material due to seismic loading. It is necessary to be defined specific zones, where material plastification is expected. Moment — curvature dependence should be defined as well.

We assume that plastification zones have size which tends to 0. That is why we use dependence between moment and rotation at specific section. Plastic moment is characteristic of transverse section and it is calculated from geometric parameters of the section.

Masses distribution to frame joints

TABLE: Assembled Joint Masses

Joint	U1	U2	U3	Height
Text	KN-s2/m	KN-s2/m	KN-s2/m	m
1	0.38	0.38	0.38	0
2	5.44	5.44	5.44	3.9
3	2.75	2.75	2.75	7.8
4	0.14	0.14	0.14	0
5	10.17	10.17	10.17	3.9
6	5.14	5.14	5.14	7.8
7	0.14	0.14	0.14	0
8	10.17	10.17	10.17	3.9
9	5.44	5.44	5.44	7.8
10	0.38	0.38	0.38	0
11	5.44	5.44	5.44	3.9
12	2.75	2.75	2.75	7.8
13	9.36	9.36	9.36	3.9
14	9.36	9.36	9.36	3.9
15	9.36	9.36	9.36	3.9
16	9.36	9.36	9.36	3.9
17	9.36	9.36	9.36	3.9
18	9.36	9.36	9.36	3.9
19	4.74	4.74	4.74	7.8
20	4.74	4.74	4.74	7.8
21	4.74	4.74	4.74	7.8
22	4.74	4.74	4.74	7.8
23	4.74	4.74	4.74	7.8
24	4.74	4.74	4.74	7.8
25	10.4	10.4	10.4	3.9
26	10.4	10.4	10.4	3.9
27	5.26	5.26	5.26	7.8
28	5.26	5.26	5.26	7.8

Table 2 — Assembled joint masses

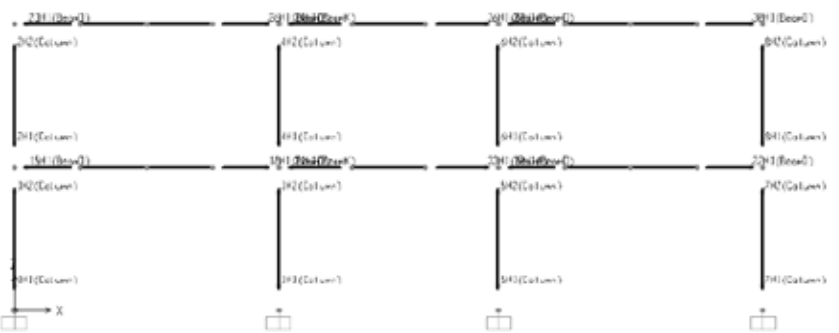

Figure 10 — Location of possible places for plastic hinges in columns and beams

Placement of plastic hinges

Plastic hinges are formed where lateral moment gets highest values. It's accepted that hinges will come near joints.

Loads for horizontal static nonlinear analysis (pushover)

We use obtained distribution of masses (equation (7), (8)) to define proportion of horizontal forces. We accept triangle distribution (Fig. 11) and force on second storey will have value of 1. The forces are proportional to the mass on this storey and the storey height. They are located on storey levels. The force on first storey (F1) is calculated with equation (9). We save these loads in load case named "push".

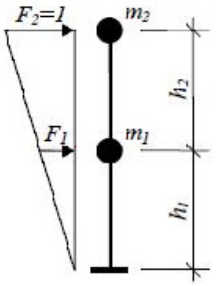

Figure 11 — Distribution of horizontal forces

Setting up pushover analysis

Horizontal monotonically increasing forces are applied after vertical loads (i.e. self-weight, serviceability loads, snow loads). So two steps of loading are used:

- Step 1: vertical loading — nonlinear analysis is used because step 2 can't start from linear analysis (fig.12). The different load types are combined according to Eurocode 1 with appropriate coefficients.
- Step 2: horizontal pushover start after vertical nonlinear analysis (Figure 13)

In step 2 horizontal increasing forces are proportional to F_1, F_2. We define maximum displacement which is monitored.

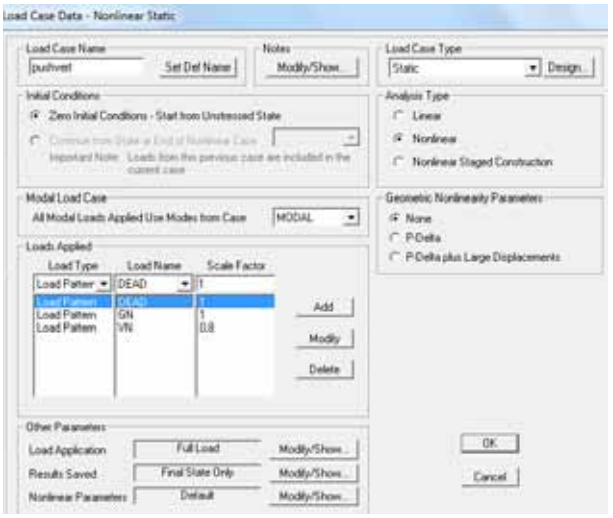

Figure 12 — Setting up step 1

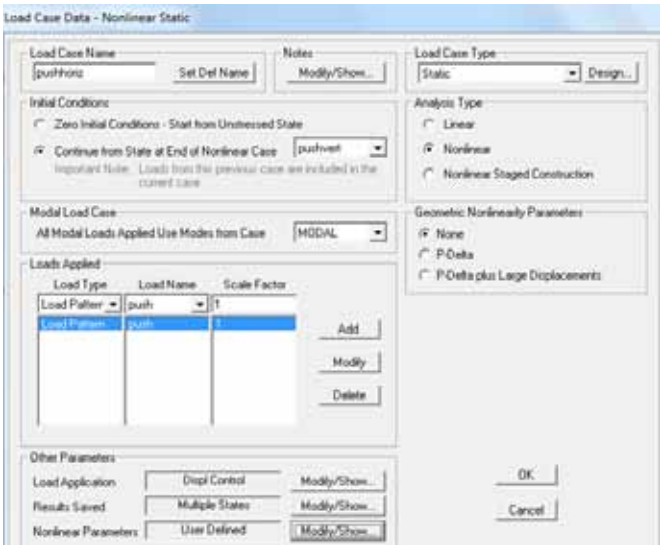

Figure 13 — Setting up step 2

Results of pushover analysis

The analysis finishes after the construction transforms into mechanism (free movement). The steel frame fulfils the requirements of capacity design — weak beams, strong columns. Therefore the choice of column and beam sections is appropriate.

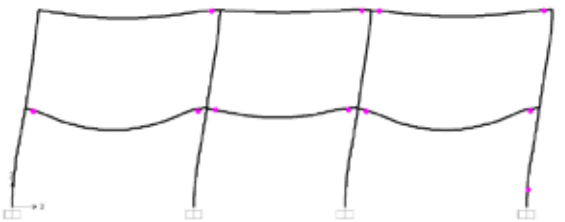

Figure 14 — Hinge plastification

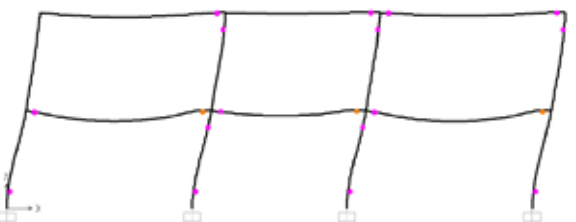

Figure 15 — Plastic hinges destruction (in orange)

Capacity curve-shearing base force Fb – crucial displacement d

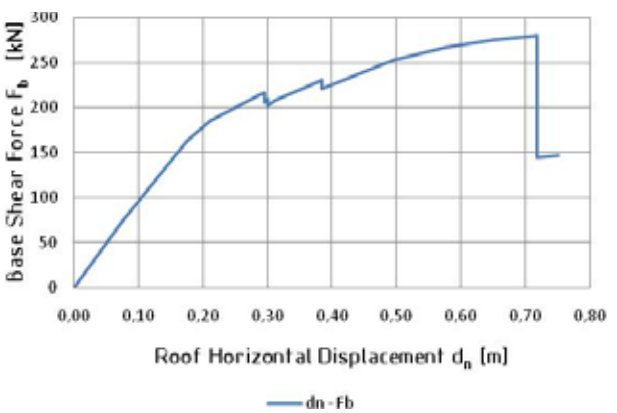

Figure 16 — Capacity curve

Equivalent Single Degree Of Freedom System

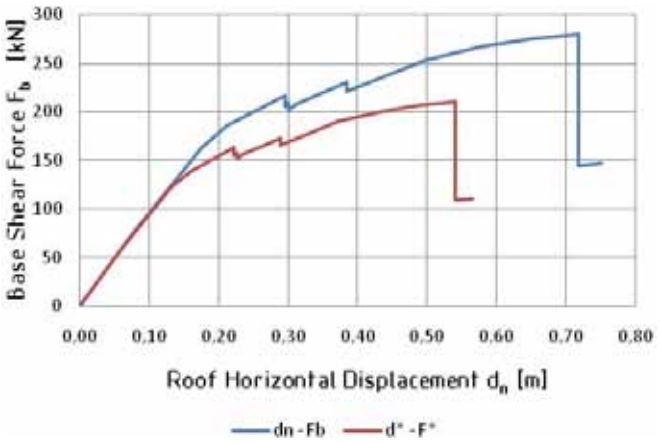

Figure 17 — ESDOFS curve

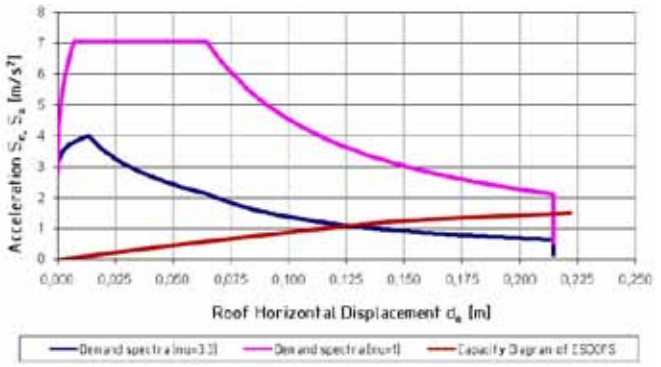

Figure 18 — Test results

Demand Spectra for constant ductility = 2 in AD format normalized to 1.0 g peak ground acceleration. From the test results we conclude — the system works in plastic condition.

References

[1] *проф. д-р инж. Росица Ганчева, (2005) Проектиране стоманобетонни конструкции за сеизмични въздействия*

[2] *CEN (2003) Eurocode 8: Design of Structures for Earthquake Resistance — Part 1: General Rules, Seismic Actions and Rules for Buildings.*

[3] *Peter Fajfar, M. EERI, A Nonlinear Analysis Method for Performance Based Seismic Design, Earthquake Spectra, Vol.16, No.3, pp. 573–592, August 2000*

[4] *проф. д-р инж. Здравко Бонев, гл.ас. д-р инж. Дилян Благов (2012) Ръководство за упражнения по Проектиране на конструкции на сеизмични въздействия*

Post-Earthquake Damage Screening of Steel Buildings using Model-Based Damage Pattern Classification

YAMAGUCHI, Mayako
Department of Architecture and Architectural Engineering, Kyoto University

KURATA, Masahiro
Disaster Prevention Research Institute, Kyoto University

NAKASHIMA, Masayoshi
Disaster Prevention Research Institute, Kyoto University

Introduction

After a large earthquake, the ability to quickly assess the structural integrity of buildings greatly contributes to the safety of building users and the smooth recovery from the disaster. In Japan, professional engineers registered as inspectors visit each building to inspect the damage. This process takes a considerable amount of time. Moreover, damage of structural members covered with architectural finishing is difficult to detect by visual inspection in many cases.

Sensors installed to measure structural responses of buildings can provide objective information on the structural integrity to building owners and decision makers in a quick manner. Such a sensing system, referred to as a structural health monitoring (SHM) system, has been explored by many researchers and practitioners in recent decades. However, SHM systems have yet to be widely implemented in buildings primarily due to initial and management costs from installing and maintaining the sensors.

This paper describes the development of a damage detection system for steel buildings using a damage pattern which enhances information acquired from a limited number of sensors. The developed system is intended to provide accurate and objective information on the damage state of the monitored building with reduced cost and labor in installing a sensing system. In the presented framework, information extracted from collected sensor data and information estimated from an antecedently prepared dataset from the structural analysis of the monitored building are assimilated using a pattern classification algorithm (i.e. decision tree in this paper) to estimate the damage intensity and location from the changes in building dynamic characteristics.

Damage detection system

The specifically designed system to assimilate limited information from acceleration or strain sensors takes the following steps: 1) analyzes the structure to obtain modal properties for a large number of damage patterns, including damage of beams, columns, and/or bases and creates a dataset, 2) constructs the decision tree for damage detection by applying a classification algorithm to the dataset, 3) identifies the properties of the building using sensors before and after the earthquake, and 4) estimates the state of damage by applying the property change rate data to the decision tree. This outlines is shown in Fig. 1.

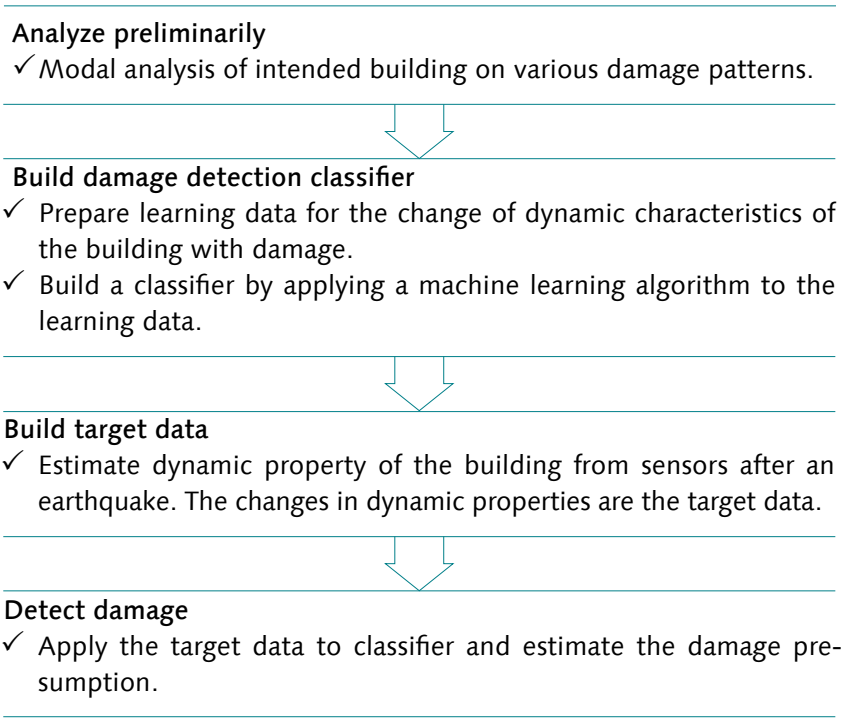

Figure 1 – Damage detection system with pre-analysis and classifier

Application to low-rise steel building

What follows presents the application of the proposed damage detection system. The building used in numerical simulations is a five story steel frame with concrete slabs located on Uji campus of Kyoto University. A damage type considered in the simulation is fracture of the bottom flange of beams near beam-to-column connections. Target data of vibration properties is obtained from system identification, which is applied to the results of time history analysis of the five story model, instead of the results from the sensor on the real structure.

Five story steel frame model

The building was modelled in a general purpose structural analysis program, SAP2000 [1], based on the measured dimensions of the five story steel frame building. Figure 2 shows the overall dimensions of the building. The beams of the building are Japanese rolled

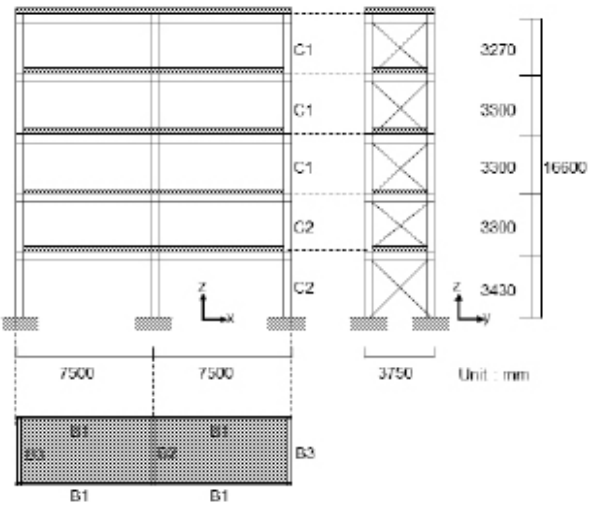

Figure 2 – 5 story steel frame building

H-section, H-500 × 200 × 8 × 11 for B1 and B3 in 1st and 2nd floor, and H-500 × 250 × 9 × 13 for 3rd to roof floor and B2 part of 1st and 2nd floor. The columns of the building are H-400 × 400 × 12 × 19 for 1st and 2nd floor and H-400 × 400 × 9 × 12 for 3rd to roof floor. The transverse direction of the building is braced with L-65 × 65 × 5.5. Steel-reinforced concrete slabs are used to construct floors and ceilings.

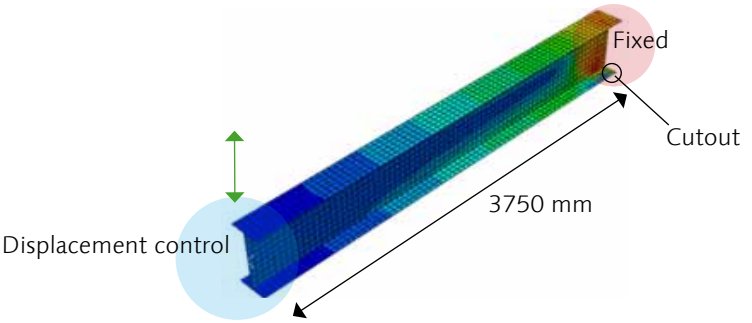

Figure 3 – FEM model of beam

	Initial stiffness falling rate	Bearing force falling rate
Positive bending	24%	41%
Negative bending	23%	39%

Table 1 – Decrease in stiffness of member property with bottom flange fracture

In the numerical simulations the effect of fractures at the end of beams induced by cyclic loading are considered, as this is a major damage mechanism that has been historically observed under strong earthquake ground motions,. For simplicity, the analysis model simulates beam fracture by reducing the cross section of the beam as shown in Fig 3.The length of the reduced section is determined to achieve the amounts of bending stiffness reduction equivalent to what observed in a high-profile beam analysis using the finite element (FE) analysis method. A beam with a fracture near the fixed end is analysed using a general purpose FE program, ABAQUS 6.10 [2]. Considering the center

part of the beam as a point of contraflexure, half of beam is modeled as a cantilever beam whose length is the half span of the structure. A cutout is made near the edge of fixed side. The bending stiffness of the beam is estimated from the pushover curve of the beam obtained by the displacement-control loading in the direction of the strong axis. Table 1 shows the results of FE analysis. When the bottom flange has a cutout of 10 mm, the bending stiffness drops by 24%.

The analysis model accounts for the contribution of the concrete slab on the bending stiffness of the beams by adding a concrete section with an equivalent width calculated following the Design Recommendations for Composite Constructions [3]. The mass of the members is distributed uniformly at each joint. The foundation is assumed to be fixed.

The steel members and concrete are assumed to be elastic with Young's moduli of 2.0×10^5 N/mm² and 2.6×10^4 N/mm² respectively.

Modal analysis for various damage patterns

The modal properties of the building with various damage patterns are obtained by modal analysis with Lanczos method in SAP2000. The parameters in the damage patterns are the number and location of damage. In total, 96 different patterns are analysed. Figure 4 shows the possible locations of damage. For example, Figure 5 and Table 2 show the mode shapes and natural frequencies of the undamaged model in the X-direction.

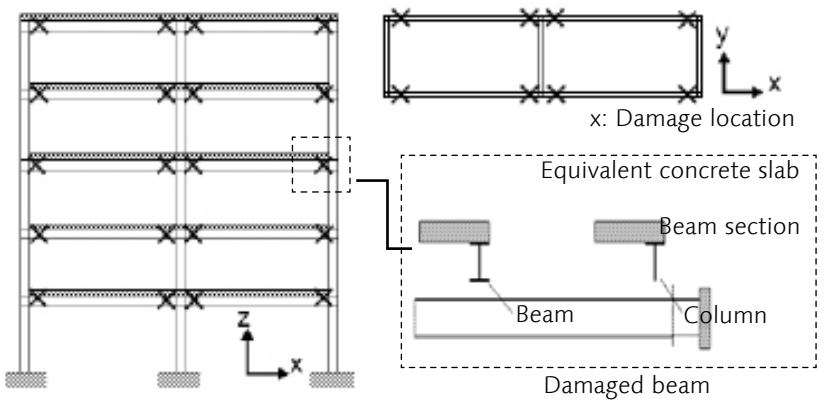

Figure 4 – Building model showing locations of possible damage at beam ends

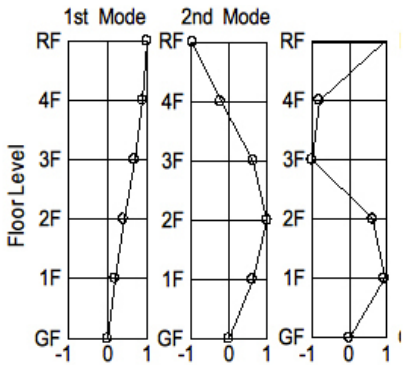

Figure 5 – Mode shapes of the undamaged building model in the X-direction

Table 2 – Natural frequencies of the undamaged building model

Mode	1st	2nd	3rd	4th	5th
Natural frequency	1.73	4.96	8.27	11.6	13.9

Classifier for damage detection

The modal properties and the associated damage patterns serve as a learning dataset for the damage detection classifier. As mentioned in the previous section, the dataset contains information for 96 damage patterns. A data-mining software Weka [4] is used to build the classifier.

Using a machine learning algorithm, the classifier which statistically learns the correlations between a damage pattern and the changes in modal properties is constructed. In the classifier, the number of damages in each story is objective variable. And the change in modal properties as explanation variable is:

$$C(d,n) = \left(\frac{U(d,n)}{U(u,n)} - 1 \right) \times 100 \quad (n = 1,2,3,4,5) \tag{1}$$

where n is the floor number, U is modal displacement at each floor normalized by roof floor displacement, of the damaged (d) and undamaged model (u).

In this study, the local additive regression of decision stumps (DS) [5] is selected as the algorithm after the trial of several famous machine learning algorithms (i.e, J48, regression of support vector machine). DS is a one-level decision tree. It searches over all possible features to split on, and for each one, search over all possible thresholds. DS does regression based on mean-squared error where each node in DS represents a feature in an instance to be predicted, and each branch represents a value that the node can take. This ensemble learning algorithm consists of the four steps explained in Fig 6.

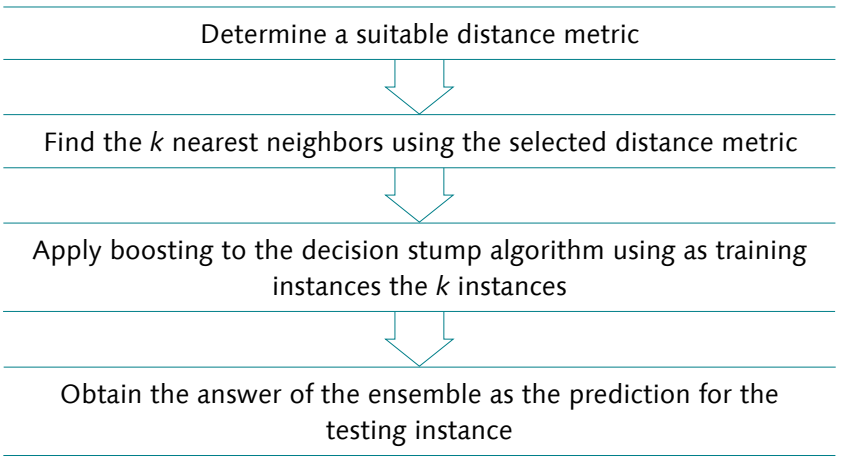

Figure 6 – Local additive regression of decision stumps

Preparation of supplied dataset

Before and after an earthquake, the vibration characteristics of buildings are estimated by experimental modal analysis using building responses that is obtained from sensors installed on the building. By supplying the changes in the characteristics to the classifier, a possible damage pattern is estimated. In the numerical simulation, the modal properties for supplied dataset are estimated from the acceleration time history at each story that are computed by transient analysis with the input ground motion as white noise, using the same model as the aforementioned modal analysis. To obtain modal frequencies and mode shapes, system identification methods are applied to the acceleration responses at each story. The data contains errors from the analysis and from the system identification process. By substituting the estimated modal properties with error into the classifier, the number of damage locations at each floor is estimated. Provided with the simulation results for several damage patterns, the accuracy of the constructed classifier is evaluated.

Time history analysis

Ambient vibrations induced by wind and traffic loadings are assumed as random white noise with broad-band frequency components. The root mean square (RMS) of the input white noise is 10 cm/s² with a sampling frequency of 100 Hz, a frequency range of 0.3 ~ 20 Hz, and a time duration of 600 s.

Modal property extraction system identification technique

For extracting modal properties, the linear direct method (LD) is applied for input and output acceleration data, and the frequency domain decomposition method (FDD) is applied for output-only acceleration data [6]. In general, LD offers more accurate estimates than FDD, but accurate information on input is not always available especially in case input of each story contains uncertain factors such

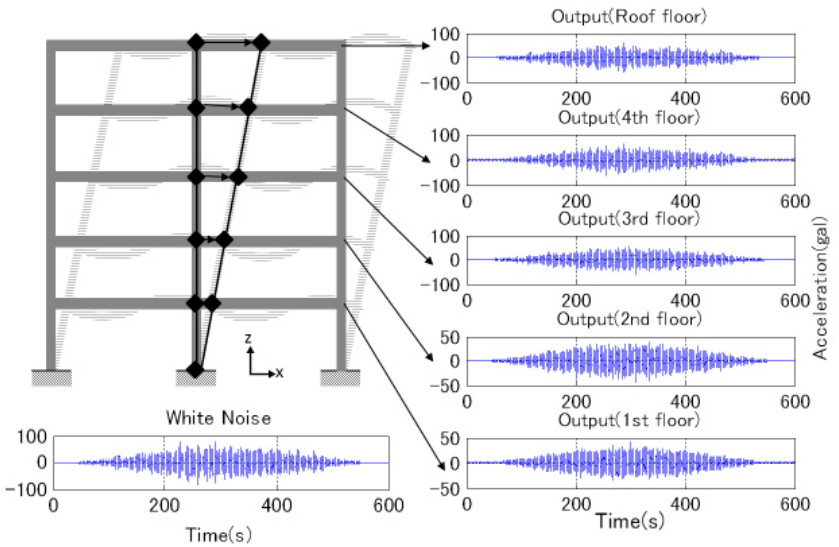

Figure 7 – Time history analysis

as strong non-stochastic wind loading. Tables 3 and 4 show the comparison of the modal analysis results and the estimates by the LD and FDD methods. Modal assurance criteria (MAC) is used to study the similarity between mode shapes [7]. LD method gives the estimates for all 5 modes, while FDD method has difficulty in estimating the 4th and 5th mode. The mode shape estimated by LD method shows very good agreements with the modal analysis results, with MAC values higher than 0.998. The MAC values for the 2nd and 3rd modes are slightly smaller for FDD method. Both methods estimate the natural frequencies for the 1st to 3rd modes with similar accuracy.

Table 3 – Comparison of modal analysis result and LD estimates

Mode	1st	2nd	3rd	4th	5th
MAC value of mode shape	1.0000	1.0000	0.9999	0.9999	0.9983
Error of natural frequency (%)	1.32	–0.71	–2.68	–4.18	–5.76

Table 4 – Comparison of modal analysis result and FDD estimates

Mode	1st	2nd	3rd	4th	5th
MAC value of mode shape	1.0000	0.9990	0.9941	–	–
Error of natural frequency (%)	0.81	–0.63	–3.73	–	–

Damage detection using classifier

The rates of change in the modal properties estimated by the system identification methods are inserted to the classifier for estimating the number of damage locations in each story. The test dataset consists of 7 amage patterns for 0 to 2 damage locations in different stories (see Table 5). Each pattern has 4 simulations in which output data includes no noise or 3 noise levels of 2.5%, 5%, 15% in terms of S/N ratio.

Indices applied for evaluating the accuracy of damage detection are the correlation coefficient (CC) and the mean absolute error (MAE) between the estimated and the actual number of damage locations. When estimation is good, the CC is close to one and MAE is close to zero. When estimation is poor, CC is close to zero and MAE becomes a larger number.

Figure 8(a) shows the comparison of damage detection accuracy for several different classifiers with variations in explanation variables (i.e., modal parameters estimated by the LD method). For instance, 3MS means that the classifier uses 1st to 3rd mode shapes. 5MSF means that the classifier uses 1st to 5th mode shapes and natural frequencies. As a result, the classifier with 1st to 3rd mode shapes (3MS) presented the best estimation. Due to the lower accuracy in identifying higher modes, the results with classifiers including the 4th and 5th mode shapes were relatively poor. On the other hand, when classifiers

included only 1st and 2nd mode shapes, the available information was not enough to classify 96 damage patterns in the learning data, and thus 1MS and 2MS gave relatively poor results. econdly, the effect of noise in sensors is evaluated by changing noise levels as 2.5%, 5%, 15% in terms of S/N ratio. Figure 8(b) shows the damage detection accuracy for different noise levels. In all cases, 1st to 3rd mode shapes (3MS) are considered. In spite of variations in each case, the accuracy tended to decrease when noise increased. For example, the CC dropped by 0.07 and the MAE increased by 0.06 when noise of 15 %was considered.

Pattern number	2nd floor	4th floor	Roof floor
	Number of damage locations		
1	1	1	0
2	1	0	1
3	0	1	1
4	2	0	0
5	0	2	0
6	0	0	2
7	1	0	0

Table 5 – Damage patterns present in the dataset

Future research subjects

Improvement of classifier

In order to identify the intensity and location of local damage such as a fracture of beam flange, a large number of sensors must be installed to a building. On-going research is to detect the change in bending-moment distribution using strain sensors (Figure 9). Such index is considered to be more sensitive to local damage compared to modal properties. Although the detection of local damage by the sensors placed in adjacent to the damage is possible, the amount of cost and labour to scatter the sensors in a building become are quite large. Therefore, how to decrease the number of sensors yet increase the accuracy becomes a challenge.

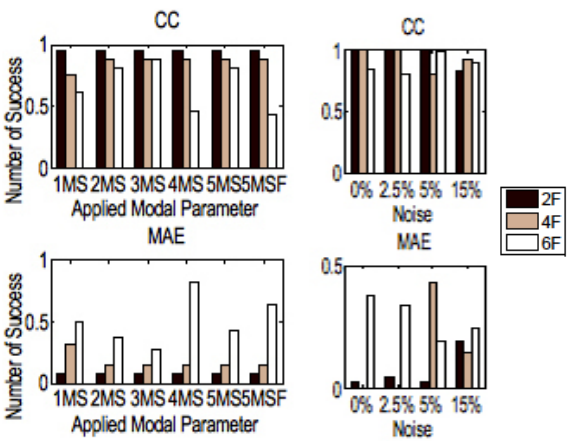

Figure 8 – Comparison of errors in damage detection using classifier: (a) Different explanation variables; (b) Different noise level

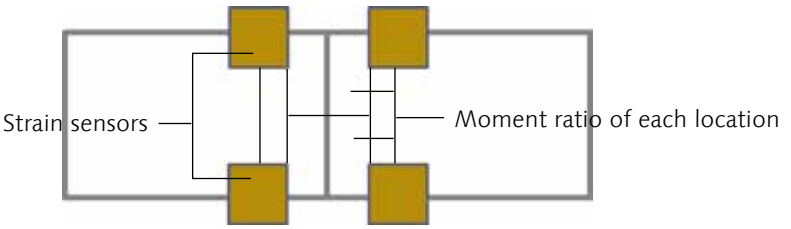

Figure 9 – Example of potential strain sensor locations (floor plan)

Shaking table test

A scale steel structure without concrete slabs was built in the laboratory at the Uji campus of Kyoto University. A series of shaking table tests are undergoing with. a measurement system contained with accelerometers, and strain sensors. Figure 10 shows the scaled steel structure mounted on the shaking table. At connections, joint panels and a beam or column are connected using five dog-born shape steel connectors; two for connecting each flange and one for web. Beam or column fractures are replicated by removing the connectors. A wireless sensing system is used to send acceleration or strain data to a main server, which reduces labour costs in wiring sensors.

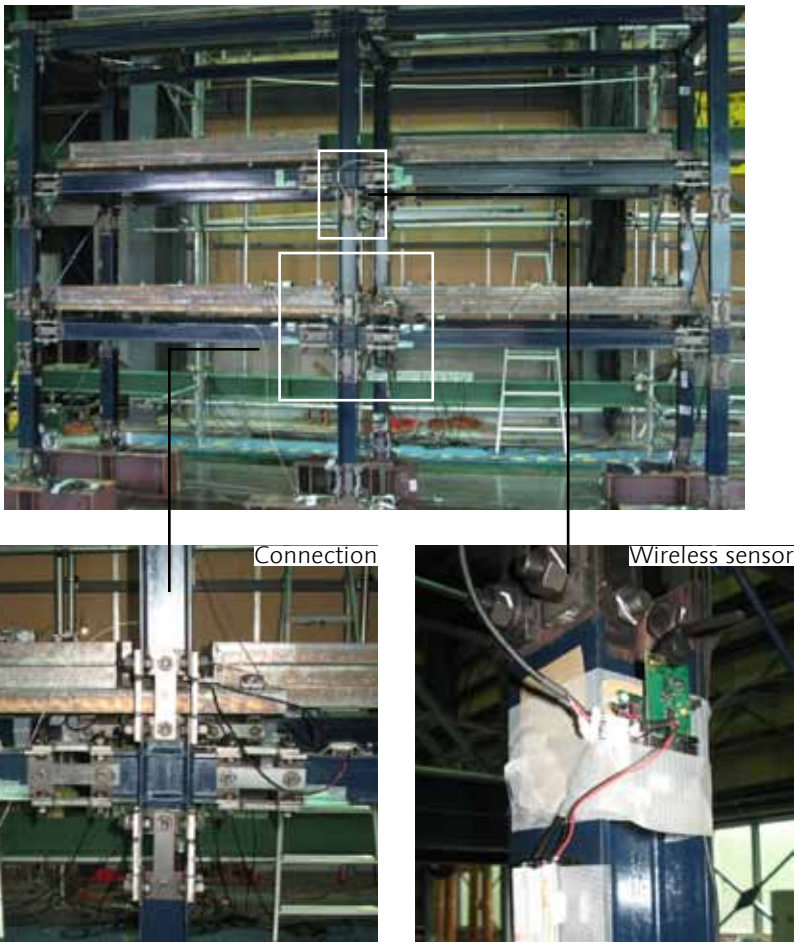

Figure 10 – Scaled model of three story steel structure

Conclusions

The development of a damage detection system using machine-learning-based classifiers for steel structures was described. Pre-analysis result showed that the changes in mode shapes differ with the various damage patterns. Using an additive regression of decision stumps, the classifier for 96 damage patterns are developed and the best accuracy was obtained when the 1st ~ 3rd mode shapes change rate was chosen as explanatory variables.

Further research is necessary to increase the robustness of the presented damage detection system for accounting higher level of uncertainties resulted from measurement noise, non-structural components and non-stochastic wind loadings. The learning dataset of 96 patterns should be expanded to consider all possible combination of damage in a building. In such case, the classifier and system identification algorithm with better performance are desirable to accommodate the increase complexity in damage detection.

References

[1] *Computers and Structures (2011). SAP2000 Documentation.*

[2] *Dassault Systems (2010). ABAQUS 6.10 Documentation.*

[3] *AIJ (2010). Design Recommendations for Composite Constructions*

[4] *The University of Waikato (2011). Weka Documentation.*

[5] *Sotiris B. Kotsiantis, Dimitris Kanellopoulos, Panayiotis E. Pintelas (2006). Local Additive Regression of Decision Stumps. Lecture Notes in Computer Science, Springer-Verlag, Volume 3955, S. 148–157.*

[6] *Rune Brincker, Lingmi Zhang, Palle Andersen (2002). Output-Only Modal Analysis by Frequency Domain Decomposition. 25th International Seminar on Modal Analysis (ISMA), Leuven/Belgium, S. 717–723.*

[7] *Randall J. Allemang (2003). The Modal Assurance Criterion (MAC): Twenty Years of Use and Abuse. Sound and Vibration Magazine,Vol. 37, No. 8, S. 14–23.*

Structural Solutions for the Construction of National Beverages Company Warehouse (NBC) Project

ZIMMO, Iyad
Civil Engineering

Abstract

This paper is intended to describe the structural analysis and design of the National Beverages Company Warehouse (NBC) to be built in Ramallah, Palestine. This building comprises of 7 floors of which 2 are underground, all with a total construction area of 3400 m² per floor. This structure was analyzed through three different design flooring system alternatives: Composite Construction, Two-way slab on beams, and flat slab. Studying these alternatives to serve for large spans and long cantilevered zones, steel manual (AISC) was used for composite construction while ACI-318 Code used in both the two-way slab on beams and flat slab systems. Software programs like SAP2000 and ETABS were used to check the results obtained from manual analyses of the structural systems. The two-way slab on beams system was applicable for underground floors for the reason of fire considerations and resistance to underground water, while composite construction system was suitable for the superstructure where large spans of composite beams obtained a level of economy, function, and safety.

Introduction

The main objective of this project is to present different structural alternatives for the design of the NBC warehouses in which these alternatives are evaluated and compared to determine the best alternative that is economical, functional, and safe. But in this paper, intention will be focused on the challenges faced in this project for using different flooring systems, and the way dealing with these challenges will contribute to the best choices. Starting with an introduction about the project, the proposed project site is located in the Industrial Zone of Bitunia — Palestine with a total floor area of 3400 m². Land uses in this industrial zone are mainly commercial, small industries, and warehouses.

The project serves for a 7 floors building (two underground floors) for multi-functions like storage areas, plant rooms, car park, maintenance workshop, and services offices.

The heights and live loads in each floor of the project are summed as following:

- Basement floor: Basement floor is 7.8 m below the ground level. This floor will serve for a car parking area with a live load of 2 KN/m^2.
- Ground floor: The ground floor is +0.0 m with a ground mezzanine of +3.90 m level. Ground floor includes warehouse area of 2606 m^2. The total area of ground floor with ground floor mezzanine is 2,980 m2 with a live load of 5 KN/m^2
- Typical floors: There are three typical floors with identical heights of 3.45 m, and they serve as an open plan offices and services with a live load of 5 KN/m^2.
- Roof floor: This floor is the last upon the floors of the building, and will not be covered, while the live load on this floor is 1.5 KN/m^2.

Structural Systems

In this section, three distinct and viable options are presented through the design requirements and the structural solutions. The section concludes with a comparison behavior between the structural systems.

Composite Construction with Steel Deck:
This system consists of structural steel deck, a concrete slab with steel mesh against shrinkage and temperature connected to a steel beam by shear connector studs to prevent the slipping between the concrete and the steel. The studs are welded through deck to the top flange of the beam. [1]

At construction stage:
For this stage, there is no composite action, but steel section is fully restrained against lateral torsional buckling by the deck and studs, hence the strength in which the beam strength is checked for only weights of slab and construction loads is: [2]

(1) $\varphi bMn = ZxFy$

On the other hand, the serviceability requirements for the beam should be checked. The loads causing deflection at the construction stage are the weight of steel beam, slab, and construction loads only. Shoring is not to be used; the steel shape and metal deck have to support the

weight of concrete by themselves. It is recommended according to the AISC Specifications that an incidental construction loads of a value of 1 KN/m² to be added if shoring is not applied for the composite construction. This requires deflection to be checked for construction and composite stages. [1] Deflection is computed by:

$$\Delta b = 5wDl2384EsIs \quad (2)$$

At composite stage

After concrete curing, there will be a unity action between steel and concrete. Hence a transformed section is obtained by converting the concrete slab into an equivalent steel section, since no slipping is permitted by the shear studs, full composite action is assumed. The strength is then tested for the dead, live, and partition loads. All loads must be resisted by the internal couple corresponding to the stress distribution at failure. The figure below shows the plastic analysis of the composite section:

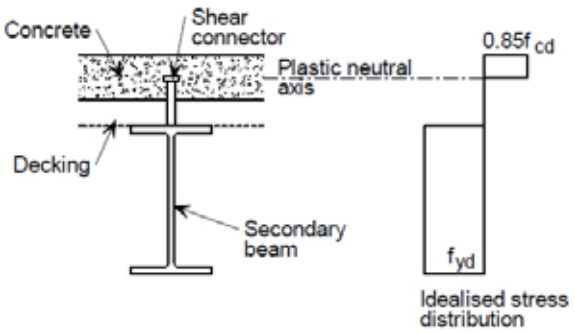

Figure 1 — Plastic analysis of composite section

Serviceability check at composite stage must comply with the deflection caused by live and partition loads. Deflection caused by live and partition loads is computed by:

$$\Delta a = 5wll2384EIeff \quad (3)$$

Strength and serviceability for full composite behavior: Strength is now tested with a reduction of the nominal capacity of the composite section. This serves as a factor of safety for flexure. Reduced nominal capacity of the composite section will be the smallest of:

$$\varphi bMn = \varphi bAsFyy = \varphi b(0.85fc'Ac)y \quad (4)$$

Since strength is checked for the composite section, serviceability requirements should be checked for the total deflection; deflection at construction stage, and deflection at the composite stage caused by live and partition loads. The limitation over the deflection is:

$$\Delta b + \Delta a < l240 \quad (5)$$

Shear Strength: [2]
All shear forces must be resisted by the web of the steel shape. Depending on the chosen steel section, the adequacy of shear can be determined.

(6) ØvVn ≥ Vu

Shear Connectors:
The horizontal shear force to be transferred between the concrete and steel (V') is equal to the compressive force in the concrete (C). After determining the controlling value of the horizontal shear force to be transferred between the concrete and steel, the number of shear connectors (N1) is determined.

Complying with all the requirements of strength and serviceability for the composite design with steel deck, a summary of the dimensions of the designed beams is made. For choosing the adequate steel section in terms of strength and serviceability, one of these two criteria will decide upon the choice of the required section.

Span length (m)	Tributary area width (m)	Beam section	Mu (KN.m)	φbMn (KN.m)	Final deflection (mm)	Allowable deflection (mm)	Controlling criteria
9.6	9.825	W27X94	1760	1760	23.1	40.1	Strength
7.5	7.5	W18X46	805	855	25.9	31.2	Strength
7.5	9.825	W21X55	1070	1115	27.2	31.2	Strength
15.0	6.4	W30X108	2051	2148	62.0	62.5	Serviceability
10.1	2.5	W12X58	377	828	41.9	42.2	Serviceability
7.5	2.5	W12X26	266	392	26.9	31.2	Serviceability
9.6	3.75	W18X46	672	875	35.6	40.1	Serviceability
7.5	3.75	W16X26	408	462	29.2	31.2	Serviceability

Table 1 — Shows the results of the composite construction design

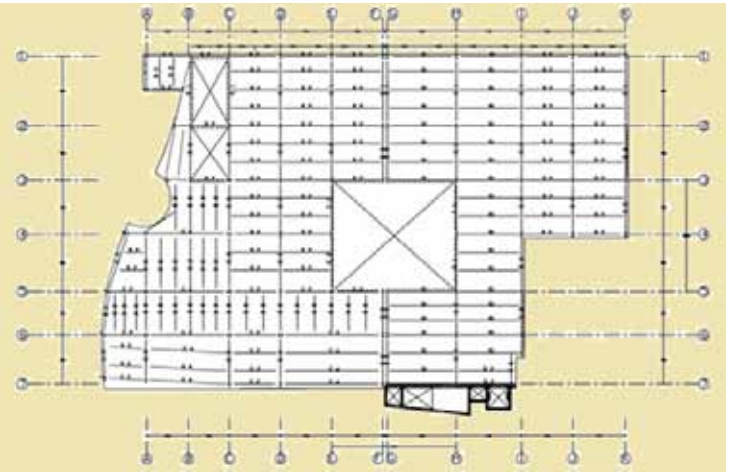

Figure 2 — Column layout for the suggested composite construction of the flooring system of the typical floor

Composite Construction in Cantilevered Zones:

The structure involves two cantilevered zones, the first with 1 m cantilever, and the second with 6 m. These two zones are treated separately. Since the first cantilevered zone has small span length of 1 m, the metal deck used in composite construction will span as a cantilever parallel to the primary beams for the 1 m distance. The metal deck along its strong axis serves for tension steel for the concrete slab and eliminates the chance of lateral torsional buckling from occurring. So the steel deck will be extended for the required length of the cantilever to comply with the cantilevered zone.

For the second cantilevered zone, the cantilever will span over a 6 m length over the first typical floor to the roof floor. To solve for this cantilever span, a truss positioned over the roof is designed to carry the distributed load of the roof and the load carried by the cantilever from floors below it. External forces and reactions of these forces act on the nodes of the truss resulting in either tensile or compressive forces in the truss members, so truss must be designed to satisfy the strength and serviceability requirements of compressive and tensile members. The load of the roof will be treated as uniformly distributed load over the truss bottom, while the loads of the floors below the truss will be treated as point loads acting at the end of the cantilevered section of the truss. [3]

Cantilevered zones of the typical floors are lifted through tension columns where each column carries the loads from its floor in addition to loads from lower floors. The tension columns are then hanged by the end of the cantilever truss where the columns assign dead and live point loads at the end of the cantilever.

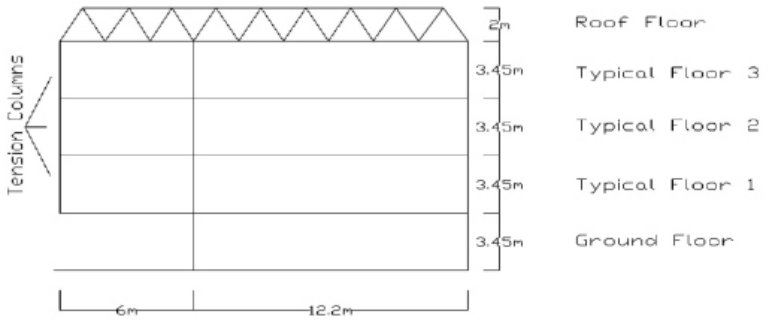

Figure 3 — Cantilevered zone section showing tension columns, truss cross-section and 6 m cantilever span

The truss will extend over two spans in which the first one extends for a length double that of the cantilever and the second which is the cantilever span. The figure below shows the modeling of the truss:

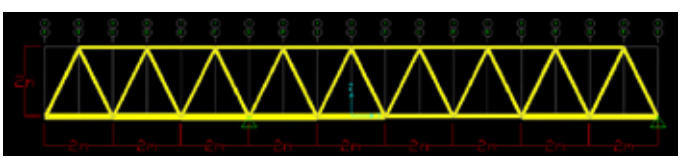

Figure 4 — Cross-section of the truss of the cantilevered zone

Analysis of the forces in the truss members shows that all upper members of the truss are in tension. On the other hand, the lower members are in compression, so the problem of lateral torsional buckling has to be solved by connecting the truss bottom with the steel deck below it. Through analysis and design of the truss members, the section that complies with the strength and serviceability requirements is W40 x 199 used for all members of the truss. Deflection at the end of the cantilevered zone equals 2.8 mm which is less than the limit of 25 mm (l240). Shown below the deformation shape of the truss:

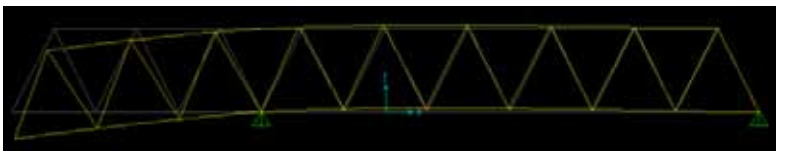

Figure 5 — Deformed shape of the truss due to point and uniformly distributed loads

or the tension columns, a tension member of W14x26 is required for the tension column in the third typical floor. This preliminary sizing of this tension column is the most critical case in which the column carries the largest loads in comparison with columns below it, so this section is generalized over the tension columns of the first and second typical floors. Serviceability requirement for the tension member is checked where (lrmin) = 126 which is less than 300.

Reinforced Concrete Options

Two way slab on beams:
One of the options in which large spans challenge can be solved is by using the system of two way slab on beams. According to ACI318-08 requirements [4], the thickness of the solid slab equals 25 cm. The beams dimensions for the exterior support of 10 m span (interior beam) are (35 x 70) cm, with 10φ25 for maximum negative, 8φ25 for positive, and 3φ25 for other negative supports. The dimensions for the beams of span 7.5 m (interior beam) are (30 x 50) cm, with 7φ25 for maximum negative, 4φ25 for positive, and 7φ25 for other negative supports. [5]

Two way ribbed slab on beams:
This option provides a reduction in the dead load of the slab, where the solid slab is replaced by an equivalent ribbed slab. The moment of inertia of the repetitive unit for the equivalent ribbed slab must be equal or greater than the 1 m cross-section of the solid slab. The equivalent ribbed slab repetitive unit to the 25 cm solid slab depth is a 10 cm topping slab, 15 cm rib width, 25 cm rib height, and (45 x 25) cm of hollow block. This reduces the dead load by 29% compared with the option of using two-way solid slab on beams.

The maximum steel reinforcement was found to be 5φ20 bars in the 10 m span at the support. For the typical floors the maximum reinforcement was found to be 4φ20 bars at the middle of the span. The beams dimensions are, for the exterior support of span 10 m (interior beam) are (35 x 70) cm, with 10φ25 for maximum negative, 6φ25 for positive, and 4φ25 for other negative support. The edge beam of span 10 m was found to be (40 x 50) cm, with 7φ25 for maximum negative, 5φ25 for positive, and 3φ25 for other negative support. The dimensions for the beams of span 7.5 m (interior beam) are (30 x 45) cm, with 5φ25 for maximum negative, 4φ25 for positive, and 5φ25 for other negative support. The edge beam of span 7.5 m was found to be (30 x 40) cm, with 5φ25 for maximum negative, 3φ25 for positive, and 5φ25 for other negative support. [5]

Reinforced concrete option in cantilevered zones:
The western side of the structure has a 6 m and 3 m cantilevers, and has to be solved by a reinforced concrete option. The interior and edge beams are extended through the cantilever and then cantilever beams were analyzed either with two or three interior spans. Sizing for the cantilever beams is now to be designed in terms of serviceability and strength. [5]

The allowable thickness for cantilever beams is (l/8) [4]. In which for 6 m span, the minimum thickness is 75 cm, and for the 3 m spans is 38 cm. The elastic deflection was determined for the 3.0 m spans (G2, G4) and found to be, for the live loading 3.5 mm and for both Dead and live loads is 8.5 mm. The 6 m span (G1) cantilever is analyzed as a grillage, in which it carries an extended beam to its end, the carried beam acts on the cantilever as a point load. In addition to the point load, a distributed load acts on the beam in which the size and the deflection are determined. The deflection for the 6 m span (G1) for live loading is 5 mm, while for both dead and live load is 11 mm. The size of the beam was determined to be (50 x 70) cm, but for serviceability requirements (50 x 75) cm beam is used.

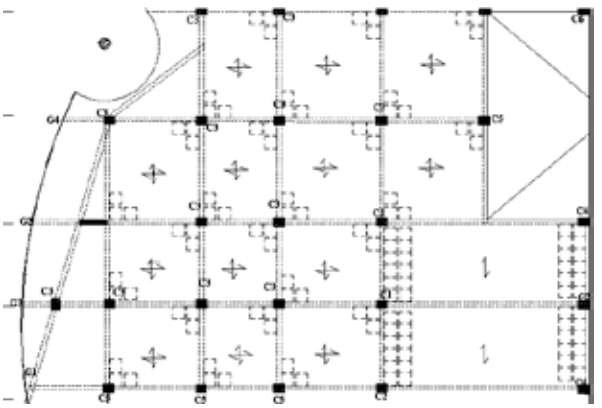

Figure 6 — Cantilevers of 3 m and 6 m in the western side of the structure

Flat Slab:

In this option, the slab directly rests on the column, and the load from the slab is directly transferred to the columns and then to the foundation. Figure 7 shows the column layout for the suggested flat slab in accordance to the ACI code [4]. The thickness of the flat slab that is considered adequate to resist the punching shear varies from region to region. Typically, it ranges from 200 mm to 300 mm.

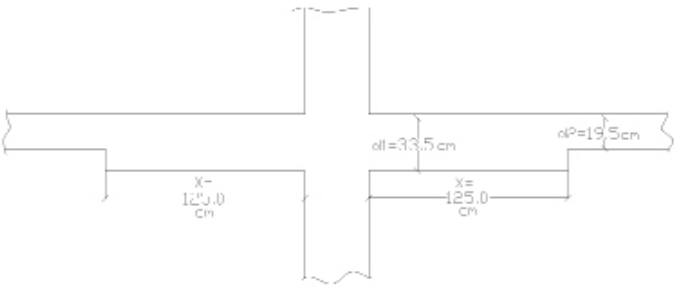

Figure 7 — Section through slab and drop panel according to ACI 13.2.5

For carrying out this project an interior panel of a flat slab with dimensions 7.5 × 7.5 m, and super imposed load 21.93 KN / m² was designed using the using ACI-318 code. Through the study of the suitability of using a flat slab for spans greater than 7.5 x 7.5 m, the option of flat slab is terminated for such case due to punching shear failure. [5]

Discussion

The flooring system for this warehouse undergoes a study through different alternatives considering reinforced concrete flooring systems versus composite and steel construction systems.

The composite construction flooring system provides an economical and effective system by taking advantage of the composite action between steel beams and concrete slab. Such system offers a light and fast-track construction. In addition, the steel deck serves as:

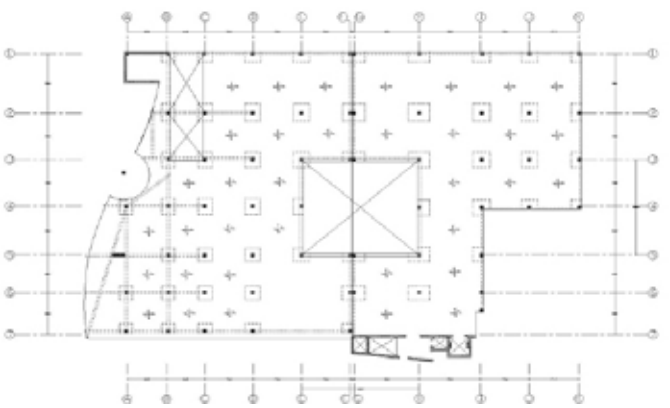

Figure 8 — Column layout for the suggested flat slab construction of the flooring system of the typical floor

– Formwork for the concrete slab, forming a permanent shatter.
– Tension steel for the concrete slab.
– A diaphragm resisting lateral torsional buckling of the beam during the construction stage and allows the beams to develop their full moment capacity.

Flat slab flooring system serves for some advantages such as:

– Easier to construct and requires simple formwork, with shorter construction time.
– Flexibility with services and quicker to cast
– Using drop panel increases shear strength of slab, increases negative moment capacity of slab, stiffens the slab and hence reduces deflection.

Two-way solid or ribbed slab are useful when considering their fire resistance and applicability for long spans and cantilevered zones. In term of fire considerations, concrete is naturally fire-resistant. It can reach high fire resistances for more than 3 hours depending on the concrete cover. The rate of temperature rise across the concrete section is low. Concrete sections can be repaired after fire if no severe damages occur in the construction members. Using concrete cover of 25 mm, 35 mm, and 50 mm protects the structure for 1 hr, 2 hrs, and 3hrs respectively. The underground car park requires 2–3 hrs to maintain a safe evacuation time for people inside the building. Steel is poor in fire resistance, and the rate of temperature rise across the section is very high with a low reparability potential after occurrence of fire. Steel fire resistance can be improved by using fire protection which is expensive. [6]

To sum up, concrete in underground car park provides this building with high fire resistance and low costs in comparison with the use of steel. This leads to the conclusion of using reinforced concrete two-way ribbed slab for the car park since flat slab can't be an option for spans larger then 7.5 m. In addition, sprinklers, manual extinguishers, and sand buckets are needed for fire extinguishing

For the maximum and typical span lengths, the composite and reinforced concrete flooring systems can serve for long spans, while through the study of using the flat slab flooring system; it will not be applicable for spans of more than 7.5 x 7.5 m. This is due to problems that may arise for longer spans due to punching shear failure. On the other hand, the increase in the steel beam cross-section in the composite construction system is more economical than the increase in the dimensions and steel in the cross-section of the two-way solid or ribbed slab flooring system.

In terms of weight, the table shown downwards clarifies the dead load weight per unit of area for each flooring system. The orientation should be towards lighter weights since it will reduce both cost and time, but it must be noted that earthquake requirements will be taken into consideration when launching the detailing process for the chosen flooring system.

Table 2 — Shows the dead load weight of the flat slab, two way solid slab, two-way ribbed slab and composite construction framing system

Type of Slabs	Typical & Ground floors (KN / m^2)
Flat slab	11.61
Two way solid slab	10.20
Two way ribbed slab	7.26
Composite system	6.42

This table indicates that the lightest flooring system in terms of the dead load is the composite construction framing system since it requires lighter weights of beams with the reduction of the amount of concrete in comparison with the rest of the other systems. On the other hand, the two-way ribbed slab system has considerably a light weight flooring system, and should be used for fire resistance in comparison to composite steel construction framing system for the use in underground floor.

Conclusion

This paper is accomplished for presenting different solutions for the flooring systems that can be used in NBC warehouse project, and the choice of the best combination of these solutions. For underground floors, reinforced concrete system is to be used by a two-way ribbed slab on beams, while for ground, typical and roof floors, composite construction flooring system will be used.

Further analysis and work of this project will be the detailed design of slabs, columns, and foundation. On the other hand, earthquake forces will be calculated according to UBC-97 code. Bill of quantities (BOQ) will be done using Microstation Triforma software in which the exact quantities will be calculated with the advantage of clash detection by modeling the structure. This leads to preparing a detailed cost estimate for the whole structure.

References:

[1] *Steel Construction Manual (2011). American Institute of Steel Construction 325–11. 14th ed.*

[2] *William T. Segui. (2006). Steel Design, Composite Construction, P. 552–610*

[3] *ACI 318, 2002, Building Code Requirements for Reinforced Concrete, American Concrete Institute, Detroit, Michigan.*

[4] *Chu–Kia Wang, Charles G. Salmon, and José A.(2008). Reinforced Concrete Design, Design of Two-Way Floor Systems, P. 620–709*

[5] *R. C. Hibbeler. (2011). Structural Analysis (8th Edition), Analysis of Statically Indeterminate Structures, P. 395–448*

[6] *J. D. Hill, G. Rhodes, S. Voller, C. Whapples.(2005).Car Park Designers' Handbook*

Modelling of soil-structure interaction in alpine regions

MARIN, Alexandru
Institute of Geotechnical Engineering, ETH Zurich

LAUE, Jan
Institute of Geotechnical Engineering, ETH Zurich

MEZGER, Florence
Institute of Geotechnical Engineering, ETH Zurich

Abstract

The understanding and quantification of soil structure interaction becomes more and more important in new projects as well as in the risk assessment of existing buildings. The recognition of local site effects in conjunction with special performance requirements imposed by different types of structures (e.g. industrial buildings) is challenging and appropriate evaluation of the soil-structure interaction is therefore neglected. The possibility of using widely available FE software to consider soil structure interaction is being explored in this contribution. The studied case is an industrial building with different types of foundations located in a glacier alpine valley with extensive deposits of alluvial material, characterized by a moderate seismicity. Performed verification procedures and calibration of input parameters are presented with the purpose of facilitating the future use of the employed software in other similar situations.

Introduction

Changes in risk perception, as well as increasing requirements arising from the corresponding changes in codes for engineering purposes, result in a need in practice for a clear, simple and efficient way to deal with field situations incorporating soil structure interaction. These have to be provided with the limitations of possible numerical modelling using available FE program and respecting the boundary conditions of modelling procedures, different ways of analysis and computation capabilities.

In this contribution, focus is given to a specific case situation, which involves the task of modelling the soil, the foundation and the soil-structure interaction for a generalised industrial building located in a

glacier alpine valley with alluvial deposits, in the area of Visp (Switzerland). Visp is characterized by a moderate seismicity (PGA = 1.6 m/s^2 according to SIA 261, 2003) and experienced an estimated moment-magnitude (M_w) of 6.4 event on July 25, 1855 (Fritsche, 2008).

The research is directly connected to COGEAR (Coupled seismogenic Geohazards in Alpine Regions), a multidisciplinary project within the Swiss Institute of Technology, funded by the Competence Centre for Environment and Sustainability (CCES). The main object of study of COGEAR is the seismic induced hazard chain and one of the main interest areas is represented by the physics of non-linear processes, which have been reported by eye witnesses about 150 years ago (Fritsche, 2008), in relation to topography and soil disposition.

Idealised Modelling

The FE modelling was performed using PLAXIS 2D. Considering the multitude of parameters and required assumptions it becomes very important to understand their influence on the reliability of results.

Soil Profile

The soil profile (Figure 1) was obtained as the result of compiling already existing data on the subsoil in the area of interest such as borehole profiles (COGEAR Platform) and soil investigation reports (Resonance, 2010; Weber et al. 2007). Additionally using shear wave velocity profiles from ambient noise array measurements (Burjanek 2011), a final simplification and verification of the model could be performed.

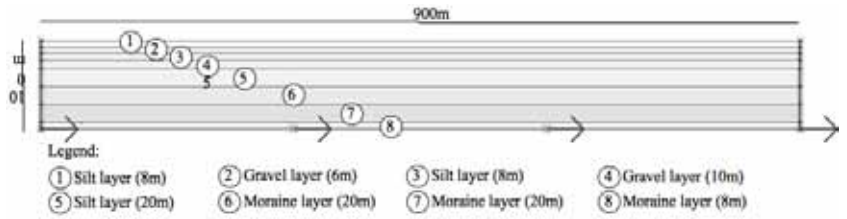

Figure 1 — Soil Model

A sensitivity analysis was performed in order to obtain the optimal width of the model, which will minimise the unwanted effect of the reflected waves. PLAXIS offers the possibility to define absorbent boundaries by means of the relaxation coefficients. By varying these coefficients from the standard values (C1 = 1 and C2 = 0.25), a change in the response spectrum can be observed. The width at which a doubling of these coefficients had an influence of less than 5% on the response spectrum was considered the optimal width. After several iterations, the final optimal value for the model width was determined to be 900 m (Figure 9) for an assumed constant depth of the soft deposits of approx. 100 m. This depth has been chosen as relevant for the site of the industrial area (comp. Roten 2009).

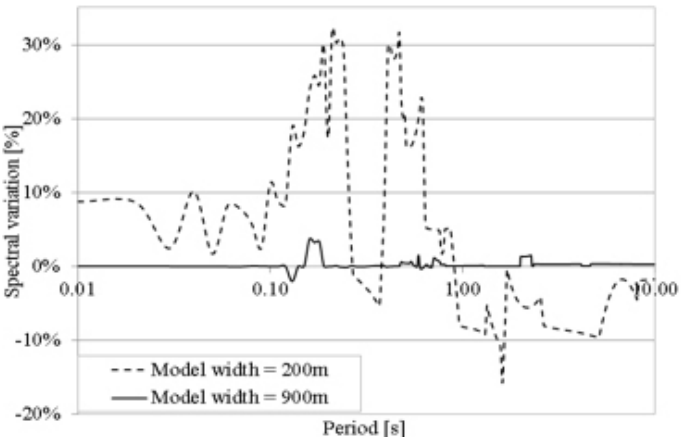

Figure 2 — Spectral variation with the increase of the relaxation coefficients

Material Parameters

For the simplicity of the calculations a Mohr-Coulomb model was employed. The set of corresponding soil parameters is given in Table 1 based on Weber et al. (2007):

Layer	Soil Type	Stiffness parameters						Strength parameters	
		v_s [m/s]	ν' [-]	G [MPa]	E' [MPa]	E_{oed} [MPa]	v_p [m/s]	ϕ' [°]	c'_{ref} [kPa]
1	Silt	200	0.3	81.63	163.3	163.3	282	33.9	1
2	Gravel	390	0.3	357	713.9	713.9	551.5	35	1
3	Silt	400	0.3	326.5	653.1	653.1	565.7	33.9	1
4	Gravel	480	0.3	540.7	1,081	1,081	678.8	35	1
5	Silt	490	0.3	490	980	980	693	33.9	1
6	Moraine	720	0.3	1,217	2,433	2,433	1,018	35	1
7	Moraine	800	0.3	1,502	3,004	3,004	1,131	35	1
8	Moraine	850	0.3	1,696	3,391	3,391	1,202	35	1

Table 1 — Soil Parameters

The interface elements between structure and soil are considered to have the same parameters as the rest of the soil elements in the data set. Therefore the PLAXIS 2D parameter called *Strength of the Interface* has been defined as rigid. One of the most important aspects of the soil parameters in the dynamic analysis is the material damping, which, in PLAXIS, is introduced by the two Rayleigh coefficients α_R and β_R. According to Park and Hashash (2004) these coefficients may be determined using the following system of equations:

$$\begin{bmatrix} \xi_m \\ \xi_n \end{bmatrix} = \frac{1}{4\pi} \begin{bmatrix} \frac{1}{f_m} & f_m \\ \frac{1}{f_n} & f_n \end{bmatrix} \cdot \begin{Bmatrix} \alpha_R \\ \beta_R \end{Bmatrix} \quad (1)$$

where f_m and f_n are two significant natural frequencies and ξ_m and ξ_m are the corresponding damping ratios.

In order to choose the most suitable pair of Rayleigh coefficients, the proposed PLAXIS model was calibrated using a frequency domain analysis in the elastic range, using the linear-equivalent analysis tool EERA (Bardet et al. 2000).

The elastic range was identified as the range where the damping values within the soil profile are under 5%. Above this threshold significant plastic deformations occur and the behaviour of the soil becomes non-linear. Four different earthquake signals (two earthquakes recorded by different seismic stations: Aquila 2009, M_w = 6.3 (Figure 3 and Figure 4) and Iceland 2008, M_w = 6.3; were employed by down-scaling them so that all the values in the damping profile derived with EERA remained under 5%. These specific earthquakes were chosen because they represent seismic motions with similar magnitudes and seismic frequency contents with those expected in Switzerland.

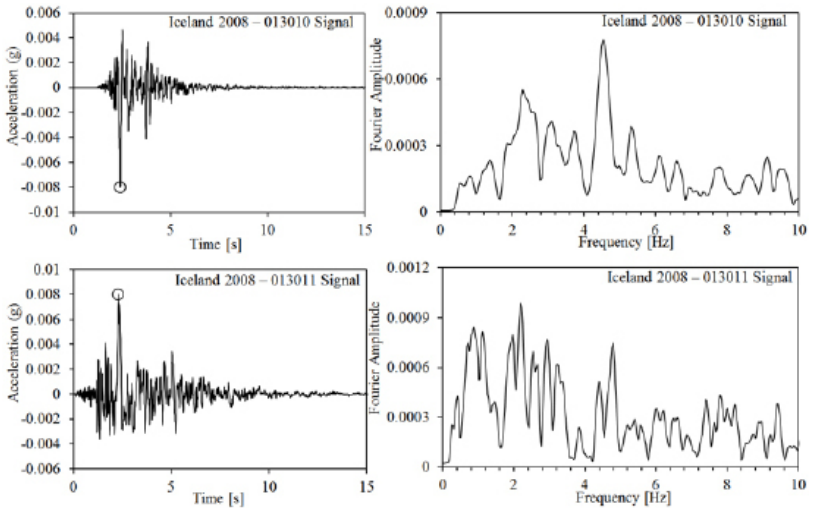

Figure 3 — Iceland earthquake signals (two different stations)

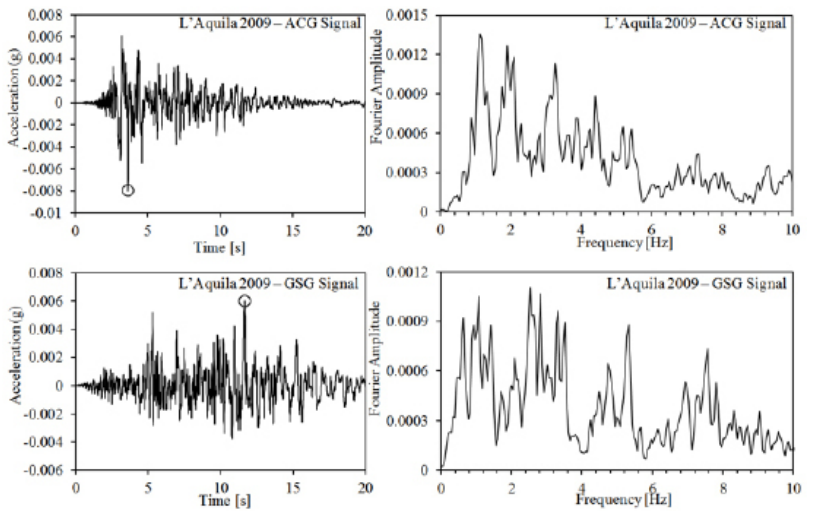

Figure 4 — L'Aquila earthquake signals (two different stations)

Calibration of the Rayleigh Coefficients

The calibration procedure consisted of a trial-and-error method for picking the right frequencies, which will lead to a good agreement between the results delivered by the time domain (PLAXIS) and the frequency domain analyses (EERA). There are already some publications (Park & Hashash, 2004; Visone & de Magistri, 2010) presenting different methods to choose the appropriate frequencies, which would deliver convergence. In the present paper the best convergence of the results was obtained for combinations between the second and another superior frequency (third, fourth, etc). The damping ratios, which are required in the equations system (1) were obtained for each soil layer from the EERA analysis The results obtained with EERA and PLAXIS for the above input signals are presented in Figures 5–8, also indicating the natural frequencies.

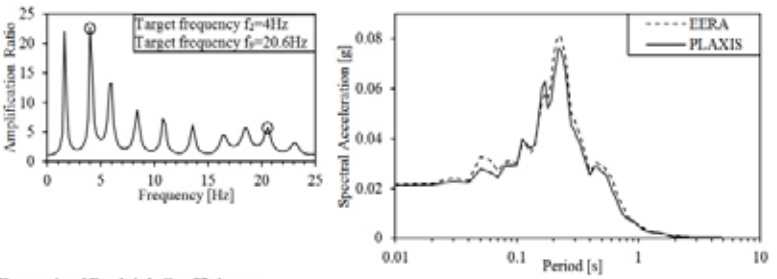

Determined Rayleigh Coefficients:

Layer	1 (Silt)	2 (Gravel)	3 (Silt)	4 (Gravel)	5 (Silt)	6 (Moraine)	7 (Moraine)	8 (Moraine)
α_R [-]	1.447	0.272	1.084	0.272	0.910	0.226	0.227	0.215
β_R [-]	0.000445	0.000084	0.000333	0.000084	0.000280	0.000070	0.000070	0.000066

Figure 5 — Calibration results for Iceland 2008 — 013010 Signal

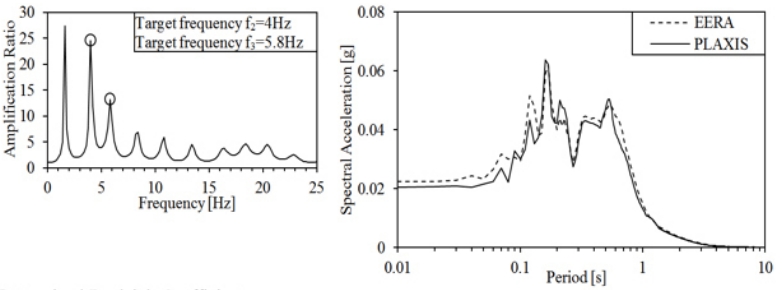

Determined Rayleigh Coefficients:

Layer	1 (Silt)	2 (Gravel)	3 (Silt)	4 (Gravel)	5 (Silt)	6 (Moraine)	7 (Moraine)	8 (Moraine)
α_R [-]	1.071	0.206	0.945	0.229	1.049	0.203	0.194	0.182
β_R [-]	0.001171	0.000226	0.001033	0.000250	0.001146	0.000221	0.000212	0.000199

Figure 6 — Calibration results for Iceland 2008 — 013011 Signal

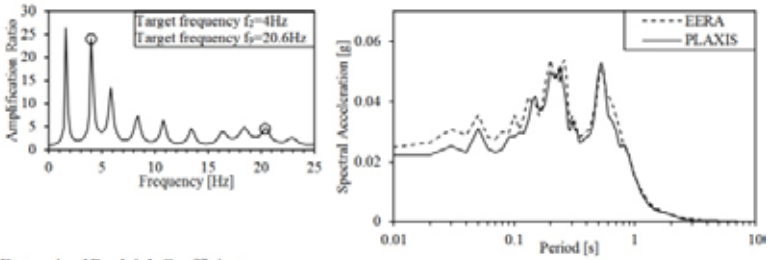

Determined Rayleigh Coefficients:

Layer	1 (Silt)	2 (Gravel)	3 (Silt)	4 (Gravel)	5 (Silt)	6 (Moraine)	7 (Moraine)	8 (Moraine)
α_R [-]	1.489	0.277	1.209	0.317	1.404	0.264	0.249	0.241
β_R [-]	0.000458	0.000085	0.000372	0.000098	0.000432	0.000081	0.000077	0.000074

Figure 7 — Calibration Results for L'Aquila 2009 — ACG Signal

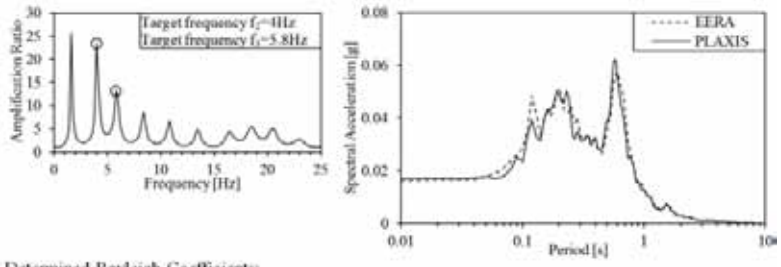

Determined Rayleigh Coefficients:

Layer	1 (Silt)	2 (Gravel)	3 (Silt)	4 (Gravel)	5 (Silt)	6 (Moraine)	7 (Moraine)	8 (Moraine)
α_R [-]	0.872	0.193	0.846	0.218	0.935	0.188	0.177	0.168
β_R [-]	0.000953	0.000211	0.000925	0.000238	0.001022	0.000206	0.000193	0.000184

Figure 8 — Calibration Results for L'Aquila 2009 — GSG Signal

Structural Elements, Foundation Types

The structural elements are simulated using plate elements, according to Mindlin's plate theory (Bathe, 1982). The superstructure was replaced using the simplifying assumption of an equivalent distributed load (including the self-weight and the live loads on the structure).

The analysis includes three types of foundations: a shallow foundation, a deep basement and a piled foundation. In the case of piled foundation, the spatial interaction between soil and pile rows was accounted for by employing sheet pile walls with reduced stiffness, as suggested by Randolph (1981) and Naylor (1982). The determined equivalent Young's Modulus resulted in a value of E = 4.04 GPa, which is 13% of the E modulus for concrete, used in the other structural elements. In order to obtain this value, the dimension of the foundation in the direction perpendicular to the 2D problem modelled by PLAXIS was assumed to be 30 m (assumption of a rectangular layout of the foundation). The 7 circular piles, of diameter D = 75 cm, were assimilated with a sheet pile wall of equivalent width d = 60 cm characterized by a reduced Young Modulus of E = 4.04 GPa (Figure 10).

Input signal

The most common earthquake mechanisms in the area of Wallis, are either strike-slip or normal fault (Deichmann & Ballarin-Dolfin 2003) at a shallow depth and therefore all computations included in this paper were performed using the 2008 Iceland (013010 Signal) earth-

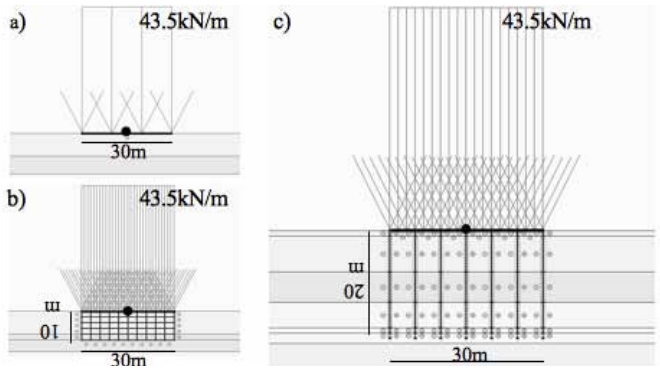

Figure 9 — Foundation layouts: a) shallow foundation; b) deep basement; c) piled foundation

quake (M_w = 6.3), which was characterized by a normal fault mechanism and an epicentral depth of 10 km (USGS, 2008). One method to obtain an input signal appropriate for the bottom of the FE model from PLAXIS is to back-calculate from the given outcrop signal an inside motion signal (which is more suitable for the non-rigid bottom layer of the FE model). This can be easily obtained in EERA by applying the input original signal to the model as an *outcrop motion* and calculating the *inside motion* corresponding to the lower most layer. This motion (Figure 11, left) is then used in the further analyses.

Results related to soil-structure interaction

The first parameter to be analysed is the acceleration acting at the foundation level (Figure 10, right) using the inside motion derived by the free field analyses.

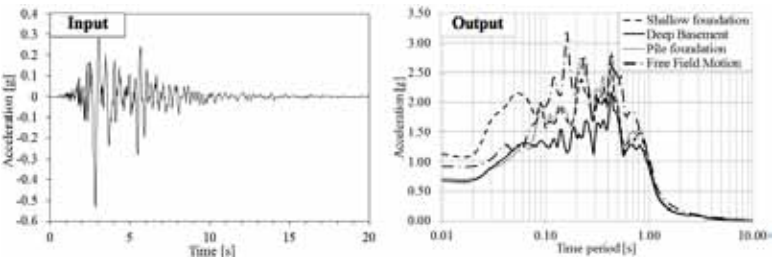

Figure 10 — Left: Input Motion (Iceland 2008 — 013010, inside motion); Right: Output acceleration spectra at foundation level

The spectral values of acceleration for the shallow and the piled foundations are larger than the ones for the deep basement, but the peaks stay at the same periods. From the point of view of the shallow foundation, these results are in perfect correlation with the reality, considering that this foundation is basically placed on top of the soil layers, where the amplification has the largest values. On the stiff side of the spectrum (periods between 0.01–0.08 s) the shallow foundation exhibits larger values than the other two.

As the foundation goes deeper in the soil deposits the amplifications are smaller and therefore the accelerations decrease. On the other hand, with the increasing depth, for a deep basement foundation, the forces acting on the exterior walls are larger. This aspect will be considered in the following paragraphs.

The interesting fact is that, from 0.08 s towards the end of the spectrum, the spectral values for the piled foundation are basically in the same range or even higher than the ones characterizing the shallow foundation. This may be explained by the fact that the piled foundations are subjected to a double action: the waves traveling through the soil itself and the waves travelling through the concrete piles.

Figure 11.shows the horizontal displacements recorded in the centre point of the foundation for the three foundations types.

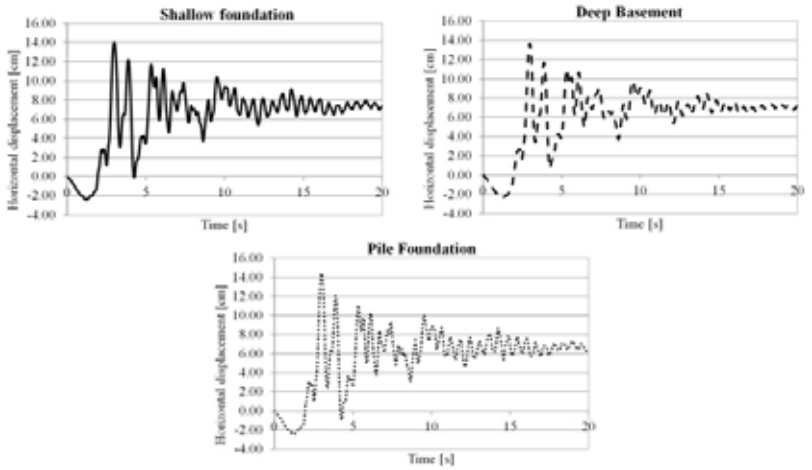

Figure 11 — Horizontal displacements for the three types of foundation (Iceland 2008 — 013010)

The recorded displacements are ranging from 13.6 cm to 14.4 cm. It becomes obvious that the smallest displacements are recorded at the bottom of the deep basement foundation system. For the cases of shallow and piled foundation the displacements are almost identical (14.0 cm for the shallow foundation and 14.4 cm for the piled foundation). This hints again to the special behaviour of the piled foundation where the raft on top of the piles is subjected to superimposed dynamic actions coming from the soil itself and from the piles, which result in a slightly increased dynamic response.

The tilting of the foundation can be also analysed and compared for the three chosen systems. Figure 12 shows the development over time of the tilting, measured as an average from three points (the right and left margins and the centre of the foundation). As expected the largest residual, permanent inclinations are recorded for the shallow foundation, with an absolute value 0.052%. The piled foundation follows with a residual tilting of 0.026% which means basically half of the value from the shallow foundation. The smallest values are recorded again for the deep basement, where an absolute average inclination of only 0.016% was recorded. For this case, the vertical displacements used in the tilt calculation, were measured on the top plate of the basement, at the same level with the piled raft and the shallow foundation mat, considering rigid box behaviour for the deep basement structure.

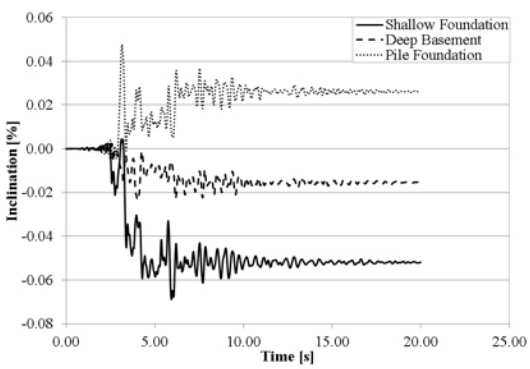

Figure 12 — Average tilting of the foundations (Iceland 2008 — 013010)

Interaction between basement walls and surrounding soil mass

Figure 13 shows the modelled behaviour using the recorded lateral displacements of the two pairs of points on the wall and in the soil from the close vicinity (Points A through D in Figure 13d). It becomes obvious that the bottom points move together with the same amplitude and frequency (Figure 13b).

On the other hand the points at the top of the wall show a different behaviour: when the motion is in the positive direction (from left to right), point A (the top of the wall) tends to move more than the point B (top of the soil mass). In this way the interface opens creating an empty space behind the wall. Considering the fact that the modelled soil is a granular material, this space will be quickly filled. When the motion occurs in the negative direction (from right to left) the observed tendency of point A (top of the wall) is to move less, to remain behind, as point B (the top of the soil mass) advances and leaves again an open space next to the wall.

Figure 13c shows the evolution of the relative displacement between the points A and B, which increases incrementally in four main events (out of which the largest one is marked with the dotted line). Important to be mentioned is the fact that the residual relative displacement of 5.9 cm is not the width of the open interface at the end of the motion. In reality the material is granular and will fill any open spaces behind the wall at least partially. Thus this value is rather another way to observe and quantify the soil-structure interaction. With time, as the interface repeatedly opens and is filled with granular material, the lateral earth-pressure acting on the wall will vary (Figure 14) and increase, as it also has been experienced with integral bridge abutments (Ng et al. 1998). The observed behaviour is in perfect accordance with previously observed data in the literature (Chari & Meyerhof, 1983; Tsang et al., 2002).

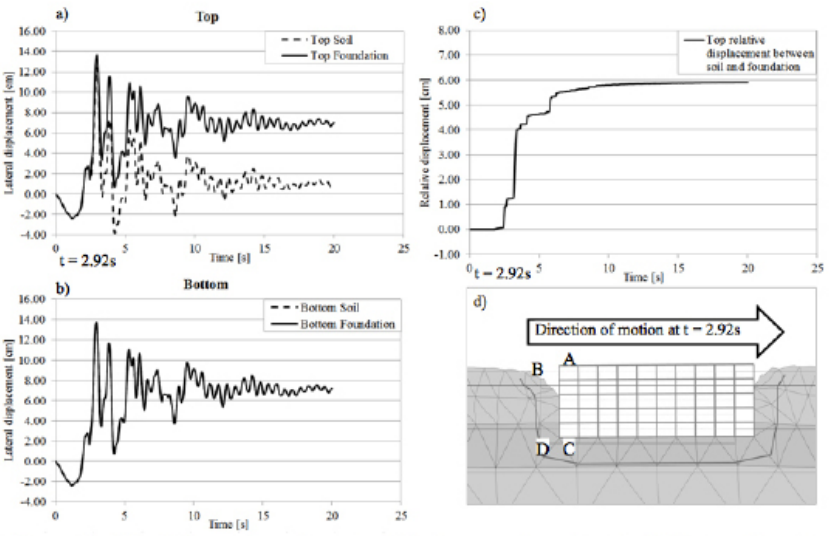

Figure 13 — Soil-wall interaction: a) top lateral displacement for wall and soil, b) bottom lateral displacement for wall and soil, c) top relative displacement, d) schematic representation of the first opening of the interface wall-soil (not to scale) — (Iceland 2008–013010)

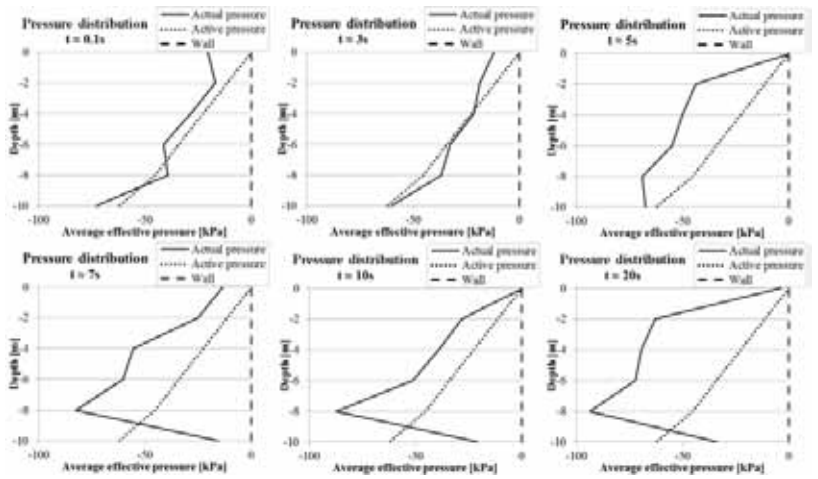

Figure 14 — Variation of the pressure with time on the left wall of the foundation basement — (Iceland 2008 – 013010)

The mechanism behind this change in the pressure profile can be explained in three steps. First, the material flows in the open interface and accumulates behind the wall. Secondly, due to material accumulation, a material densification will start to localize. Finally, as a result of the densification, the stiffness of the system increases in the denser area. The stresses are transferred from the lower stiffness areas (top and bottom) to this area, causing higher pressures on the wall.

Performance based design perspective and conclusions

The results presented above matched, in all cases, expected and already observed behaviour, confirming in this way the reliability of the employed methods and software. The motivation behind this reiteration was introduced in the context of Performance Based Design tendencies observed especially in the Swiss Norms. According to SIA 260 (2003), paragraph 2.2 (Figure 15) the design of a structure involves a service criteria agreement, which has to be defined in a dialogue between the client and the designers of the project.

2.2	**Service criteria agreement**
2.2.1	The service criteria agreement shall be formulated on the basis of a dialogue between the owner and the design engineers.
2.2.2	The service criteria agreement comprises: - general aims for the use of the construction works - ambient conditions and third party requirements - operational and maintenance requirements - special requirements of the owner - objectives of protection and special risks - code-related requirements.
2.2.3	The objectives and the degree of protection shall be determined on the basis of a risk evaluation.

Figure 15 — SIA 260 Basis of structural design (Par. 2.2)

Thus, there are two sides of the project, which have to be compared and matched in advance: the required performance, which is given by the service criteria requested by the client (owner) and the predicted performance, offered by the designer. Considering the required boundary conditions the performance of the proposed solution can only be evaluated by means of boundary criteria using simplified calculations or by numerical simulations. The alternative of reliable cal-

culations and designing charts involves, in the case of seismic design, a serious database of past events. In Switzerland, an area of moderate seismicity, this matter is very delicate as the recorded significant events are very few and a reliable set of results is therefore difficult to obtain. The other alternative of using simulations in order to deliver predicted performance provided the motivation of performing the above mentioned FE modelling. In this way it becomes very important to have a clear, straight-forward, simple and in the same time efficient method to approach design situations from the performance based perspective.

The finite element analysis for the sub-structure of an industrial building located in an alpine valley filled with fluvial sediments was conducted. The material input parameters for the 2D model were obtained from already existing data and the dynamic parameters were calibrated using the frequency domain analysis in the linear range. Finally the obtained results showed that the widely available PLAXIS software can actually provide a reasonable approach to the performance based design of structures, even though, in case of pile foundations, a 3D analysis should be preferred.

The effect of the super-structure on the entire system cannot be neglected, but as the target of the present paper was actually to confirm and present a possible approach of the performance based design, this effect was not effectively analysed. Joining together an appropriate modelling of the superstructure with the model presented in this paper will lead to a consistent qualitative and quantitative analysis.

References

Antes, H., Jessberger, H. L., Schmid, G., Chow, N., Forchap, E., Grundhoff, T., Laue, J., Le, R., Siemer, T. (1996). Dynamic and cyclic soil-structure interaction. In Krätzig et al. Eds. Dynamics of Civil Engineering Structures, pp. 451-532. A. A. Balkema, Rotterdamm.

Bathe, K. J. (1982). Finite element procedures in engineering analysis. Prentice-Hall, Englewood Cliffs.

Burjanek, J. (2011). Development of 3D Velocity Model for Visp area. Presentation at: Third Annual Meeting of COGEAR, January 2011.

Chari, T. R. & Meyerhof, G. G. 1983. Ultimate capacity of rigid single piles under inclined loads in sand. Canadian Geotechnical Journal, 20. pp. 849–854.

COGEAR Platform. (2010). https://geodata.ethz.ch/cogear/
Deichmann, N. & Ballarin-Dolfin, D. (2003). Seismotektonische Karte der Schweiz. Schweizerisches Erdbeben Dienst.

Bardet, J. P., Ichii, K. & Lin, C.H. (2000). EERA. A computer program for equivalent — linear earthquake site response analyses of layered soil deposits. University of Southern California. Department of Civil Engineering.

Fritsche, S. (2008). Large historical earthquakes in Switzerland. Multidisciplinary studies on damage fields and site-effects. Dissertation no. 17710. ETH Zurich.

Naylor, D.J. (1982). Finite element study of embankment loading on piles. Report for the Department of Transport (HECB). New Jersey.

Ng, C., Springman, S. M. & Norrish, A. (1998). Soil-structure interaction of spread-base integral bridge abutments. Soils and Foundations, 38(1). pp. 145–162.

Park, D & Hashash, Y.M.A. (2004). Soil damping formulation in non-linear time domain site response analysis. Journal of Earthquake Engineering, 8(2). pp 249–274.

Randolph, M.F. (1981). Pilot study of lateral loading of piles due to soil movement caused by embankment loading. Report for Department of Transport (HECB).

Résonance Ingénieurs-Conseils SA. (2010). Réévaluation du danger de liquéfaction du sol sur le site de Lonza à Viége. Rapport technique RT 226.26/CL/MK.

Roten, D., Fäh, D., Bonilla, L. F., Alvarez-Rubio, S., Weber, T. M. & Laue, J. (2009). Estimation of non-linear site response in a deep alpine valley. Geophysical Journal International, 178. pp. 1597–1613. doi: 10.1111/j.1365-246X.2009.04246.x.

SIA 261. (2003). Actions on structures. Registered code of the Swiss Standards Association. Zürich.

SIA 260. (2003). Basis of structural design. Registered code of the Swiss Standards Association. Zürich.

Tsang, N. C. M., England, G. L., Dunstan, T. (2002). Soil-Structure interaction of integral bridge with full height abutments. 15th ASCE Engineering Mechanics Conference. Columbia University, New York.

US Geological Survey. (2008). Iceland region earthquake 2008. ShakeMap Archive ID: sqba2008.

Visone, C. & de Magistris, F. S. (2010). Comparative study on frequency and time domain analyses for seismic site response. Electronical Journal of Geotechnical Engineering, vol. 15.

Weber, T., Laue, J. & Springman, S. M. (2007). Geotechnical laboratory tests for identification of soil parameters for the cyclic mobility model of sandy soil from Visp (VS). IGT Internal Project no. 4698. ETH Zürich.

Fatigue Analysis of a Steel Bridge Included in a High-Speed Railway Line

Rocha, João Francisco
University of Porto, Portugal

Delgado, Raimundo
University of Porto, Portugal

Calçada, Rui
University of Porto, Portugal

Abstract

The dynamic behaviour of bridges has been largely studied since the collapse of the first railway bridges. This dynamic behaviour is particularly important in high speed railway bridges which are usually exposed to important cyclic loading. These cyclic loads can lead to fatigue phenomenon in several structural elements of the bridge. Consequently, fatigue must be properly taken into account either during the design of new structures or during the assessment of existing ones.

The present paper focuses the fatigue analysis of an existing bowstring steel bridge in a high-speed railway line. A Finite Element Model of the bridge was developed and dynamic analyses of real train passage were made in order to obtain the structure response in terms of deformations, accelerations and stresses. This study is carried out according to the Damage Accumulation methodology and is based on the Eurocode procedures for fatigue analysis. Furthermore, a parametric analysis of the classification of the constructive details is performed in order to understand its influence regarding the structural fatigue damage.

Introduction

The dynamic behaviour of bridges has been largely studied. This dynamic behaviour is particularly important in railway bridges, especially in high speed lines, which could give rise to important resonant effects. Furthermore, railway bridges are usually exposed to important cyclic loads which make them sensitive to fatigue phenomenon. This phenomenon is especially important in high speed lines because of the high stresses induced in the steel elements by the heavy loads. This paper presents the fatigue analyses of an existing bowstring bridge based on the Damage Accumulation Method. This methodology allows the calculation of the fatigue damage induced by real traffic

scenarios. The principal steps for the fatigue damage assessment are: the definition of a traffic scenario and the selection of the suitable S–N curves to describe the fatigue resistance of the materials, the calculation of the stress history at each critical point of the structure (structural elements or constructional joint details), the identification of the extreme values of the stress history, the calculation of the stress range histograms (carried out through the Rainflow Method) and the calculation of the accumulated damage through the Palmgren-Miner rule.

The traffic scenario and the S–N curves must be chosen according to EN 1991, Part 2 [1] and EN 1993, Part 1–9 [2], respectively. Then, the stresses time histories are determined using the FE model. The local peaks of stresses are identified and the Rainflow Method is applied to convert the data into stress range histograms. The S–N curves cannot be directly applied to the stress history to calculate the fatigue damage unless all the stress amplitudes are constant. Thus, the Palmgren-Miner rule is applied to the stress histograms to account for the different stress ranges. According to this rule the fatigue damage should be the sum of all the partial damage for each stress range:

$$D = \sum_{i=1}^{n} \frac{n_{Ei}}{N_{Ri}} \quad (1)$$

where i is the number of different stress ranges, n_{Ei} the number of cycles for each stress range and N_{Ri} the number of resisting cycles for the respective stress range according to S–N curves. The fatigue limit criterion is D = 1.

For the fatigue analyses of an existing bridge, it is necessary to classify the structural profiles and the joint components. This step should be done according to the detail specification of [2]. Only with a correct classification of the constructional details can the fatigue damage be accurately assessed. Figure 1 presents three types of constructional details for three different types of fatigue failure.

Case Study

The present case study is a bowstring Bridge located in the Belgium high speed line, between Brussels and Köln. The Prester Bridge has an

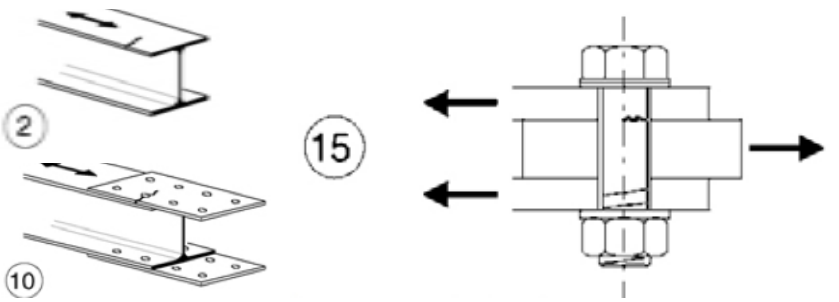

Figure 1 — Constructional details for classification (adapted from [2])

orthotropic metallic deck hanged by two lateral arches. These arches have a rectangular hollow section linked by four tubular hollow section girders. The deck has two main I-shape girders along the span at each side, forty-one T-shape cross girders, and twelve U-shaped longitudinal stiffeners (Figure 2). The arches are connected to the main girders by eleven squared hollow section hangers at each side of the deck. The total length of the bridge span is approximately 136 m covered by an 18 mm thickness steel slab.

(a) (b)

Figure 2 — Prester Bridge: a) side view and b) bottom view

The metallic bridges usually have complex joint details between the structural elements. Although the bridge presents both welded and bolted joints, the present work focuses only in the last ones. As an example, Figure 3 illustrates two types of bolted joints adopted in the Prester Bridge.

(a) (b)

Figure 3 — Bolted joint details: a) cross girders, b) hangers

For the dynamic analysis of the bridge, the three-dimensional model developed in [3] was used. A few improvements were made to this model in order to obtain the required stresses. The finite element model of the Prester Bridge was developed with shell elements for the deck and beam elements for the rest of the structural elements, such as hangars, main beams and arches. The track was modelled through beam elements for the rails and spring elements for both the pads and the ballast stiffness. The mass of the ballast, sleepers and rails was included on the shell elements of the deck. The FE model was developed with the software ANSYS10.0 (Figure 4).

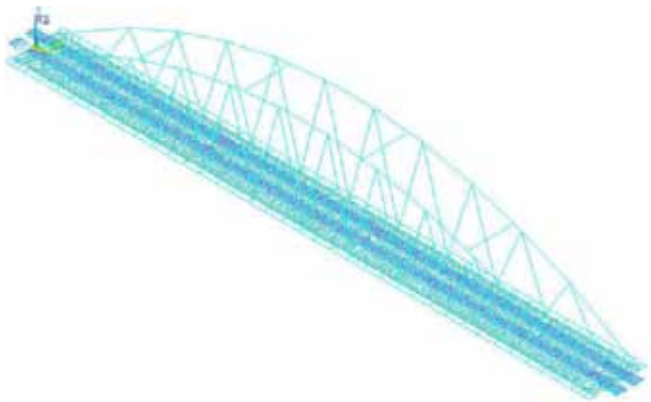

Figure 4 — FE model of the Prester Bridge

Fatigue Analysis

The dynamic analyses of the crossing of the real train on the bridge were performed considering a linear-elastic model. The modal superposition method was applied in the calculations. According to EN 1990-A2 [4], the scope of the modal analysis must be within the range of frequencies of [0-30] Hz, resulting in 246 modes of vibration (some examples at Figure 5).

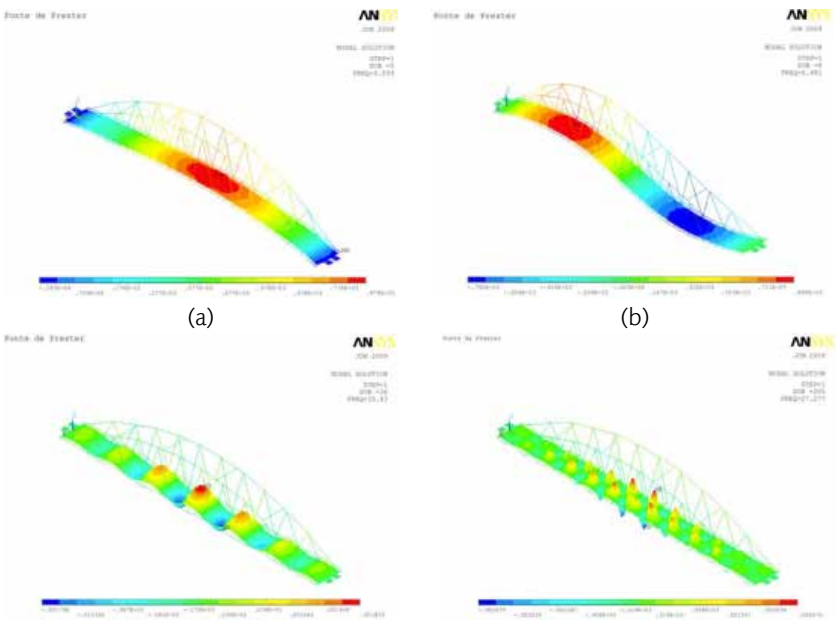

Figure 5 — Vibration modes of the Prester Bridge:
a) and b) global modes,
c) Intermediate modes and
d) Local modes

Since the bridge is located in the high speed line between Belgium and Germany, the train used in the fatigue analyses is the Thalys train. A traffic scenario of 50 train passages/day is considered. This train is approximately 393 m long, has a load per axle of 170 kN and a circulating speed of approximately 300 km/h. The fatigue analysis was performed for the range of speeds of [250–500] km/h, considering a time step of 2 milliseconds. The values considered for the damping ratios of each vibration mode are described in [5].

The fatigue damage was analysed on the rolled steel profiles and their bolted joints. Three different parts of the bolted joints are analysed in the present work: the rolled steel profile with holes, the cover plate and the bolts. The classification of these constructional details was performed according to [2] and for further details [5] should be consulted. The fatigue damage results presented in this study are shown in percentage, i.e., 100% of fatigue damage corresponds to the fatigue limit criterion.

Main Girders

The main girders are one of the most important structural elements of the bridge. So, it is important to carry out an accurate analysis of the damage over the years. According to the classification of the structural elements and joint details specified in [5], the fatigue damage of the main girders is presented in Figure 6.

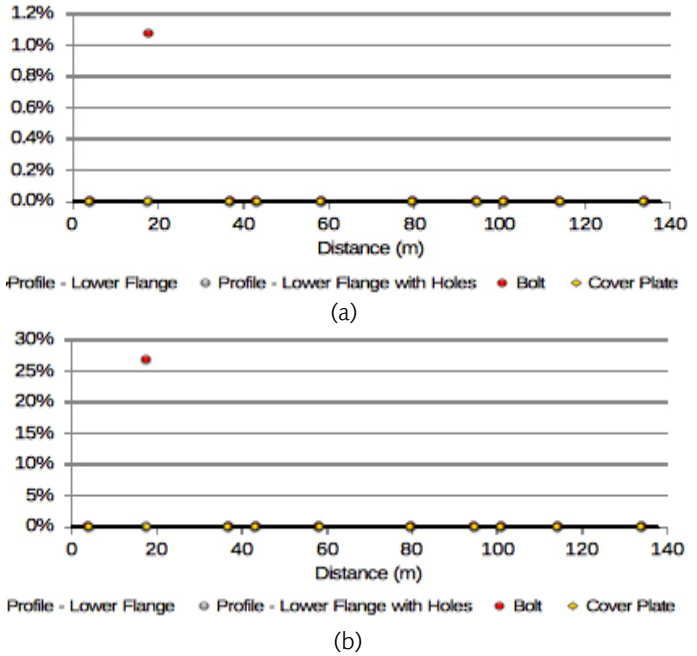

Figure 6 — Fatigue Damage on the main girders:
a) speed of 350 km/h,
b) speed of 450 km/h

The results presented in Figure 6 show that the fatigue damage for 100 years is significantly low for the speed of 350 km/h (only the bolts at the joint at approximately 17 m have some damage). Similar conclusions can be withdrawn for the speed of 450 km/h where damage only occurs on the bolts. In this case, the damage is close to 25% of the fatigue damage limit. The conclusions are similar for several other circulating speeds. However, for a speed of 490 km/h it is possible to observe higher fatigue damage even for the rolled steel profile.

Cross Girders

For the analyses of the T-shape cross girders the same details of the joints are considered. The results of the fatigue damage of one of the cross girders, located approximately at 19 m, can be observed in Fig. 7. Fatigue damage in the cross girders is only registered for speeds higher than 450 km/h.

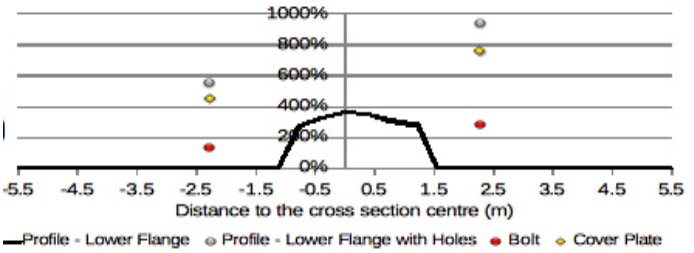

Figure 7 — Fatigue Damage on a cross girder for the speed of 490 km/h

The results presented show that the reduced flange of the girder is the critical section. However, the cover plate has almost the same value of damage over 100 years. It can be also noted that the rolled profile has higher damage in the centre of the cross section of the bridge. Obviously, fatigue damage values over 100% are not admissible, i.e., the fatigue life for these details is under 100 years.

Longitudinal Stiffeners

The U-shape longitudinal stiffeners do not have joints or any other bolted connection details. This way, only the results of the rolled steel profile are presented. Only the results for the longitudinal stiffener under the centre of the track are presented because it is the section which is exposed to higher stress range.

The longitudinal stiffeners are very sensitive to vibration caused by rail traffic. Since the rigidity of these elements is relatively low high fatigue damage values can be observed in some locations for a speed of 350 km/h (Figure 8).

Hangers

The hangers, like the arches and the main beams, are one of the most important structural elements of the bridge. These elements transfer the loads from the main girders to the arches. They have two different bolted joints, the first one between the square hollow section of the hanger and the I-shape rolled profile and the second between this profile and the main girder. The results of the fatigue damage for all hangers are in Figure 9. Through the analysis of the results presented in Figure 9, it is concluded that for the speed of 350 km/h the fatigue damage on the bolts (either first or second joint detail) are relatively high and very close to the limit criterion. For the train speed of 450 km/h, this limit is exceeded on the bolts of five of the hangers. However, it was not for the same hangers that registered the higher fatigue damage for the speed of 350 km/h.

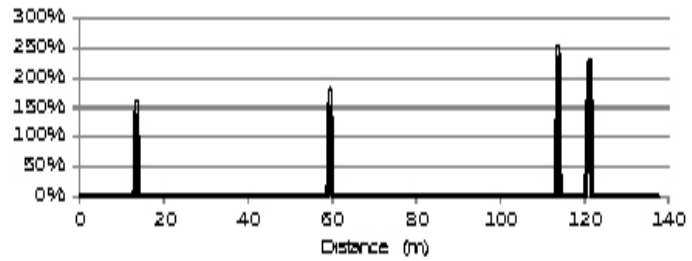

Figure 8 — Fatigue Damage over a longitudinal stiffener flange for the speed of 350 km/h

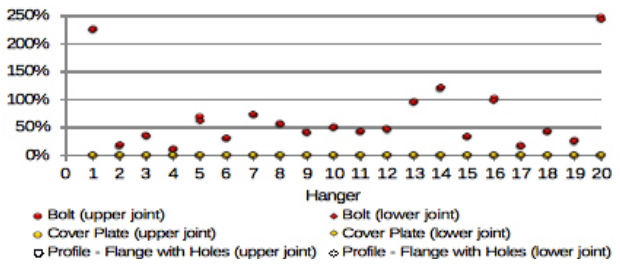

Figure 9 — Fatigue Damage for the hangers:
a) speed of 350 km/h,
b) speed of 450 km/h

Parametric Fatigue Analysis

As a final analysis, a parametric study was performed in order to understand the influence of the fatigue resistance classification of the constructional details and also the influence of the frequency range on the damage of the structure.

Detail Categories

The constructional details classification of an existing bridge can be ambiguous. So, the calculation of the fatigue damage may not be accurate. To understand the influence of this classification, a parametric analysis is carried out considering three suitable categories of resistance for each constructional detail. For the main girders and the longitudinal stiffeners only the rolled steel profiles can be classified differently. In the case of the cross girders, it is possible to apply different categories to the rolled profile and the cover plates. The hangers are a specific case because the classification of almost every component offers no doubt. The only exception is the cover plates that can be classified one or two categories higher.

Main Girders

As mentioned before, the classification of the constructional details can be ambiguous. To understand how important the classification of resistance of the constructional details is for the fatigue damage two categories of resistance are analysed for the main girders (one upper and one lower) in addition to the reference category (112 MPa) [5].

As it can be seen in. Figure 10, for the category of resistance of 125 MPa the fatigue damage is almost zero (for a train speed of 490 km/h). However, when the lower category is considered, the fatigue damage increases almost 60%, in the cases where damage already exists.

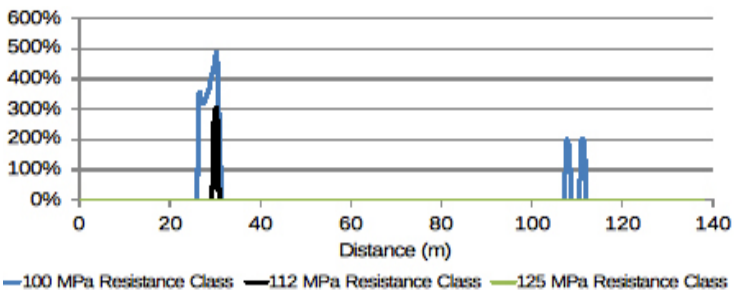

Figure 10 — Comparison of the fatigue damage of the main girders for the speed of 490 km/h

Cross Girders

In the case of the cross girders three categories of resistance for the rolled profiles and the cover plates are analysed. Figure 11 presents the results of the comparison with the reference category (112 MPa). Figure 12 shows the comparison between three categories of resistance of the cover plate. The main concern in the cross girder must be the holed flange of the steel profile. However, since there is no other category of resistance for this type of detail, the parametric analysis is considered only for the cover plate.

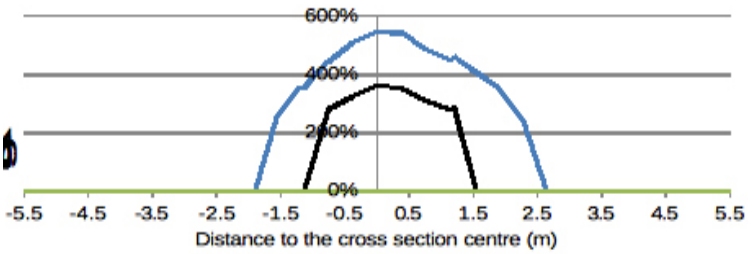

Figure 11 — Comparison of the fatigue damage of the rolled steel profile of a cross girders for the speed of 490 km/h

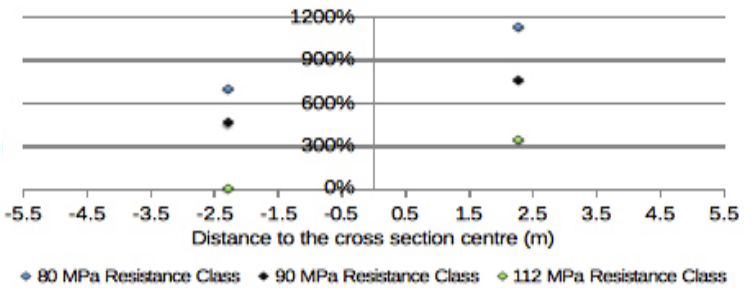

Figure 12 — Comparison of the fatigue damage of the cover plate of the joint of a cross girders for the speed of 490 km/h

The analysis of Figure 11 shows that the damage for the upper category of resistance is practically zero. This is valid as long as this option is correctly justified. However, the consideration of the lower category results in an increase of the structural fatigue damage of over 50%. As it can be seen in Figure 12, the consideration of the upper category of resistance reduces significantly the final damage of the cover plate.

Longitudinal Stiffeners

As mentioned before, the longitudinal stiffeners are very sensitive to vibrations caused by rail traffic. Therefore, it is observed that the fatigue damage is already high for a train speed of 350 km/h. However, in terms of project management, the category of resistance can be decided in order to improve the damage over the years. In this case, applying a profile with an upper category of resistance can improve the fatigue resistance of this element. Figure 13 presents the comparison between the reference category and an upper resistance category.

As it can be seen, for the speed of 350 km/h, an increase of the resistance category improves the fatigue damage in an important way. It can also be seen that the reduction of fatigue damage for speeds over 350 km/h is relevant in the case of consideration of the category of resistance of 80 MPa.

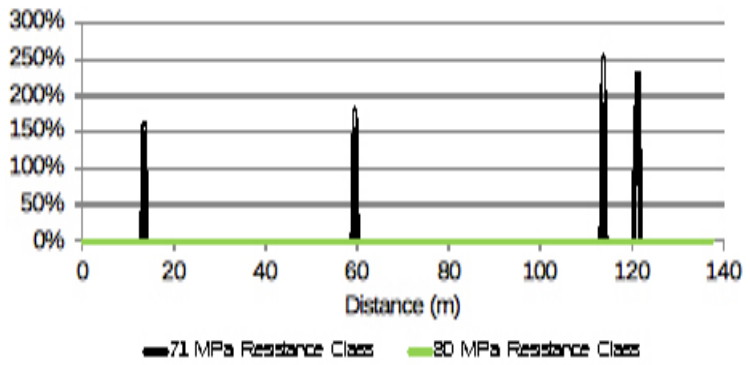

Figure 13 — Comparison of the fatigue damage of a longitudinal stiffener flange for the speed of 350 km/h

As it can be seen, for the speed of 350 km/h, an increase of the resistance category improves the fatigue damage in an important way. It can also be seen that the reduction of fatigue damage for speeds over 350 km/h is relevant in the case of consideration of the category of resistance of 80 MPa.

Hangers

The results presented in Figure 9 show that the fatigue damage on the hangers occurs essentially on the bolts. The only way to reduce this problem is applying preloaded bolts to this type of joints. In that case, the shear force is not taken into account because the resistance is due to the friction between the steel plates. This way, the fatigue analysis is not performed in these elements.

Frequency Range

The dynamic analyses of the bridge considered the range of frequencies from [0–30] Hz. For an accurate fatigue analysis this may not be sufficient. Therefore, a dynamic analysis is carried out considering frequencies until 42 Hz. The next sections presents the comparison between the results obtained for the cross girders and the hangers for different frequency limits.

Cross Girders

The cross girders are one of the elements more subjected to intermediate and local modes of vibrations, essentially present in frequencies higher than 30 Hz. Figure 14 presents the results for the steel profile and for the cover plate of one of the cross girders.

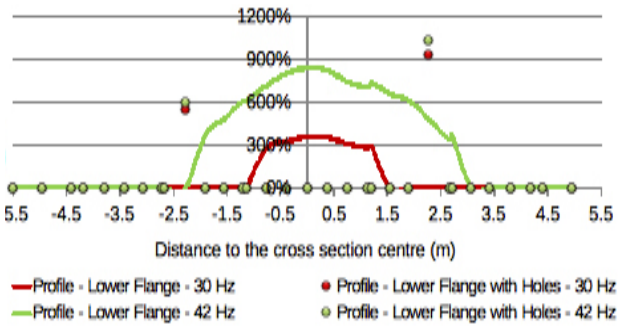

Figure 14 — Comparison of the fatigue damage of a cross girder for the speed of 490 km/h

As expected, accounting for a larger number of vibration modes can influence the final results of the fatigue damage. As shown in Figure 14 accounting for frequencies up to 42 Hz generates a higher fatigue damage, especially at the centre of the cross girder.

Hangers

The hangers are one of the essential structural elements of the bridge. Hence, an accurate prediction of the fatigue damage is important. Figure 15 presents the results of the fatigue damage for the hangers, considering frequencies up to 42 Hz.

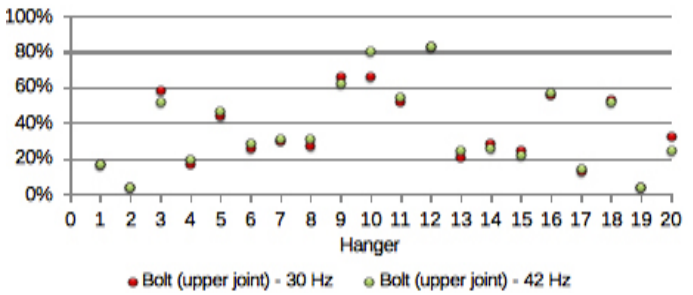

Figure 15 — Comparison of the fatigue damage on the hangers for the speed of 350 km/h

These results show that accounting for a larger range of frequencies directly affects the fatigue damage of the hangers. However, it cannot be said that frequencies up to 42 Hz have a negative impact on the fatigue damage because not all of the hangers present a higher damage comparing to the first analysis.

Conclusions

This work focuses on the fatigue analysis of the principal structural elements of a bowstring bridge inserted in a high speed railway line. A procedure for the fatigue analysis was presented based on the Damage Accumulation Method. The Thalys train was considered for the fatigue analysis.

The case study used was presented and consisted on a bowstring bridge. The structural elements analysed were the main girders, the cross girders, the hangers and the longitudinal stiffeners. The bolted joints details were also analysed. The classification of the resistance category of the profiles and the joint details was done according to the Eurocodes.

The fatigue analysis showed that the main and cross girders do not have relevant fatigue damage for train speeds below 400 km/h. In the case of the hangers it was observed that for a train speed of 350 km/h some hangers already present significant fatigue damage. However, the main fatigue damage is registered on the longitudinal stiffeners due to their low rigidity. In these elements, high levels of damage occur for speed of 350 km/h.

The fatigue analysis is sensible to various aspects of the dynamic analysis. To reduce the uncertainty of the results a parametric analysis was performed. The first topic analysed was the influence of the fatigue resistance classification of the constructional details according to the Eurocodes. It was shown that with small changes on the specificities of the joints details, the fatigue damage can be reduced. The second topic analysed was the frequency range that should be considered in the dynamic analysis. It was concluded that the cross girders are very sensitive to the vibration modes between 30 Hz and 42 Hz. The hangers present a lower sensibility to this increase of number of vibration modes. However, in general, the increase of the frequency range results in an increase of the fatigue damage.

References

[1] *CEN (2003). EN 1991-2 — Eurocode 1: Actions on structures — Part 2: Traffic loads on bridges. Brussels.*

[2] *CEN (2005). EN 1993-1-9 — Eurocode 3: Design of Steel Structures — Part 1–9: Fatigue. Brussels.*

[3] *Albuquerque, C., (2008). "Dynamic behaviour of high speed railway bridges with orthotropic deck", MSc. Thesis (in Portuguese). Faculty of Engineering of University of Porto. Porto.*

[4] *CEN (2005). EN 1990-A2 — Eurocode 0: Basis of Structural Design — Annex A2: Applications for Bridges. Brussels.*

[5] *Rocha, J. F., (2009). "Fatigue Analysis of high speed railway steel bridge with orthotropic deck", MSc. Thesis (in Portuguese). Faculty of Engineering of University of Porto. Porto.*


ENERGIE

Classification of timber–steel connections and the behaviour of semi rigid joints

GEČYS, Tomas
Department of Steel and Timber structures, Vilnius Gediminas technical University, Lithuania

Abstract

Semi rigid mounting joints of glued laminated timber elements are connections which are fully assembled on construction site and capable to take bending moments, axial and shear forces. The need of new type semi rigid timber elements' connections is obvious. Possibilities of glued laminated timber elements' manufacture are wide: straight element's length may be till 40 m or curved axis elements with dimensions till 10 meters in height. So every day manufacturers, erectors and others face with transportation problems of non–standard oversized elements. Semi rigid mounting joints are used for this purpose. Non–standard oversized glued laminated timber elements are cut into standard transportation dimensions in factory and fully assembled into integral element on construction site using semi rigid mounting joints. In this article the main types of timber joints are discussed and the classification according to strength and stiffness is presented. The influence of joint's rotational stiffness on effective length of element is discussed. Laboratory experiments of semi rigid timber joints which are carried out by author are discussed.

Introduction

Glued laminated timber is universal structural material which is widely used in glued laminated timber elements' manufacture ([4]). Glued laminated timber elements may be straight or curved axis till 40 m in length and till 2.20 m in height.

The critical point of glued laminated timber elements is design and manufacturing of joints ([3]). Timber is anisotropic material with different physical and mechanical properties along and perpendicular to the grain. Joint can easily collapse because of exceeded stress in one

direction while in other direction there will be safe stage of stress. The main collapse form is timber splitting along the gain which cause in sudden loss of bearing capacity ([4]).

All timber structures' joints generally treated as pinned (taking axial and shear forces) or rigid (taking axial, shear forces and bending moments). Analysing timber–steel joints in more detail, third type of joints can be distinguished; it is semi rigid joints ([9]). An example of semi rigid mounting timber joint with steel plates and dowels is shown in Figure 1.

In timber structures almost all connections (between column and foundation or column and beam) can be treated as semi rigid joints. Timber element joint's rotational stiffness is analysed by dividing joint into components. All joints where large compression stresses arise in contact zone perpendicular to the grain can be treated as semi rigid connections because modulus of elasticity perpendicular to the grain is about 7 times less than along the grain.

It is reasonable to take into account the real joint's behaviour when we need to design optimal cross sections of frame elements'. Taking into account the real behaviour of joints there is possibility to redistribute bending moments of frame elements' ([1]). Element's joints rotational stiffness has great influence on element's effective length.

Classification of timber–steel joints

As it was mentioned before, traditionally all timber–steel joints are divided into two types: pinned (Fig. 2) and rigid (Fig. 3). In Figure 2 there is pinned support which can easily rotate around steel dowel and such joint does not cause any bending moments in timber element at the support.

Figure 1 — Semi rigid beam to beam mounting joints in glued laminated timber structures in Moscow sport centre (joints are shown in the circle)

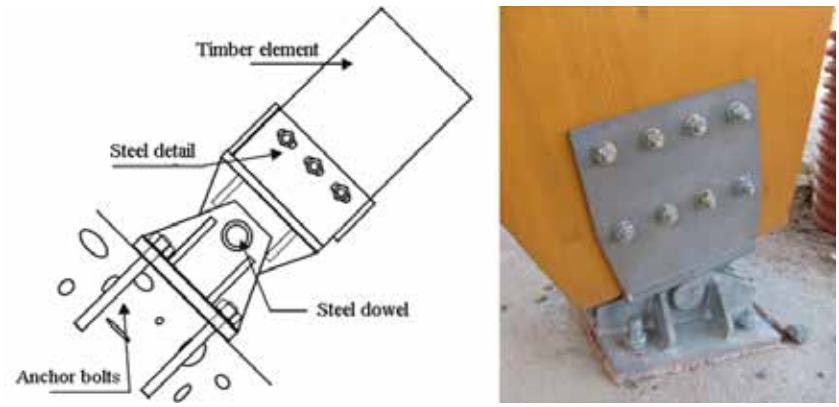

Figure 2 — Glued laminated timber element's pinned support

In Figure 3 there is rigid mounting joint with glued in steel rods. Based on previous studies which experimentally and theoretically analysing glued in rods in timber structures, it can be said that such joints create tight contact between timber and steel because even at failure the displacement between timber and steel rod is about 0.5–0.8 mm ([3]).

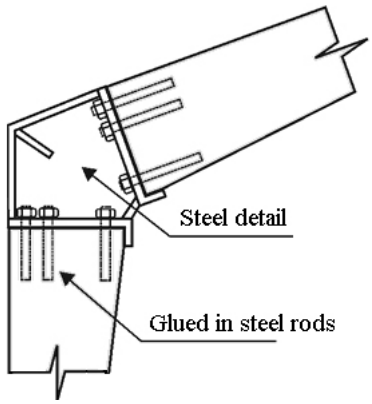

Figure 3 — Rigid mounting joint of glued laminated timber frame

In Figure 4 these is schematic view of semi rigid timber steel joint. Analysing timber joints' rotational stiffness it was noticed that almost all joints in timber structures which are assumed as rigid, can be treated as semi rigid, except flocked connections which are shown in Fig. 3.

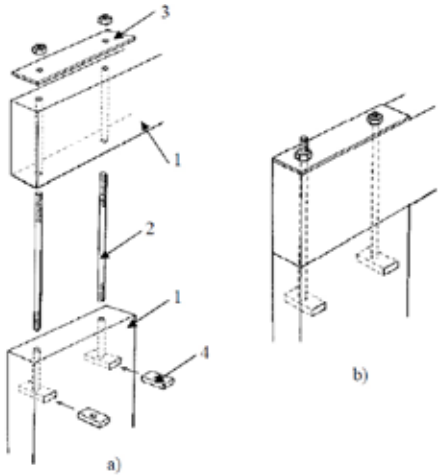

Figure 4 — Semi rigid timber steel mounting joint:
1 — timber element,
2 — steel bar,
3 — steel plate,
4 — increased washer

Timber joints can be classified according to strength (Table 1) and rotational stiffness (Table 2) ([6]). Classification according to stiffness is based on element's effective rigidity (EI/L) and initial joint's stiffness ($S_{j,ini}$). In normative documents there are no classifications of timber joints according to strength and stiffness. Classification of steel joints presented in EN 1993-1-8. Comparing timber and steel joints' classification, it can be noticed that semi rigid timber joints' rages are narrower than steel.

Table 1 — Timber joints' classification according to strength

Joint	Condition
Full strength	$M_{j,Rd} \geq 0.85\ M_{full\text{-}stregth}$
Partly strength	$0.25\ M_{full\text{-}stregth} < M_{j,Rd} < 0.85\ M_{full\text{-}stregth}$
Pinned	$M_{j,Rd} \leq 0.25\ M_{full\text{-}stregth}$

Table 2 — Timber joints' classification according to stiffness

Joint	Condition
Rigid	$S_{j,ini} \geq 12\ EI/L$
Semi rigid	$0.5\ EI/L < S_{j,ini} < 12\ EI/L$
Pinned	$S_{j,ini} \leq 0.5\ EI/L$

From Table 1 it is seen that joint can be treated as full strength joint when joint's strength is more than $0.85\ M_{full\text{-}stregth}$ so there is no such requirements as for steel joints. In steel joints' classification there are two cases when joints are treated as full strength, it is for frames with bracing and without bracing. When frames are with bracings, there are smaller restrictions for rigid joints and the use of them is wider ([1]).

Previous studies and types of analysis

Increasing demand for material savings and searching for rational connections' solutions, it was started to analyse the actual behaviour of the joint. Semi rigid timber steel joints analysed by: laboratory experiments ([5, 7]), computer simulation and component method ([5]). Laboratory experiment is one of the most popular types of analysis. Using laboratory experiments joints are analysed in: beam to beam connections ([7]), corner frame connections ([8]). Usually finite element modelling of connections is used together with laboratory experiments to validate results ([5, 8, 9]).

One of requirements for semi rigid as well for rigid timber joints is elimination of the initial movement of the joint. So it means that joint's components need to be provided with initial pretension of pre-compression. This problem is being solved by various methods: using bolts with initial pretension and steel details ([8, 9]), using timber or steel wedges ([5]), using filler to fill gaps between timber and steel ([3]).

Using different thickness wedges, there is possibility to obtain joints with different rotational stiffness. Thickness of wedge influences rotational stiffness, especially initial, but it does not have influence on final bearing capacity of the joint ([5]).

Joint's strength and stiffness are analysed by component method. Analysing joint by component method, joint is divided into separate components and than analysed strength and stiffness of each component ([2, 6]). In Fig. 5 semi rigid timber joint with separate components is presented. In Fig. 5 only components with timber compression are presented. While analysing such joint's behaviour (strength and stiffness), steel details (steel detail and bar) must be taken into account.

Joint's strength analysis usually performed using component method: calculating each component bearing capacity and than joint's bending bearing capacity is determined. Bearing capacity of timber element compression can by found from equation 1:

$$F_{u,i} = A_i \cdot f_{c,\beta,d} \qquad (1)$$

In equation 1:

A_i — area of component i,
$f_{c,\beta,d}$ — strength of timber in compression.

After calculation of each component bearing capacity, bearing capacity of the joint can be found from equation 2:

$$M_u = \sum_i F_{u,i} \cdot z_i \qquad (2)$$

In equation 2:

$F_{u,i}$ — bearing capacity of component i,
z_i — distance from component's i area centre to centre of joint's rotation.

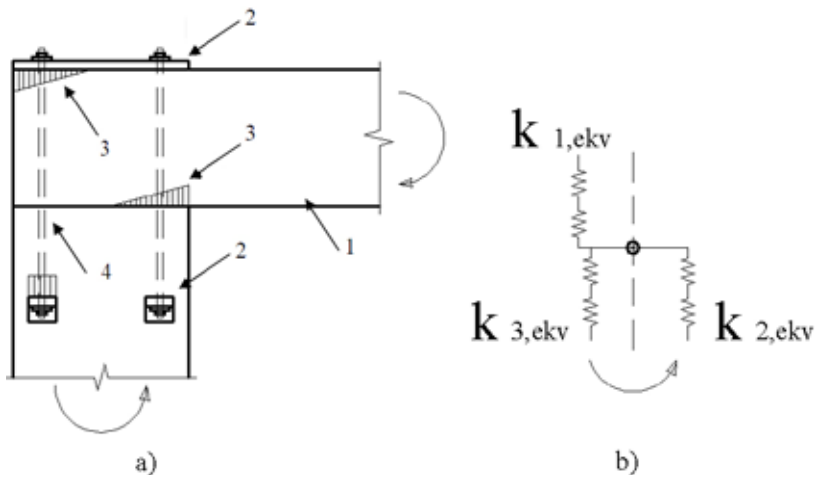

Figure 5 — Semi rigid timber steel mounting joint:
a) joint's scheme, b) strength and stiffness components,
1 — timber element,
2 — steel detail,
3 — contact stress,
4 — steel bar

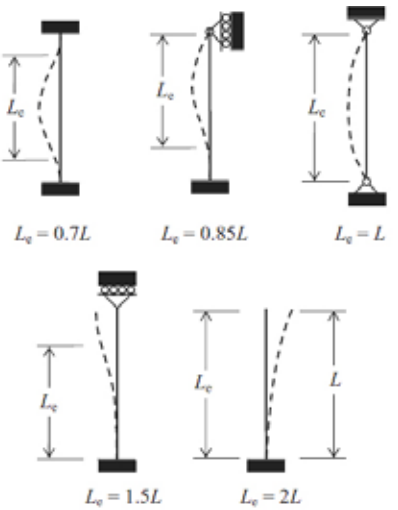

Figure 6 — Traditional cases of determining the effective length of timber element

Influence of joints' rotational stiffness on element's effective length

Joint's rotational stiffness has high influence on element's effective length. Traditional element's end joints' and length coefficients are shown in Figure 6. These effective lengths are the same according to EC5 and Lithuanian timber structures design codes.

When taking into account element's joint rotational stiffness, the effective length can be increased or decreased. Some cases of determination element's with semi rigid joints, effective length are shown in Fig. 7 ([1]).

Generally, truss elements are treated as beams taking only axial tension and compression forces, so their effective lengths' coefficients are equal to 1.0. This is not correct assumption because usually there are more than two bolts, so there is no free rotation at the joint. The same case is with frame's corner joint between column and beam. When taking into account joints' rotational stiffness there is possibility to reduce element's effective length.

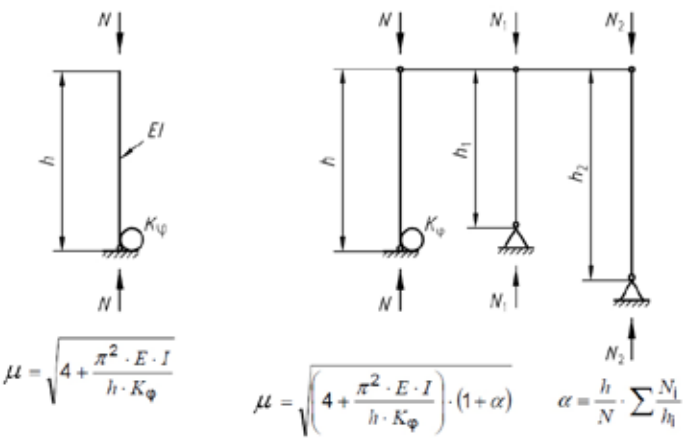

Figure 7 — Some examples of determination the effective length of the element when taking into account the support rigidity

The main design principles of semi rigid mounting timber steel connections

The most responsible part in semi rigid timber steel joint is reliable steel detail's anchoring in timber element. In fact, four design principles which are used to anchor steel detail into timber element can be identified. The simplest method is to use steel plates and bolts to fix steel detail into timber ([14, 15]). Another way is to use glued in steel rods to anchor mounting steel details. The third method to anchor steel detail is to use wedges or fillers to fill the gap between timber and steel. This method's superiority is that using wedge the initial rotational stiffness of the joint can be controlled or just to ensure tight initial contact between timber and steel by using fillers. One more method is to use large diameter circular section steel details, which are anchored in timber by studs. Peter Bertsche developed this solution in mounting timber elements' joints ([16]).

Laboratory experiments of new type semi rigid timber steel connections are being done in Vilnius Gediminas technical university. Experimentally and theoretically analyzed connection is made of three different materials: the main element is timber, steel details are used to connect these elements and the third material is filler which is used to fill the gap between timber and steel, so that timber and steel would have initial contact before loading. Two types of fillers are used: two component polyurethane based filler and the other is cement based filler.

Conclusions

1. Joint's rotational stiffness has great influence on distribution of bending moments in frame's elements. It is useful to take into account the actual behaviour of joints when we need to design > optimal cross sections of timber elements.
2. Joint's effective length in some cases can be reduced when taking into account joint's actual behaviour, especially for joints which are tend to be as pinned.
3. Semi rigid timber elements' joints can be analysed by: laboratory experiments, computer simulation (modelling by finite element) or component method (analytically). Usually finite element modelling is done with laboratory experiments to validate results.
4. All timber elements' rigid connections where high stresses perpendicular to the grain occur must be treated as semi rigid joints.
5. First laboratory experiments of semi rigid joints showed that there is possibility to use fillers (to fill gaps between timber and steel and to create tight initial contact between these three materials) in semi rigid timber steel joints.

References

[1] *Racher, P. (1995). Moment resisting connection. Proceedings of Timber Engineering STEP I, C16/1-C16/10, Center Hount.*

[2] *Jirka, O., Mikes, K. (2010). Semi–rigid joints in timber structures. An International Journal for Engineering and Information Sciences, 5(2): 19–26.*

[3] *Gečys, T., Gurkšnys, K., Rasiulis, K. (2011). Jungties įklijuotojo plieninio sriegtojo strypo ir medienos elgsenos tyrimas. Engineering Structures and Technologies, 3(1): 5–15.*

[4] *Guan, Z., Rodd, P. D. (1999). Hollow steel dowels — a new application in semi–rigid timber connections. Engineeri ng Structures, 23 (2001): 110–119.*

[5] *Guan, Z. W., Kitamori, A., Komatsu, K. (2008). Experimental study and finite elemet modelling of Japanese "Nuki" joints — Part two: Racking resistance subjected to different wedge configurations. Engineering Structures, 30 (2008): 2041–2049.*

[6] *Chang, W. S., Hsu, M. F., Chen, C. J. (2004). Estimating rotational stiffness of timber joints by using fractional factorial experiments combined with computer simulation. 8th World Conference on Timber Engineering, Lathi, Finland.*

[7] *Komatsu, K., Hosokawa, K. (1998). Glulam semi–rigid portal frames composed of hardwood wedges and metal wares. Proceedings of the 5th World Conference on Timber Engineering, 2: 246–253, Montreux, August.*

[8] *Vašek, M. (2008). Semi rigid timber frame and space structure connections by glued-in rods. WCTE 2008 Conference Proceedings, Vol. 1, S. 207, Miyazaki, Japan.*

[9] *Vašek, M., Vyhnalek, R. (2006). Timber semi rigid frame with glued–in–rods joints. WCTE 2006 Conference Proceedings, Vol. 1, S. 275, Portland Oregon State University, Portland.*

[10] *Kermani, A. (1996). A study of semi–rigid and non–linear behaviour of nailed joints in timber portal frames. International Journal of Forest Engineering, 7(2): 17–33.*

[11] *EN 1995-1-1:(2004). Eurocode 5. Design of timber structures. Part 1–1: General–Common rules and rules for buildings.*

[12] *EN 1993-1-8:(2003). Eurocode 3. Design of steel structures. Part 1–8: Design of joints.*

[13] *STR 2.05.07:(2005). Medinių konstrukcijų projektavimas. Vilnius, 2005.*

[14] *Awaludin, A., Smittakorn, W., Hayashikawa, T., Hirai, T. (2007). M–theta curve of timber connection with various bolt arrangements under monotonic loading. Journal of Structural Engineering, Vol. 53/A 853–862.*

[15] *Bruehl, F., Kuhlmann, U., Jorissen, A. (2011). Consideration of plasticity within the design of timber structures due to connection ductility. En gineering Structures, 33 (2011) 3007–3017.*

[16] *Steiniger, M. (2003). Tensile strength and performance of the INDUO–heavy timber connector in combination with structural composite lumber and Douglas fir. Master's thesis, The University of British Columbia, Vancouver, Kanada.*

Numerical simulations of pseudo-dynamic full-scale test on a three story — one span — three bays steel frame

IOAN, Adriana Mirela
Politehnica University of Timisoara, Romania

Abstract

The proposed research aims at reducing the repair costs and downtime of a structure hit by an earthquake, and consequently more rational design approach in the context of sustainability. These objectives are to be attained through removable dissipative members and re-centring capability of the structure, concepts that are to be implemented in a dual structure, obtained by combining steel eccentrically braced frames with removable bolted links with moment resisting frames. Numerical simulations and experimental tests were done in order to assess the performance and investigate the possibility to replace bolted links within a realistic structure following significant inelastic deformations and the practical feasibility of the replacement procedure. Practical solutions regarding order in which bolted links need to be replaced are proposed. Once the seismic link is removed from the structure, this system slowly releases the accumulated forces and the structure comes back to its initial position.

Introduction

Different strategies can be employed in order to reduce damage to structures under moderate to strong earthquakes. The most radical solutions are base isolation and various implementations of active and semi-active structural control. Other strategies rely on supplemental damping conferred to the structure through various devices based on viscous, friction, or yielding dampers. More or less efficient for reduction of structural damage, all these solution have the disadvantage of requiring specialised knowledge at the design stage and during erection, need for careful maintenance and high initial cost. Alternatively, a conventional design can be employed, but with the dissipative members realised to be removable (e.g. through bolted connections),

allowing replacement of the dissipative elements damaged as a result of a moderate to strong earthquake, and reducing the repair costs. For the structure to be repairable, in addition to constraining inelastic deformations to removable dissipative members, the permanent (residual) drifts should be eliminated.

The proposed research aims at reducing the repair costs and downtime of a structure hit by an earthquake, and consequently more rational design approach in the context of sustainability. These objectives are to be attained through removable dissipative members and re-centring capability of the structure, concepts that are to be implemented in a dual structure, obtained by combining steel eccentrically braced frames with removable bolted links with moment resisting frames. The bolted links are intended to provide the energy dissipation capacity and to be easily replaceable, while the more flexible moment resisting frames would provide the necessary re-centring capability to the structure. The columns of the structure are to be realised from high strength steel, in order to keep these members in the elastic range even under strong seismic input. The validation of the proposed solution is to be realised through a pseudo-dynamic test of a full-scale model of a dual eccentrically braced structure at the European Laboratory for Structural Assessment (ELSA) facility at JRC in Ispra.

Removable bolted links in eccentrically braced frames

Application of the concept of removable dissipative members to eccentrically braced frames (EBFs), where links act as dissipative zones, is presented in Figure 2. The connection of the link to the beam is realized by a flush end-plate and high-strength friction grip bolts. The

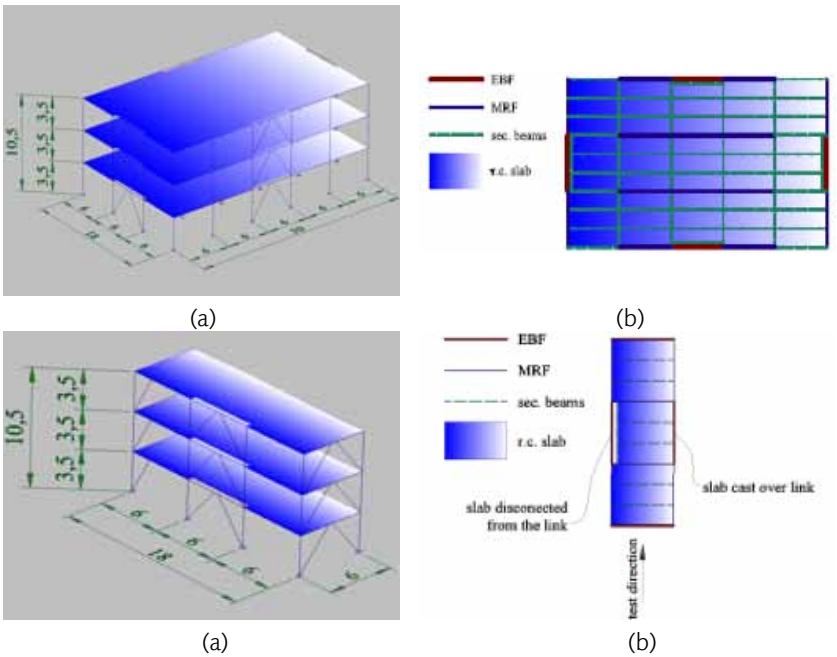

Figure 1 — General view (a) and plan layout (b) of the test structure

main advantage over other dissipative devices is the fact that removable links can be designed using methods readily available to structural engineers and can be fabricated and erected using procedures standard to the profession.

Three series of experimental tests on removable link assemblies were carried out at the "Politehnica" University of Timisoara in order to determine cyclic performance of bolted links and to check the feasibility of the removable link solution (Stratan & Dubina 2004 [1], Dubina et al. 2008 [2], Danku, 2011 [3]). The first series of tests was realised on isolated links (see Figure 3a–b), while the other two on almost full-scale model of a single bay and single storey eccentrically braced frame with removable link (see Figure 3c). Tests on links showed an important influence of the connection on the total response of the bolted link, in terms of stiffness, strength and overall hysteretic response. Shorter links were found to be suitable for the bolted solution, as plastic deformations were constrained to the link, while the connection response was almost elastic, allowing for an easy replacement of the damaged link. At the frame level, the experimental tests showed that the removable link solution is feasible. Inelastic deformations were constrained to the removable links alone, all other frame members and connections remaining in the elastic range. Additionally, it was possible to replace the damaged removable links with new elements.

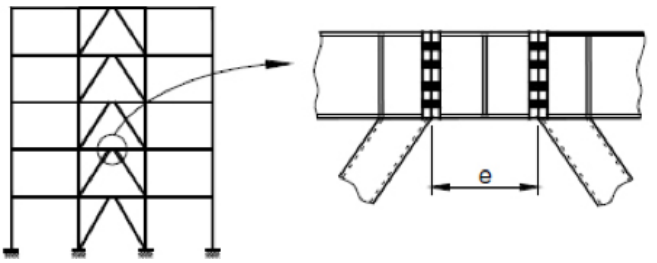

Figure 2 — Bolted link concept

Bolted extended end-plate connections for eccentrically braced frames with link-column connection configuration were previously investigated experimentally by Ghobarah & Ramadan (1994) [4]. Their inelastic performance was found to be similar to fully-welded connections. Balut & Gioncu (2003) [5] suggested a replaceable solution for links in eccentrically braced frames, and investigated more in detail two replaceable "dog-bone" solutions in moment-resisting frames:

(a) (b) (c)

Figure 3 — Experimental test on removable bolted link (a), tests on almost full-scale frame with bolted links (b) and test on almost full-scale model of a single bay and a single storey eccentrically braced frame with removable link (c).

one using an I-beam extended end-plate bolted connection, and another one consisting of two channels bolted using high-strength friction-grip bolts to the beam. Mansour et al. (2006) [6] investigated experimentally replaceable shear links composed of two bolted back-to-back channels. The links exhibited a ductile behaviour, with stable hysteretic response, but the connections were found to be critical in the design of removable links.

Dual-frame re-centring systems

Most of the structures designed to modern code procedures would experience inelastic deformations even under moderate seismic action, with permanent (residual) displacements after the earthquake. Repair is difficult in such cases. Solutions providing self-centring of the structure exist, but are technically demanded (post-tensioned strands, shape memory alloy devices, etc.). An alternative solution is the one that provides re-centring capability (as opposed to self-centring), through removable dissipative members and dual (rigid-flexible) structural configuration.

Past numerical and experimental research on removable link assemblies and eccentrically braced frames with removable links showed that this is a feasible solution for earthquake resistant construction. However, there are critiques to the removable link solution. One concerns permanent (residual) deformations of the structure after a damaging earthquake, which can lead to difficulties in replacing removable links.

This issue can be solved by realising a structure as a dual one, by combining eccentrically braced frames (EBFs) with moment-resisting frames (MRFs). The elastic response of the flexible subsystem (MRF) can provide the re-centring capability to the structure, once the links damaged during an earthquake are removed. For this principle to be efficient, the flexible subsystem should remain in the elastic range. A possible way to favour this is to realise some members from high-strength steel. Additionally, the residual deformations of the link should allow bolt removal. If these deformations are too large, it is possible to slowly release the residual stresses and deformations in the link by removing part of the link through flame cutting prior to removing the bolts, eliminating thus the residual stresses in the link.

An idealized dual system consisting of two inelastic springs connected in parallel is shown in Figure 4a. In order to provide the re-centring capability, the flexible subsystem should be kept in the elastic range up to the displacements at which the rigid subsystem attains its ultimate plastic deformation capacity. However, a conventional dual system that satisfies this condition will not return to the initial position following deformations into the inelastic range, even if permanent

displacements δ_{pD} in the dual system are smaller than the ones that would be obtained in a rigid system alone δ_{pr} (see Figure 4b). Permanent deformations can be eliminated if the rigid subsystem is realised to be removable. Upon unloading of the dual system, there is a permanent displacement δ_{pD}, and corresponding residual forces in the flexible (F_{pf}) and rigid (F_{pr}) subsystems. Once removable dissipative members are dismantled, stiffness and strength of the system is provided by the flexible subsystem alone ($F_{pr} = 0$). If the flexible subsystem is still in the elastic range, it will return the system to the initial position, implying zero permanent deformations (see Figure 4c).

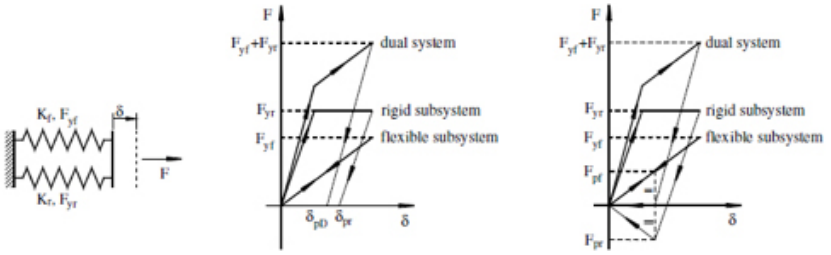

Figure 4 — Simplified model of a generalized dual system (a), and permanent deformations in a conventional dual system (b) and in a dual system with removable dissipative members (c)

Design of full-scale frame to be tested at JRC Ispra

The test structure (Figure 1) has 3 spans of 6 meters, 1 bay of 6 meters and 3 stories of 3.5 meters each. The main lateral load resisting system is composed of the two eccentrically braced frames. The beams on the other direction have pinned ends and are composite steel-concrete beams. The columns are fixed at the base. Columns are made of HEA240 profiles. Beams in the moment resisting frames are made of IPE240 profiles. Braces are made of HEB200 profiles and the beams in the braced frames are HEA240, while links are made of welded H sections 230 x 170 x 12 x 7 mm (for the lower two levels, where the dimensions represent: h x b x t_f x t_w) and 230 x 120 x 12 x 4 mm (for the upper level).

The columns are fabricated of high strength steel S460, while all the other elements are fabricated of mild carbon steel S355, except links that are of S235 steel.

A 4.9 kN/m² dead load and 3.0 kN/m² live load were considered. The building is analysed for stiff soil conditions (ground type C according to EN1998-1), characterised by 0.19 *g* peak ground acceleration and T_C = 0.6 s. A behaviour factor q = 4 (ductility class M) and inter-storey drift limitation of 0.0075 of the storey height are used.

In order to account for the nonlinear behaviour of the structure, plastic hinges were assigned to the elements in the sections where the moments and forces are maximum, according to the different modes of failure of the elements as follows:

– For the links — shear force-displacement type plastic hinge assigned at the middle of the bar
– For the MRF beams — moment-rotation type plastic hinge at the ends of the bar
– For the EBF beams and for the columns — moment-rotation type plastic hinges, accounting for axial force — bending moment interaction, assigned at the ends of the bar
– For the braces — axial force-displacement type plastic hinges at the middle of the bar

For the links, the peak force was set equal to 2 times the yield force (Barecchia et al. [7]), while for all the other elements is to 1.25 times the yield force. Flexibility of the link bolted connections was accounted for by an equivalent reduced link stiffness.

All of the above plastic hinges were modelled according to FEMA356 [8]. Pushover analyses were made (Figure 5) in order to assess the performance of the structure.

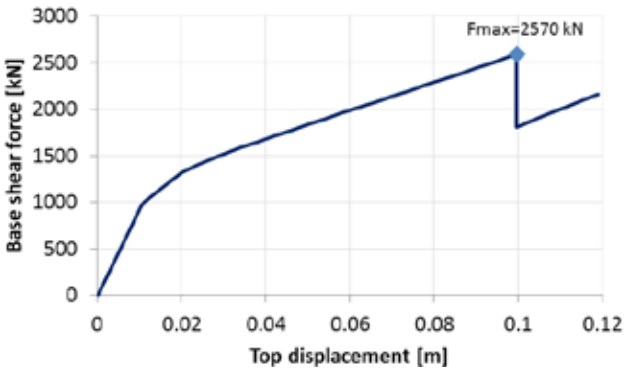

Figure 5 — Pushover curve

Numerical simulations of the test

Numerical simulations were done in order to investigate the possibility to replace bolted links within a realistic structure following significant inelastic deformations and the practical feasibility of the replacement procedure. Practical solutions regarding order in which bolted links need to be replaced were proposed. The link removal procedure uses a tensioned brace in series with a viscous damper system in order to allow smooth release of forces locked in the links due to plastic excursions. The link removal will take place after pseudo-dynamic simulation of seismic loading on the structure, following the steps outlined below:

– the installation of the bracing systems in the moment resisting frames of one span;
– the elimination of the links by flame cutting;
– the release of brace force through the damper;
– the elimination of the bracing systems.

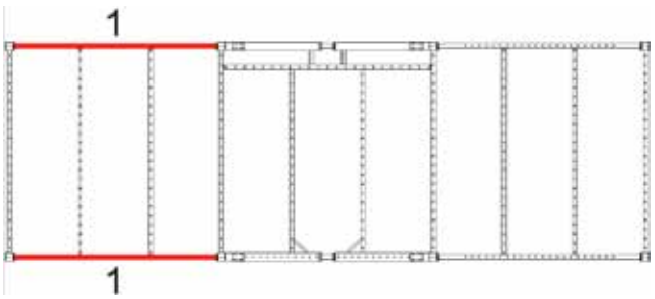

Figure 6 — Bracing systems layout per storey

This procedure will repeat for every storey, beginning from the last storey towards the first.

Because of the damper's presence, the two bracing systems per storey are to be unloaded simultaneously (see Figure 6).

Also an important factor of the link removal procedure is the height-wise link removal order.

In order to simulate the link removal procedure following a damaging earthquake, the static nonlinear staged construction analysis from SAP2000 was used. This analysis allows sequential application and removal of loads and/or parts of the structure. Nonlinear structural behaviour is possible. There was established, on a 2D model of the test structure, that the link removal order to be from up towards down, as described in the following figures:

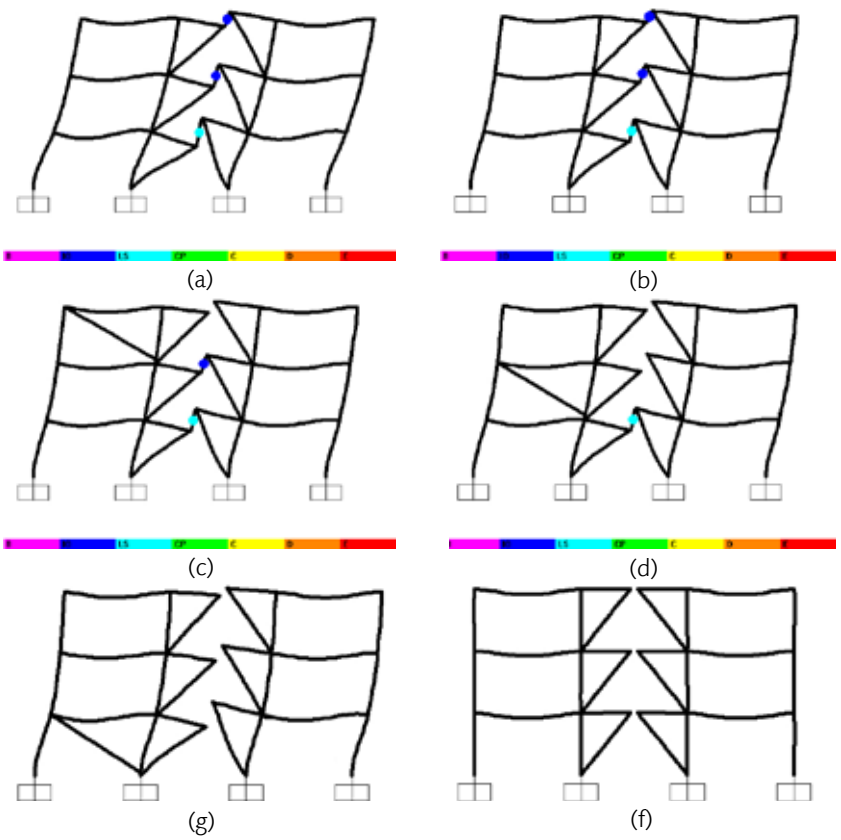

Figure 7 — Height-wise link removal order

Firstly the structure is loaded with gravitational forces and afterwards with lateral forces up to a displacement corresponding to the maximum pushover force (Figure 7a), then it is unloaded (Figure 7b). After installing the bracing systems at the third level, the link is removed (Figure 7c) and afterwards, the brace forces are released through braces with dampers. The procedure is repeated for the second (Figure 7d) and the first levels (Figure 7e) and, in the end, there are removed the bracing systems from the first storey (Figure 7f) and the structure comes back to its initial position.

Conclusions

Bolted links are the dissipative components in the DUAREM tests structure. Residual forces and deformations are present in the links after they have experienced plastic excursions during an earthquake. Removing a damaged link involves redistribution of residual forces to other parts of the structure, more precisely from eccentrically braced frame to moment resisting ones. Numerical simulation of the link removal order showed that there is negligible redistribution of forces among storeys. Therefore, the link replacement procedure can be performed on a storey by storey basis, starting from the least loaded to the most loaded one (from the upper storey toward the lower one).

The technically easiest way to release the forces in links is by flame cutting the web and flanges of the link. However, there is concern that this solution might lead to a sudden release of link shear force and therefore might be dangerous to the operating personnel. Therefore an improvement of the solution was analysed in the present report. It employs some bracing systems (a tension brace in series with a damper) that are installed in one moment resisting bay prior to link removal. Once the links are flame cut, the forces locked in the links are smoothly transferred to the temporary bracing system. Once all links from a storey are removed, all structural components from that storey are in elastic range of response. Therefore, as the brace forces are released through braces with dampers, the structure recovers its initial (plumb) position, becoming free of any locked-in forces.

References

[1] *Stratan, A. & Dubina, D. 2004. Bolted links for eccentrically braced steel frames. Proc. of the Fifth AISC/ECCS International Workshop "Connections in Steel Structures V. Behaviour, Strength & Design", June 3–5, 2004. Ed. F.S.K. Bijlaard, A. M. Gresnigt, G. J. van der Vegte. Delft University of Technology, The Netherlands, pp. 223–232*

[2] *Dubina, D., Stratan, A., Dinu, F. 2008. Dual high-strength steel eccentrically braced frames with removable links. Earthquake Engineering & Structural Dynamics, Vol. 37, No. 15, p. 1703–1720*

[3] *Danku, G., 2011. Study of the development of plastic hinges in composite steel-concrete structural members subjected to shear and/or bending. PhD thesis. Politehnica University of Timisoara*

[4] *Ghobarah, A. & Ramadan, T. 1994. Bolted link-column joints in eccentrically braced frames. Engineering Structures, Vol. 16 No. 1: 33–41*

[5] *Balut, N. & Gioncu, V. 2003. Suggestion for an improved 'dogbone' solution. STESSA 2003, Proc. of the Conf. on Behaviour of Steel Structures in Seismic Areas, 9–12 June 2003, Naples, Italy, Mazzolani (ed.), A. A. Balkema Publishers, p. 129–134*

[6] *Mansour, N., Christopoulos, C., Tremblay, R. 2006. Seismic design of EBF steel frames using replaceable nonlinear links. STESSA 2006 — Mazzolani & Wada (eds), Taylor & Francis Group, London, p. 745–750*

[7] *Barecchia, E., D'Aniello, M., Della Corte, G., Mazzolani, F. M., Landolfo, R., (2006). "Steel eccentric braces".*

[8] *FEMA 356, 2000. Prestandard and commentary for the seismic rehabilitation of buildings. Federal Emergency Management Agency.*

Micro and macro modeling of internal erosion and scouring with fine particle dynamics

KONDO, Akihiko
Nagoya Institute of Technology, Nagoya, Japan

MAEDA, Kenichi
Nagoya Institute of Technology, Nagoya, Japan

WOOD, David Muir
University of Dundee, Dundee, UK

Abstract

When water flows through a broadly graded soil, internal erosion has been occurred, and it can lead to narrowing grading and sink hole. We approached this phenomenon by model test and DEM simulation, focusing on the local deformation and failure between its occurrence and internal erosion. The process of internal erosion was modelled by progressively removing the finer particles while maintaining the sample under constant stresses for some different gradings. Even if stresses were hold, microstructures in soil which is network of contact force chains in soil were changed. Analysis results remind us that the first-order effect of narrowing grading is the raising of the critical state line in the compression plane. The performance of the model was shown and validated. We succeed in developing constitutive modelling of deformation of soil subjected to internal erosion, based on analysis results by discrete element modelling of fine particle removal.

Introduction

Recently, damage to the ground caused by caving, which is a sudden settlement of ground surface including formation of holes in ground, has occurred not only in Japan, but also throughout many parts of the world. The damage occurs at various locations, such as the ground behind revetment due to water level fluctuation and circumferential areas of deteriorated city infrastructures. From in-site investigations of areas prone to caving, the formation of a loosened region and a change of grading distribution to narrow grading mixture (percolation of fine particles) were confirmed in the circumferential ground. The particle percolation itself does not cause macroscopic changes such as the occurrence of sinkholes, but microscopic dynamics such as the

clogging of fine particles and internal erosion induce local deformations and eventual deformation. In this paper, the process of erosion was reproduced in discrete element method analysis, and then a continuum model based on the DEM simulation results was developed.

DEM modeling of deformation and failure of soil by internal erosion

Numerical simulation procedure and tests

Two-dimensional DEM employing PFC2D was used for the analysis described in this chapter (Wood and Maeda, 2008; Wood, Maeda and Nukudani, 2010). The main parameters used in two-dimensional DEM were detailed in a previous paper (Maeda and Hirabayashi, 2006). In the present study, only circular particles were used and four gradings were prepared, as shown in Fig. 1(a). The grain size ratio RD was used as a grain size index, where D_{min} was changed under D_{max} = 100 mm (R_D = 2, 5, 10, and 20). A biaxial compression test was performed under a nongravity condition. By moving four wall elements (nonfriction), the stress and strain of the specimen were controlled. In addition, all of the stress was effective stress. The direction of the maximum principal stress was set as *y* direction, and normal-strain $\square_{xx}$ and $\square_{yy}$, volumetric strain $\square_{v}$, mean principal stress σ_m, and maximum shear stress τ_m were used.

We conducted three kinds of tests according to external actions as shown in Figure 2. While maintaining the stress state (mean principal stress) as a constant, current particles with minimum diameter were forcibly removed from each of the four gradings shown in Figure 1(a).

Due to the generation of the internal unbalance force following the removal, macroscopic deformation was induced. The removal was considered to be the simulation of the particle percolation, and the removal was repeated until the diameter of the removed particles reached 5% of the original particle diameter or $\square_{yy}$ > 25%.

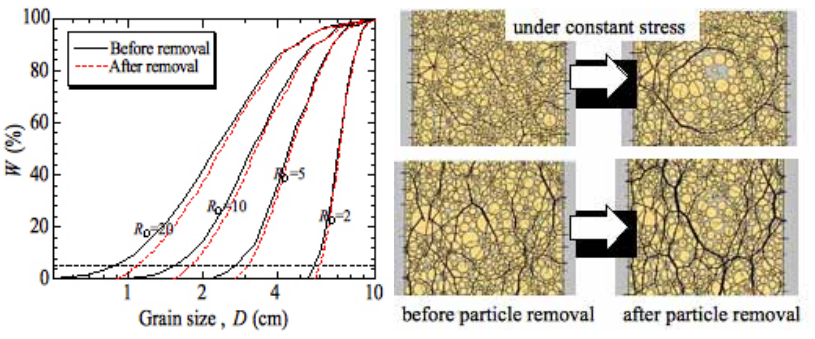

(a) (b)

Figure 1 — Samples used and DEM analysis appearance; (a) gradings of samples used for DEM (solid curves) and grading reached by removal of particles; (b) appearance of stress chain caused by one particle removal.

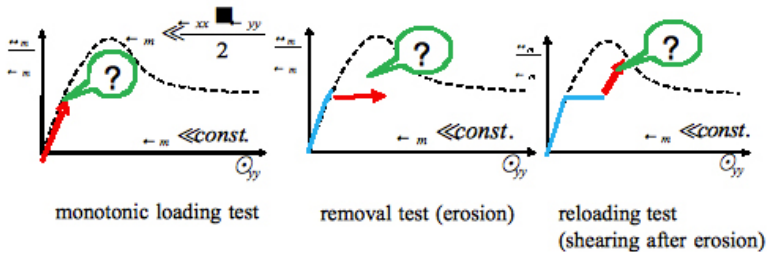

Figure 2 — Test cases and condition; monotonic loading, removal test of fine particle under constant stress and reloading test after removal test.

Monotonic loading test — intact shearing —

To understand only the effect of worsened grading distribution, behaviors of deformation and deformation were investigated using the volume change of the entire specimen consisting of a material without internal erosion, and the specific volume v (= 1 + e). Figure 3 shows a response at the time of monotonic loading on the densest material. This figure shows that when the compaction state (D_r) is the same, the same behavior is observed regardless of the grading. As shown in this figure, the same flow rule can be used.

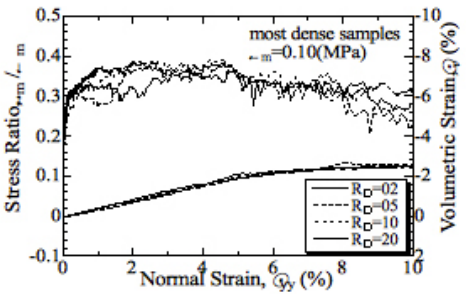

Figure 3 — Stress-strain-dilatancy responses for monotonic loading test with different gradings.

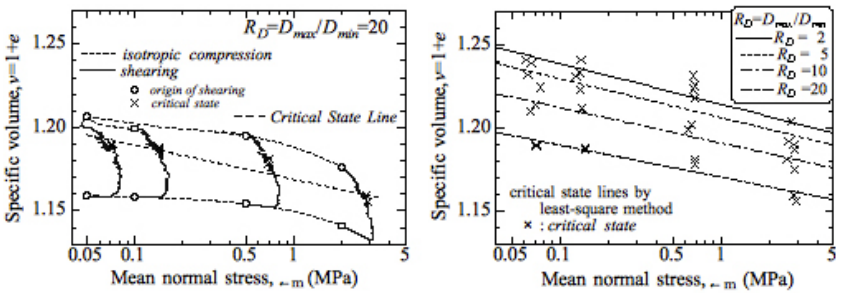

Figure 4 — Critical state line (CSL): (a) CSL for R_D = 20, (b) grading effect on CSLs.

Fig. 4(a) shows a change in the specific volume when the most dense and loose materials are sheared at various values of mean normal stress (σ_m). As shown in this figure, when σ_m is the same, the critical state is reached at a certain specific volume regardless of the density. The straight line connecting σ_m exhibits the critical state of the specific volume, and the specific volume at the critical state is regulated according to the material. Figure 4(b) shows the critical state lines of samples with different grading. The specific volume is smaller with a larger R_D. This is why under the same compaction energy, a material is compacted more easily (D_r becomes higher) when the grading is superior.

Removal test — internal erosion —

Figures 5 (a, b) demonstrate axial deformation and dilatancy behavior, respectively, when the removal test was performed. These figures show only the results at R_D = 10 in the dense state. In these figures, the deformation volume generated when a particle was removed is exhibited by the distance between dots. When the number of removed particles increased and the grading was worsened (a decrease in R_D), axial strain developed. When the stress ratio was high (above 0.271), a deformation larger than 10% was generated that resulted in deformation.

Figure 6(a) shows the results obtained by the monotonic loading and removal tests in the relationship between the specific volume v and R_D. In this figure, the curves to complement the relationship between the critical specific volume v_{cs} (σ_m = 0.1 MPa) and R_D at each grading are interpolated. As shown in this figure, the void ratio of the specimen increased as R_D worsened. The reason for this was that although the void equal to the volume of the removed particle increased, the compression deformation due to the structure change following the removal was smaller than the volume in question. A series of removal tests revealed that deformation occurred when the current specific volume v of the specimen approached the critical specific volume v_{cs}, which had been altered due to the grading change. Figure 6(b) shows a conception diagram of the deformation and deformation behaviors shown in Figure 6(a).

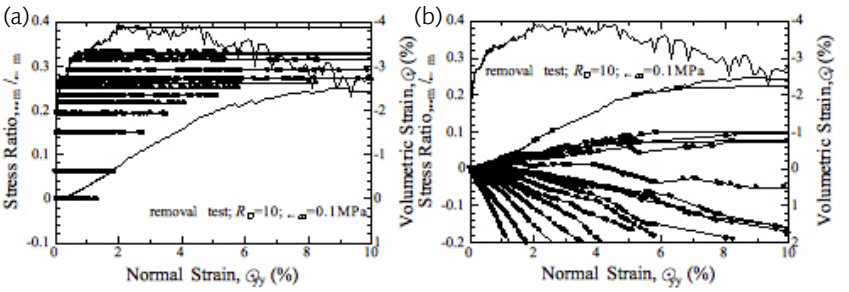

Figure 5 — Removal tests (initial grading R_D = 10; mean stress 0.1 MPa): (a) stress ratio; (b) strain paths (dashed line, monotonic shearing; solid lines, particle removal).

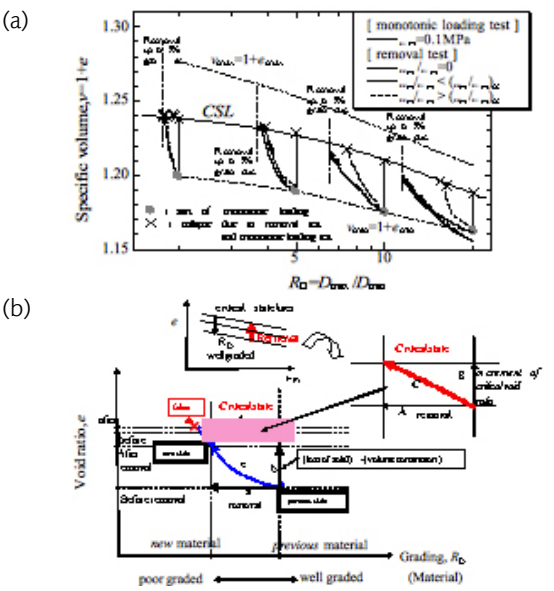

Figure 6 — Change in specific volume by removal of fine particles: (a) specific volume change of the specimen and in the critical state following the change in the grading under a constant stress ratio removal tests (initial grading R_D = 10; mean stress 0.1 MPa); (b) a conception diagram of Fig. 6(a).

Reloading test — shearing after erosion —

Figures 9(a, b) show the axial deformation and the dilatancy behavior of the specimen in the shear after the removal test. The specimen after the removal reached the critical state without exerting the peak strength and dilatancy that could be exerted. The stress ratio in the critical state during the reloading phase was the same as that in the critical state before the removal test. It is known that deformation and destruction behaviors of soil depend on the levels of density and stress, and the critical state can be systematically understood using these behaviors. For the critical state, parameter $\psi = v - v_{cs}$ is known to be one of the important indices. This is expressed through the difference between the current specific volume v and the critical specific volume v_{cs}. The state parameter is an index for the compaction state of soil that is not expressed by the level of the void ratio, but instead by the relative void level against the critical state. When $\psi > 0$ ($v > v_{cs}$), soil is evaluated to be in the loose state. When $\psi < 0$ ($v < v_{cs}$), soil is evaluated to be in the dense state. When $\psi = 0$ ($v = v_{cs}$), soil is evaluated to be in the critical state.

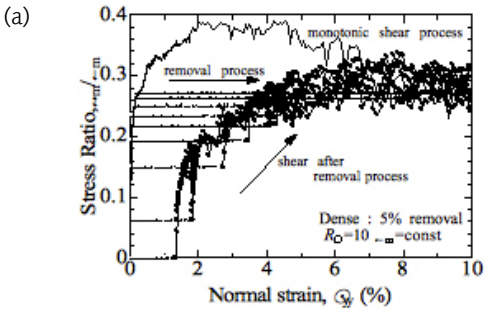

Figure 7 — Reloading tests (initial grading R_D = 10; mean stress 0.1MPa): (a) stress ratio; (b) strain paths.

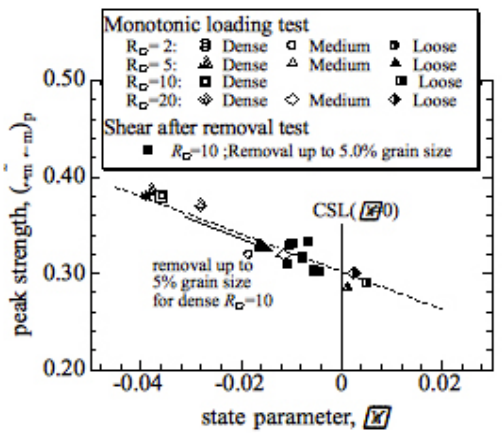

Figure 8 — Peak strength and state parameter with and without particle removal.

Continuum modeling of deformation and failure of soil by internal erosion

Formulation of mechanism

We developed a continuum model to express the deformation-failure behaviors of soil due to internal erosion (Wood and Maeda, 2008; Wood, Maeda and Nukudani, 2010). Since a model was constructed based on a change in the grading distribution due to the fine particle percolation, the change in the grading must be clearly examined without depending on the initial conditions. The grading index IG is expressed by the area ratio of the current grading (ABC in Fig. 9) to the limiting grading (ABD in Fig. 9). In addition, I_G is 0 in the grading distribution consisting of a single particle diameter, and it is 1 in the limiting grading. Since I_G is obtained based on the area ratio, it is greatly affected by the maximum particle diameter D_{max}, the minimum particle diameter D_{min}, and R_D, which is the ratio between them.

The particle removal causes an increase in the specific volume v, volumetric shrinkage due to the confining pressure, and worsening of the grading distribution (δI_G) due to material defect. These changes in the material itself interact with each other. To formulate these changes, the change in the specific volume is examined, focusing on the specific volume in the critical state (δv_{CS}) using the state parameter ψ. Here, ψ must be changed from ψ_A to ψ_B. The amount of change ($\delta\psi$) can be expressed as the sum of the specific volume increment (δv), volumetric shrinkage due to the confining pressure (δv_1), and volumetric shrinkage due to the second plastic mechanism (δv_2) of the volume of the percolated particle. A previous report[2] described the above matter in detail.

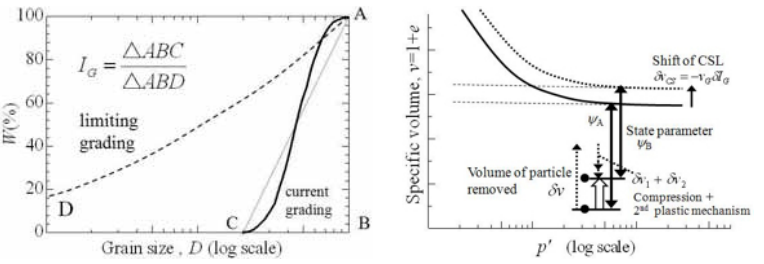

Figure 9 — Definition of grading index I_G (as ratio of areas ABC and ABD) and the shift operation of critical state and change in specific volume with particle removal.

Continuum model performance and verification

Figure 11 shows the axial deformation and dilatancy behaviors when δI_G was input. The generated strain was larger when a particle was removed in the state where the stress ratio was higher. Therefore, these figures can display an increase in the generated strain with an increase in the number of removed particles. Figure 12 illustrates behaviors when reloading was performed on the specimen in which the grading distribution had been changed to a particle diameter of 5%. We can see a reduction of the peak strength and an increase in the compression tendency in sample subjected to erosion as shown in Figure 7.

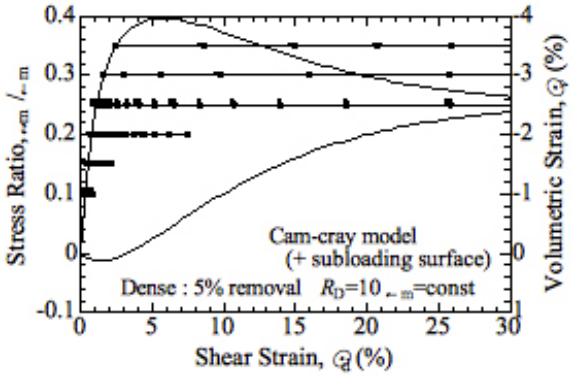

(a)

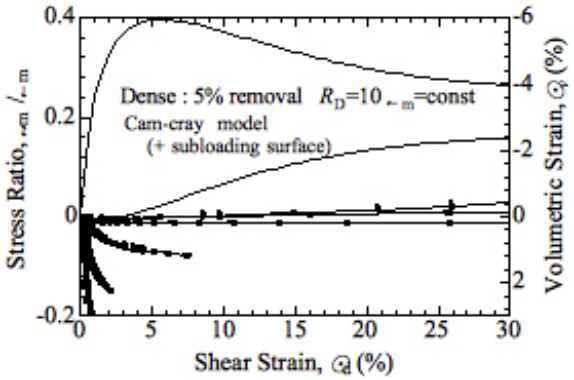

(b)

Figure 11 — Removal test simulated by continuum model for erosion: (a) stress ratio; (b) strain paths.

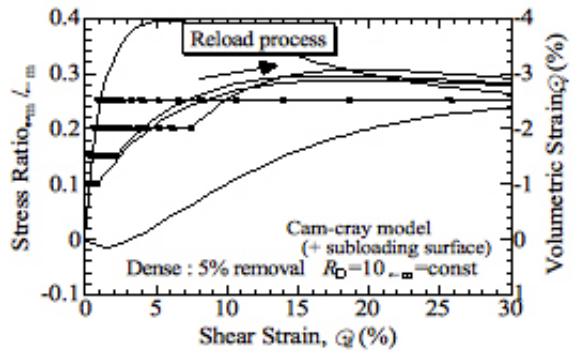

(a)

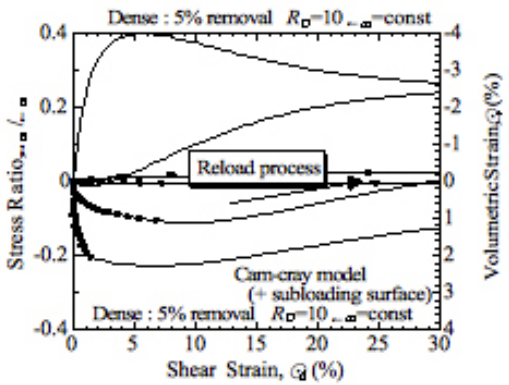

(b)

Figure 12 — Reloading test simulated by continuum model for shearing after erosion: (a) stress ratio; (b) strain paths.

Conclusion

We succeeded in developing constitutive modelling of deformation of soil subjected to internal erosion, using analysis results obtained by DEM modelling of fine particle removal. As for the modelling concept, it can be reproduced by transferring of critical state stress ratio based on the behaviour of state parameter based on the traditional continuum scheme.

References

[1] *Maeda, K. & Hirabayashi, H. (2006). Influence of grain properties on macro mechanical behaviors of granular media by DEM, Journal of Applied Mechanics JSCE, 9: 623–630*

[2] *Maeda, K., Miura, K. & Toki, S. (1995). Mechanical properties of elliptic microstructure formed in granular materials. Soils and Foundations, 35(2): 1–13.*

[3] *Maqsood, S. T., Schwarz, J. (2008). Analysis of building damage during the 8th October, 2005 Earthquake in Pakistan. Seismological Research Letters, 79(2), S. 163–177*

[4] *Kenichi MAEDA et al. (2010). — Stress-chain based micromechanics of sand with grain shape effect, Granular Matter, 12(5), 499–505.*

[5] *Wood, D. M. & Maeda, K. (2008). — Changing grading of soil: effect on critical states, Acta Geotechnica 3: 3–14.*

[6] *Wood, D. M., Maeda, K. & Nukudani, E. 2010. — Modelling mechanical consequences of erosion, Geotechnique 60(6): 447–457.*

Reports

Project 1 — System Identification, Model Updating and Simulation

ZABEL, Volkmar
Bauhaus Universität, Weimar

CABBOI, Alessandro

GALVAN, Giulio

GEČYS, Tomas

MALVEIRO, Joel

MONTENEGRO, Pedro

ROCHA, João Miguel

TRIBUTSCH, Alexander

VOUKIA, Dimitra

YAMAGUCHI, Mayako

Introduction

The aim of this project was to evaluate the dynamic behaviour of the Pöppelmannbrücke footbridge in order to assess the levels of the human induced vibrations and the possible effects on the comfort for the end users. The first step was to create FE models of the structure to investigate the modal properties, which have been subsequently verified by ambient and forced vibration tests. By processing the first, it was possible to identify mode shapes and eigenfrequencies of the structure, while using the forced vibration data, the damping properties of the footbridge have been calculated. Model updating has then been performed both with numerical methods and manual tuning of the unknown boundary conditions as to achieve a higher degree of precision of the numerical models which have finally been used to assess the levels of human induced vibrations according to the guidelines SETRA and HiVoSS. Furthermore, a TMD was designed and a parametrical study on the mass ratio of the device was conducted.

Case study

The considered footbridge is Pöppelmannbrücke and is located in the city of Grimma, Saxony. It was first constructed in 1719 and during its history was destroyed and rebuilt several times. During a flood in August 2002 the structure reported severe damage yet again therefore the city of Grimma decided to rebuild it. The new structure, a steel arch bridge spanning 65 meters, was attached to the historical remainings. The construction started in 2009 and the footbridge will be opened to the public in August 2012. Field vibration tests were performed in the earlier stages of design and construction, however a tuned mass damper was recently installed and further vibration testing was required.

Figure 1 — The flood in 2002

Figure 2 — The bridge in August 2012

Numerical models

Three numerical models of the bridge were created in order to reproduce the geometry and the behaviour of the structure. The softwares used were ANSYS, Straus7/Strand7 and SLANG. The models include the archs, the main girders, the deck and the longitudinal stiffeners as well as the cross girders. 12 DOFs beam elements were employed for the arches, the main girders and the cross girder. The presence of the longitudinal stiffener was simulated with an increase of the bending stiffness of the deck, defined by 20 DOFs shell elements.

The boundary conditions at the end of the deck are the main source of uncertainty: the end of the structure cantilevers out of the bearings and there is also some uncertainty in the bearing stiffnesses. Therefore, it was decided to put translational and rotational springs at the end of the bridge deck which in later stages of the investigation have been calibrated.

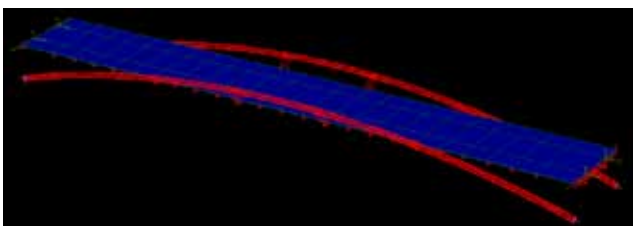

Figure 3 — The FE model (Straus 7)

Figure 4 — Accelerometer and measurement equipment

Experimental tests

6 bi-axial accelerometers were utilized to measure the acceleration response of the structure in vertical and lateral direction. A sampling frequency of 204.8 Hz was selected. An accelerometer and the measurement equipment is depicted in Figure 4.

Five configurations of sensor locations were considered, see Table 1 and Figure 5. Configuration 1 to 4 were chosen to identify the mode shapes of the bridge at 18 nodes. Therefore, two accelerometers were placed at reference nodes 4 and 15, while the other four remaining sensors were used as roving sensors in four configurations. Configuration 5 includes only nodes at or near the center of the bridge.

Sensor	Config 1	Config 2	Config 3	Config 4	Config 5
REF1	4	4	4	4	4
REF2	15	15	15	15	15
MP-1	3	5	1	2	5
MP-2	8	9	7	6	6
MP-3	10	11	12	13	13
MP-4	14	16	17	18	14

Table 1 — node number of sensor location for five configurations

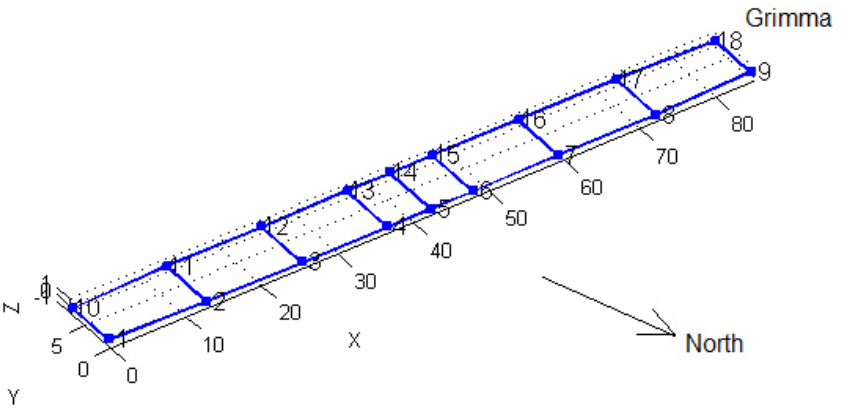

Figure 5 — sketch of node numbers along the bridge deck

Measurements

Measurements 1 to 4 correspond to ambient vibration test with sensor configuration 1 to 4. Measurements 5 to 30 were conducted with sensor configuration 5. In contrast to the first four measurements, where only ambient vibrations with released TMD had been measured, the following include bouncing, jogging and ambient tests with released or blocked TMD, respectively.

Only a selected number of measurements were utilized for the further investigations, which are presented in Table 2.

Measurement	Configuration	Duration [s]	type	TMD
1	1	600	ambient	released
2	2	600	ambient	released
3	3	600	ambient	released
4	4	600	ambient	released
5	5	80	bouncing/free decay	released
6	5	60	bouncing/free decay	released
15	5	600	ambient	released
26	5	600	ambient	blocked
28	5	150	bouncing/free decay	blocked
30	5	60	bouncing/free decay	released

Table 2 — Node number of sensor location for five configurations

System identification

SSI based identification of modal properties

The data collected during the ambient vibration tests were processed with MATLAB and the MACEC toolbox. A high pass filter was applied to the selected measurements and the data points were decimated by a factor of 4 in order to improve the signal quality and avoid aliasing issues.

The signal of data set from 1 to 4 and 15 was then analysed by the use of Stochastic Subspace Identification [4] and for every data set the eigenfrequencies and the corresponding mode shapes were identified in the stabilization plot.

The MACEC toolbox allows for combination of subsequent identifications in order to better identify the mode shapes of the structure and to distinguish structural modes from numerical ones. The identification was carried out when the TMD was already installed and released, and as the data available for blocked TMD condition is scarce and of poor quality, all of the identification process refers to the structure with the TMD.

Mode	Frequency [Hz]	Damping [%]	Mode Shape	Modal Phase Collinearity
1	2.5993	2.3340	V bending	0.96288
2	2.6993	1.6227	V bending	0.99911
3	3.0949	1.2028	H bending and twisting	0.96029
4	3.9539	0.48701	V bending	0.74309
5	4.0526	0.26181	twisting	0.99782
6	5.7934	0.40022	twisting	0.99758
7	6.6590	0.72283	V bending	0.99832
8	7.7364	0.54935	twisting	0.99409
9	8.6178	0.73039	bending	0.99409

Table 3 — Model identification by SSI technique

Validation of identified damping ratios by free decay tests.
Bouncing test were performed to assess the damping properties of the foot bridge and to validate the outcomes of the system identification procedure. A group of 10 to 12 people was synchronizing with the expected first natural frequency (2.6 Hz) to excite the structure to a clearly measurable amplitude response. When an appropriate level of vibration was accomplished, bouncing was stopped in order to measure the free decay.

Accelerations were recorded both, in vertical and lateral direction, at 6 nodes located near the centre of the bridge (4, 5, 6, 13, 14 and 15). A Butterworth filter of order 2 with cut-off frequencies at 1.5 and 3.5 Hz was applied to clean the data for the following identification. Damping was estimated by the Logarithmic Decrement method considering the first 7 to 13 peaks of the free decay and averaging of the identified values.

Four measurements were considered for the evaluation, listed in Table 4. Only vertical records of nodes 5 and 14 were taken into account to minimize disturbances due to the higher, anti-symmetric modes. Mean values of the identified dimensionless damping coefficient and frequency are also provided in Table 4.

Measurement	No. of people bouncing	TMD	Identified damping coefficient [%]	Identified frequency [Hz]
5	11	released	2.9	2.7
6	11	released	2.7	2.7
30	12	released	2.8	2.7
28	12	blocked	0.3	2.6

Table 4 — Free decay tests

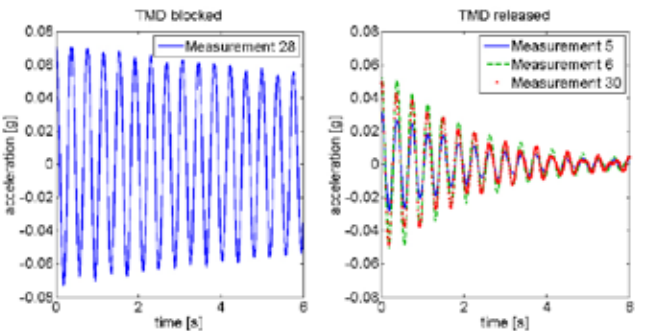

Figure 6 — free decay, comparison of response with blocked and released

The exemplary response of the discussed four measurements is shown in Figure 6.

Model updating

Description of the models

In most cases, the modal parameters obtained from the numerical models are not in correspondence with the experimental values. Characteristic properties of the structures, such as modulus of elasticity of the materials or properties related to the supports may need to be adjusted. In this sense, the use of calibration techniques of numerical models based on experimental results has shown strong growth, in order to minimize the differences between numerical and experimental results. It is an iterative process that consists in the minimization of one objective function through the variation of various properties of the numerical model. The objective function, shown in equation [1], depends on the numerical and experimental natural frequencies and also the coordinates for each mode of vibration according to the experimental measurement points.

$$J(x) = \sum_{i=1}^{N_{freq}} \frac{\left(f_i^{num} - f_i^{exp}\right)^2}{\left(f_i^{exp}\right)^2} + \sum_{i=1}^{N_{freq}} \sum_{j=1}^{N} \frac{\left(u_{ij}^{num} - u_{ij}^{exp}\right)^2}{\left(u_{ij}^{exp}\right)} \quad (1)$$

The calibration of the numerical models was performed using the OptimTool from the MatLab calibration toolbox. The function "minsearch" finds the minimum of an objective function, starting at an initial estimate of the numerical parameters. For the calibration of the numerical models only the stiffness of the supports were considered as variables to change. Figure 7 shows the difference between the numerical and experimental natural frequencies for both models.

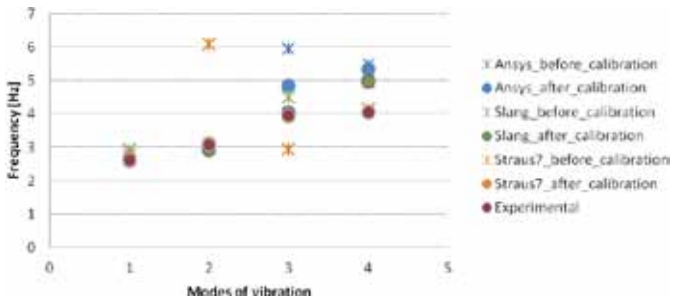

Figure 7 — Comparison between measured and numerical frequencies

According to Figure 7 the frequency of the first mode of vibration obtained in all the numerical models, before the calibration process, are closed to the one measured in the experimental tests. After the calibration the first frequency of all the three models converged to the measured result.

For the others modes of vibration, there are a huge variability in the frequencies before the calibration, especially for the third and fourth modes (second bending mode and torsion mode). However, the calibration process allowed a better approximation between the numerical and experimental results for all the other frequencies, except for the third and fourth modes in the ANSYS model. This could be explained by errors in the bearing and geometrical properties of the model that couldn't be fixed during the calibration process.

Figure 8 shows the first 4 modes of vibration of the numerical model developed in the commercial software Straus7, which was after used in the assessment of human induced vibration levels.

Assessment of the vibration levels

Guidelines

The deck vibration level was assessed by two different methodologies: the SETRA guideline and the HiVoSS guideline. SETRA is the French guideline to the assessment of pedestrian induced vibrations on footbridges. HiVoSS is an European guideline for the assessment of human induced vibration on steel structures.

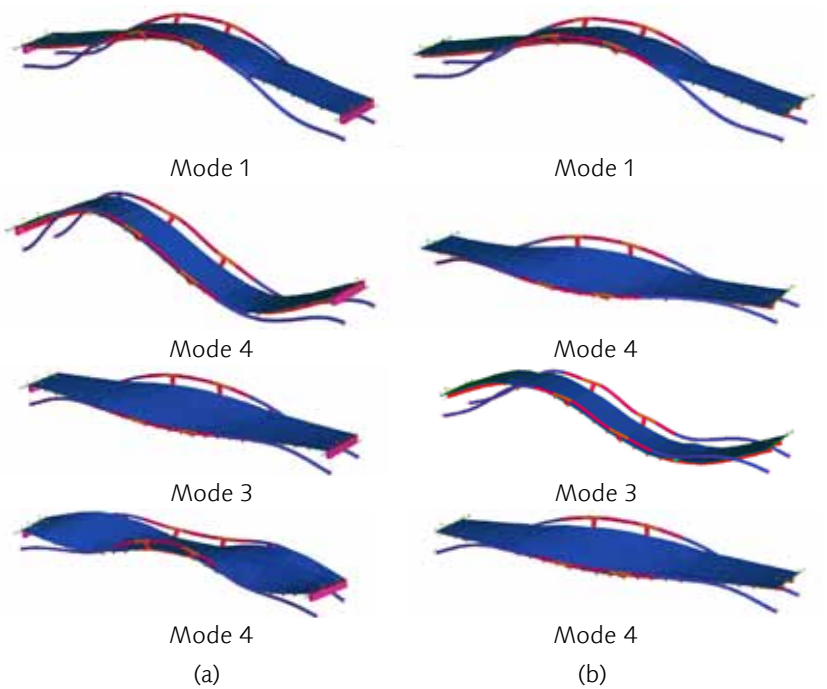

Figure 8 — Modes of vibration: (a) before and (b) after the calibration process

Both methodologies introduce a few basic assumptions in order to simplify the process of obtaining the deck accelerations. In both cases the random number of pedestrians, *N*, is substituted by an equivalent number of uniform pedestrians, *Neq*. These methodologies assess the dynamic behaviour for each mode separately and only take into account frequencies below 5 Hz.

Regarding the pedestrian loading the two methodologies have some differences. SETRA defines three pedestrian densities: 0.5 p/m², 0.8 p/m² and 1 p/m², while HiVoSS defines 5 different pedestrian densities: 15 p/deck, 0.2 p/m², 0.5 p/m², 1 p/m² and 1.5 p/m².

The equivalent number of pedestrians is function of the deck's surface area, the pedestrian density and the damping:

$$N_{eq} = 10.8\ \sqrt{\xi_j N}\ ,\ d < 1 \qquad (2)$$

$$N_{eq} = 1.85\ \sqrt{N}\ ,\ d \geq 1 \qquad (3)$$

The equivalent loading is uniformly distributed and depends on the equivalent number of pedestrians, *Neq*, the weight of the pedestrian, *G*, the dynamic loading factor, α, and the reduction factor, ψ.

$$q_{eq} = \frac{N_{eq}}{S} \cdot \alpha_{eh} \cdot G \cdot \psi_{eh}\,(f_j) \qquad (4)$$

The two guidelines have also some slight differences regarding the reduction factor which can lead to some differences in the acceleration levels on the deck, which is shown in Figure 9.

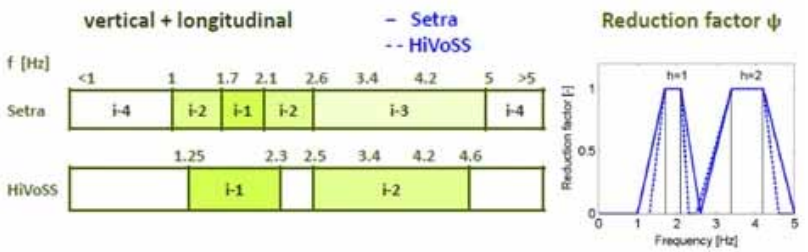

Figure 9 — Reduction factor for vertical modes

Furthermore, SETRA also requires the calculation of the natural frequencies accounting for the pedestrians mass whereas HiVoSS only requires this calculation if the pedestrians mass is higher than 5% of the modal mass.

The maximum acceleration for each mode is determined according to Eq. (5):

$$\ddot{u}_{j,emax} = \frac{\sum q_{eq} \cdot S_i \cdot \left|\varphi_j\right|}{2 \cdot \xi_j} \cdot max\left[\left|\varphi_{j,p(i)}\right|\right] \qquad (5)$$

Simulations

The vibration assessment was performed only for the updated model. Several damping scenarios were analysed including the theoretical and experimental results. In the first scenario the structural damping was considered to be constant and the damping used was 0.4%, which corresponds to the mean value suggested by the guidelines for steel structures. In Figure 10 the maximum accelerations obtained for each mode and for the several pedestrian densities are presented.

The second and third scenarios took into account the damping values obtained in the experimental tests. The second scenario did not include the additional damping provided by the TMD, whereas in the third scenario this was taken into consideration. The maximum accelerations for the second scenario are presented in Figure 11.

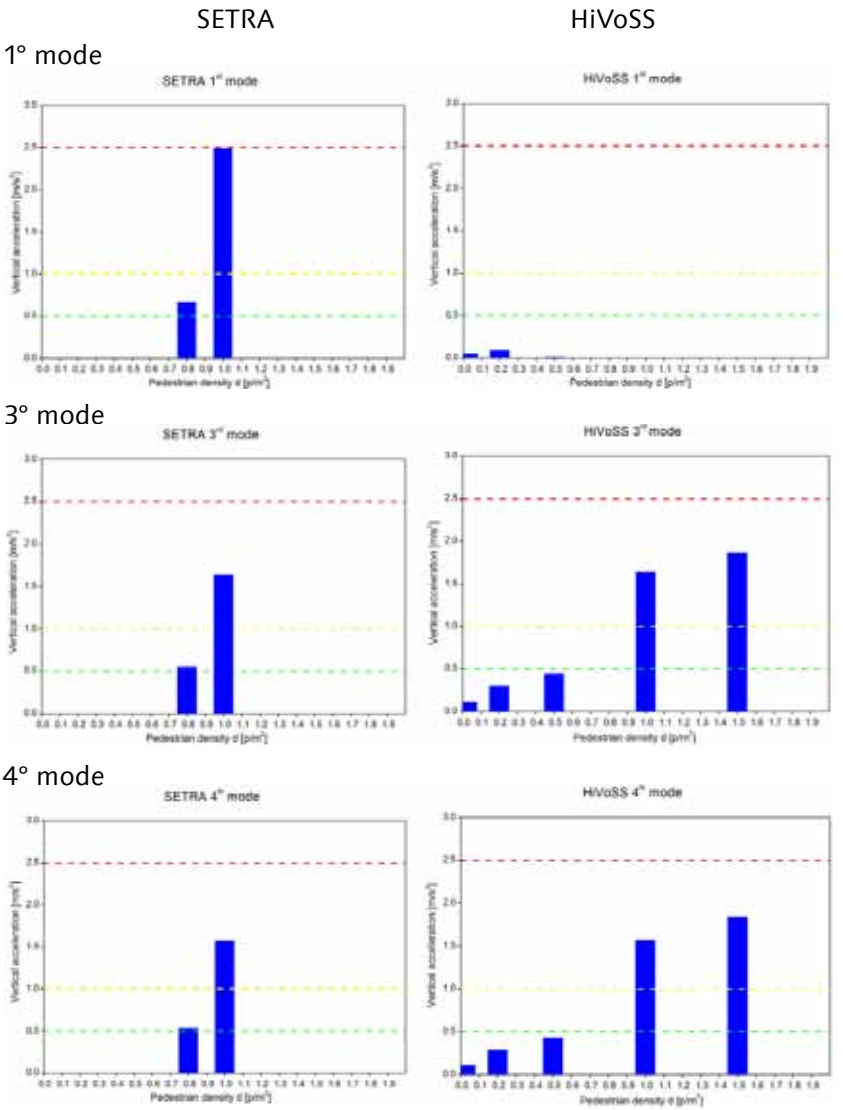

Figure 10 — Vertical acceleration assessment for $\xi = 0.4\%$

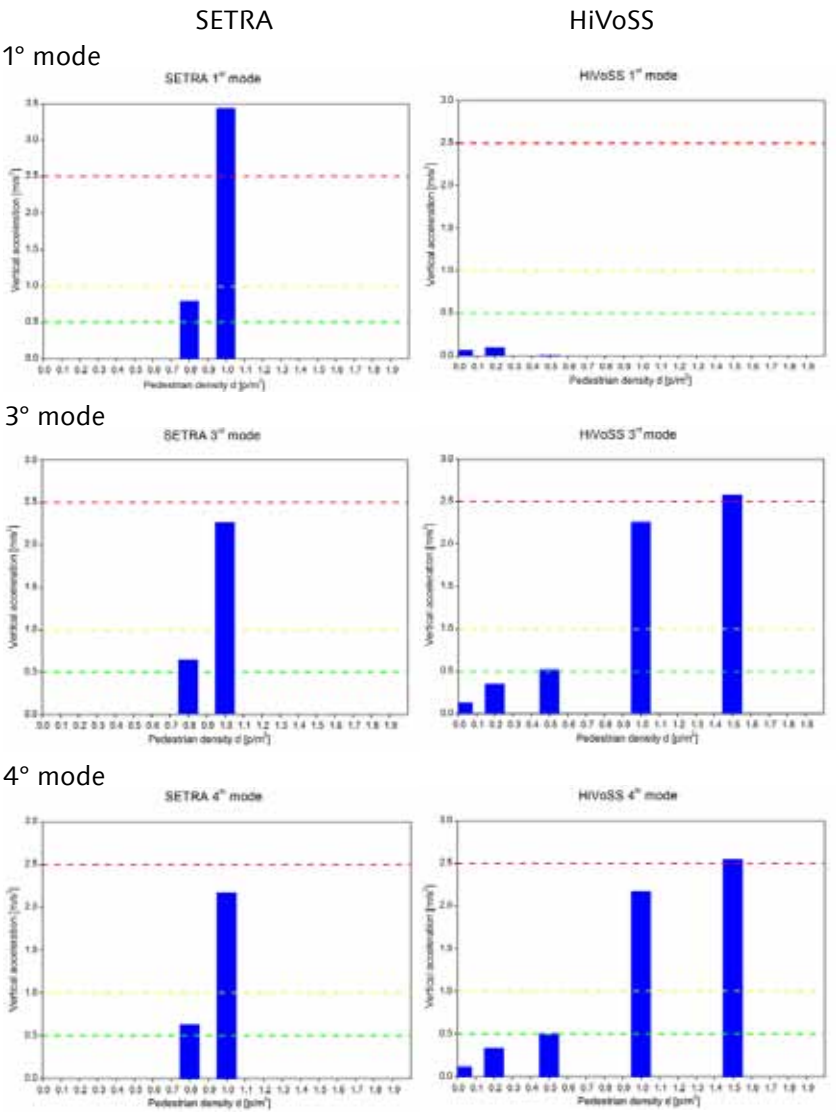

Figure 11 — Vertical acceleration assessment for experimental damping

Figure 12 illustrates the maximum acceleration obtained for the third scenario where the TMD was active.

Discussion

In general the increase of the pedestrian density leads to higher accelerations of the bridge deck. However, there are some exceptions which can be explained by the variation of the reduction factor. For the current case study this occurs for the analysis of the first mode using the HiVoSS guideline. This is due to the fact that for frequencies ranging from 2.3 Hz to 2.5 Hz this guideline suggests the use of a reduction factor of 0.

The reduction factor also explains the differences obtained by the two guidelines. Although the functions are quite similar the acceleration level can be significantly different. This shows that the acceleration level on the bridge deck is highly dependent on this parameter.

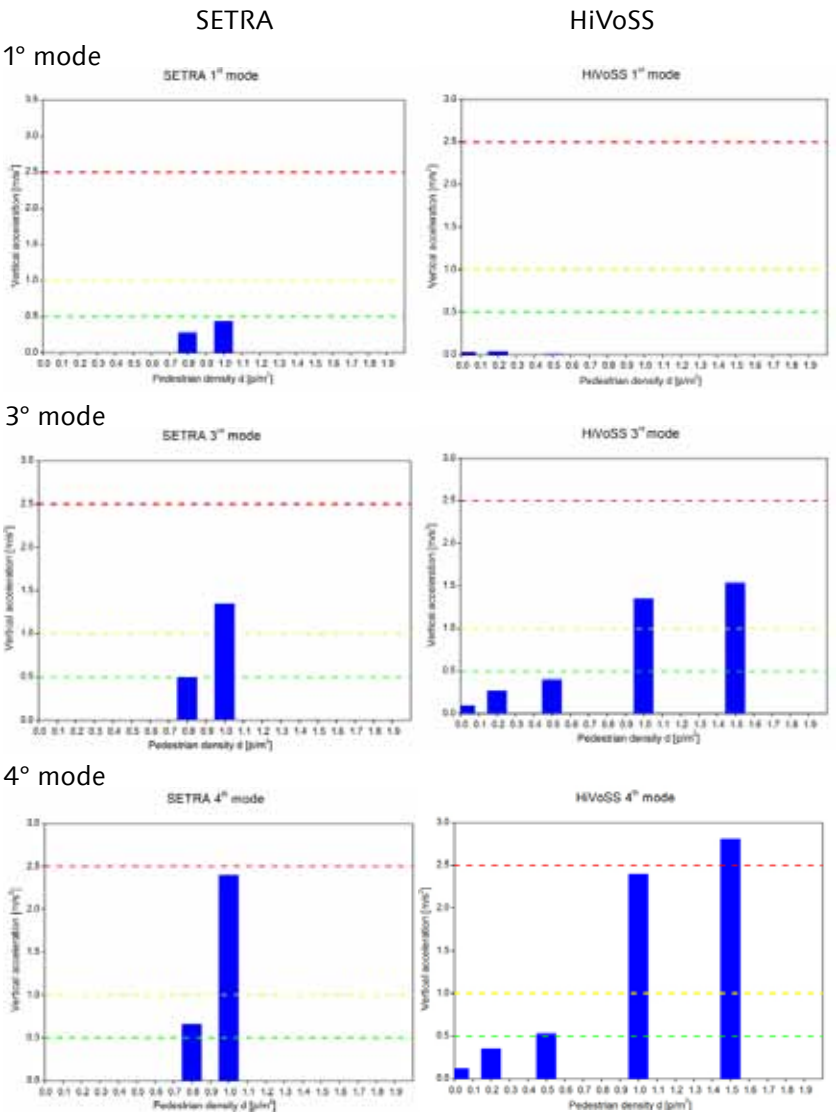

Figure 12 — Vertical acceleration assessment accounting for TMD damping

Comparing the first and second scenarios some differences can be noticed. The identified damping ratio during the experimental tests was lower than the mean value suggested in the guidelines (0.29% vs 0.4%). This explains the higher accelerations obtained for the second scenario. For the third scenario the damping was estimated for each mode separately and took into account the additional damping due to the TMD. An important decrease of the acceleration levels can be seen particularly for the first mode. This confirms the effectiveness of the TMD on the control of the deck vibrations. For this scenario some unacceptable accelerations can be observed for the 4th mode. This can be explained by the experimentally identified damping ratio for this mode (ξ = 0,26%). This value seems to be too low and it might not be accurate since the torsional mode was not well excited during the experimental tests.

Tuned mass damper (TMD)

Design

The main aim of a tuned mass damper design and installation to this bridge is to reduce the 1st mode vibration response. Figure 13 illustrates the general steps of design of a tuned mass damper (TMD) [1].

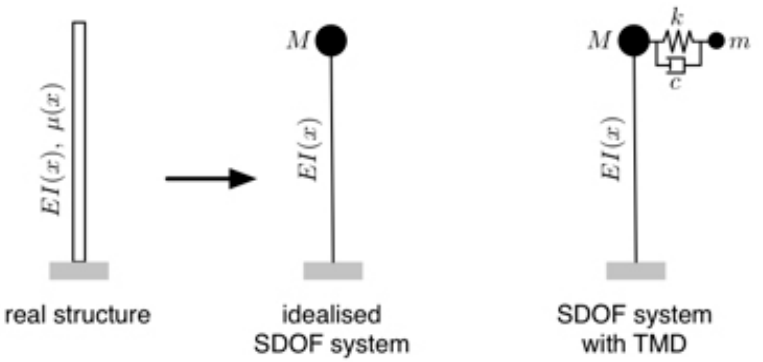

Figure 13 — General steps for a TMD design

The amplitude ratio x/x_{stat} of the main mass as a function of the four essential variables μ, c/c_c, f, g is given by

$$\frac{x}{x_{stat}} = \sqrt{\frac{\left(2\frac{c}{c_c}gf\right)^2 + \left(g^2 - f^2\right)^2}{\left(2\frac{c}{c_c}gf\right)^2\left(g^2 - 1 + \mu g^2\right)^2 + \left[\mu f^2 g^2 - \left(g^2 - 1\right)\left(g^2 - f^2\right)\right]^2}}$$

In equation 5:
$\mu = m/M$ — ratio between absorber (TMD) and main system mass,
C_C — critical damping,
f — frequency ratio (natural frequencies),
g — forced frequency ratio,
x — dynamic deflection of system,
x_{stat} — static deflection of system.

Application

The optimal attachment position corresponding to the maximum of the 1st mode shape is located in the middle of the bridge. A non-optimal position leads to a decrease of the effective TMD mass ratio.

Figure 14 shows the results of tuned mass damper design. While designing the TMD, the parametric analysis with different mass of TMD was made to see the influence of TMD mass to x/x_{stat} ratio. A range of TMD mass from 1 t to 5 t, including the actual design of 2.3 t, was considered in this study.

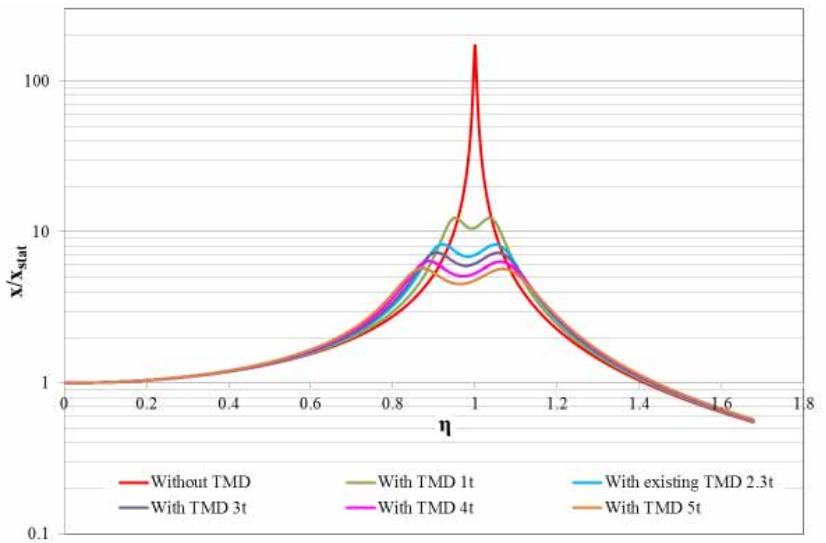

Figure 14 — A tuned mass damper's parametric analysis results

From Figure 14 it can be seen that a higher mass results in a decreased response. The practical engineer has to decide on the actual mass according to the required response reduction.

References

[1] *Den Hartog, J. P. (1985). Mechanical Vibrations, Dover Publications, Mineola, New York.*

[2] *HiVoSS — Human Induced Vibrations of Steel Structures (2008).*

[3] *Setra — Guide to assessing pedestrian induced vibratory behavior of footbridges (2006).*

[4] *Van Overschee, P. De Moor , B. Subspace identification for linear systems: theory, implementation and applications, Kluwer Academic Publishers, Boston, London, Dordrecht (1996).*

Project 2 — Soil-Structure Interaction Simulation and Experimental Validation

WUTTKE, Frank
BUW, Weimar, Germany

KAFLE, Binod
BUW, Weimar, Germany

ANDREEV, Stoyan
Risk Engineering LTD.
Sofia, Bulgaria

HOANG, Vu
Waseda University Tokyo, Japan

KONDO, Akihiko
Nagoya Institute of Technology, Japan

KRAUS, Ivan
University of Osijek, Croatia

KURIMOTO, Yuhei
Nagoya Institute of Technology, Japan

MAEDA, Keita
Waseda University Tokyo, Japan

MARIN, Alexandru
Swiss Federal Institute of Technology Zurich, Switzerland

NAKAYA, Hiroki
Waseda University, Tokyo

Abstract

The project deals with the study of soil structure interaction (SSI) through experimental study and the numerical validation by the use of available finite element code and the Macroelement, incorporating, interaction between the structural forces, Elsto-Plastic soil behaviour and the interface between the soil and the foundation. The response of Macroelement consisting of few constitutive parameters incorporating SSI, which is able to predict the prognosis of the displacement, serves as the realistic tool for the study of SSI.

Introduction

Soil Structure Interaction (SSI) is referred as the phenomenon in which the motion of the soil and the motion of the structure are interdependent and both of them are influenced by each other. According to [1] SSI is defined as *'The process in which the response of the soil influences the motion of the structure and the response of the structure influence the motion of the soil.'* This interdependency in the response of the soil and structure and the role played by the interface, between the foundation and the soil, brings intrinsic complexity to solve the problem. This complex behavior of SSI can be conceived by the use of elasto-plastic strain hardening Macroelement constituting coupled system of super structure, soil half space and the boundary between them. The use of granular model likes Macroelement consisting of few constitutive parameters and capable of delivering high ended results, reduces the ambiguity of model response and the complexity in the analysis of the system under consideration. (Fig. 1), shows the pictorial representation of Macroelement, consisting of forces from structure and the arbitrary elasto-plastic region of soil under consideration of Macroelement.

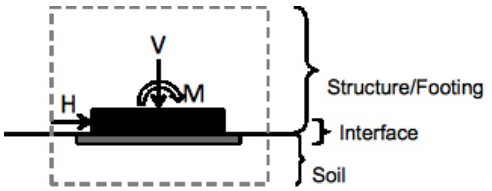

Figure 1 — Pictorial representation of Macroelement of shallow footing

Experimental Studies

Static bearing capacity test was carried out in a box of size 1 m x 0.5 m x 0.5 m in dimension. Oven dry Hostun sand was filled in layers and compacted to obtain the void ratio of 0.76, with the height of 0.42 m. The surface was then leveled, and a rough rigid square, steel footing was placed over the sample, (Fig. 2). Displacement controlled loading at the rate of 0.0025 mm/s was applied on the footing, until the failure load was reached.

Figure 2 — Footing under centric vertical loading

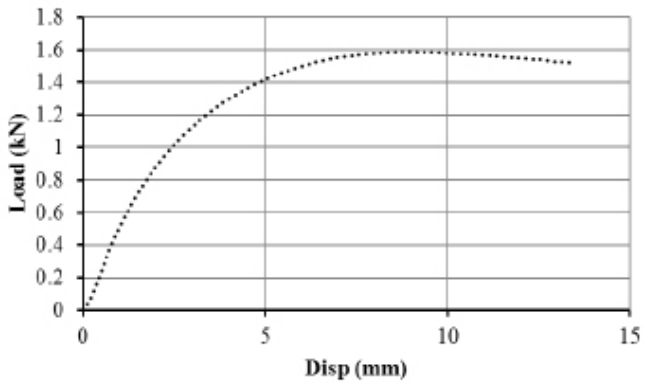

Figure 3 — Load displacement behaviour of Footing

The stiffness of the soil decreases with the increase in time of loading at the constant rate of loading. This variation of the stiffness during the test was recorded by the use of bender elements, embedded in the soil at different depth (Fig. 4.), from the surface. By observing the change of shear-wave velocity, the change in stiffness was calculated at different depths, at different time steps. (Fig. 5), shows the transmitted and received signal from the bender element. The time of first arrival of shear wave velocity across the footing was calculated to obtain the instantaneous stiffness from (Eq. 1 and Eq. 2).

(1) $$G_{max} = p \cdot V_s^2$$

(2) $$E_{max} = 2G_{max}(1+v)$$

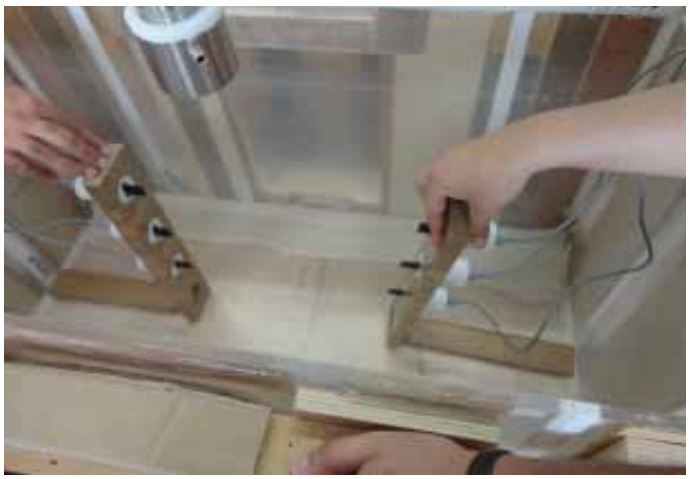

Figure 4 — Placement of bender-elements below the footing at different depths

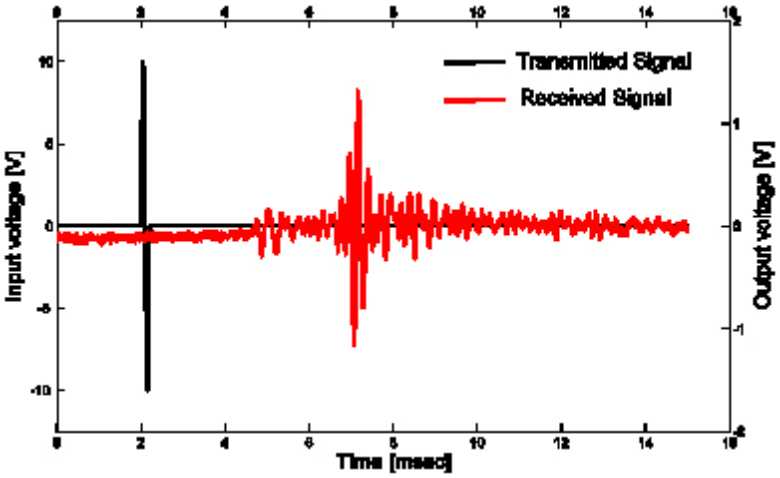

Figure 5 — Received and transmitted signal of Bender Element

Numerical Studies

Numerical validation of the experimental results, obtained from the test was done, by the use of available finite element code. PLAXIS was used to simulate the test results by the use of two different constitutive models, Mohr-Coulomb and the Hardening-soil Small strain Soil Model. 15 nodded triangular element for plain strain case was used to model the behaviour (Fig. 6 and 7).

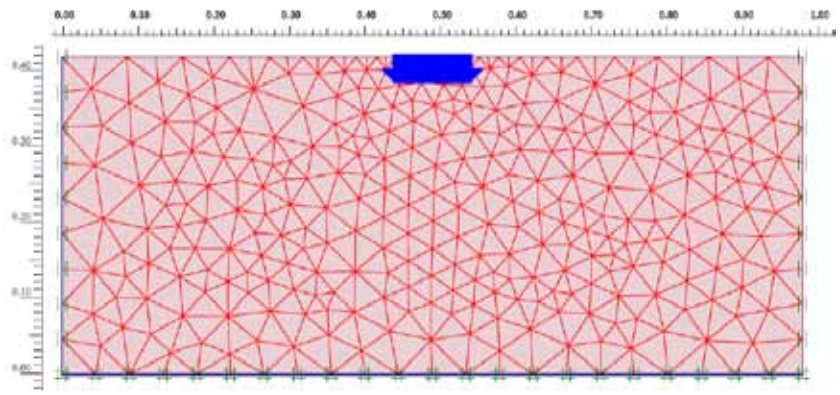

Figure 6 — Mesh layout for PLAXIS Simulation, Mohr-Coulomb Soil Model

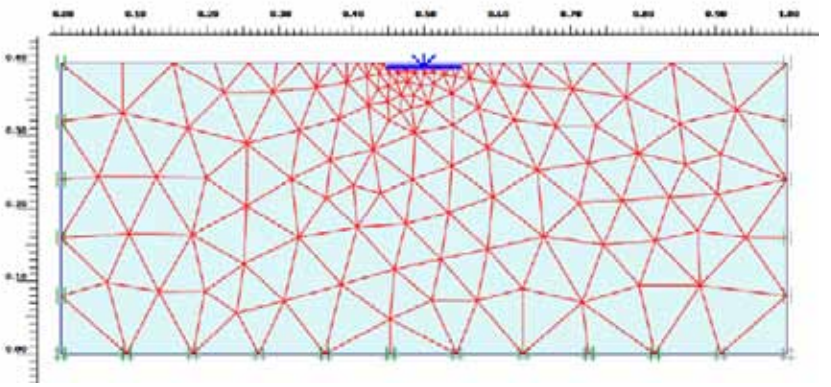

Figure 7 — Mesh layout for PLAXIS Simulation — Hardening-Soil Small Strains Soil Model

Constitutive Modelling

A Macroelement from [2], constituting structural component, the interface between soil and foundation, the interaction between the different forces with inclusion of single surface hardening soil model is used herein. The parabolic failure criteria taking account of both inclined and eccentric forces in three-dimensional space, is as follows, [2] (Fig. 8);

$$f\,(Q\,,\,p_c) = h^2 + m^2 - \xi^2\left[1 - \frac{\xi}{p_c}\right] = 0 \tag{3}$$

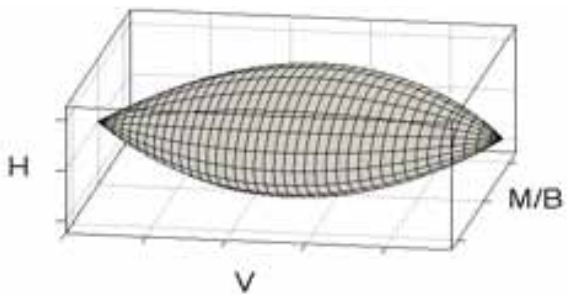

Figure 8 — 3-D failure envelope in V, H, M/B space

By the introduction of new function called plastic potential denoted by g, the expression for the increment of plastic displacement for a given state of forces(Q) and the given incremental displacement is obtained as;

$$dq^p = \Lambda\,\frac{\partial g}{\partial Q} \tag{4}$$

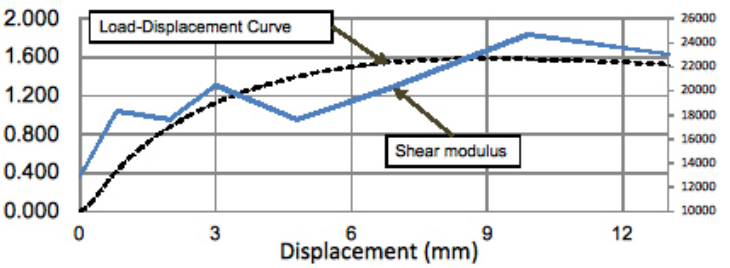

Figure 9 — Change in stiffness with the increase in displacement during the monotonic loading of footing.

Results

The numerical response of the load deformation behaviour of rigid square footing was obtained by the use of finite element code excluding the effect of SSI and the Macroelement which includes the effect of SSI. The degradation of stiffness at the depth of 10 cm from the surface of footing, during the loading was obtained by the use of bender-element (Fig. 9).

Numerical response from PLAXIS by the use of Mohr-Coulomb Soil Model (Fig. 10), was obtained at three iteration steps with the final value of stiffness E = 8785.3 kPa. Whereas, by the use of Hardening-Soil Small Strain Soil Model, numerical response for load deformation behaviour, was obtained with the final value of stiffness, E = 13400 kPa, (Fig. 11).

The numerical response of the Macroelement which includes the effect of SSI provides the prognosis of the displacement under static loading from small to large displacement, including the failure. (Fig. 12), shows the comparative study of numerical response of load deformation behaviour, with the experimental result.

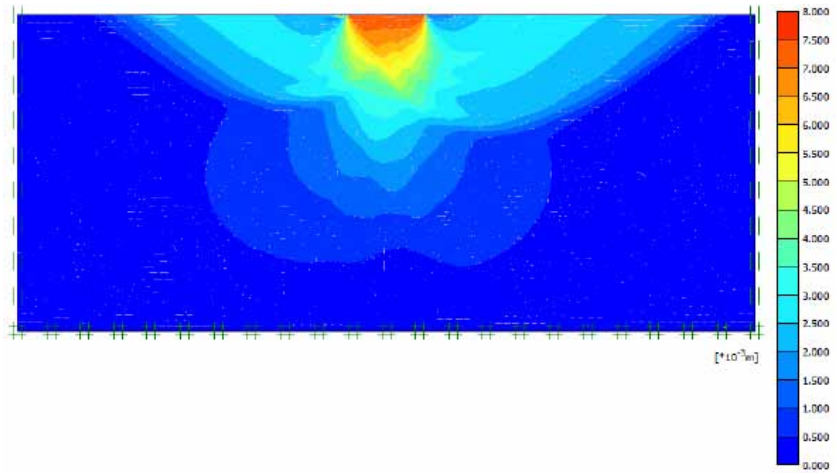

Figure 10 — Deformation of soil obtained from PLAXIS Simulation, Mohr-Coulomb Soil Model

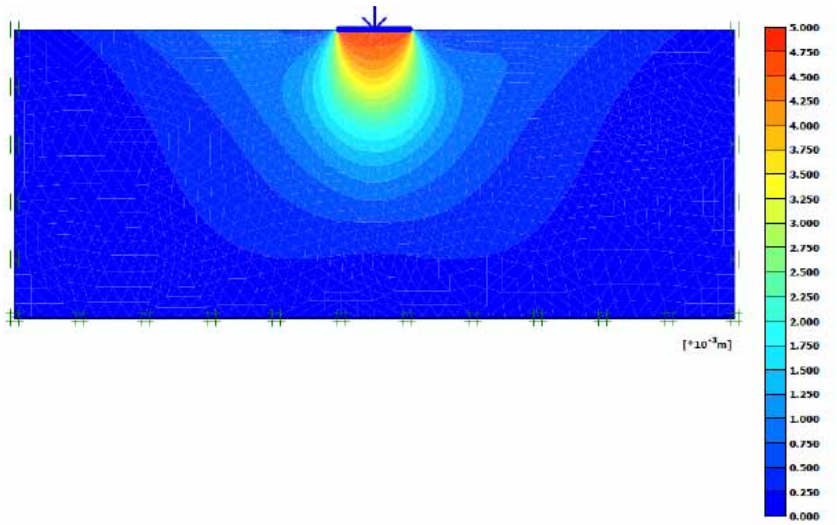

Figure 11 — Deformation of soil obtained from PLAXIS Simulation — Hardening-Soil Small Strains Soil Model

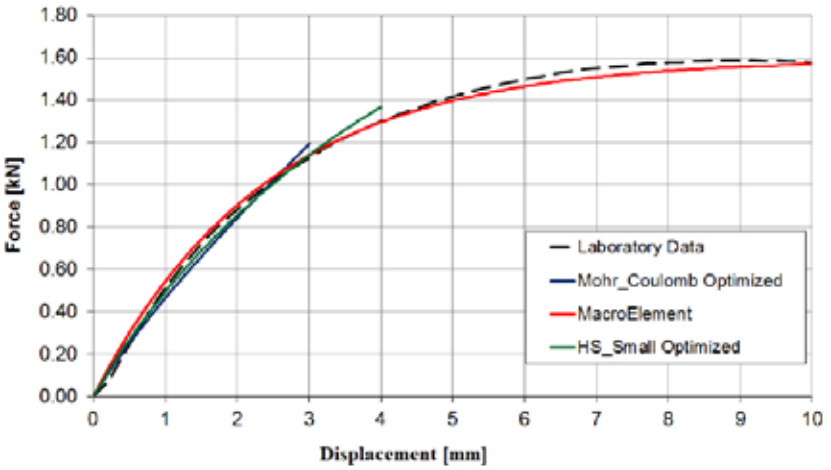

Figure 12 — Numerical response of load deformation behaviour.

Conclusion

The effect of SSI on the numerical response was studied by the use of single surface hardening Macroelement. The comparative study of the model response by the use of PLAXIS for two different constitutive models, Mohr-Coulomb Soil Model and Hardening-Soil Small Strain Soil Model showed that the numerical response can only be obtained for small deformation. For the large deformation the model response is conservative. On the other hand Macroelement is able to predict the prognosis of deformation in the complete range of loading including failure. The pronounced decrease in soil stiffness was also observed by measuring the shear wave velocity obtained by the use of bender elements.

References

[1] *Kramer, S. L. (1999), "Geotechnical Earthquake Engineering" Pearson Education, Inc.*

[2] *Nova, R. and Montrasio, L. (1991). "Settlement of shallow foundations on sand." Geotechnique, 41(2), 243–256.*

Project 3 — Evaluation of seismic performance of a template design RC school building before and after strengthening

ABRAHAMCZYK, Lars
Bauhaus-Universität Weimar

GENES, M.Cemal
Mustafa Kemal University

ANDIC, Halil Ibrahim
METU, Ankara, Turkey

BONEV, Todor
BOSHNAKOV, Simeon
UACEG, Sofia, Bulgaria

ELYAMANI, Ahmed
Technical University of Catalonia, Spain

GRUBISIC, Marin
GFOS, Osijek Croatia

HAVLIKOVÁ, Ivana
Brno University of Technology, Czech Republic

UDREA, André
BUW, Weimar, Germany

UGURLU, Tolga
YELEN, Burcu
MKU, Hatay, Turkey

STILIANOPOULOU, Lily
NTUA, Athens, Greece

TSONEV, Aleksander
UACEG, Sofia, Bulgaria

ZIMMO, Iyad
Birzeit University, Palestine

Abstract

The aim of the project was to introduce the participants into advanced requests in the field of earthquake engineering. The studies were concentrated on a template design RC school building (Figure 1), which revealed low seismic resistant in the past earthquakes in Turkey. Therefore the Turkish Government started after the damaging events in 1999 a campaign to investigate and strengthen these buildings all over Turkey.

In the frame of these campaign one typical school building, with quite similar ground plans to the school building which failed during the Bingöl Earthquake in 2003 could be instrumentally investigated before and after strengthening.

The participants of the project assessed the performance of the structure before and after the applied strengthening measures on the basis of measured building response data and evaluate the earthquake resistant design. They carried out damage prognosis for the given seismic action and compared it with the real occurred damage after the Bingöl EQ by using modern software tools.

Introduction

School buildings belong to the building class of higher priority according to the common code requirements, because of their use as meeting point and shelter in the immediate aftermath of a disaster as well as their high occupancy rate.

The major part of the school buildings (80%) were constructed before 1997, which means according to the requirements of the 1972 earthquake code and under the consideration of obsolete seismic demands. In many cases rules of earthquake resistant design were not applied.

The devastating Marmara Earthquake (17th August 1999) and Bingöl Earthquake (1st May, 2003) caused heavily damages and collapses on a serious number of school buildings. Therefore the Turkish Government initiated a programme for the systematic inspection of school and hospital buildings in Turkey together with the application of strengthening measures for governmental buildings with poor performance.

In the frame of a project the project partner of the summer course Mustafa Kemal University could accompany a strengthen measure of a school building by dynamic investigation.

Study Object

General Information

The considered school building is one of three school buildings in Hatay (Turkey), which could be dynamically investigated before and after strengthening. It is a 3-story RC frame structure building and was constructed in 1997 according to the 1972 earthquake design code (see Fig. 1).

Figure 2 show the modification of the ground plan by the replacement of non-structural masonry infill walls with reinforced concrete structural walls (red walls), which is a common strengthening technique in Turkey to increase the building capacity and to decrease the maximum displacements. The chosen school building is thus representative for a large number of school buildings in whole Turkey before and after strengthening.

Evaluation of the structural system

A first evaluation of the study object before and after strengthening was carried out on the basis of regularity and construction details check. The general layout obeys with the regularity criteria of an earthquake resistant designed structure which will be confirmed by the check of the location of the centre of mass (red point) and rigidity (blue point) in Figure 2.

The location of the centre of mass and rigidity a translational behaviour of the building in both directions can be expected under seismic action due to the quite small distances between as well as the location

Figure 1 — Front view of the study object [1]

of both points. That means in case of the unstrengthen structure only less additional forces can be expected due to torsional behaviour. Due to the retrofitting of the structure the centre of rigidity was shifted, thus a larger distance occurred and the influence of torsional motion will become higher.

The reinforcement details are in general of poor quality, which was also the highest motivation for the retrofitting.

Observed building performance after the Bingöl EQ

The magnitude 6.6 Bingöl (Türkiye) earthquake on May 1, 2003 caused severe damages and collapse to school buildings (see Figure 3). The comparison of the general layouts from the damage structures and the study object indicates the representativeness of the studied object and provides the opportunity to adopt the experiences from the Bingöl earthquake to the study area Antakya. Thus, the results of the damage prognosis can be compared with the observed damages on school building with a nearly identical (template) design for a known seismic action.

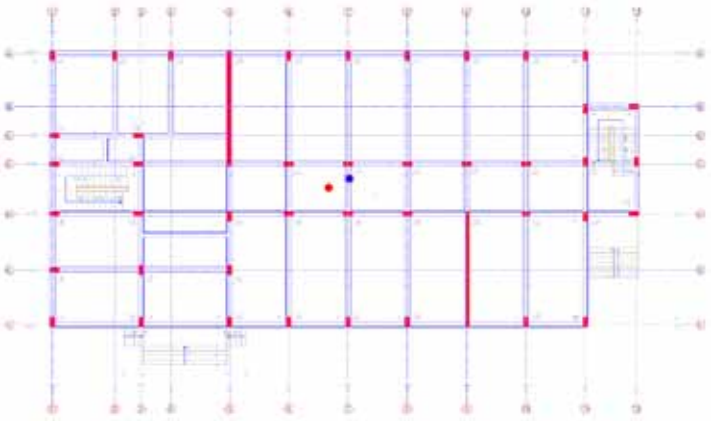

a) Before strengthening

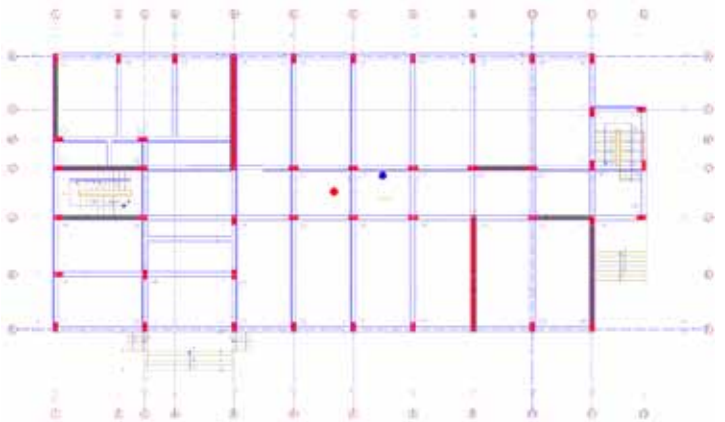

b) After strengthening

Figure 2 — Ground plan of the study object

Figure 3 — Damage of a school building caused by the 1st May Bingöl earthquake [2]

Experimental tests

Building response measurements

Mustafa Kemal University carried out building response measurements before and after strengthening of the school building in 2011. The building was equipped with five triaxial velocity sensors Type MS2004+ and the corresponding recorder Type MR2002 (SYSCOM Inc.). The sensors are oriented at the main axis of the building. In general, two sensors were installed in two opposite corners on the roof and two sensors in the same corners on a mid-floor story. The fifth sensor was installed in the middle of the ground floor. Sensor number six was installed outside of the building (see scheme in Figure 4).

A "lightweight" exciter (transportable by two men; covering a frequency range between 1 and 15 Hz) was successfully applied [3].

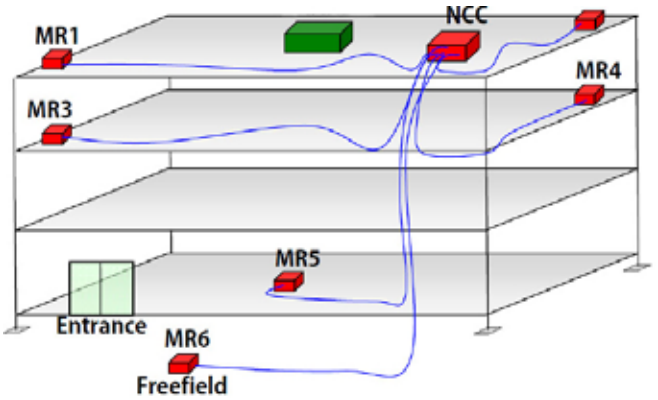

Figure 4 — Applied instrumentation scheme [1]

Elaboration and interpretation of the measured data

Different programmes were applied to determine the eigenfrequencies and corresponding mode shapes. The ambient and forced vibration data were conditioned with the programme MATLAB for the use in the programme ARTeMIS, the MATLAB toolbox MACEC as well as MATLAB routines.

The signals were than analysed by the application of FFT techniques [3] and use of the Stochastic Subspace Identification Method [1]. Thus only the programme ARTeMIS and the toolbox MACEC provide directly a sketch of the mode shape.

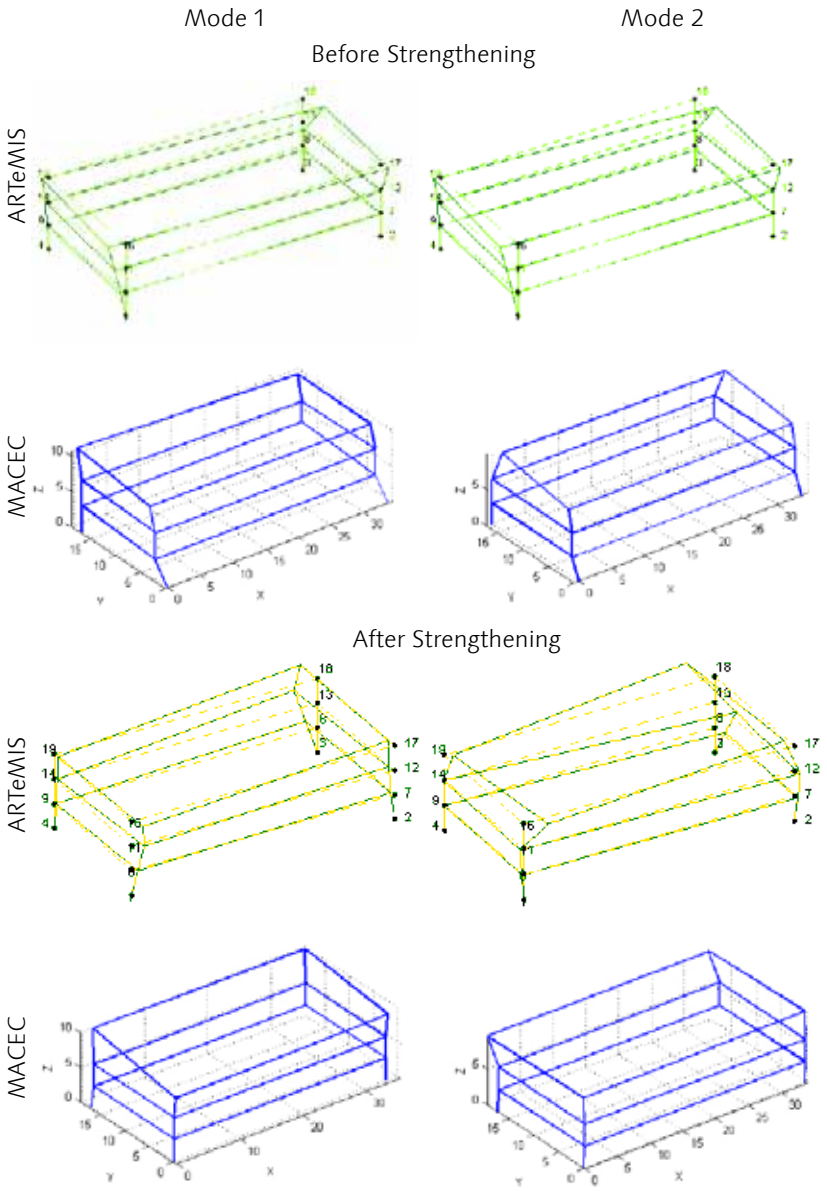

Figure 5 — Determined characteristic modes before and after strengthening by the use of instrumental data

The pure analysis of the data by the application of FFT techniques only identifies the natural frequencies of the building at each measurement point.

Figure 5 show the first two mode shapes analysed with the programme ARTeMIS and MACEC, which could be determined for the building before and after strengthening with. It can be clearly seen,

Figure 6 show the normalized FFT response values from the sensor MR1 and MR3 in x- and y-direction before and after strengthening; the normalization accounts for different amounts of weights which were used during the measurements to cover the whole frequency band [3]. Especially in the case without strengthening clear peaks can be determined, which indicate the highest amplification of the introduce signal due to the resonance to the natural frequencies of the building in each direction.

Table 1 provide the summary of the determined first structural frequencies. The comparisons show quite identical results for the first two modes (f_1, f_2) before and after strengthening. But it has to be noted, that the identification of the natural frequencies by the FFT approach only might be lead to other results, because at some sensors no clear peak can be identified and a comparison to other sensors or approaches is recommended.

Table 1 — Determined fundamental frequencies from the experimental testing

	Frequency [Hz]			
Software	before strengthening		after strengthening	
	f_1	f_2	f_1	f_2
MACEC	6.90	7.50	8.30	9.12
ARTeMIS	7.08	7.52	8.25	9.03
FFT	6.79	7.25	8.25	8.97

Analytical Studies

For the building investigated, a 3-dimensional model was created using the software tools ETABS and Sap2000. Provided construction plans of the building supplied the required geometrical data. Material properties for the given quality were assumed according to the Turkish standards.

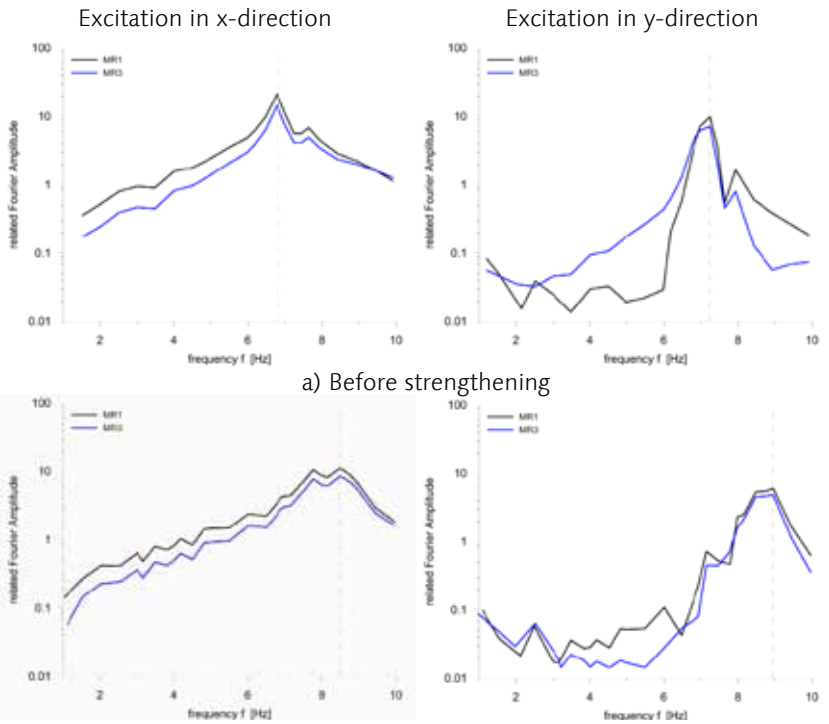

a) Before strengthening

b) After strengthening

Figure 6 — Recorded building response (normalized FFT Amplitude) at Sensor MR1 and MR3 for excitation in x- and y- direction

Columns were generally assumed as rigidly connected to the underground. Floors were modeled as rigid diaphragms; roof constructions were taken into account by planar loads. Masonry infill walls were neglected to reduce the modeling and analysis effort, because of the limited time window.

The material parameters for concrete were assumed to have characteristic cube strength of 16 MPa (as denoted in construction plans). Reinforcement was assumed to be of Turkish steel grade S220a (220 MPa yield strength and 10% strain at ultimate strength; generally smooth, not profiled), also corresponding with specifications in plans.

Figure 7 show the 3D model before and after strengthening modeled with beam and shell elements. The adaption of beam elements for the added shear walls was necessary to apply nonlinear hinges for the push over analysis.

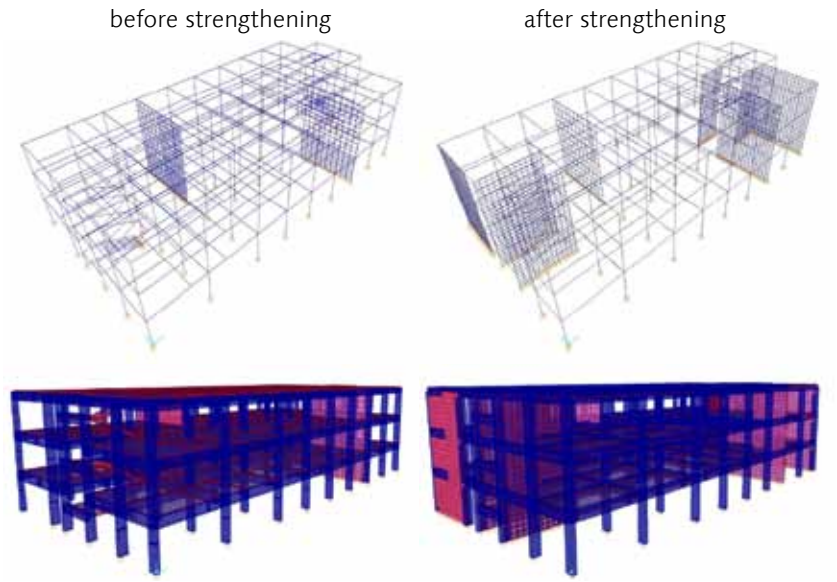

Figure 7 — 3D model before and after strengthening (Using shell elements for the modeling of the structural walls)

The fundamental periods of the buildings, which were known due to the dynamic recordings, were used as a measure for the calibration of the stiffness parameters. Young's Moduli were reduced (in comparison to recommended values given in code specifications) for all elements of identical material. In the frame of the project the goal was not to achieve a perfect match for the building. Congruency of the main mode shapes and frequencies/periods was nevertheless seen as important.

Table 2 shows the comparison of the experimental and first analytical (without calibration) determined fundamental periods of the school building before and after strengthening. The calibration of the model was foreseen by the link of SAP2000 with an optimization MATLAB program prepared by the participants of Project 5. Due to technical problems and limited time only the communication could be realized and the routine be rune. A final calibration could not be achieved.

Therefore the natural frequencies of the analytical model are so far not comparable with the results from the measurement, which indicates the need of model calibration. The results show, that modeling of complex 3D structures bases on the construction plan can lead to much different dynamic behavior and thus to un-conservative seismic load assumption (see Figure 8).

	Period [sec]			
Software	before strengthening		after strengthening	
	T_1	T_2	T_1	T_2
MACEC	0,145	0,133	0,120	0,110
ARTeMIS	0,141	0,133	0,121	0,111
FFT	0,147	0,138	0,129	0,118
SAP2000	0,310	0,180	0,135	0,132

Table 2 — Comparison of the fundamental periods before and after strengthening

Damage Prognosis

Nonlinear static pushover analysis was applied to determine the building capacity in form of the capacity spectrum in x- and y-direction and to carry out a damage prognosis. The N2-method proposed by Fajfar [4] was applied to investigate the response of the school building to a design spectrum excitation. A design spectrum according to the Turkish seismic code and assuming different PGA level, factor of building importance class I = 1.0, and subsoil conditions Z2 was used. For a PGA of 0.4 *g* corresponding to the highest seismic zone no intersection between the capacity spectrum and the design spectrum resulted; thus, according to the calculations performed here, the building would not be able to withstand an earthquake corresponding to the required specifications. Further calculations were carried out in order to determine the level of peak ground acceleration the building could resist. The value of PGA = 0.33 *g* was found to be the threshold for total collapse (see Figure 9).

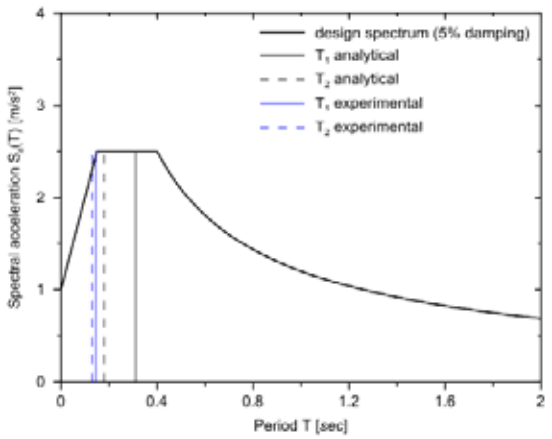

Figure 8 — Indication of the influence of the considered characteristic periods on the example of the Turkish Code Spectrum

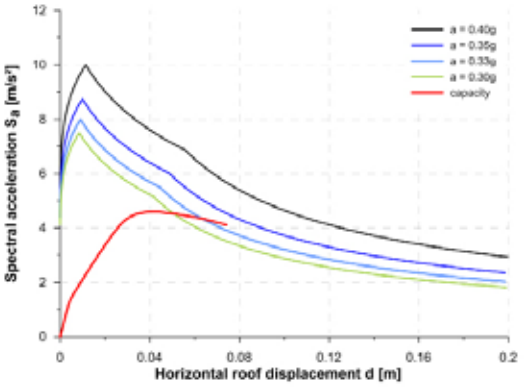

a) x-direction

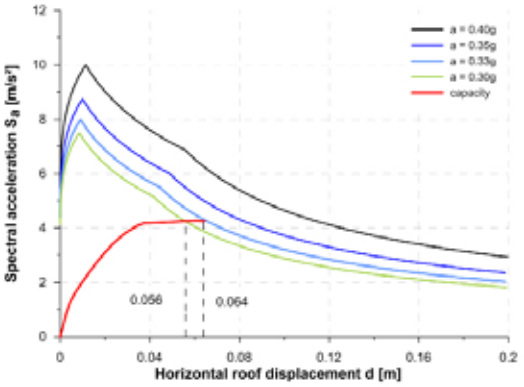

b) y-direction

Figure 9 — Demand spectrum in x- and y- direction by the application of N2-method

Conclusions

In the frame of the project a damage prognosis was carried out for a 3-story RC frame school building under the use of building response measurement data and modern software tools. Experimental testing at the building could be done before and after strengthening of the structure by the project partner MKU, who provided the data for the project. For the strengthening of the structure shear walls were added to increase the building capacity and to decrease the maximum displacements.

The provided building response data were analyzed to determine the principle fundamental periods and corresponding mode shapes, which were used for the calibration of the structural models. The comparisons of the experimental and first analytical periods indicate the necessity of model calibration. First analytical results indicate a much weaker behavior of the structure, which can lead to un-conservative seismic load assumptions.

Estimations of structural performance were conducted using site-specific response spectra reflecting subsoil conditions of class Z2 according to Turkish code and the application of the N2-Method. The results for the origin structure indicate that the vulnerability of the 3-story school building does not fulfill the requirements by the design code. For the site considered ground acceleration of 0.4 g will cause heavy damages

or collapse of the building. The structure is only capable to withstand ground motion smaller than 0.33 g. There was a need to strengthen the structure. The check of the sufficiency of the carried out strengthening measures could not be realized in the frame of the project.

References

[1] *Genes M.C. (2011). Forced vibration testing of school buildings before and after strengthening process. Bauhaus Summer School — Model Validation and Simulation 2011, Presentation*

[2] *Schwarz, J., Abrahamczyk, L., Lang, D.H., Maiwald, H. (2004). Ingenieuranalyse von Erdbebenschäden: Das Bingöl (Türkei) Erdbeben vom 1. Mai 2003. Bautechnik 81, 6, pp. 445–460.*

[3] *Abrahamczyk, L., Schwarz, J. (2009): Vibration measurements on an 8 story office building in Bern (Switzerland). In Proceedings Workshop on — Case studies of seismic building instrumentation and monitoring. Bauhaus-Universität Weimar*

[4] *Fajfar P. (2000): "A nonlinear analysis method for performance based seismic design." Earthquake Spectra 2000; 16(3): 573–592.*

Project 5 — Calibration of Numerical Models with Applications in Civil Engineering

AKANSEL, Vesile Hatun
Middle East Technical University, Turkey

BANKIR, Sahin
Mustafa Kemal University, Turkey

OLIVEIRA, Luciane Marcela Filizola
School of Engineering of São Carlos, University of São Paulo

FARAONIS, Periklis
Aristotle University of Thessaloniki, Greece

KADĚROVÁ, Jana
University of Technology, Brno

KOILANITIS, Ioannis
Aristotle University of Thessaloniki, Greece

LAHMER, Tom
Bauhaus-Universität Weimar, Germany

PAPADOPOULOS, Savvas
Aristotle University of Thessaloniki, Greece

SKIADA, Dafni
Aristotle University of Thessaloniki, Greece

TÓTH, Adrienn
BME, Department of Structural Engineering, Hungary

Abstract

The course aimed in understanding and testing well-known optimization tools for the nonlinear problem of parameter identification for problems occurring in civil engineering applications. The students worked on 4 different classes of optimizers and applied them to both academic ad real world examples

Introduction

It is a common practice in engineering to calibrate numerical models against sets of measurements in order to predict the structures' behaviour more precisely.

In particular in civil engineering, structures may have been built recently, where the design was supported with the help of numerical models. As now, after the construction phase, first loads are acting on the structure, its responses can be observed. With this, the model used in the design process can be validated posteriorily. Additionally, the model parameters can be tuned in that way that the model's prediction coincide with the measured data as good as possible.

This tuning, solving an inverse problem, can effectively be solved with methods of finite dimensional nonlinear optimization tools.

Gradient and Newton Methods

Classical approaches in the field of nonlinear optimization are Gradient-based and Newton-type methods. These methods are motivated by studying necessary and sufficient conditions of optimality. These class of optimizers are generally supported by mathematical analysis

concerning convergence and convergence rates. In this course gradient methods with line-search strategies and a so-called quasi-Newton method, where the Hessian matrix is approximated by a rank two update according to the BFGS approach are tested The latter approach allows to approximate Hessians and to use Newton directions in the optimizer instead of gradient directs, which depending on the topology of the optimizing problem may tend to zig-zagging leading to slow convergence.

Direct Search Methods

It is not always possible to calculate gradients in a satisfying manner, mainly due to missing differentiability of the cost functional. In these cases it can be advisable to apply gradient free methods, so called direct search methods. A very effective and well-proven method is the algorithm according to Nelder-Mead, which bases on simplex. A simplex is the connection of (n + 1) points in the parameter space, where n is the number of parameters which need to be identified. Now, the strategy is to replace always the vertice which has the largest value in the cost function. The replacement is done by reflecting this point to the centroid of all other points. A series of expansion and contraction approximates a kind of line search. After finding a new point, the vertices are sorted again and the vertice with the worst cost function value is again replaced. Being close to an optimum, the simplices start to shrink.

Optimizers based on Swarm Intelligence

Another class of optimizers is motivated by swarm intelligence, where every member of the swarm has its own flight direction and velocity, however generally for the whole swarm there is one global flight direction. Applying such methods one can run global searches. With a high probability, the methods will converge to a global minimum; however, there is no guarantee for this. As the particles are spread randomly on the set of all admissible input parameters, the probability in finding the global optimum is increased using more particles. However, more particles mean higher numerical efforts, which can become a challenge when the computing time of the model is high.

Bayesian Updating

In Bayes Framework the optimization corresponds in maximizing the likelihood (the probability that the model parameters fit well to the measurements). The advantages of the Bayesian approach are that information of the prior knowledge of the sought-for-quantities can be taken into account. Accordingly also any knowledge about uncertainties in the measurements are evaluated, which allows at the end for a qualitative assessment of the identified parameters in terms of

probability density functions. Comparing them, information can be provided if sufficiently many measurements have been available in order to detect the parameters sharply, i.e. with a low uncertainty.

Application and Results

The methods have been applied to identify characteristic data of an Harmonic Oscillator. The model is the solution of the equation of motion in 1 D. The second order differential equation is solved analytically including the three parameters

- Stiffness (k)
- Damping (c)
- Mass (rho)

From recorded time signals, these parameters need to be identified. The cost function measures the squared difference between computed and simulated signals for a set of time steps. In Figure 1 the recorded data are plotted as blue points. The model' solution with initially guessed parameters resulted in the green curve. After the calibration, simulation results, i.e. the red line, and measurements are in good agreement.

Besides the calibration of the parameters we discussed questions of unique identifiability and tried to visualize this by the help of countor plots. In the following figures, always one parameter was kept fixed, the others varied and isolines of the cost function have been computed and visualized.. From these plots one can graphically detect the optimal parameter pairs leading to a good fit. In case that both the menachical stiffness and the mass are unknown, the problem has infinitely many solutions, see Figure 3. Adding a regularizing term in the definition of the cost function, any deviation from the initial guess is penalized. This approach helps in finding a solution from the infinitely many combinations of mass and stiffness which provide a good fit.

Summary

In this course a series of optimization methods have been implemented by the students. The methods provided the bases for calibrating some numerical models against measured data of the other groups in the second part of the summer academy.

Students of the calibration course could help the others to get things quickly run. It has shown, that in particular when little a priori knowledge is given, the method according to Nealder-Mead showed the most robust optimization results when beeing applied to more complex models in engineering. Being close to solution, gradient-type and Newton methods showed good performances.

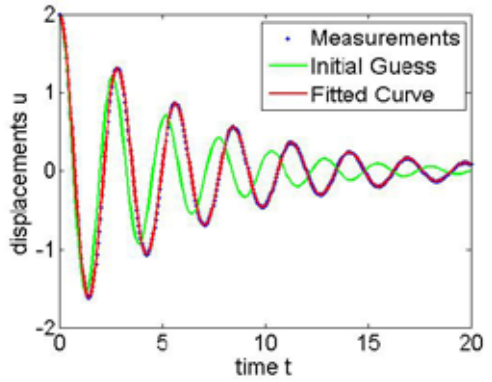

Figure 1 — Measured, simulated and fitted displacements of the harmonic oscillator

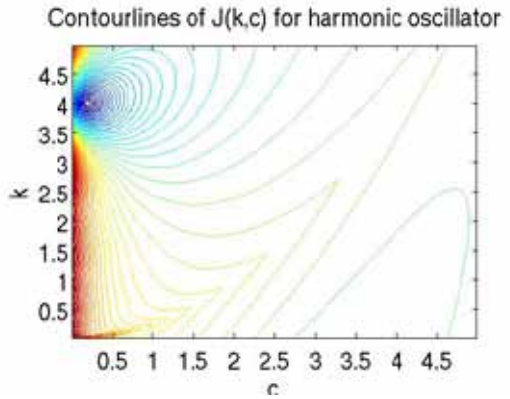

Figure 2 — Contour lines of the cost function with assumed known mass. Stiffness and damping are varying. The optimum is in point (0.2, 4).

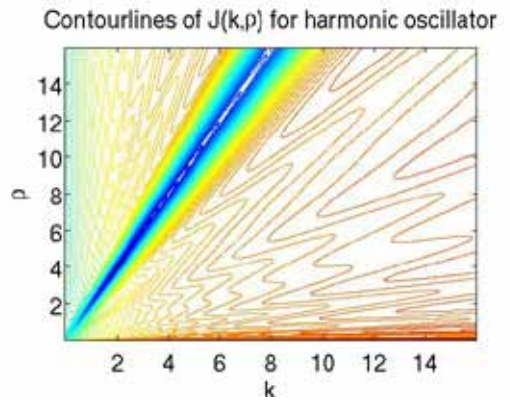

Figure 3 — Contor lines of the cost function with assumed known damping. Stiffness and mass are varying.A clearly distinghuishable minimal point cannot be identified.

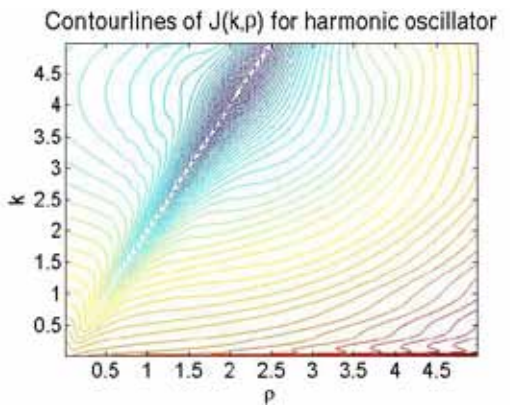

Figure 4 — Same as previous Figure. However, the cost function includes a penalty term, which allows to find a minimum in (2.2, 4.1).

Project 6 — Long-span Bridge Aeroelasticity

Abstract

The project deals with the structural modelling and dynamic analysis of long-span bridges under wind excitation. A realistic simulation of the structural behaviour first requires the analysis of the geometric stiffness under self-weight. Based on this, the dynamic response of the structure due to various critical wind excitation phenomena will be simulated numerically. These include turbulence-induced buffeting, vortex-induced vibrations and instabilities like flutter.

The project uses Computational Fluid Dynamics (CFD) simulations to determine the aerodynamic properties of the bridge girder. These will then be used on the full three-dimensional bridge model to assess the aeroelastic behaviour of the structure.

Four work teams have been constituted to carry out four different topics related to bridge aerodynamics: influence of windshields on bridges, improvement of aerodynamic behaviour of cross-section geometry, vortex-induce vibration on bridges and flutter instability.

A brief description of them and the main results achieved are presented below.

MORGENTHAL, Guido
BUW, Weimar, Germany

ABBAS, Tajammal
BUW, Weimar, Germany

DANYILDIZ, Bekir
MKU, Hatay, Turkey

HENAO PUERTA, Alejandra
UNC, Manizales, Colombia

SÁNCHEZ CORRIOLS, Abraham, UPM, Madrid, Spain

DE BORTOLI, Marta
UNIPD, Padova, Italy

HEGYI, Peter
BUTE, Budapest, Hungary

ABERLE, Marcus
KUAS, Karlsruhe, Germany

LESGIDIS, Nikolaos
AUTH, Thessaloniki, Greece

ROCHA, João Francisco
FEUP, Porto, Portugal

BUDAHAZY, Viktor
BUTE, Budapest, Hungary

KOLEVA, Tatyana
UACEG, Sofia, Bulgaria

KISHAIJA, Paul
BUW, Weimar, Germany

Study of the influence of windshields on bridge sections

DANYILDIZ, Bekir
MKU, Istambul, Turkey

HENAO PUERTA, Alejandra
UNC, Manizales, Colombia

Abstract

This paper analyses the effect of windshields on the aerodynamic behaviour of bridges. To that end, numerical simulations have been carried out by modelling the interaction between the airflow and three different cross-section geometries: a standard bared cross section formed by a simple box girder with two cantilevers on both sides, the standard section with vertical full windshields curved on top, and the standard section with porous windshields. VXflow, a particle-based CFD code, have been used to perform these numeric simulations. The post processing have been done with MatLab.

Introduction

Wind protection barriers (or windshields) are widely used in all bridges that are subject to constant wind actions in order to protect the traffic of vehicles (and pedestrians) against sudden variations of wind speed (gusts), and other effects that may cause a number of instabilities, especially on trucks, and represent a dangerous problem. Figure 1 shows the influence of wind on vehicles over the bridge, through the display velocity field. Blue tones correspond to low speeds, and the red colour to higher wind speeds.

The addition of the barriers is counterbalanced by the increase of the bridge area exposed to wind, resulting in an increase of the wind forces acting on the structure. Bridge cross sections must be designed also considering this action. Altering the cross-sectional geometry should be taken into account also in the study of aeroelastic of bridge. With the adding of windshields, fluid-structure interaction is modified, and may lead to the emergence of larger dynamic vibration problems motivated by vortex shedding, whose frequency is mainly influenced by the section geometry and the wind speed.

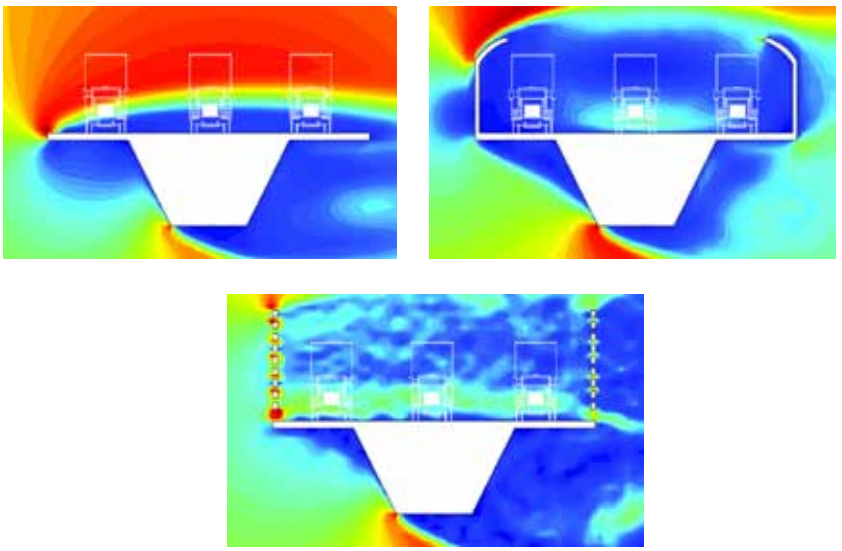

Figure 1 — Effect of windshields on traffic (velocity field visualization obtained by numerical simulations)

Case Study

Three different cross-sections have been considered: the standard bared box girder section with two cantilevers on both sides, the standard section with windshields curved on top, and the standard section with porous windshields (see Figure 2). The vertical dimension of windshields is 4.0 m, as recommended on various standards to achieve a adequate protection against wind effects on traffic crossing the bridge. Figure 3 shows some examples of actual bridges windshields.

Figure 2 — Sections models performed: standard, curved and porous

Figure 3 — Some examples of windshields on real bridges

Static simulation tests

Regarding to the values of the drag coefficient (C_D, Figure 4) as a function of different angles of attack (α), it is found that the standard section is the one with the lowest values. The highest values correspond to the cross section with porous windshields. The drag coefficient for standard section with windshields curved on to is slightly lower because of its better aerodynamic behaviour. Regarding to the time history of the lift coefficients (C_L, Figure 5), it is observed that the section with windshields curved on top has the major values. Dynamic effects caused by the wind will be more important in this section. The lowest mean lift coefficient corresponds to the section with porous windshields.

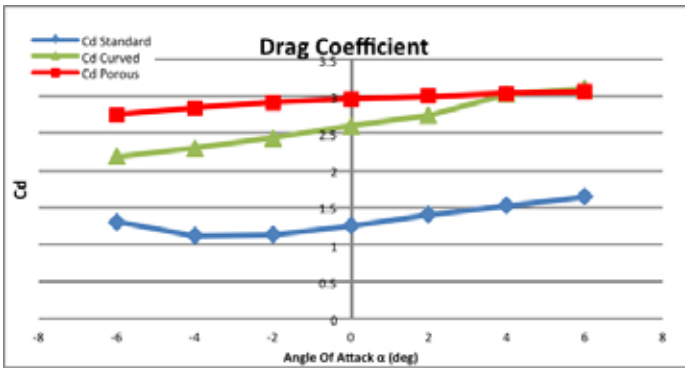

Figure 4 — Drag Coefficient of cross-sections

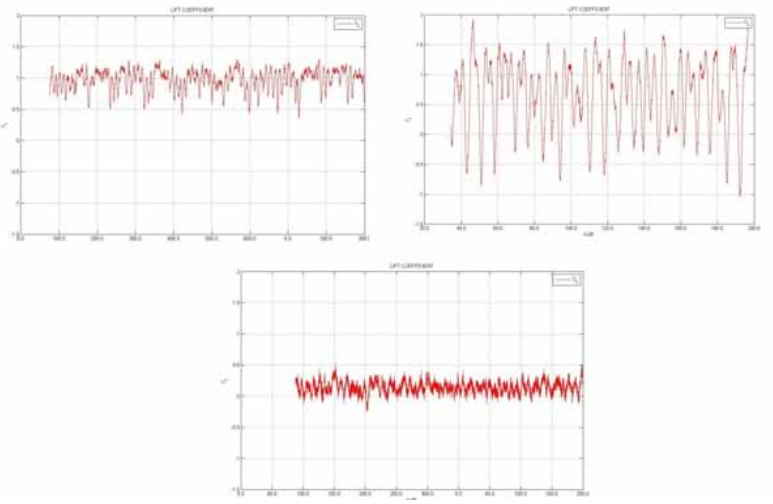

Figure 5 — Time history for lift coefficient of the three cross-sections (CL) : standard (top left), with rounded windshields (top right), and porous windshields (bottom)

Table 1 shows a summary of force coefficients for the three cross-sections considered

	STANDARD SECTION	CURVED SECTION	POROUS SECTION
CL	0,96	0,67	0,3
CD	1,25	2,60	2,96
CM	0,19	0,22	0,33

Table 1 — Force coefficients for the three cross-sections performed

Conclusions

In view of the above results, it follows that the section with full windshields and curved on top presents a better behaviour against wind effects on traffic. However, this section also has the major force coefficients, indicating that static wind actions are greater, and also possible effect due to dynamic vibration that may suffer as a result of fluid-structure interaction phenomenon.

Since it is important to protect traffic from the destabilizing effects of wind and, at the same time, to have reasonable values for force coefficients, the section with porous windshields is the optimal solution to be used.

References

[1] *Morgenthal, G. "VXflow Primer" version 0.994, Weimar, Germany, May 2012*

[2] *SIMIU, E., SCANLAN, R. "Wind Effects on Structures" John Wiley & Sons, Inc., New York, USA, 1996, Chaps. 6 and 14.*

Improvement of aerodynamic instability on bridge sections

DE BORTOLI, Marta
UNIPD, Padova, Italy

HEGYI, Peter
BUTE, Budapest, Hungary

Abstract

The aerodynamic behaviour of Lillabælt bridge cross-section is discussed in this paper. Four cross sections are investigated to compare their aerodynamic properties (force coefficients), and analyse the vortex-induced vibration phenomenon. Among the numerical results, also a brief theoretical introduction is provided.

Introduction

Lillebaelt or New Little Belt Bridge (Figure 1) is a suspension bridge situated over the Little Belt strait in Denmark. The total length of the bridge is 1.080 m, with a central span of 600 m and two side spans of 240 m each. The two piers have a total height of 113 m and stand on deep pile foundations. The bridge was opened in 1970. The corresponding cross section can be seen in Figure 2. Due to its geometry, the bridge was likely to be sensitive to wind-induced oscillations, and this is the reason why it was largely analyzed. In fact, other bridges with similar structural characteristics — suspended bridges with very slender decks — had shown problems in the past, for example the Tacoma Bridge in Washington, USA.

Figure 1 — The Lillebaelt Bridge

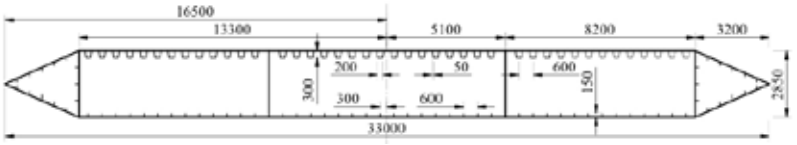

Figure 2 — Original cross section of Lillebaelt Bridge

Moreover, the geographical environment is characterized by steady wind speeds, which worsen the aerodynamic phenomenon. In this paper we will compare the original cross section with three other cross sections to observe the different behaviour of them. VXflow, a particle-based CFD is used to study the wind-structure interaction phenomenon.

Static analyses

Introduction

The wind velocity was set to 15 m/s to simulate a realistic case. The same cross sectional depth, 2,85 m is used for all the cases, in order to compare the force coefficient properly. Different wind directions from –4° to 4° are studied to analyse the influence of the angle of attack. Also, the boundary layer around the section to assess the comfort levels for truck drivers is analysed.

Cross sections

A sketch of the four cross sections can be seen in Figure 3. The original section has triangular fairings, while one of the proposed cross sections has round fairings and the other one is a bare rectangular section. The fourth one is an original cross section equipped with windshields.

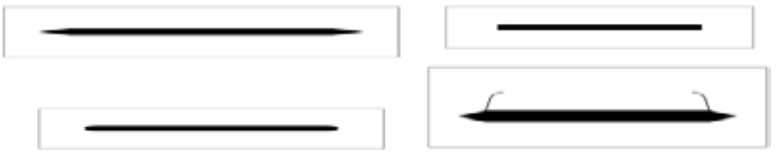

Figure 3 — Considered cross sections

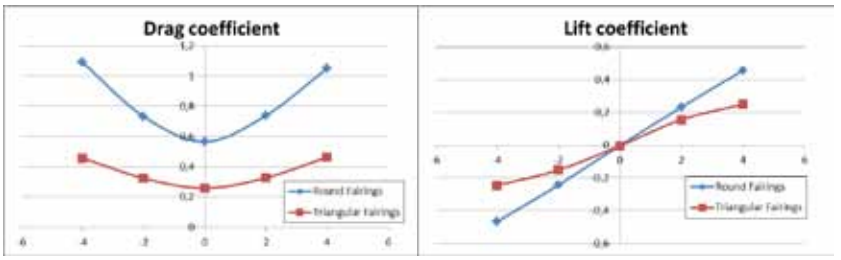

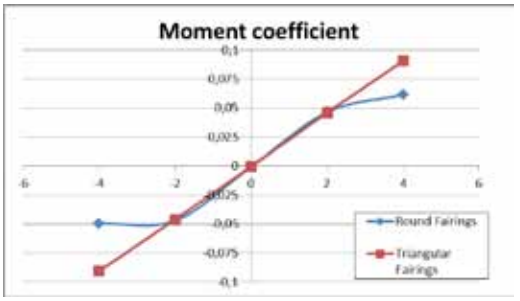

Figure 4 — Drag, lift and moment coefficient in the case of different wind directions

Results

Force coefficients

Figure 4 shows the drag and lift coefficients corresponding to the cross sections with triangular and round fairings. It can be observed that the triangular cross section has lower drag and lift force coefficients than the rounded one. Since the derivative of lift coefficient of the triangular cross section is smaller than the rounded one, the triangular section is less sensitive to buffeting phenomenon, because it will be less excited by the varying wind velocity directions.

In Figure 5, the force coefficients are compared in the case of horizontal wind velocity. It is clear again that the triangular cross section has optimal properties comparing to the other sections. The cross section with the windshields shows worse behaviour in terms of lift and moment coefficients, as a consequence of his larger depth and its asymmetry about the horizontal axis.

Boundary layers and vortex formation

In Figure 6, lower velocities are marked with blue, while higher velocities are in red colour. The smaller the blue region around the cross section, the more efficient the shape is. It can be observed that around the rectangular section there are some blue areas, which indicates that the wind flow is very whirling. The same can be observed in the case of the cross section with windshields. However, the windshield has a positive effect on the velocity in the area of the traffic. The average wind speed decreased drastically because of the windshield, but based on Figure 7 it can be observed that the direction of the velocity is varying, because vortices are formed between the shields. The rounded and triangular sections are more efficient since they hardly influence the wind flow around them. This is also their disadvantage, because the wind acting over the traffic is not reduced by anything.

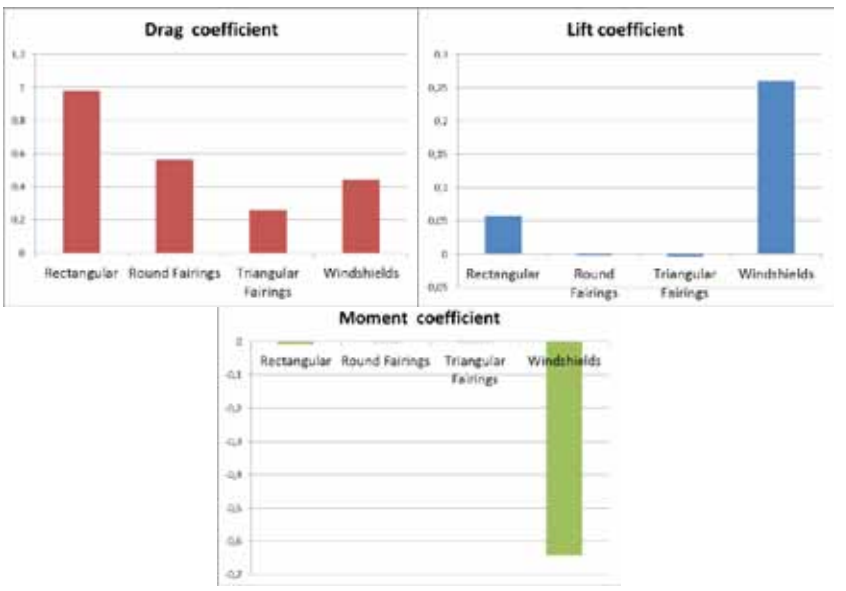

Figure 5 — Force coefficient for horizontal wind velocity

Dynamic analysis

Overview

In the wind speed-displacement graphic (Figure 8) there are two clear peaks: the first one occurs for lower velocities and identifies the critical wind speed for vortex induced vibrations (VIV), while the second and higher peak represents the instability caused by flutter. We focused our dynamic analysis on the first peak only. When the critical wind speed is reached, the displacements increase and maintain a constant pattern, thus reaching a limited value. This is the difference with the flutter instability, in which the wind energy is too high and produces increasing amplitudes of displacements. In the VIV, however, the peak is reached when the vortex frequency approaches the natural frequency associated to a considered mode shape, causing a resonance phenomenon.

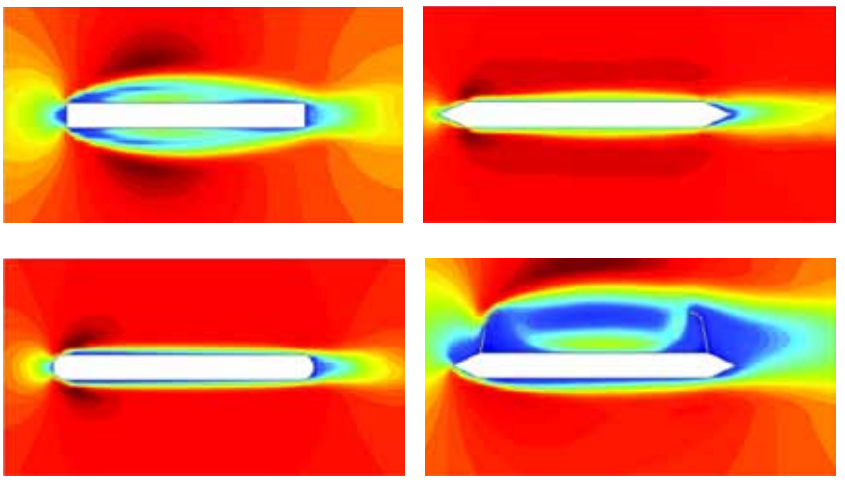

Figure 6 — Boundary layers of the cross sections

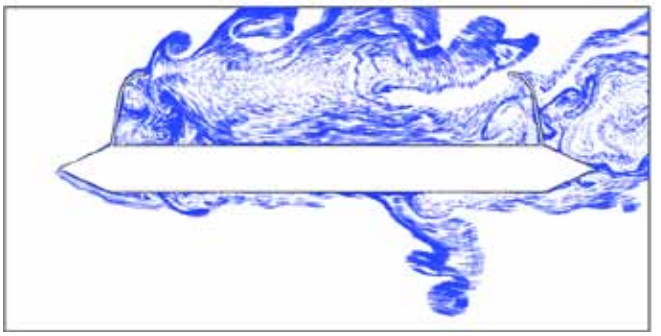

Figure 7 — Vortices between the windshields

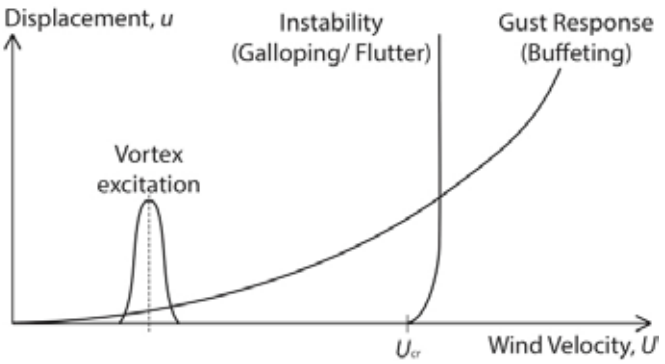

Figure 8 — Critical wind velocities

Each mode shape frequency can be excited by the vortex-induced vibrations, so at least the first 4–5 modes should be taken into account to identify critical wind speeds. The critical wind speed is reached when the displacements do not show higher oscillations but they are steady while wind speed is kept.

In Figure 9 the spectral density of lift coefficient ($S(C_L)$) is drawn against the Strouhal number. A region should be defined to identify the upper and lower border of the possible resonance. In this zone dynamic analysis should be performed to define accurately the VIV phenomenon. The bordering velocities can be evaluated using the following equation:

$$V = \frac{f \cdot D}{St} \tag{1}$$

where f is the vortex shedding frequency, D is the total depth of cross section, St is the Strouhal number.

Figure 9 shows the spectral density of lift coefficient against the Strouhal number for the cross section with windshields. Strouhal number value is located between 0.05 and 0.07, for which the lower velocity is 6,4 m/s and the upper one is 8,9 m/s.

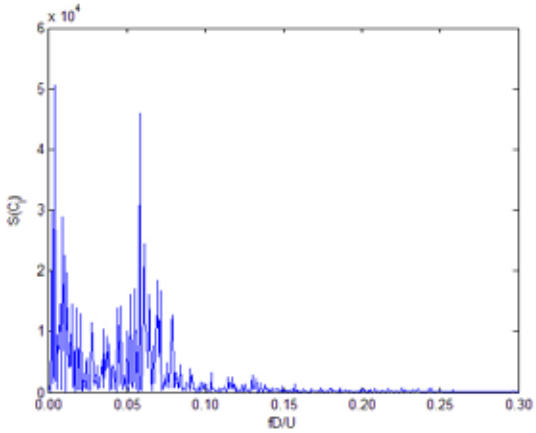

Figure 9 — Strouhal-number diagram

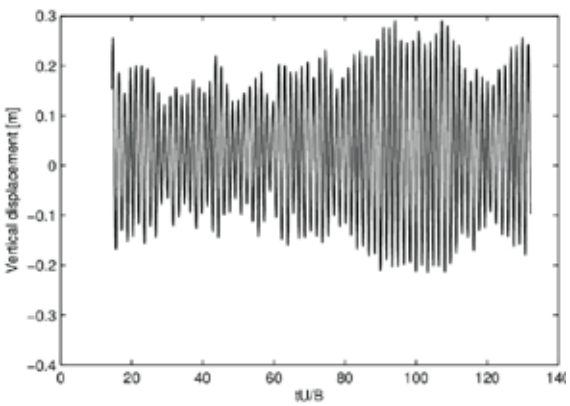

Figure 10 — Vertical displacements

We performed analysis assuming wind speeds of 7.0, 7.5, 8.0 and 8,5 m/s. Natural vibration frequency associated to the first vertical mode shape is f = 0.156 Hz and D = 2.85 m. A very low value for the damping ratio is used (ζ = 0,1%) in order to have visible magnitudes for vertical displacements. The modal mass is 11,100 kg/m.

The analysis was carried out assuming these numerical values. The steadiest vertical displacements were observed in the case of 8.0 m/s, they are shown in Figure 10.

The critical wind speed depends on the modal mass, the less mass is excited, the more evident are the effects. Although, the analysis was performed only considering the first vertical mode shape, which is characterized by a frequency of 0,156 Hz, further dynamic analyses should be carried out considering higher natural vibration frequencies.

References

[1] *Morgenthal, G. "VXflow Primer" version 0.994, Weimar, Germany, May 2012*

[2] *SIMIU, E., SCANLAN, R. "Wind Effects on Structures" John Wiley & Sons, Inc., New York, USA, 1996, Chaps. 6 and 14.*

Study of vortex-induced vibrations on Volgograd Bridge

ABERLE, Marcus
KUAS, Karlsruhe, Germany

LESGIDIS, Nikolaos
AUTH, Thessaloniki, Greece

ROCHA, João Francisco
FEUP, Porto, Portugal

Abstract

This paper investigates force coefficients, Strouhal number and critical wind speed to estimate the aerodynamic performance of the Volgograd Bridge. A global FEM model was created using a commercial software package to determine the relevant dynamic parameters. Vertical displacements were obtained using a particle-based CFD code for a wide range of wind speeds. Numerical results show significant amplitudes even for moderate wind speeds. To reduce these vortex-induced vibrations (VIV) to an acceptable limit, tuned mass dampers (TMD) are used and their effects are also studied.

Introduction

Long span bridges are usually sensitive to wind loads. Since the collapse of the Tacoma Bridge in Washington many studies concerning the dynamic response of bridges were initiated in order to acquire more information on aeroelastic phenomena. These findings play an important role in the design process regarding the structural safety of bridges.

Several aerodynamic phenomena are capable of initiating critical vibrations in bridge structures such as buffeting, vortex-induced vibrations, galloping and flutter, among others. Vortex-induced vibrations can be an important issue for the safety of the bridge in cases when vortex shedding frequency and natural vibration frequency associated to one mode shape coincide, resulting in a resonance phenomenon.

An interesting case of vortex-induced vibrations was observed the 20th of May 2010 when the Volgograd Bridge (Figure 1) experienced vertical vibrations with maximum amplitudes of up to 71 cm.

Figure 1 — Volgograd Bridge oscillating due to wind excitation

Most of the problems observed in vortex-induced vibrations phenomena are directly connected to the geometry of the cross section. Regarding this, the current study tries to reproduce the measured response using various numerical methods and discussing some possible solutions.

Case Study

The Volgograd Bridge crosses the Volga River in the city of Volgograd (Russia). It is a long continuous steel girder, distributed in 10 spans with a total length of 1211. There are three main spans in the centre of 155 m long. The steel bridge deck consists of a box girder section strengthened with interior stiffeners (Figure 2). The continuous bridge beam as well as the cross section were modelled using the commercial software SOFiSTiK [1]. To simplify the dynamic calculations, the stiffeners were replaced using an equivalent thickness for the top and the bottom plate of the box section as shown in Figure 3. The cross-sectional properties of the simplified model were callibrated using experimental measurements of the Volgograd Bridge.

The internal pier to beam connenctions were modeled using pinned supports. A similar process was used for the abutments with an additional restraint of the torsional degrees of freedom at each abutment. The mass of the deck was modelled using 30 equally spaced lumped masses along each span.

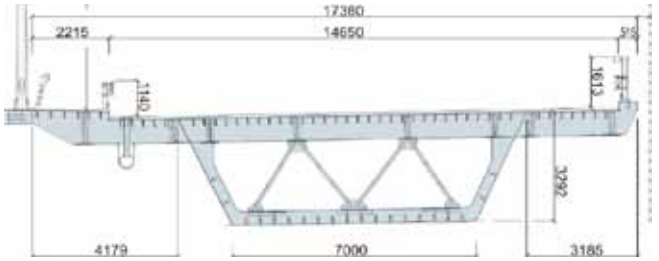

Figure 2 — Cross section of the Deck

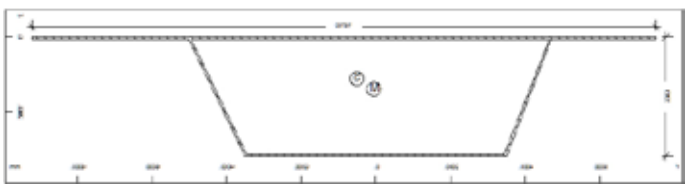

Figure 3 — Simplified deck cross section (SOFiSTiK FEM model)

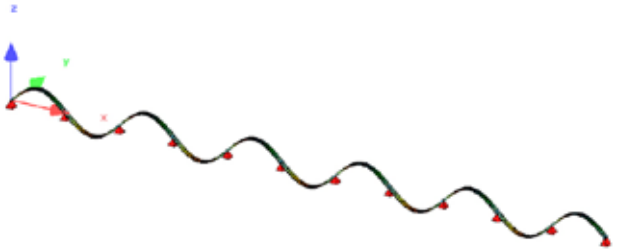

Figure 4 — Volgograd bridge 1st bending mode

A modal analysis of the first 10 modes was performed on the global beam model. In the present study only the first vertical bending mode, with a frequency of 0.44 Hz (Fig. 4), was utilized for the following calculations.

Static Analysis

To model the aerodynamic properties through the VXflow code [2], it is first necessary to discretize the perimeter of the cross-section and to specify the number of panels running in an anti-clockwise manner around the section as shown in Figure 5.

Figure 5 — Cross section of the deck (VXflow Model)

The vortex particle method in which VXflow is based [3], allows the user to obtain the force coefficients as well as the Strouhal number for a specified cross-section. Their knowledge then allows the determination of further parameters such as critical wind speed that identifies vortex-induced vibrations problems.

VXflow provides also the force coefficients shown in .

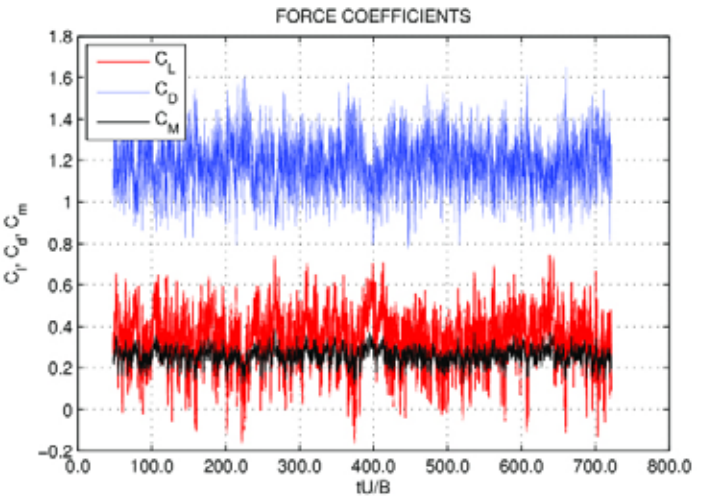

Figure 6 — Static Forces Coefficients

The mean force coefficients are as follows:

Lift Coefficient — $C_l = 0.34$
Drag Coefficient — $C_d = 1.18$
Moment Coefficient — $C_m = 0.26$

The Strouhal number for the cross-section given in Figure 5 can be identified from the spectral density plot of the lift forces given by VXflow [2]. Hence, the Strouhal number for the cross-section of the Volgograd Bridge is approximately St = 0.12 (Figure 7).

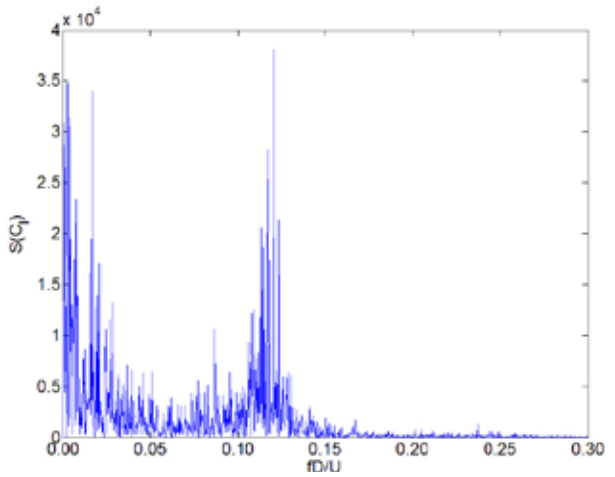

Figure 7 — Spectral density of lift forces

With knowledge of the Strouhal number, the cross-sectional reference depth and the first bending frequency of the structure it is then possible to calculate the critical wind speed for vortex-induced vibrations:

$$St = \frac{f \cdot D}{U} \rightarrow U_{crit} = \frac{f \cdot D}{St} = \frac{0{,}44 \cdot 3{,}8}{0{,}12} = 13{,}9\ m/s \quad (1)$$

where f = 0,44 Hz = first bending frequency of the structure
D = 3,8 m = reference depth
St = 0,12 = Strouhal number

Dynamic Analysis

The dynamic analysis performed with VXflow can then be used to determine the vertical displacements of the bridge for a wind speed range from 10 m/s to 20 m/s with increments of 1 m/s. However, from 13,1 m/s to 15 m/s vertical displacements were calculated in steps of 0.1 m/s. The modal mass of the first bending mode is 2500 kg/m and the modal stiffness is 19110 N/m². As the Volgograd bridge is a steel structure, the damping ratio (ζ) adopted for the present study is 0,3%. A plot of maximum vertical displacements is shown in Figure 8. A local peak can be observed associated to a wind speed of 14.7 m/s.

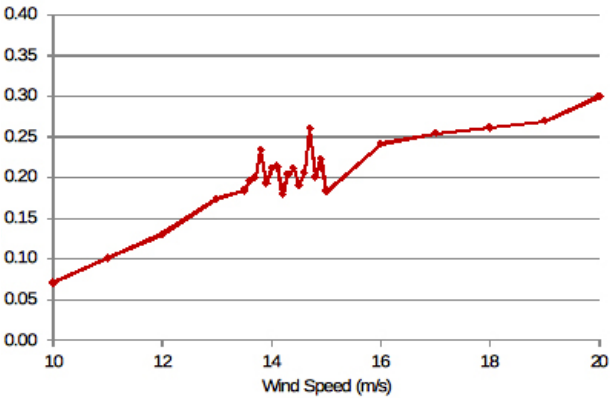

Figure 8 — Maximum vertical displacement for different wind speeds

In order to understand the evolution of the displacement for three different wind speeds, the time histories for 10 m/s, 14,7 m/s and 15 m/s are presented in Figures Figure 9 to Figure 11. As can be seen, positive displacements are higher than negative displacements. This is due to the fact that the cross section is not symmetrical respect to its horizontal axis. Also, vertical displacements for a wind speed of 14,7 m/s are considerably larger than the others. This is the critical value that identifies the VIV phenomenon.

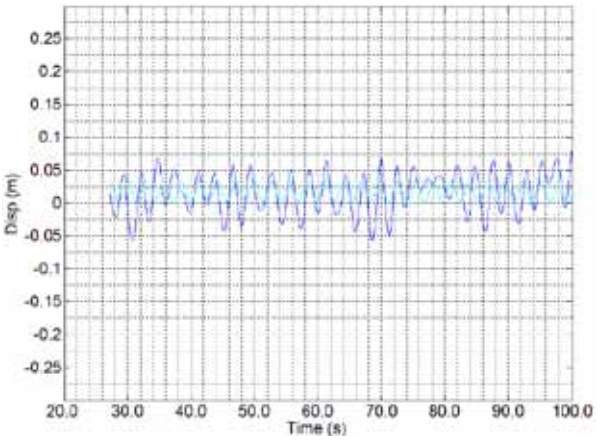

Figure 9 — Vertical displacement for a wind speed of 10 m/s

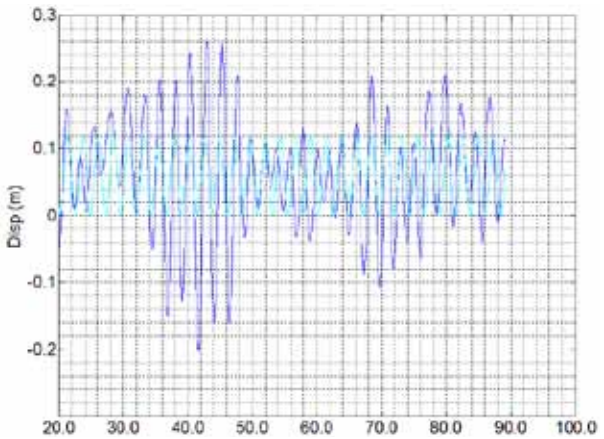

Figure 10 — Vertical displacement for a wind speed of 14,7 m/s

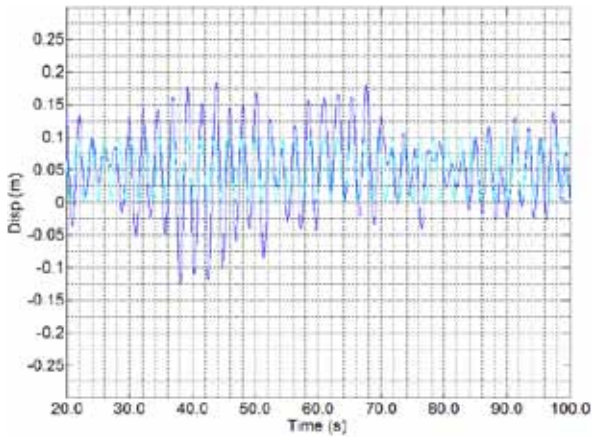

Figure 11 — Vertical displacement for a wind speed of 15,0m/s

A visualization using vortex-streaks generated on the airflow as a consequence of wind wind-structure interaction for a wind speed of 14.7 m/s can be seen in Figure 12.

The increase of vertical displacements for some critical wind speeds can generate some comfort problems or even fatigue damage of the structural elements of the bridge. In order to reduce them, tuned mass dampers (TMD) can be employed. For the Volgograd Bridge, these problems were minimized through TMD for the first three principal modes of vibration.

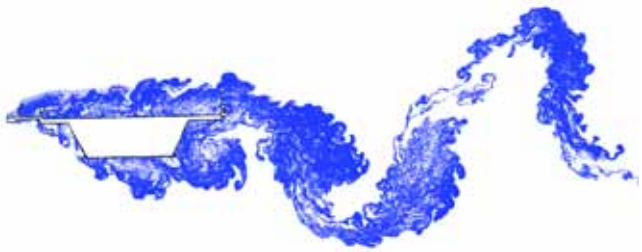

Figure 12 — Visualization of vortex formation through VXflow

Conclusions

This study presents the importance of wind-structure interaction analysis for long span bridges. Vortex-induced vibrations can influence on the bridge safety in cases when the vortex-shedding frequency and the natural vibration frequency of the bridge are close. As shown, for moderate constant value of the wind speed some amplification of the displacements of the cross section centre can be observed. This fact is due to the wind flow through the cross section. This study shows the feasibility of numerical methods to predict vortex-induced vibrations in some structures. This has been achieved by using a commercial finite element program for the determination of the dynamic properties of the structure in combination with the particle-based CFD code. It also helps to decide which countermeasures could be used in order to minimize such vibrations.

References

[1] *SOFiSTiK TUTORIAL, Version 10.21-99*

[2] *Morgenthal, G. "VXflow Primer" version 0.994, Weimar, Germany, May 2012*

[3] *Morgenthal, G. "Aerodynamic Analysis of Structures Using High-resolution Vortex Particle Methods" PhD Dissertation, Department of Engineering, University of Cambridge, UK, Oct. 2002*

Flutter analysis of Machang Bridge (South Korea)

BUDAHAZY, Viktor
BUTE, Budapest, Hungary

KOLEVA, Tatyana
UACEG, Sofia, Bulgaria

KISHAIJA, Paul
BUW, Weimar, Germany

Abstract

The aim of this paper is to investigate the flutter behaviour of the Machang Bridge by performing a 2-DOF-section model analysis. Aerodynamic studies are essential for slender bridges. Fluttering and aerodynamic properties can be improved by modifying the original section geometry. Three different sections were chosen and static, forced and dynamic simulations were performed and compared.

Introduction

The Machang Bridge is 1,7 km-long, dual two-lane bridge and it joins the cities of Masan and Changwon in the southern region of South Korea. The project features a 740m, cable-stayed bridge with a main span of 400m, side spans of 175m and two 164m-high, H-shaped

Figure 1 — The Machang cable-stayed Bridge in South Korea

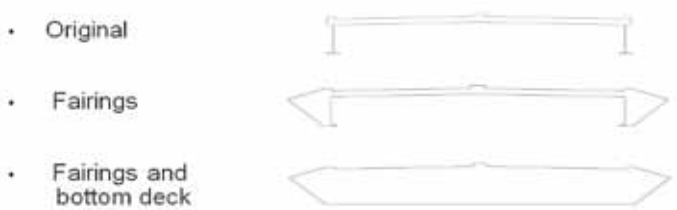

Figure 2 — Analysed cross sections

pylons. The bridge deck is composite, consisting of concrete slab on steel plate girders. The bridge opened to traffic in July 2008, shortening the commute between the twin cities by 30 minutes.

Flutter is a self-excited oscillatory instability, which is caused when aerodynamic forces supply energy to the oscillating structure and amplitude of the motion progressively increases. This behaves as "negative damping" and it occurs at any wind speed higher than a critical value, which is known as flutter limit.

Classical flutter is an aerodynamic phenomenon in which rotation and vertical translation couple together in a flow-driven, unstable oscillation. In this case the negative aerodynamic damping occurs and deformations reach such a level that failure happens [1].

Cases of analysis

Static simulations

The results show that the drag force has been reduced by more than 50% for the modified geometry of the cross-section.

	Cross Section numbers		
	CR 1	CR 2	CR 3
C_L	–0.27279	–0.5102	–0.19482
C_D	–0.91905	0.48555	0.49897
C_M	–0.01676	0.034571	0.017325

Table 1 — CL CD CM results for the three sections

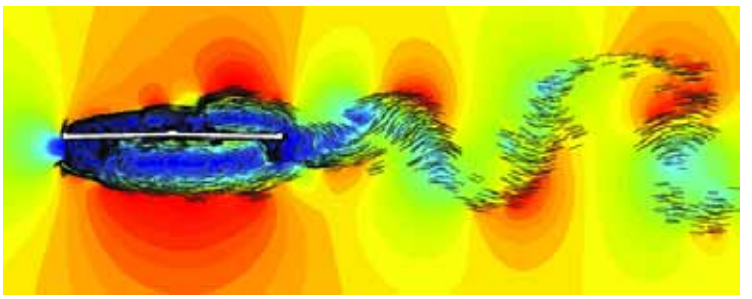

Figure 3 — Visualization of velocity field of original cross section (#1) with VXflow

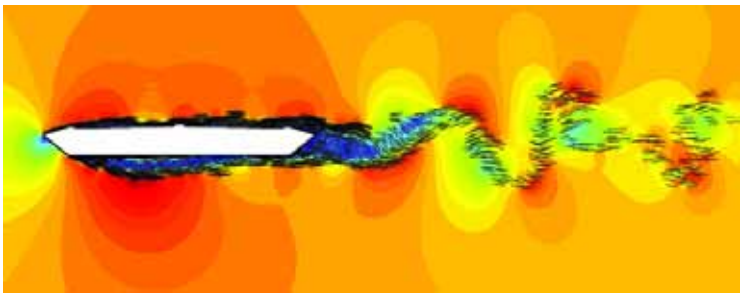

Figure 4 — Visualization of velocity field of modified cross section (#3) with VXflow

Forced oscillation tests

In case of forced vibrations, the structure is forced in heave and pitch oscillation with pre-determined frequency and amplitude. The aerodynamic derivatives are then calculated from the measured lift and moment and the critical wind speed is computed [1].

For the aerodynamic forces on a bridge cross-section, Scanlan proposed a set of expressions. It assumes that the self excited lift FL and moment FM may be treated as linear in displacement h and rotation α and their first derivatives.

The equations of motion are given in linearized form:

$$F_L = \frac{1}{2}\rho U_\infty^2 B\left[KH_1\frac{\dot{h}}{U_\infty} + KH_2\frac{B\dot{\alpha}}{U_\infty} + K^2H_3\alpha + K^2H_4\frac{h}{B}\right] \quad (1)$$

$$F_M = \frac{1}{2}\rho U_\infty^2 B\left[KA_1\frac{\dot{h}}{U_\infty} + KA_2\frac{B\dot{\alpha}}{U_\infty} + K^2A_3\alpha + K^2A_4\frac{h}{B}\right] \quad (2)$$

where H_i and A_i depend on the section geometry; U_∞ is wind flow velocity; h is the vertical displacement amplitude; α is the rotation amplitude.

A_i and H_i are known as aerodynamic or flutter derivatives and are measured only if the body is in oscillatory state.

In this paper the results of three different sections are compared by defining the A_2 values for each one of them, which represents torsional moment induced by pitching motion velocity. In order to define these derivatives, pitch forced oscillation cases are performed separately from the heave forced oscillation ones.

A_2 parameter can be used to predict the critical wind speed for each section. We can assume that section is unstable when the A2 curve becomes positive, which simplifies the flutter problem avoiding the influence of other flutter derivatives, which are less important than the first one (Figure 5).

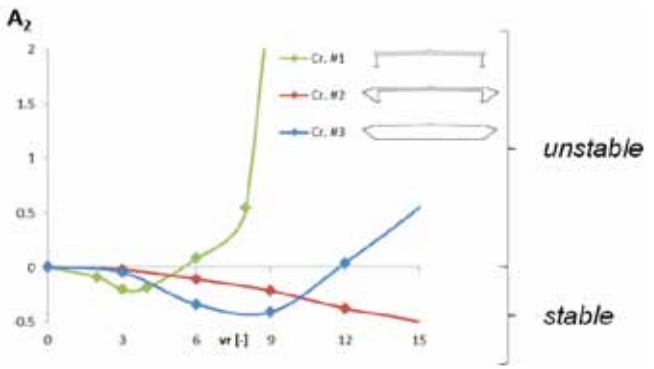

Figure 5 — A_2–V_R graphics

Flutter instability wind speeds can be predicted from as the point in with A2* becomes positive for each cross-section geometry. A2* values are normally given as a function of reduced wind speed ($v_{,red}$), which is equal to $v_{,red} = v \cdot T/B$, being v = wind speed, T = oscillation period corresponding to the modal shaped of the bridge (rotation, in this case) and B = section width (chosen as the reference geometry). With the improved two other sections, we move the instability wind speed to a higher value by getting a positive value for A2 at a higher reduced wind speed (v_{red})

Dynamic analysis

Cross section	Wind speed [m/s]				
	55	65	75	85	95
#1	✓	✓	✗	✗	✗
#2	✓	✓	✓	✓	✓
#3	✓	✓	✓	✓	✓

✗ Instable
✓ Stable

Table 2 — Critical wind speed for associated to flutter instability

The dynamic analysis shows that the original section becomes unstable when the wind speed reaches 75 km/h, while the modified cross sections are stable even at higher wind speeds. By using the triangular fairings on the borders, the bridge shows a stable behaviour under a wind speed of 95 m/s, which is the maximum expected wind speed in this region (typhoons effects). The closed section is the most stable, but only with the triangular fairings we are able to improve the cross-section behaviour section against flutter (torsional galloping, in this case).

Conclusions

- The behaviour of Machang Bridge was examined and evaluated
- The modification of the section reduces static wind forces. Drag and lift forces were decreased.
- The dynamic wind forces were also decreased. The fluttering is avoidable using only the fairings.

References

[1] *Abbas, T., Flutter analysis of suspension bridges using a two-stage numerical approach & flutter derivatives, Masters Thesis, 2011*

[2] *Morgenthal, G. "VXflow Primer" version 0.994, Weimar, Germany, May 2012*

[3] *Morgenthal, G. "Aerodynamic Analysis of Structures Using High-resolution Vortex Particle Methods" PhD Dissertation, Departament of Engineering, University of Cambridge, UK, Oct. 2002*

Excursion Report — City tunnel Leipzig 11th August 2012

According to the schedule of the Bauhaus Summer School, we started our excursion towards Leipzig on the August, 11th 2012 around 8:30 am at the Atrium in Weimar. It was one of the most exciting tours out of Weimar which had been fixed for the participants of Summer School "Model Validation and Simulation".

The bus was full of 50 persons out of whom 46 were students from the different universities of the different countries from Asia to Europe and South America. The tour was quite successful on both educational and cultural aspects. We visited an inner city railway construction site at Markkleeberg, at which a lot of specialities have to be considered and the City-Tunnel Leipzig which was one of the most attraction of our educational visit where we had seen the combination of latest engineering technologies applied to the reality. It was a great journey in the context of sharpening and shaping the engineering knowledge and experiences.

Figure 1 — Network of Central German suburban railways

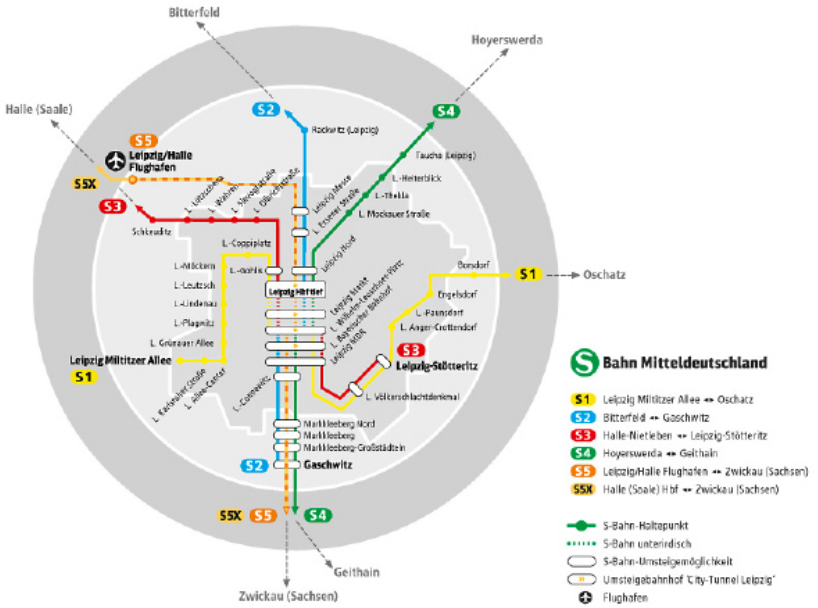

Figure 2 — Networking of Leipzig city map

Brief description of Leipzig City Tunnel:

The Leipzig city tunnel is the final and central component of the railway system restructuring process in Greater Leipzig. The completion of the tunnel will not only bring improvements to the suburban train system — transport between the region and the city will also be improved, and the tunnel will give a major impetus to the development of the city's transport system.

The tunnel provides a direct rail link between the area to the south of the city and the central station in the northern part of the city centre. Until now, trains travelling along the north-south axis have had to circumvent the city centre — a time-consuming process. In future, they will simply travel underneath it. In this way the Leipzig city tunnel will make regional rail traffic faster, more efficient and more convenient for passengers across the board. The fast north-south axis below Leipzig city centre will reduce total travel time by as much as 40 minutes on some routes. The city tunnel is the fast transport hub for central Germany. The S-Bahn urban railway network for the Central German region is the new backbone of S-Bahn and regional rail transport in the Leipzig/Halle conurbation. As of late 2013, six new S-Bahn urban railway lines will link the business region around Halle and Leipzig with the surrounding area faster and more efficiently, ensuring much shorter journey times by rail. The benefits will be felt by the entire region – economically, environmentally and in terms of a better quality of life. [1]

The Leipzig city tunnel has two 1.438 km long tunnels, one in each direction, and four underground stations — Bayerischer Bahnhof, Wilhelm-Leuschner-Platz, Markt and Hauptbahnhof (Central Station). The

shells of the tunnel and the stations have already been completed; work is currently in progress on fitting out the interiors of the four stations and preparing the tunnels for the trains. [1]

Tunnelling (brief features)

- The tunnel boring machine (TBM) has been designed and tailored to the specific needs of the city tunnel and the local soil conditions
- The shield diameter is 9.0 m
- The total weight of the TBM is 1,100 Mton
- Including the trailing section, the TBM has a length of 65 m
- The TBM has a total connected load of 2.5 MW
- The TBM is driven by 14 pairs of presses. Their maximum pressing power is 65 MN
- The integrated stone crusher is capable of crushing stones up to 80 cm edge length
- To pre-explore the ground, the TBM has been provided with a special seismic system capable of recognising any anomalies or boundaries of a bed 40 m in advance

Puskar Rijal
(author at the Bauhaus Summer School – Model Validation and Simulation)

[1] *http://www.citytunnelleipzig.de/de/kontakt-informationen/english-information.html (last visit 10/2012)*

Impressions from the Excursion:

a) Group picture of most of the participants

b) Enjoining Lunch at restaurant Bayrischer Bahnhof

c) Sightseeing in Leipzig city

d) Getting back to Weimar

Figure 3 — General Impressions

a) Introduction to the construction site

b) Questions by participants

c) Walk over railway under construction

d) Strenghtening of the ambutment by anchors

e) Reinforcement detailings

Figure 4 — Impressions from the construction site Markkleeberg

a) Waiting for entry to the subway station at Leipzig main station

b) Introduction to the metro station

c) Cabrio train tour at the city tunnel

d) Model of the drilling maschine at the InfoBox

e) Getting out from video season

f) Information about the construction of the City tunnel at the InfoBox

Figure 5 — Impressions from the city tunnel tour

Bauhaus Summer School

In the frame of the Bauhaus Summer School a diversified programm was organized. The participants were invited to participate at different activities like sightseeing tours, slogan parties, gaming night or a rubber rafting tour.

With the slogan "Bonvena" we welcome all the participants to Weimar. With music and good food the ice was fast brocken. Everyone comes wearing the colours of their home country or those of the country whose language they're going to learn at the Summer School.

In the frame of a guided city tour the participants could discover Weimar and its historical places, history and presence. Also trips to other cities like Berlin and Leipzig were offered.

Further a diversified evening programm were organized. The participants could show their talents at the legendary Bauhaus Song Contest and could come in contact with other people during the international gaming night. There was also a big final ceremony with the motto “Back to the 50's — Let's twist again."

IMPRESSUM

Schriftenreihe des Instituts für Konstruktiven Ingenieurbau

der Bauhaus-Universität Weimar

HERAUSGEBER

REDAKTION

Dipl.-Ing. Lars Abrahamczyk, Dr.-Ing. Jochen Schwarz,

Prof. Dr.-Ing. habil. Frank Werner

Satz

Lena Schindler

BEZUGSMÖGLICHKEIT

Verlag der Bauhaus-Universität Weimar

Fax +49 (0) 3643 58 11 56, E-Mail verlag@uni-weimar.de

DRUCK

docupoint Magdeburg GmbH

UMSCHLAGGESTALTUNG

Ulrike Mönnig

HAFTUNGSAUSSCHLUSS

This project has been funded with support from the European Commission.
This publication [communication] reflects the views only of the author, and the Commission cannot be held responsible for any use which may be made of the information contained therein.

Lifelong Learning Programme

http://nbn-resolving.de/urn:nbn:de:gbv:wim2-20130805-19969

ISBN 978-3-86068-502-0